CAMPUS group
Departamento de Química
Facultad de Ciencias
Universidad Autónoma de Madrid

Instituto Madrileño de Estudios Avanzados
en Nanociencia

Charge transfer between organic molecules and epitaxial graphene on metals

A thesis submitted for the degree of:
Doctor in Chemistry

Candidate:
Daniele Stradi

Supervisors:
Prof. Dr. Fernando Martín García and Dr. Cristina Díaz Blanco

June, 2013

[This page has been intentionally left blank]

Acknowledgements

During the past four years as a PhD student, I had the great pleasure of being a part of the *CAMPUS* group at the *Department of Chemistry* of the *Autonomous University of Madrid* and of the *Madrid Institute for Advanced Studies in Nanoscience*. At this point, I would thus like to gratefully acknowledge a number of people.

First and foremost, I would like to thank my supervisors Prof. Dr. Fernando Martín García and Dr. Cristina Díaz Blanco. I am deeply indebted to Fernando for having accepted me in its truly interdisciplinary research group, and to Cristina for her enormous patience. They have supported my project with enthusiasm, keen interest, and their guidance throughout this thesis has been invaluable.

In addition, I would especially like to thank the following people who have contributed to the development of this thesis:

- Prof. Dr. Rodolfo Miranda, for giving me the opportunity of being involved in the exciting and dynamic scientific environment of IMDEA-Nanoscience institute.
- Prof. Dr. Amadeo Vázquez de Parga, for being an exceptional friendly, and supporting collaborator, and for sharing with me all its knowledge in scanning tunnelling microscope techniques and physics during our numerous scientific discussions.
- Prof. Dr. Andres Arnau Pino, for inviting me many times at the Donostia International Physics Center in San Sebastian, for the incalculable number of illuminating discussions on almost every aspect of my calculations, and for the trust he put in me.
- Prof. Dr. Manuel Alcamí Pertejo, for its continuous support, its dedication and its advices.
- Dr. Enrico Gnecco, for having introduced me to the field of atomic force miscoscopy, and for involving me in the project of atomic force microscopy over graphene on Ru(0001).
- Dr. Daniel Sánchez Portal, for its numerous critical and constructive advices on electronic structure calculations.
- Dr. Sara Barja, Manuela Garnica and Dr. Fabián Calleja for perfoming all the spectacular scanning tunnelling microscopy measurements on graphene on Ru(0001) and on the TCNQ monolayers adsorbed on this surface, which complement the theoretical work presented in this thesis.
- Dr. Sascha Koch, for performing all the atomic force microscopy measurements on graphene on Ru(0001).

- Prof. Dr. Mads Brandbyge, for hosting me at the Danish Technical University in Copenhagen and for introducing me into the field of electronic transport.

- Prof. Dr. Pablo Ordejón, for inviting me at the CIN2 in Barcelona and for the very interesting discussion concerning the calculation of phonons in graphene on Ru(0001).

I would like to thank all the members of the committee of this thesis, Prof. Dr. Manuel Yañez Montero, Prof. Dr. Francesc Illas Riera, Prof. Dr. Gianfranco Pacchioni, Prof. Dr. Nicolas Agrait de la Puente, Prof. Dr. Jean-Pierre Gauyacq, Dr. Maria Veronica Ganduglia Pirovano, Dr. José Ángel Martín Gago.

I would also like to acknowledge all the institutions that generously founded my fellowship (FPI-UAM program), and allowed me to run the calculations on top-class supercomputers (Centro de Computacíon Científica de la UAM and Red Española de Supercomputación).

A big thank you also to all the past and the present members of the Department of the Chemistry at UAM, which provided a stimulant, friendly and familiar environment where I could profitably develop my research.

Finally, I would like to express my most sincere gratitude to my father and to all the members of my family, to all my friends spread all around the world, and to Ane, which have been always at my side, and shared with me all the best and the worst moments of the past five years.

Resumen

Gracias a la combinación única de propiedades electrónicas, mecánicas y ópticas, el grafeno, un material bidimensional compuesto por una sola lámina de carbonos sp^2, ha surgido recientemente como un material prometedor para ser empleado en la próxima generación de dispositívos tecnológicos. Sin embargo, hay varios puntos importantes que todavía no se han abordado. En particular, se debe conseguir abrir un *gap* energético suficientemente grande en su estructura electrónica, sin alterar sus peculiares propiedades electrónicas. Por otra parte, se deben elaborar rutas no invasivas para lograr un dopaje estable. Esto hace que el estudio de la interacción de grafeno con otras interfaces sea de fundamental importancia.

El dopaje por medio de moléculas tecnológicamente relevantes se ha propuesto como uno de los métodos mas eficaces para sintonizar las propiedades electrónicas del grafeno de manera eficaz. Sin embargo, los detalles precisos de la interacción molécula-grafeno quedan todavía en gran parte sin explorar. En este sentido, las monocapas de grafeno epitaxial sobre superficies de metales de transición son sistemas ideales para aclarar las propiedades de estas interfaces. Hoy en día, muestras de grafeno pueden ser crecidas sobre metales en dominios grandes y uniformes. Esto hace que estos sistemas sean sustratos ideales para la deposición de las monocapas moleculares. Por último, pero no menos importante, su carácter extendido permite explorar sus propiedades a escala nanométrica, por medio de técnicas de sonda como la microscopía de efecto túnel (STM) y la microscopía de fuerza atómica (AFM).

Esta tesis está dedicada a la caracterización de la interfase formada por el aceptor de electrones 7,7′,8,8′-tetracianoquinodimetano (TCNQ) y una monocapa de grafeno epitaxial crecida sobre una superficie de Ru(0001) (*gr.*/Ru). Por medio de cálculos precisos de estructura electrónica de gran escala, basados en la teoría del funcional de la densidad (DFT), se han estudiado las propiedades estructurales, electrónicas y mecánicas de *gr.*/Ru. Después de la caracterización de la superficie, se han investigado las propiedades electrónicas de los monómeros moleculares, de los dímeros y de las monocapas completas.

El grafeno epitaxial sobre Ru(0001) da lugar a una superestructura fuertemente ondulada, debido a la falta de correspondencia entre la constante reticular del grafeno, y la del sustrato metálico. A traves del uso combinado de modelos simplificados para esta superficie, y otros más sofisticados que consideran la formación de la superestructura de grafeno corrugado de manera realista, se ha demonstrado que las interacciones de van der Waals alteran considerablemente la geometría de la monocapa de grafeno, y reducen en un cuarto su corrugación. Tal reducción mejora considerablemente el acuerdo entre los perfiles de la superestructura obtenidos a partir de las imagenes STM simuladas y los perfiles medidos experimentalmente.

Se ha encontrado que la naturaleza ondulada de la superestructura de grafeno induce un confinamiento en dos dimensiones de los estados electrónicos localizados en la superficie. En particular, las características espectrales observadas en los experimentos de espectroscopía de efecto túnel (STS) cerca del nivel de Fermi se han asociado con la presencia de estados electrónicos fuertemente localizados por debajo de las regiones altas de la superestructura corrugada. Por otra parte, se ha confirmado que un estado vacío de intercara está fuertemente localizado en las regiones bajas de *gr.*/Ru, y se ha demonstrado que este estado es el que da lugar a la inversión de contraste observada experimentalmente en las imágenes STM medidas a voltajes muy positivos. Las propiedades mecánicas de *gr.*/Ru se han investigado mediante la simulación de la indentación, por medio de una sonda, de las regiones altas de la superestructura. Se ha encontrado que estas regiones responden de manera perfectamente reversible a grandes deformaciones, lo que confirma la sugerencia de medidas de AFM que las regiones altas de *gr.*/Ru pueden deformarse reversiblemente bajo compresión.

Los resultados obtenidos para una molécula de TCNQ aislada adsorbida en *gr.*/Ru indican que el sustrato transfiere un electrón a la molécula, y que este electrón desapareado permanece localizado en la molécula gracias a la presencia del grafeno, que desacopla de manera eficiente los estados moleculares de los del metal. Esta predicción ha sido confirmada por medidas STS, que muestran la presencia de una resonancia Kondo cuando la punta se coloca por encima de la molcula. El carácter magnético de las moléculas se conserva en el dímero y en la monocapa, debido a la formación de estados electrónicos intermoleculares deslocalizados. Los cálculos realizados en la monocapa molecular sin sustrato indican que estas bandas son casi planas, lo que es un requisito para el desarollo de estados fundamentales magnéticamente ordenados. En efecto, la presencia de orden magnético en la monocapa de TCNQ se ha confirmado por medidas experimentales de STM polarizado en espin.

Abstract

Thanks to the unique combination of extraordinary electronic, mechanical and optical properties, graphene, a two-dimensional material formed by a single sheet of sp^2 carbon atoms, has recently emerged as a promising material to be employed in the next generation of technological devices. Nevertheless, several important points still remain to be addressed. In particular, a sufficiently large energy gap must be opened in its electronic structure, without altering its peculiar electronic properties. Moreover, non-invasive routes to achieve stable doping must be devised, as well as methods to add new functionalities which are not intrinsically present in the pristine material. This makes the study of the interaction of graphene with other interfaces of fundamental importance.

Doping by technologically relevant molecules has been proposed as one of the methods to tune the electronic properties of graphene in an effective way. However, the precise details of the molecule-graphene interaction are still largely unexplored. In this sense, epitaxial graphene monolayers on transition metal surfaces are ideal systems to shed light on such interfaces. Nowadays, graphene samples can be grown on metals in large and uniform domains, which makes them ideal substrates for the deposition of molecular monolayers. Last but not least, their extended nature allows to address their properties at the nanoscale, by means of scanning probe techniques such as scanning tunnelling microscopy (STM) and atomic force microscopy (AFM).

This thesis is devoted to the characterization of the interface formed by the molecular electron acceptor 7,7′,8,8′-tetracyanoquinodimethane (TCNQ) and an epitaxial graphene monolayer grown on Ru(0001) surfaces (*gr.*/Ru). By means of accurate large scale electronic structure calculations based on density functional theory (DFT), the structural, electronic and mechanical properties of *gr.*/Ru have been studied. Following the characterization of the surface, the electronic properties of the molecular monomers, the dimers and the complete monolayers have been investigated.

Epitaxial monolayer graphene on Ru(0001) forms a strongly corrugated superstructure due to the mismatch between the lattice constant of graphene and that of the metallic substrate. Through the combined used of simplified models for this surface, and large models that account realistically for the formation of the corrugated graphene superstructure, it is shown that van der Waals interactions alter considerably the geometry of the graphene monolayer, and reduce its corrugation by one fourth. Such a reduction improves considerably the agreement between the perfiles of the superstructure obtained from the simulated STM images and the experimentally measured ones.

The corrugated nature of the graphene superstructure is found to induce a two-dimensional confinement of the electronic states localized at the surface. In particular, the spectral features

observed in scanning tunnelling spectroscopy (STS) experiments close to the Fermi level are associated with the presence of electronic states strongly localized below the high regions of the corrugated superstructure. Moreover, an unoccupied interface state is confirmed to be strongly localized in the low regions of *gr.*/Ru, and it is demonstrated that this state is at the origin of the inversion of contrast observed in the experimental STM images measured at high positive bias voltages.

The mechanical properties of *gr.*/Ru are investigated by simulating the indentation of the high regions of the superstructure by a probing tip. Such regions are found to respond in a perfectly reversible way to heavy deformations, confirming the suggestion made by AFM measurements that the high regions *gr.*/Ru can be reversibly deformed under compression.

Results for an isolated TCNQ molecule adsorbed on *gr.*/Ru indicates that the substrate transfer one entire electron to the molecule, and that this unpaired electron remains localized on the molecule thanks to the presence of graphene, that decouples efficiently the molecular states from those of the metal. This prediction is confirmed by STS, which shows the presence of a Kondo resonance when the tip is positioned above the molecule. The magnetic character of the molecules is found to be preserved in the dimer and the monolayer, due to the formation of delocalized intermolecular electronic states. Calculations performed on the free-standing monolayer indicate that such bands are almost flat, which is a prerequisite to develop magnetically ordered ground states. Indeed, the presence of magnetic order in the TCNQ monolayer is confirmed by spin-polarized STM experimental measurements.

Contents

Nomenclature

SXRD Surface x-ray diffraction

2PPE Two photon photoemission

AFM Atomic force microscopy

AIM Atoms in molecules

ARPES Angle resolved photoemission

BOA Born-Oppenheimer approximation

BOMD Born-Oppenheimer molecular dynamics

BZ Brillouin zone

CHC Core hole clock

CR Charging ratio

CVD Chemical vapour deposition

DFT Density functional theory

DOS Density of states

EA Electron affinity

FFT Fast Fourier Transform

GGA Generalized gradient approximation

GTO Gaussian Type Orbitals

HAS Helium atom scattering

HOMO Highest occupied molecular orbital

KFPM Kelvin force probe microscopy

KS Kohn-Sham

LAPW Linearly augmented plane waves

LCAO Linear combination of atomic orbitals

LDA Local density approximation

LDOS Local density of states

LEED Low energy electron diffraction

LUMO Lowest unoccupied molecular orbital

MD Molecular dynamics

PAW Projector augmented waves

PDOS Projected density of states

PES Photoemission spectroscopy

PES Potential energy surface

PP Pseudopotential

SCF Self consistent field

SOMO Singly occupied molecular orbital

SP-STM Spin-polarized scanning tunnelling microscopy

STM Scanning tunnelling microscopy

STO Slater type orbitals

STS Scanning tunnelling spectroscopy

SUMO Singly unoccupied molecular orbital

TCNQ 4,4′,8,8′-tetracyanoquinodimethane

TDSE Time-dependent Schröedinger equation

TISE Time-independent Schröedinger equation

TTF Tetrathiofulvalene

vdW van der Waals

XC Exchange-Correlation

XPS X-ray photoemission spectroscopy

List of Figures

Part I

Introduction

Technological revolutions in modern society have always been associated with the human capabilities to shape new materials. As a matter of facts, present advances in digital technology, inconceivable only few decades ago, would have been impossible without the efforts of silicon manufacturing industry. After silicon, graphene is strongly believed to be the material that will mark the following step in this process. First isolated in 2004, it has introduced the completely new field of two-dimensional crystals. In only ten years, research on graphene has received enormous worldwide attention [1], as certified by the recently fast-growing number of patents related to graphene [2, 3], dedicated research center and large pan-european funding programs [4], which culminated in 2010 in the awarding of the Nobel prize by graphene discoveres, A. Geim [5] and K. Novoselov [6].[1]

This thesis deals with the theoretical simulation of molecular adsorption on epitaxial monolayer graphene grown on transition metal surfaces. The primary aim is to understand and characterize those factors governing molecular auto-organization on these surfaces, by means of accurate realistic electronic structure calculations. Because of the presence of the graphene layer, new electronic phenomena arise at these interfaces after the deposition of molecular electron acceptors. Therefore, the entire study encompasses different topics, which are briefly reviewed in this introduction. In Section 1.1, the basic properties of graphene are outlined. Molecular functionalization of graphene is introduced in Section 1.2 as an effective method to tune the characteristics of the graphene sheet and add new functionalities. Section 1.3 describes the very different surfaces that can be obtained by growing graphene on different transition metal surfaces. Finally, Section 1.4 gives a very brief overview of the widely explored field of molecular self-assembly on single crystal metal surfaces, focussing on the influence on the charge redistribution at the surface, and describes the very first attempts that have been made to characterize of molecular self-assembly on epitaxial graphene on metals.

1.1 Graphene: a material with new and exciting properties

Graphene [8, 9, 10] is nothing more than a 2D honeycomb lattice of sp^2 hybridized carbon atoms. Although is was thought to be thermodynamically unstable, and therefore impossible to exist [11, 12], the unique characteristics of its electronic structure, such as the presence of singularities and its semi-metallic nature, have been recognized for about sixty years. This intensive theoretical research has been due to the fact that many properties of other carbon allotropes can be described in terms a perturbation of the graphene original electronic structure [13]. For graphite, this perturbation results by piling several graphene layers on top of the other. Fullerenes [14] can be created from graphene with the introduction of pentagons, which create a positive curvature. Finally, nanotubes [15] can be formed by rolling-up a single graphene ribbons along a given direction.

The extraordinary properties of graphene [16] are a direct consequence of its peculiar elec-

[1] ... as well as by the "subtle" commentaries that Geim received when trying to approach big multinationals companies to patent the discovery [7].

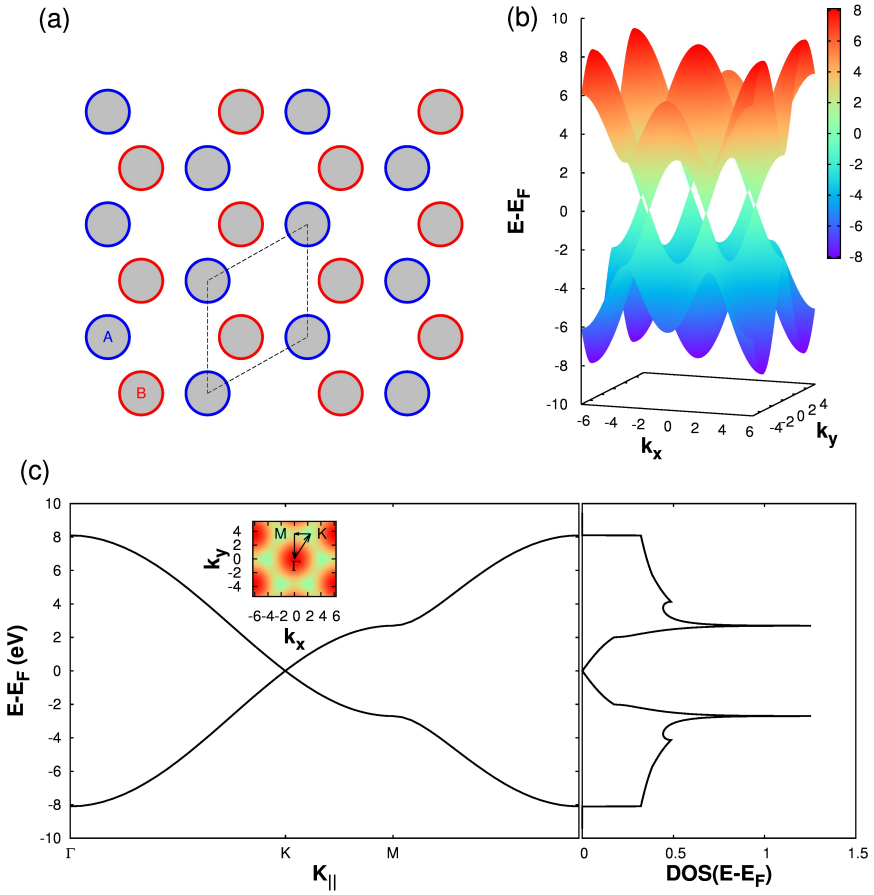

Figure 1.1: (a) structure of graphene. Different colors are used for sublattice **A** (blue) and **B** (red). The black dashed lines indicate the graphene unit cell. (b) π electronic bands of graphene obtained with a tight-binding model of graphene, setting $t = 2.7eV$ and $t' = 0$. (c) Band structure (left panel) along the high symmetry directions of the Brillouin zone (see inset) and corresponding density of states (right panel).

tronic structure. The sp^2 hybridization of each carbon atom leads to a trigonal planar structure, in which the sp^2 orbitals lying in the plane form strong σ bonds ($a \approx 1.42$ Å), while the $2p_z$ orbitals form an aromatic network that extends above and below the graphene plane. The σ bands have a filled shell, and, hence, form a deep valence band. The presence of such σ network gives to graphene an exceptional mechanical strength. Nevertheless, because it extends only along the xy-plane, the 2D sheet is still extremely flexible in the normal direction. This conferees to graphene a combination of robustness and flexibility that cannot be encountered in any other material. Indeed, the Young modulus of suspended graphene membranes, with linear sizes of hundreds of nanometers, has been estimated to be of the order of 1.0 TPa [17]. Nevertheless, its most peculiar characteristics are probably due to the extended aromatic network formed by the $2p_z$ orbitals. The most simple description of this π network can be made by considering a tight-binding Hamiltonian for the π electrons in the honeycomb lattice formed by the carbon atoms [18]. This honeycomb lattice is better described by dividing it in two compenetrated hexagonal sub-lattices, defined as **A** and **B** (see Fig. 1.1 (a)). Each sub-lattice has lattice parameters $\mathbf{a}_1 = \frac{a}{2}\left(3, \sqrt{3}\right), \mathbf{a}_2 = \frac{a}{2}\left(3, -\sqrt{3}\right)$, and reciprocal lattice-vectors $\mathbf{b}_1 = \frac{a}{2}\left(1, \sqrt{3}\right), \mathbf{b}_2 = \frac{a}{2}\left(1, -\sqrt{3}\right)$[1]. Given this lattice, one can construct a tight-binding Hamiltonian considering that the electrons can hop on the nearest neighbour and next-nearest neighbour lattice sites [18]:

$$H = -t \sum_{\langle i,j\rangle,\sigma} (a^\dagger_{i,\sigma} b_{j,\sigma}) - t' \sum_{\langle i,j\rangle,\sigma} (a^\dagger_{i,\sigma} a_{i,\sigma} b^\dagger_{j,\sigma} b_{j,\sigma}) \tag{1.1}$$

where $a_{i,\sigma}$ ($b_{i,\sigma}$) and $a^\dagger_{i,\sigma}$ ($b^\dagger_{i,\sigma}$) are annihilation and creation operators for the electron with spin σ on the site of the sublattice **A** (**B**), and t and t' are the nearest neighbour and next-nearest neighbour hopping energies. The solution of this tight-binding Hamiltonian gives energy bands of the form [18]:

$$\begin{aligned} E_\pm(\mathbf{k}) &= \pm t\sqrt{3 + f(\mathbf{k})} - t' f(\mathbf{k}) \\ f(\mathbf{k}) &= 2\cos\sqrt{3}k_y a + 4\cos\left(\frac{\sqrt{3}}{2}k_y a\right) + 4\cos\left(\frac{3}{2}k_x a\right) \end{aligned} \tag{1.2}$$

where $\mathbf{k} = k_x + k_y$ is a 2D wavevector, and the plus and minus sign are for the bonding π and anti-bonding π^* bands. t is approximatively 2.7 eV. For $t' = 0$, electron-hole symmetry is preserved, and therefore the electronic spectrum is symmetric with respect the Fermi energy. Fig. 1.1 (b-c) shows the electronic bands of graphene obtained using this approximated Hamiltonian. The most striking property is certainly the presence of singularities at the Fermi energy, where the π and π^* electronic bands touch only at well defined points in space. These points lie at the corners of the 1^{st} Brillouin zone in the reciprocal space, and are called K and K' points, depending on wether they are associated with the **A** or **B** hexagonal lattices describing the

[1] For the definition of lattice parameters and reciprocal lattice vectors see Chapter 2

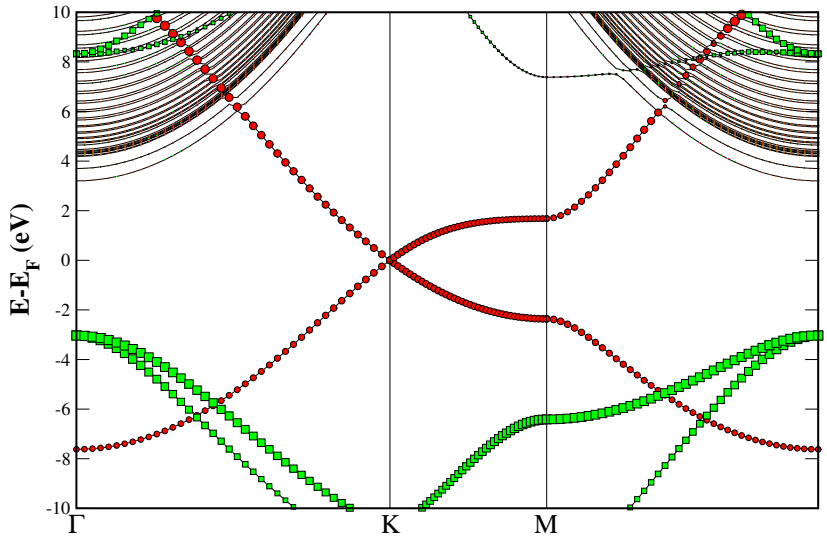

Figure 1.2: Band structure of graphene obtained with DFT/PBE and a plane-waves basis set. The π and $\pi*$ electronic bands are indicated with red circles, whereas the σ and $\sigma*$ electronic bands are indicated with green squares.

full honeycomb lattice of graphene. Thus, the common distinction made for all other materials between metal and insulators does not apply in graphene. In fact, in the latter, the number of electronic states at the Fermi level is zero, but there is not a finite gap between the occupied and unoccupied electronic bands. A second, even more astonishing, consequence of this peculiar electronic structure becomes evident if one considers how the electronic bands disperse, *i.e.*, how their energy (E) change with the momentum $\mathbf{k}$, moving away from the Fermi level. In the region around ± 1 eV with respect to the Fermi level, the dispersion is linear. Thus, the E($\mathbf{k}$) relation around the K, or K', may be described trough the relation [18]:

$$E_{\pm}(\mathbf{k}) = \pm \hbar v_F \mathbf{k} \tag{1.3}$$

where $v_F \approx 1 \times 10^6 m/s$ is called the *Fermi velocity*, which is about 1/300 of the speed of light. Thus, low lying excited electrons in graphene move extremely fast. This result is in striking contrast with the usual description of the free electron gas in terms of the Schrödinger equation, where $E(\mathbf{k}) = \frac{\mathbf{k}^2}{2m_e}$. This means that electrons in graphene in the close vicinity of the Fermi level are not described appropriately by the non-relativistic Schrödinger equation. lnstead, they are relativistic particles, described more correctly by Dirac-like equations such as that of Eq. 1.3 [19, 20]. For this reason, the K and K' points are also called *Dirac points*, and the regions of the π and π^* close to them the *Dirac cones*.

These electronic structure imparts a number of exceptional properties to the monolayer [21, 22]. Due to its zero-band gap character, graphene exhibits a strong ambipolar effect, so

that charge carriers can be either electrons or holes with concentrations as high as 10^3 cm^{-2}. Experiments have also reported charge carrier mobilities as high as 200,000 cm^2 V^{-1} s^{-1} on suspended graphene samples [23] and of even 500,000 cm^2 V^{-1} s^{-1} for supported graphene on boron-nitride samples [24]. In addition, due to its strictly 2D character, graphene has high transparency [25] (up to 97.4% optical transmittance [26]), and exceptional thermal conductivity (∼5000 W m K^{-1}) [27].

A more realistic description of graphene, based on the use of more advanced electronic structure methods [28] (see Chapter 3), reveals further peculiar characteristic features. For example, it can be seen that, as a consequence of the sp^2 hybridization, the σ and π electronic bands do not interfere with each other, even if they cross in energy at $E - E_F \approx$ - 6 eV. Moreover, at difference with the results presented in Fig. 1.1, electron-hole symmetry is broken. Finally, well defined electronic states can be distinguished in the unoccupied region of the electronic spectrum above ∼3 eV. These are weakly bound Rydberg-like *image potential states* [29], that graphene exhibits similarly to metals [30, 31].

1.2 Molecular functionalization of graphene

The peculiar electronic properties of graphene, such as the combination of very high electronic mobilities and extraordinary strength, has boosted the efforts to explore the potential of graphene for electronics application [32, 33, 34, 35, 36]. Thus, in only few years, several prototypes of graphene-based electronic devices have already been developed, including ultra-fast nanoscale transistors [37, 38], resonators [39, 40] and optically transparent electrodes [26, 25, 41].

However, in order to fully exploit the potential of graphene for electronics, several fundamental limitations must be overcome. The absence of a gap, for example, constitute a problem for the development of graphene transistors, in which stable on/off conditions must be achieved. For efficient electronic performance, the possibility to achieve a precise control of the number of carriers in the monolayer is also important. Moreover, it would be desirable to add new functionalities that are not intrinsically present in the graphene layer, such as magnetism. Consequently, considerable efforts are being made in understanding how it could be possible to modify the structure of graphene to tailor the properties of interest.

The functionalization of graphene with molecules [42, 43, 44], in this sense, looks like a promising alternative. Band gap opening can be achieved by hydrogenation [45], and magnetic properties have been observed in graphene after partial hydrogenation [46]. In addition, covalent functionalization of graphene with organic molecules has been also explored [47, 48, 49], employing, *e.g.*, diazonium salts [50]. However, although the electronic and chemical properties of graphene can be effectively tailored by covalent functionalization, the native electronic structure and physical properties of the monolayer are unavoidably disrupted, which directly leads to a severe decrease in the charge carrier mobility [51, 52].

An alternative way that has been pursued to overcome these limitations has been that of exploiting the aromatic character of the graphene monolayer, and functionalize it by molecular

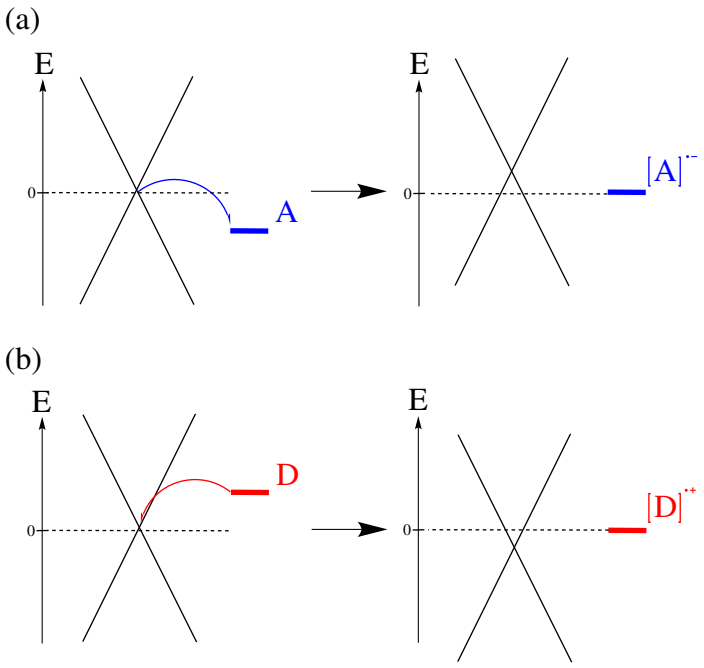

Figure 1.3: Schematic diagram of graphene doping by electron acceptors and donors. (a) If the EA of the acceptor (A) is higher than the Fermi energy of graphene, electron transfer of 1 electron occurs from graphene to the acceptor. Graphene becomes p-doped and the electron acceptor becomes a radical anion. (b) If the IP of the donor (D) is higher than the Fermi energy of graphene, electron transfer of 1 electron occurs from the donor to graphene. Graphene becomes n-doped and the electron donor becomes a radical cation.

physisorption. Indeed, the electronic properties of graphene have been found to be largely affected by the presence of even weakly adsorbed molecular species. The early attempts showed that the number of charge carriers in graphene can be modified by the adsorption of various gases, including NH_3, H_2O and NO_2 [53]. Those gases have been detected at remarkably low concentrations, and NO_2 has even been detected in the extreme limit of single molecules [53, 54]. This extreme sensitivity is a direct consequence of the vanishing density of electronic levels at the Fermi level of graphene, which makes them extremely sensible to even small variations of the carrier concentration. For this reasons, the first examples of molecular doping of graphene have pointed out the fact that this materials could be used as a sensor for chemical detection at the single molecule level [55, 56, 53].

Organic molecular acceptors and donors have been also widely used to achieve stable doped graphene [57]. In this respect, the presence of aromatic electronic clouds in such molecules allow them to interact only weakly on the graphene surface, via π-π staking interactions. In this case, graphene doping is achieved via surface transfer doping, *i.e.*, through the charge transfer at the interface between the surface adsorbate and the substrate [58]. By using molecules with either electron donating, or electron withdrawing functional groups, graphene has been

successfully doped with holes (p-type doping) and electrons (n-type doping). Electron acceptor (donor) molecules induce an electron transfer from (to) graphene, thus effectively doping it with holes (electrons). In this process, the most important parameters that determine the extent of the charge transfer are the 1^{st} *electron affinity* (EA) and the 1^{st} *ionization potential* (IP) of the molecule. If the molecule has a high EA, higher than that of the graphene Fermi level, electrons are transferred from graphene to the *lowest unoccupied molecular orbitals* (LUMO) of the molecule. Thus, hole doping of graphene also implies a negative charging of the molecule. Conversely, the opposite process occurs if the IP is higher than the graphene Fermi level. In that case, electron doping of graphene occurs and the molecule is charged positively (see Fig. 1.3).

The feasibility of such charge transfer doping has been demonstrated theoretically for the most common electron acceptors and electron donors molecules (TTF, TCNQ, F4-TCNQ, PTCDA, TCNE)[1] [59, 60, 61, 62, 63]. In this case, charge transfer smaller than 0.5 electrons / molecules have been reported[2]. Experimentally, synchrotron based *photoemission spectroscopy* (PES), have provided direct evidence for the surface transfer p-type doping of epitaxial graphene on SiC[3] [64]. Similarly, it has also been shown that by carefully tuning the number of electron acceptors on the same surface, the slight p-type doping induced in the epitaxial graphene layer can be fully compensated, thus effectively obtaining a perfectly neutral epitaxial graphene layer [65]. By employing switchable molecules, light driven doping has been also achieved [66]. Moreover, theoretical proposals have addressed the possibility of modifying the characteristics of the molecule-graphene interaction simply by means of the molecular orientation [60].

In summary, this by no means complete introduction on the possiblity of adding new functionalities to graphene through molecular adsorption, shows that the characterization and engineering of the processes that govern the charge transfer at the graphene-metal interface is an effective way to add new functionalities to graphene, by exploiting the well-established and flexible methods of organic and supramolecular chemistry [67, 68].

1.3 Epitaxial graphene on single crystal metal surfaces

Graphene has been known to be present on the surface of metals long before the isolation of the free-standing membrane in 2004 [69, 70]. In fact, the formation of carbon overlayers has been observed on the surfaces of, *e.g.*, Pt(111) [71, 72] and Ru(0001) [73], where characteristic *low energy electron diffraction* (LEED) patterns have been observed after annealing to high temperatures. The origin of these LEED patterns has been associated with the formation of graphitic layers on the surface, due to the segregation of carbon impurities from the bulk. In the context of heterogeneous catalysis, the formation of such overlayer is particularly important, because, for

[1] TTF: tetrathiofulvalene; TCNQ: 7,7′,8,8′-tetracyanoquinodimethane, F4-TCNQ: tetrafluoro-7,7′,8,8′-tetracyanoquinodimethane; PTCDA: perylene-3,4,9,10-tetracarboxylic dianhydride; TCNE: tetracyanoethilene

[2] For TCNQ, the molecule investigated in this work, the charge trasnfer is calculated to be 0.34 electrons / molecule [62].

[3] Note that, contrary to what occurs in the substrate that will be discussed in this thesis, graphene on SiC is practically decoupled from the substrate, and hence can be considered as almost free-standing graphene.

reactions involving hydrocarbons, the formation of a carbon overlayer on the catalyst surface is one of the primary reasons for the catalyst deactivation. However, the actual verification that such overlayers are formed by one single carbon sheet has been possible only with the advent of the *Scanning Tunnelling Microscope* (STM)[1] [74, 75].

Graphene has been first isolated by mechanical cleavage (*i.e.*, exfoliation) of graphite samples [76]. This technique results in high quality graphene, but it is very unlikely to produce samples large enough for scalable production and device fabrication. Thus, the growth of graphene on metallic substrate has regained attention, as a feasible way to produce large and uniform graphene samples. At present, there are two well-established methods to prepare graphene on metallic substrates [77]. In the first one, the monolayer is created directly from the segregation of the bulk material at high temperatures. In the second one, graphene is created directly on the surface using chemical vapour deposition (CVD), *i.e.*, via thermal decomposition of small hydrocarbons. Using this method, large and uniform graphene domains have be achieved, and graphene samples of even ∼1 inch sizes have been obtained [26]. Efficient transfer methods have allowed the so-grown graphene to be transferred efficiently to arbitrary substrates [78].

Similarly to molecules, transition metal contacts have been proposed as a possibile way to tune the electronic properties of graphene and introduce new functionalities [79, 80]. The initial interest in investigating the contact with graphene have been due to the fact that the electronic transport measurements through a graphene sheet require contacts to metal electrodes. Consequently, the detailed understanding of the characteristics of the interface between graphene and metals is of primary importance for the development of graphene-based electronics. Depending on the characteristics of the metal, the graphene-metal interaction, and the properties of the resulting epitaxial graphene layer, have been found to vary dramatically. Thus, depending on the nature of the underlying metal, the properties of an epitaxial graphene surface can be dramatically different. In particular, graphene-metal interfaces substrates can be divided principally in two types, depending on the strength of the graphene-metal interaction. In a first approximation, this depends on the position of center of the metal *d*-band with respect to the Fermi level [81]:

- **Weakly interacting graphene-metal interfaces**
  For metals in which the center of the *d*-band is ∼2 eV below the Fermi level, the interaction with graphene is relatively weak. This is the case of Cu(111) [82], Pt(111)[83, 84], Ir(111) [85, 86, 87, 88]. On these substrates, the characteristic features of the graphene electronic bands are essentially preserved. The graphene-metal distance is usually ∼3 Å, very similar to the interplanar distance in graphite (∼3.35 Å). However, the presence of a metallic surface induces shift of the Dirac point, thus effectively doping the supported graphene sheet. Indeed, this prediction has also been experimentally verified by *e.g.*, *angle resolved photoemission* (ARPES) experiments performed on epitaxial graphene monolayers grown, *e.g.*, on Ir(111) [45, 87] surfaces. This shift is a direct consequence of the different work function between the graphene monolayer (4.5 eV) and the metal. Thus by varying the

[1] See Appendix A.1 for a description of the method

metal substrate, it is possible to control the amount of hole or electrons in excess in the monolayer. In addition, the weak interaction between the graphene monolayer and the metal makes that multiple rotational domains on the same surface are easily formed by varying the experimental growth conditions [83, 84, 86].

- **Strongly interacting graphene-metal interfaces**
  For metals in which the center of the *d*-band is less than ∼2 eV below the Fermi level, the interaction with the graphene is much stronger, and the electronic structure of the monolayer is strongly perturbed. This is the case, for example, for Ru(0001) [74, 75, 89], Re(0001) [90], Co(0001) [91], Rh(111) [92], Ni(111) [93, 94]. On these metals, the graphene π electrons interact directly with the d_{z^2} orbitals of the topmost layer of the underlying metal surface, forming strong directional bonds [89]. As a consequence of this covalent bonding, the average graphene-metal distance lowers to ∼2 Å, much less than that present in weakly interacting metals. Due to this interaction, large electronic gaps, of ∼1-3 eV [95, 96, 97], open around the *K*-point. These modifications in the electronic structure of graphene are usually accompanied by strong charge redistribution at the graphene-metal interface, indicating the formation of new states in which the contribution from the substrate and the graphene is important. Therefore, the electronic structure of graphene on strongly interacting transition metals is considerably modified, so that the graphene and the substrate cannot be strictly considered as two separated entities. At difference with weakly bound graphene-metal interface, the strongest interaction between graphene and the underlying metal in most of the cases results in single orientational domains.

The structure of graphene on metallic substrates is further complicated when a considerable lattice mismatch (larger than ∼1 Å) is present between graphene and the underlying metal. This is the case, for example, of graphene grown on Ru(0001) [98, 75, 89, 99, 100], Rh(111) [92], Re(0001) [90], or Ir(111) [88]. On these metals, superstructures with larger periodicities are formed, which can be described in terms of moiré patterns [101]. The presence of a moiré necessarily implies that the positions of the graphene atoms, with respect to those of the metallic surface, vary periodically within the moiré unit cell [89]. Thus, in some regions the interaction is going to be more favourable, leading to stronger bonding, whereas in other regions the interaction is going to be less favourable, leading to weaker bonding. The difference in the strenght of the interaction between the weakly interacting regions and the strongly interacting regions is fundamental to determine the characteristics of the resulting moiré [89]. On weakly interacting metals, the presence of the moiré pattern can be seen as only a weak periodic perturbation to the graphene. This is the case, for example of graphene grown on Ir(111), where the moiré arises as a result of a very weak modulation in the bonding strength across the periodic superstructure [88]. Consequently, on such surfaces the periodic potential induced by the presence of the moiré has only reduced effects on the characteristics of the adsorbed graphene sheet, and the basic characteristics of the graphene electronic structure remain practically unaltered [45, 87]. On the other hand, on strongly interacting metal surfaces, the difference in the interaction between

the strongly interacting regions and the weakly interacting regions is usually much larger. This induces strong periodic perturbations on both the geometry and the electronic structure of the graphene layer, as evidenced, *e.g.*, by the strongly corrugated topographical images observed in STM, and by the appearance of different peaks relative to the 1*s* core-level of carbon in *X-ray photoemission spectroscopy* (XPS) [102]. Graphene grown on Ru(0001) (*gr.*/Ru), which is the surface considered in this work, falls under this second category. As it has been the first structure of this type to be observed [98], and it is by far the most widely studied and characterized [98, 75, 89, 99, 100, 103, 100, 104], it is usually considered as the prototype of all graphene moiré superstructures on strongly interacting substrates. However, as it will be discussed in Chapter 6 and Chapter 7, several of the precise details of its structure were poorly understood when we started this thesis, since there were several controversies in the interpretation of the experimental results. Thus, a significant part of this work has been devoted to build a reliable model for this surface, which is capable to reproduce at best the experimental observations.

1.4 Molecular self-assembled monolayers on epitaxial graphene on metal surfaces

Molecular self-assembly at single crystal metal surfaces has been extensively investigated [105, 106, 107, 108, 109], due to the fundamental interest in organic-metal interfaces for electronic and optoelectronic applications [110, 111]. When molecules are deposited on a surface, they may tend to form globally ordered structures, similarly to what happens in living organisms [68]. The possibility to self-assembly is strictly dictated by the competition among all the local interactions occurring between the molecules, and between the molecules and the surface [105]. Spontaneous organization results only in the case in which one, or only few, interactions, prevail over the others, thus becoming the driving force for the molecules to order in a particular pattern.

In real devices, the precise structure of the molecule-metal interface ultimately determines its properties, and therefore its functionality [114]. Thus, achieving control over the effects responsible for molecular auto-organization at surfaces is fundamental to exploit such a technology in functional devices. However, at present, very little is known about the factors that govern such phenomena, and the predictive synthesis of self-assembled monolayer at surfaces is still unachievable. Therefore, present research today aims at selecting case studies for self-assembly, and elucidating the role of the mechanisms that drive the formation of a particular structure.

Taking advantage of the know-how accumulated in the last decades concerning the role of non-covalent interactions in supramolecular chemistry [68][1], research has principally focussed on how intermolecular interactions determine the observed molecular structures [106]. Nowadays, it is generally accepted that, in those cases in which the interaction with the surface is rather weak, molecule-surface interactions only determine the adsorption geometry of the individual molecules, whereas auto-organized patterns are formed only when the molecules are able to form directional bonds [115, 116, 117, 118]. Conversely, there is much less physical understanding on those forces that determine the self-assembly process when the substrate plays a major role [119].

[1] Non-covalent interactions may include electrostatic, dispersive and H-bonding.

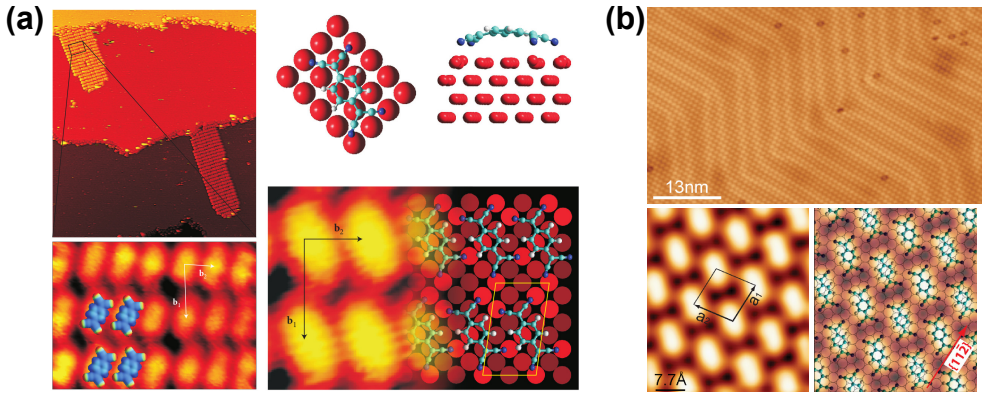

Figure 1.4: (a) On Cu(100) surfaces, the self assembly of TCNQ on can be understood only by considering a very distorted geometry for the molecule and the substrate, which results from the charge redistribution at the interface due to the strong molecule-surface interaction. Images adapted from Ref. [112]. (b) On Au(111) surfaces, the interaction of the molecule is much weaker, and the self-assembly is dictated by intermolecular interactions. Images adapted from Ref. [113].

One of the main complications is the fact that on reactive surfaces, molecules with heteroatoms, such as oxygen, nitrogen or sulfur, tend to form strong covalent bonds with the surface, in a process that involves usually a strong charge redistribution at the molecule-substrate interface [120]. Thus, the structure of the adsorbed molecular species differ completely from that of the same molecule in the gas-phase [112, 121, 120]. Moreover, the strong molecule-surface bonding may also mediate a surface reconstruction, that also influences the ordering process [122, 112]. Of particular interest to this work is the fact that the first clear example of the dominant role of substrate-molecule interaction on molecular self-assembly has been observed for TCNQ molecules self-assembled on Cu(100) [112] (see Fig. 1.4 (a)). In that case, observed self-assembled pattern could only be explained by considering the cooperative effects of the charge transfer at the interface, and of the complex reconstruction at both sides of the molecule-surface interface mediated by this charge transfer, which involved significant distortions both in the molecular geometry, and in the surface atoms. On the other hand, a completely different behaviour has been observed for TCNQ monolayers on Au(111) [113] (see Fig. 1.4 (b)). In the latter case, the interaction with the substrate is rather weak, and consequently the intermolecular interactions govern molecular organization.

The growth of ordered molecular monolayers on epitaxial graphene has been observed experimentally for the first time for PTCDA[1] aromatic molecules adsorbed on graphene on SiC(0001) [125]. On such semiconductor, the graphene electronic structure is almost unperturbed by the presence of the underlying substrate. Thus molecular ordering has been found to be dictated mainly by molecule-molecule interactions. Nevertheless, successful functionalization of the

[1] PTCDA: perylene-3,4,9,10-tetracarboxylic dianhydride.

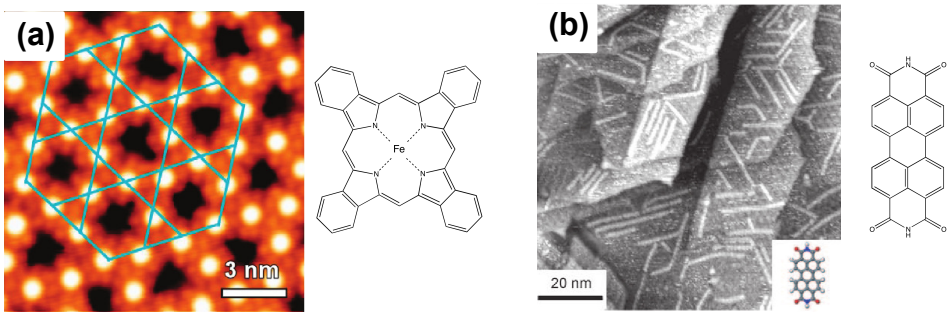

Figure 1.5: The two first examples of molecular self-assembly on strongly interacting graphene-metal interfaces. (a) Iron-phtalocyanine on epitaxial graphene on Ru(0001). Image adapted from Ref. [123]. PTCDI on epitaxial graphene on Rh(111). Image adapted form Ref. [124].

graphene monolayer was claimed, because of the appearance of characteristic features in the measured scanning tunnelling spectroscopy spectra (see Appendix A.2) clearly different form those of pristine graphene on SiC(0001) [125].

Thus, the next step towards the characterization of self-assembled monolayers on epitaxial graphene structure has been that of considering how a modification of the graphene morphology and of its electronic structure influences the molecular structures. By introducing a substrate which modify substantially the graphene monolayer, one introduces a new degree of freedom in the list of factors that determine the property of the interface. Through the careful combination of the properties of the molecule and those of the underlying metal, new phenomena may occur with respect to molecular layers on free-standing, or almost free-standing graphene.

The studies addressing molecular self-assembly on graphene grown on strongly interacting metal surfaces are still extremely scarce. In the first-ever report of molecular adsorption on graphene-metal surfaces, phtalocyanines and metal-phtalocyanines have been adsorbed on *gr.*/Ru [123] (see Fig. 1.5 (a)). In these case, it has been observed that the graphene monolayer has a strong influence of the geometry of the self-assembled monolayer, because the molecules tend to adsorb only on selected surface sites. This peculiar property has allowed the contruction of a Kagome lattice[1] formed by the metallic centers of the metal-phtalocyanines on the surface of *gr.*/Ru. Moreover, intramolecular resolution has been observed with STM. This latter fact suggests that, very similar to the case of ultra-thin films of alkali-halides [126, 127], the graphene acts as a buffer layer, and decouples the molecular states from those of the underlying metal. Similarly, a strong influence of the moiré structure has been reported for PTCDI[2] molecule and its derivatives adsorbed on the surface of epitaxial graphene on Rh(111) [124] (see Fig. 1.5 (b)). Also in that case, it has been observed that the molecules tend to adsorb preferentially on some regions of the graphene moiré. A commensurate match between the molecule and the moiré structure

[1] A Kagome lattice is a two dimensional lattice composed of interlaced triangles whose lattice points have four neighbouring points each, and it is considered the most geometrically frustrated magnetic system.

[2] PTCDI: perylene-3,4,9,10-tetracarboxylic diimide

has been suggested to result in the alignment of the molecules into extended one-dimensional chains, in striking difference with the packed structure obtained for the self-assembly of the very similar PTCDI molecule on graphene on SiC(0001). In both cases, a weak interaction between the molecule and the underlying substrate was assumed, and the possibility of charge transfer between the surface and the molecule, and its influence on the self-assembly, was not considered. Other subsequent similar studies lead to similar conclusions [128, 129, 130, 131, 132, 133, 134]: (i) the graphene layer acts as a buffer layer, and therefore decouples the molecular states from those of the metal; (ii) the graphene acts as a template, so that the molecules adsorb only on selected regions of the graphene moiré.

1.5 Motivation and Objectives

Epitaxial graphene monolayers grown on metallic surfaces thus appear as ideal candidates to characterize, at the nanometer scale, the effects of charge transfer at molecule-graphene interfaces, which have been briefly introduced in Section 1.2. As it has been mentioned in Section 1.3, large and relatively defect-free monolayer graphene domains can be grown on the low-index surfaces of metals [70, 77]. Therefore, such domains can be effectively considered as clean surfaces where molecules can be deposited and where they can self-assemble. Scanning probe techniques [135] then allow to address the structure and the electronic properties of the resulting molecular patterns at the atomic level, thanks to the conductive character of the substrate, as confirmed by a number of already existing examples [123, 124, 128, 129, 130, 131, 132, 133, 134], reported in Section 1.4.

The use of such interfaces thus makes it possible to explore with unprecedented details the effects of metallic contacts on the properties of the graphene monolayers, and their consequences on the adsorbed molecular layers. Indeed, the choice of the most appropriate substrate for this particular purpose is crucial. In weakly interacting graphene-metal interfaces, the electronic structure of the graphene remains almost unperturbed, so that the molecules will behave almost as if they were adsorbed on a free-standing graphene sheet. On the other hand, in strongly interacting graphene-metal interfaces, the properties of the graphene layer are considerably modified, and the effects of such modifications on the properties of the molecular monolayer are likely to be much larger than in the case of weakly interacting graphene-metal interfaces. Therefore, strongly interacting graphene-metal interfaces appear to be the most promising ones to explore the effects of graphene modifications on the properties of self-assembled monolayer on epitaxial graphene on metals.

At present, experimental results addressing the molecular self-assembly on epitaxial graphene on metallic surfaces are still extremely scarce. One reason for this is certainly the intrinsic complexity of graphene-metal surfaces, which makes it difficult to characterize their details and to develop a conceptually simple understanding of the molecule-surface interaction. Theoretical calculations thus represent a unique tool to support and interpret new experimental results, and provide guidance on how new experiments should be designed.

In this respect, the main aim of this thesis is the characterization of the interface formed by the electron acceptor molecule 7,7′,8,8′-tetracyanoquinodimethane (TCNQ) [136], and the surface formed by an epitaxial graphene monolayer grown on Ru(0001) [74, 75]. The entire work has been carried out in close collaboration with experimental groups specialized in the use of scanning probe techniques. In this collaborative effort, the theoretical calculations have been used to support and provide insight into the experimental results, as well as to predict the appearance of new electronic phenomena, which existence has been subsequently verified by the experiments.

The accurate description of the surface is a fundamental prerequisite for a reliable theoretical modelling of any molecule-surface interface. Therefore, the first objective of this work has been the construction and validation of a reliable model to describe the *gr.*/Ru surface. This issue is far from being trivial, mostly because the experimental data available that were available at the beginning of the thesis lead to contradictory conclusions [100, 137, 138, 75, 139, 140, 141, 142, 143, 144, 145]. Consequently, at the beginning of this thesis the experimentally determined geometry of the surface was unknown. In view of this, the model employed to describe *gr.*/Ru has been designed to describe, at least, all the essential features of the system. In particular, the formation of the moiré pattern [139, 89] has been accounted for realistically. Consequently, this choice has involved the use of large unit cells, formed by hundreds of atoms, which has imposed some serious limitations on the possible methods to describe the electronic structure. To maintain a good compromise between accuracy and computational efficiency, *density functional theory* (DFT) [28, 146] has been employed. For similar reasons, van der Waals interactions, that generally are not described accurately by DFT, have been taken into account qualitatively by using an efficient semi-empirical correction scheme [147]. Within this computational framework, the calculations performed by using these large unit cells have been complemented by a qualitative analysis performed on simpler models for the *gr.*/Ru surface, in which the moiré is not taken into account.

The structural, electronic, and mechanical properties of the theoretical model describing the *gr.*/Ru moiré have been validated against reliable experimental data. In particular, its electronic properties have been compared with *scanning tunnelling microscopy* (STM) [148, 149, 149] and *scanning tunnelling spectroscopy* (STS) measurements on *gr.*/Ru, whereas the mechanical properties have been checked against *atomic force microscopy* (AFM) [150] experiments performed on the same samples. All the STM, STS and AFM data have provided complementary informations on the geometry of *gr.*/Ru. The entire validation process has been accomplished by simulating the corresponding experiments, within the approximations imposed by the computational methods employed [135].

This theoretical model has been then used to investigate the adsorption of TCNQ on *gr.*/Ru. TCNQ has been chosen because it is one of the most common molecular electron acceptors, which has been extensively characterized both theoretically [151, 152] and experimentally [153, 154]. Due to its acceptor properties, it also exhibits a very rich chemistry, as demonstrated by its ca-

pability to form charge-transfer salts that exhibits metallic [155] as well as magnetic properties [156]. Moreover, as it has been shown in Section 1.4, its has been already demonstrated that TCNQ monolayers can self-assemble on solid surfaces, with very different patterns that can be formed depending on the precise characteristics of the underlying surface and on the charge redistribution at the organic-metal interface [112, 113]. These characteristics make TCNQ an ideal molecule to address the effects of charge transfer on the molecular auto-organization on *gr.*/Ru. To describe the progressive formation of molecular monolayers on this surface, the adsorption of an increasingly larger number of molecules has been studied. The isolated monomers, the dimers and the full ordered monolayer have been considered, which are representative of the molecular structures observed experimentally. Also in this case, the reliability of the calculated structures has been assessed by simulating the corresponding STS and STM experiments. On the basis of the results obtained for the molecular species, complementary calculations have been performed for the molecular structures in the gas-phase and on simplified models for the *gr.*/Ru surface, in order to obtain a comprehensive understanding of the electronic interactions that drive the formation of the ordered molecular layers.

1.6 Outline of the thesis

This dissertation is organized as follows: the second part of the manuscript presents the fundations of the methodology organized in four chapters. Chapter 2 is devoted to expose the basic concepts related to the solution of the electronic structure problem in periodic systems. Chapter 3 describes how such concepts are implemented in the DFT framework. In Chapter 4, the principal tools used for the analysis of the electronic structure of the system, obtained by using DFT, are introduced. Finally, Chapter 5 explains how scanning probe experiments can be simulated by using DFT.

The results obtained during this thesis are presented in the third part. The chapters are based on articles published (or submitted) in international journals of chemistry and physics. Chapter 6, Chapter 7 and Chapter 8 deal with the characterization of the structural, electronic, and mechanical properties of the *gr.*/Ru, respectively. Chapter 9 consider the adsorption of TCNQ on *gr.*/Ru, and provides a detailed analysis of the electronic properties of the resulting adsorbed molecular species. The most relevant conclusions are drowned in the fourth (Spanish) and fifth (English) part of the Thesis. Some appendices are included to provide further informations on the working principles of the experimental methods that have been simulated, as well as additional results supporting those presented in the main text.

Part II

Theoretical methods

2 Electronic Structure of periodic systems

In this Chapter, the basic concepts related to the application of electronic structure methods to periodic systems, such as the bulk and the surfaces of crystalline solids, are introduced. In Section 2.1, the Shrödinger equation is presented, in its time-dependent and time-independent formulations, as a general tool to compute the electronic structure of many-body systems. Then, in Section 2.2, the Hellmann-Feynman theorem, which allows to calculate the forces experienced by the nuclei for a given electronic configuration, is derived starting from the time-independent Shrödinger equation. Section 2.3 deals with the Born-Oppenheimer approximation, which further simplifies the treatment of the many-body problem by considering the motion of the electrons and nuclei independently. In Section 2.4 and Section 2.5, the Bravais lattice and the reciprocal lattice are described, and used to introduce, in Section 2.6, the Bloch's theorem and the solution of the monoelectronic Schrödinger equation in a periodic potential. The formal definitions of band structure and density of states are given in Section 2.7. The last two sections deal with more technical problems associated with practical electronic structure calculations: Section 2.8 defines the most common scheme used to sample efficiently the electronic structure of a periodic solid, while Section 2.9 describes how this can be achieved, without loss of accuracy, in the case of metals.

2.1 Schrödinger equation

In the attempt to describe the physics of complex chemical systems, such as bulk solids and surfaces, we have to confront with a complex many-body problem: matter consists of mutually interacting atoms, and every atom, in turn, consist of electrons interacting with each other and with the nuclei. The Schrödinger equation provides an elegant solution to this problem, because it allows to describe, exactly, systems formed by all these interacting particles.

According to wave mechanics [157], any physical state of a system composed by electrons and nuclei can be described, at any time t, by a wavefunction $|\Phi(\mathbf{r}, \mathbf{R}, t)\rangle$, where $\mathbf{r}$ and $\mathbf{R}$ are vectors representing the electronic and nuclear degrees of freedom, respectively. The general expression describing the time evolution of such wavefunction,

$$\hbar i \frac{\partial}{\partial t} |\Phi(\mathbf{r}, \mathbf{R}, t)\rangle = \hat{H} |\Phi(\mathbf{r}, \mathbf{R}, t)\rangle, \tag{2.1}$$

is known as the *time-dependent Schrödinger equation* (TDSE).

If we now assume that the non-relativistic Hamiltonian $\hat{H}$ in Eq. 2.1 does not depend on time, for a given system formed by n electrons and N nuclei, $\hat{H}$ can be described as:

$$\begin{aligned}\hat{H} &= \hat{T}_N(\mathbf{R}) + \hat{T}_e(\mathbf{r}) + \hat{V}_{Ne}(\mathbf{R},\mathbf{r}) + \hat{V}_{NN}(\mathbf{R}) + \hat{V}_{ee}(\mathbf{r}) \\ &= -\sum_{\alpha=1}^{N}\frac{\hbar^2}{2M_\alpha}\nabla_\alpha^2 - \sum_{i=1}^{n}\frac{\hbar^2}{2m_e}\nabla_i^2 - \sum_{\alpha=1}^{N}\sum_{i=1}^{n}\frac{Z_\alpha q_e^2}{r_{\alpha i}} \\ &+ \sum_{\alpha=1}^{N}\sum_{\beta>\alpha}^{N}\frac{Z_\alpha Z_\beta q_e^2}{r_{\alpha\beta}} + \sum_{i=1}^{n}\sum_{j>i}^{n}\frac{q_e^2}{r_{ij}},\end{aligned} \tag{2.2}$$

where $\nabla^2 = \frac{\partial^2}{\partial x^2}\mathbf{i} + \frac{\partial^2}{\partial y^2}\mathbf{j} + \frac{\partial^2}{\partial z^2}\mathbf{k}$, α and β refer to the N nuclei, and the indexes i and j to the n electrons. In Eq. (2.2), $\hat{T}_N(\mathbf{R})$ and $\hat{T}_e(\mathbf{r})$ represent the kinetic nuclear and kinetic electronic operators, respectively. $\hat{V}_{Ne}$ is the potential operator which describes the attraction between electrons and nuclei, with $r_{\alpha i}$ being the distance between the nucleus α and the electron i. The other two potential terms, $\hat{V}_{NN}$ and $\hat{V}_{ee}$, represent the internuclear and interelectronic repulsion operator, $r_{\alpha\beta}$ being the distance between the nuclei α and β, and r_{ij} being the distance between the electrons i and j, respectively. Assuming that $|\Psi(\mathbf{r},\mathbf{R})\rangle$, the time-independent wave function, is an eigenvalue of $\hat{H}$, it is possible to make the following *ansatz*:

$$|\Phi(\mathbf{r},\mathbf{R},t)\rangle = |\Psi(\mathbf{r},\mathbf{R})\rangle|f(t)\rangle, \tag{2.3}$$

where $|f(t)\rangle$ is a generic function, which describes the time evolution of $|\Phi(\mathbf{r},\mathbf{R},t)\rangle$. Substituting Eq. 2.3 in Eq. 2.1, the following expression is obtained:

$$-\frac{\hbar}{i}\frac{1}{|f(t)\rangle}\frac{\partial|f(t)\rangle}{\partial t} = \hat{H}|\Psi(\mathbf{r},\mathbf{R})\rangle. \tag{2.4}$$

By making both sides of Eq. 2.4 equal to a constant, it is possible to separate it in a set of two independent differential equations:

$$\frac{\partial|f(t)\rangle}{|f(t)\rangle} = -\frac{iE}{\hbar}dt, \tag{2.5}$$

$$\hat{H}|\Psi(\mathbf{r},\mathbf{R})\rangle = E|\Psi(\mathbf{r},\mathbf{R})\rangle. \tag{2.6}$$

Eq. 2.5 is a time-dependent equation, while Eq. 2.6 is known as the *time-independent Schröedinger equation* (TISE). Since $\hat{H}$ is hermitian, the constant E is a real number, that correspond to the energy of the state represented by the eigenfunction $|\Psi(\mathbf{r},\mathbf{R})\rangle$.

Taking $|f(t)\rangle = e^{-\frac{i}{\hbar}Et}$, it follows that

$$|\Phi(\mathbf{r},\mathbf{R},t)\rangle = |\Psi(\mathbf{r},\mathbf{R})\rangle e^{-\frac{i}{\hbar}Et}. \tag{2.7}$$

Eq. 2.7 represent the so-called *stationary states*, in which the system has a well-defined energy and a *probability density* constant on time:

$$\langle \Phi(\mathbf{r}, \mathbf{R}, t) | \Phi(\mathbf{r}, \mathbf{R}, t) \rangle = |\Psi(\mathbf{r}, \mathbf{R})|^2. \tag{2.8}$$

Similarly to the TDSE, also the TISE exhibits a dependence on time. However, in the latter this dependence enters only as a wave phase, which makes the energy and the probability density time-independent. The *spectrum* of solutions of the TISE depends on n and N, and it can vary from a set of discrete states, such as in an isolated molecule or atom, to a *continuum* of states, such as in an infinite periodic solid. Among the different solutions, the lowest-energy one plays a key role in chemistry and physics, and is commonly referred to as the *ground state*.

2.2 Hellmann-Feynman theorem

In principle, the evaluation of the force acting on the nucleus α, $\mathbf{F}_\alpha$, in a system formed by N atoms, involves the numerical computation of the gradient of the energy with respect to the displacement of each nucleus α in the three cartesian directions:

$$\mathbf{F}_\alpha = -\frac{dE}{d\mathbf{R}_\alpha} = -\nabla_\alpha E. \tag{2.9}$$

For systems where N is large, this could turn in a cumbersome problem. In this respect, the Hellmann-Feynman theorem provides a straightforward way to obtain the force $\mathbf{F}_\alpha$.

The theorem can be demonstrated by considering the TISE in its mean value form:

$$E = \langle \Psi(\mathbf{r}, \mathbf{R}) | \hat{H} | \Psi(\mathbf{r}, \mathbf{R}) \rangle. \tag{2.10}$$

By computing the gradient ∇_α of Eq. 2.10, it can be seen that the expectation value of $\hat{H}$ can be connected with the variation of the system's energy with respect to an arbitrary variation of the coordinate $\mathbf{R}_\alpha$:

$$\begin{aligned} \nabla_\alpha E =& \nabla_\alpha \langle \Psi(\mathbf{r}, \mathbf{R}) | \hat{H} | \Psi(\mathbf{r}, \mathbf{R}) \rangle \\ =& E \langle \nabla_\alpha \Psi(\mathbf{r}, \mathbf{R}) | \Psi(\mathbf{r}, \mathbf{R}) \rangle \\ &+ \langle \Psi(\mathbf{r}, \mathbf{R}) | \nabla_\alpha \hat{H} | \Psi(\mathbf{r}, \mathbf{R}) \rangle \\ &+ E \langle \Psi(\mathbf{r}, \mathbf{R}) | \nabla_\alpha \Psi(\mathbf{r}, \mathbf{R}) \rangle. \end{aligned} \tag{2.11}$$

In addition, since the wave function $|\Psi(\mathbf{r}, \mathbf{R})\rangle$ is normalized:

$$\langle \Psi(\mathbf{r}, \mathbf{R}) | \Psi(\mathbf{r}, \mathbf{R}) \rangle = 1, \tag{2.12}$$

the following two expressions are verified,

$$\nabla_\alpha \langle \Psi(\mathbf{r},\mathbf{R})|\Psi(\mathbf{r},\mathbf{R})\rangle = 0, \tag{2.13}$$

$$\langle \nabla_\alpha \Psi(\mathbf{r},\mathbf{R})|\Psi(\mathbf{r},\mathbf{R})\rangle = -\langle \Psi(\mathbf{r},\mathbf{R})|\nabla_\alpha \Psi(\mathbf{r},\mathbf{R})\rangle, \tag{2.14}$$

and Eq. 2.11 is reduced to

$$\nabla_\alpha E = \langle \Psi(\mathbf{r},\mathbf{R})|\nabla_\alpha \hat{H}|\Psi(\mathbf{r},\mathbf{R})\rangle. \tag{2.15}$$

Eq. 2.15 represents the Hellmann-Feynman theorem for a time-independent wave function [158, 159]. One of the peculiarities of the Hellmann-Feynman theorem, is that its accuracy depends critically on the functions which are used to represent the variational wave function[1]. In fact, whenever a variational wavefunction of the form

$$E\langle \Psi(\mathbf{r},\mathbf{R})|\Psi(\mathbf{r},\mathbf{R})\rangle = \langle \Psi(\mathbf{r},\mathbf{R})|\hat{H}|\Psi(\mathbf{r},\mathbf{R})\rangle, \tag{2.16}$$

is used, with E and $|\Psi(\mathbf{r},\mathbf{R})\rangle$ representing the variational energy and the unnormalized wavefunction, Eq. 2.11 becomes

$$\begin{aligned}\nabla_\alpha E\langle \Psi(\mathbf{r},\mathbf{R})|\Psi(\mathbf{r},\mathbf{R})\rangle =& \langle \Psi(\mathbf{r},\mathbf{R})|\nabla_\alpha \hat{H}|\Psi(\mathbf{r},\mathbf{R})\rangle \\ &+\langle \nabla_\alpha \Psi(\mathbf{r},\mathbf{R})|\hat{H}-E|\Psi(\mathbf{r},\mathbf{R})\rangle \\ &+\langle \Psi(\mathbf{r},\mathbf{R})|\hat{H}-E|\langle \nabla_\alpha \Psi(\mathbf{r},\mathbf{R})\rangle.\end{aligned} \tag{2.17}$$

When the variational wavefunction is exact, Eq. (2.17) is reduced to Eq. 2.15 only in the case in which the set of functions representing $|\Psi(\mathbf{r},\mathbf{R})\rangle$ does not depend on the atomic positions [160]. On the other hand, for functions that do depend on the atomic positions, the last two terms in Eq. 2.17, known as Pulay forces [161], have to be evaluated explicitly.

2.3 Born-Oppenheimer approximation

The presence, in the Hamiltonian operator (Eq. 2.2), of the cross term $\hat{V}_{eN}$, that depends both on $\mathbf{r}_i$ and $\mathbf{R}_\alpha$, makes the solution TISE practically unfeasible for systems of formed by more than just few particles. Fortunately, due to the large mass mismatch between electrons and nuclei, $\frac{m_e}{M_\alpha} \sim \frac{1}{1000}$, the latter can be considered almost frozen, compared to the former. This fact allows us to factorize the total wavefunction into a nuclear wavefunction, $|\chi(\mathbf{R})\rangle$, and an electronic wavefunction, $|\psi(\mathbf{r};\mathbf{R})\rangle$, the latter depending only parametrically on the nuclear positions:

$$|\Psi(\mathbf{r},\mathbf{R})\rangle = |\psi(\mathbf{r};\mathbf{R})\rangle|\chi(\mathbf{R})\rangle, \tag{2.18}$$

[1] The functions used to represent the variational wave functions are usually referred to as the *basis set*, see Section 3.5.1 and Section 3.5.2

where the semicolon in $|\psi(\mathbf{r};\mathbf{R})\rangle$ expresses the parametric dependence of the electronic wavefunction on $\mathbf{R}$.

Indeed, Eq. 2.18 is still a solution of the TISE (Eq. 2.6):

$$\begin{aligned}\hat{H}|\Psi(\mathbf{r},\mathbf{R})\rangle =&\Big[\hat{T}_N(\mathbf{R})+\hat{T}_e(\mathbf{r})+\hat{V}_{eN}(\mathbf{r};\mathbf{R})\\ &+\hat{V}_{NN}(\mathbf{R})+\hat{V}_{ee}(\mathbf{r})\Big]|\psi(\mathbf{r};\mathbf{R})\rangle|\chi(\mathbf{R})\rangle\\ =&E|\psi(\mathbf{r};\mathbf{R})\rangle|\chi(\mathbf{R})\rangle. \end{aligned} \tag{2.19}$$

However, it has to be noted that the nuclear kinetic energy operator $\hat{T}_N(\mathbf{R})$ still couples indirectly the nuclear and electronic degrees of freedoms, due to the parametric dependence of $|\psi(\mathbf{r};\mathbf{R})\rangle$ on $\mathbf{R}$:

$$\begin{aligned}\hat{T}_N|\Psi(\mathbf{r},\mathbf{R})\rangle =&-\sum_{\alpha=1}^{N}\frac{\hbar^2}{2M_\alpha}|\psi(\mathbf{r};\mathbf{R})\rangle\nabla_\alpha^2|\chi(\mathbf{R})\rangle\\ &-\sum_{\alpha=1}^{N}\frac{\hbar^2}{M_\alpha}\nabla_\alpha|\psi(\mathbf{r};\mathbf{R})\rangle\nabla_\alpha|\chi(\mathbf{R})\rangle\\ &-\sum_{\alpha=1}^{N}\frac{\hbar^2}{2M_\alpha}|\chi(\mathbf{R})\rangle\nabla_\alpha^2|\psi(\mathbf{r};\mathbf{R})\rangle. \end{aligned} \tag{2.20}$$

The *Born-Oppenheimer approximation* (BOA) [162] consists in imposing that $\nabla_\alpha|\psi(\mathbf{r};\mathbf{R})\rangle = 0$. This is justified whenever the transition energies between different electronic states are much larger than the transition energies between different rotational and vibrational states associated with a single electronic state. Hence, under this approximation, the last two terms of Eq. 2.20 can be neglected.

From a physical point of view, the BOA assumes that the electronic wavefunction adjusts instantaneously to the nuclear one. Therefore, within the BOA, the TISE (Eq. (2.6)) can be re-written as

$$\Big[\hat{T}_N(\mathbf{R})+\hat{V}_{NN}(\mathbf{R})+\hat{H}_{el}|\psi(\mathbf{r};\mathbf{R})\rangle\Big]|\chi(\mathbf{R})\rangle \approx E|\chi(\mathbf{R})\rangle, \tag{2.21}$$

where $\hat{H}_{el}$ is the *electronic Hamiltonian*:

$$\hat{H}_{el} = \hat{T}_e(\mathbf{r})+\hat{V}_{eN}(\mathbf{r};\mathbf{R})+\hat{V}_{ee}(\mathbf{r}). \tag{2.22}$$

In this context, the term $\hat{V}_{eN}(\mathbf{r};\mathbf{R})$, which describes the parametric dependence of $\hat{H}_e$ on the nuclear positions, is referred to as the *external potential*. The expectation value of the electronic Hamiltonian defined in Eq. 2.22 represent the electronic energy:

$$E_{el} = \langle\psi(\mathbf{r};\mathbf{R})|\hat{H}_{el}|\psi(\mathbf{r};\mathbf{R})\rangle, \tag{2.23}$$

Therefore, when the nuclei are fixed in space, the potential energy of the system will be determined by adding to Eq. 2.23 the internuclear repulsion term:

$$E_{PES} = E_{el} + V_{NN}(\mathbf{R}), \tag{2.24}$$

This function, which also depends parametrically on the nuclear positions, provides a potential for the nuclear motions, and therefore takes the name of *potential energy surface* (PES). Once the PES has been determined, the motion of the nuclei can be computed under the same assumption used for the electronic problem, by considering a nuclear Hamiltonian for the motion of the nuclei in the averaged field of the electrons:

$$H_{nuclear} = \sum_{\alpha=1}^{N} \frac{\hbar^2}{2M_\alpha} \nabla_\alpha + E_{PES}. \tag{2.25}$$

The solutions of this nuclear Schrödinger equation:

$$H_{nuclear}|\Psi(\mathbf{r},\mathbf{R})\rangle = E_{tot}|\Psi(\mathbf{r},\mathbf{R})\rangle, \tag{2.26}$$

describe the vibrations, rotations and translations of the system. In the rest of the manuscript, we will deal exclusively with the electronic Hamiltonian, and therefore we will use $\hat{H}$ and $\hat{H}_{el}$ as synonyms.

2.3.1 Born-Oppenheimer molecular dynamics

Within the simplified electron-nuclear problem resulting from the BOA, the dynamics of the system can be described using semiclassical dynamics, thereby considering electrons and nuclei as quantum and classical objects, respectively. In fact, classical mechanics can be obtained from quantum mechanics by imposing the *classical limit*, *i.e.*, $\hbar \to 0$ [163].

Considering explicitly the index for each k-th electronic state $|\psi_k(\mathbf{r};\mathbf{R})\rangle$ with energy $E_{el,k}$, the following expression for electronic equation is obtained:

$$\hat{H}_{el}|\psi_k(\mathbf{r};\mathbf{R})\rangle = E_{el,k}|\psi_k(\mathbf{r};\mathbf{R})\rangle. \tag{2.27}$$

Accordingly, the PES of this state will be determined by:

$$E_{PES,k} = E_{el,k} + V_{NN}(\mathbf{R}). \tag{2.28}$$

Assuming that the solutions of Eq. 2.27 are known, if the eigenfunctions $|\psi_k(\mathbf{r};\mathbf{R})\rangle$ are orthonormal, and the set of eigenvalues associated with $\hat{H}_e$ is finite, it is possible to apply the *Born-Oppenheimer ansatz* [164, 165] by expanding the total time-dependent wave function

$|\Phi(\mathbf{r},\mathbf{R},t)\rangle$, in terms of eigenfunctions of $\hat{H}_{el}$:

$$|\Phi(\mathbf{r},\mathbf{R},t)\rangle = \sum_{k=1}^{\infty} |\psi_k(\mathbf{r};\mathbf{R})\rangle|\chi_k(\mathbf{R},t)\rangle. \tag{2.29}$$

Inserting Eq. 2.29 into the TDSE (Eq. 2.1), and multiplying by $\langle\psi(\mathbf{r};\mathbf{R})|$, leads to a set of coupled differential equations:

$$\begin{aligned} i\hbar\frac{\delta|\chi_k(\mathbf{R},t)\rangle}{\delta t} &= \left[\hat{T}_N(\mathbf{R}) + E_{PES,k}\right]|\chi_k(\mathbf{R},t)\rangle \\ &+ \sum_{k'=1}^{\infty} C_{k,k'}|\chi_k(\mathbf{R},t)\rangle, \quad k = 1,2,3,...,\infty. \end{aligned} \tag{2.30}$$

In Eq. 2.30, $C_{k,k'}$ are the coupling operators determining the coupling between the states $|\chi_k(\mathbf{R},t)\rangle$ and $|\chi_{k'}(\mathbf{R},t)\rangle$. Retaining only the diagonal terms $C_{k,k}$ leads to the *adiabatic approximation*, in which is assumed that the motion of the nuclei proceeds without changing the electronic k-th state. If the diagonal terms $C_{k,k}$, which constitute a correction to the adiabatic eigenvalue E_k of Eq. 2.30, are also removed, the Born-Oppenheimer approximation is retrieved:

$$\left[\hat{T}_N + E_{PES,k}\right]|\chi_k(\mathbf{R},t)\rangle = i\hbar\frac{\delta|\chi_k(\mathbf{R},t)\rangle}{\delta t}. \tag{2.31}$$

At this point, to derive the classical equations for the nuclear motion from the quantum mechanical ones, the time-dependent nuclear wavefunction has to be rewritten in terms of an amplitude $A(\mathbf{R},\mathrm{t})$ and a phase factor $S(\mathbf{R},\mathrm{t})$ [164, 166]:

$$|\chi(\mathbf{R},t)\rangle = A(\mathbf{R},t)e^{\frac{i}{\hbar}S(\mathbf{R},t)}. \tag{2.32}$$

In Eq. 2.32, $A(\mathbf{R},\mathrm{t})$ and $S(\mathbf{R},\mathrm{t})$ are always real and $\mathrm{A}(\mathbf{R},\mathrm{t}) > 0$. Transforming the nuclear wavefunction, and separating the real and imaginary parts, Eq. 2.31 can be rewritten in terms of the new variables $A(\mathbf{R},\mathrm{t})$ and $S(\mathbf{R},\mathrm{t})$:

$$\frac{\delta S(\mathbf{R},t)}{\delta t} + \sum_{\alpha}\frac{1}{2M_\alpha}(\nabla_\alpha S(\mathbf{R},t))^2 + E_{PES,k} = \hbar^2\sum_{\alpha}\frac{1}{2M_\alpha}\frac{\nabla_\alpha^2 A(\mathbf{R},t)}{A(\mathbf{R},t)}, \tag{2.33}$$

$$\frac{\delta A(\mathbf{R},t)}{\delta t} + \sum_{\alpha}\frac{1}{M_\alpha}(\nabla_\alpha A(\mathbf{R},t))(\nabla_\alpha S(\mathbf{R},t)) + \sum_{\alpha}\frac{1}{2M_\alpha}A(\mathbf{R},t)(\nabla_\alpha^2 S(\mathbf{R},t)) = 0. \tag{2.34}$$

In the classical limit, Eq. 2.33 becomes very similar to the Hamilton-Jacobi formulation of the equation of motion in classical mechanics [167]:

$$\frac{\delta S(\mathbf{R},t)}{\delta t} + \sum_{\alpha}\frac{1}{2M_\alpha}(\nabla_\alpha S(\mathbf{R},t))^2 + E_{PES,k} = 0. \tag{2.35}$$

Therefore, considering the transformation $\mathbf{P}_\alpha = \nabla_\alpha S(\mathbf{R},t)$ it is possible to derive the corre-

sponding newtonian equations of motion, for the nuclear coordinates $\mathbf{R}_\alpha$ and their conjugated *momenta* $\mathbf{P}_\alpha$:

$$\mathbf{M}_\alpha \frac{\delta^2 \mathbf{R}_\alpha}{\delta t^2} = \frac{\delta \mathbf{P}_\alpha}{\delta t} = -\nabla_\alpha E_{PES,k}. \tag{2.36}$$

In Eq. 2.36, $E_{PES,k}$ represent the PES of the k-th electronic state. Thus, the nuclei move according to classical mechanics in the instantaneous PES generated by the electrons. As a result, within this approximation, the forces on the nuclei can be obtained straightforwardly by solving the TISE for the given k-th electronic state at the instantaneous configuration of the N nuclei, and then propagating the nuclei classically:

$$E_{PES,k} = \langle \psi(\mathbf{r};\mathbf{R}) | \hat{H}_{el} | \psi(\mathbf{r};\mathbf{R}) \rangle + V_{NN}(\mathbf{R}) \tag{2.37}$$

$$\mathbf{M}_\alpha \frac{\delta^2 \mathbf{R}_\alpha}{\delta t^2} = -\nabla_\alpha E_{PES,k} \quad N = 1, 2, 3, ..., N. \tag{2.38}$$

This approach is referred to as *Born-Oppenheimer molecular dynamics* (BOMD).

2.4 Bravais lattice

In a three-dimensional periodic system, the atomic positions are repeated at regular intervals in space. The set of translation operations that specify how these periodically repeated units are arranged, is called the *Bravais lattice* [168]. A Bravais lattice may be also conveniently described as that set of points described by a position vector $\mathbf{R}$ of the form

$$\mathbf{R} = \sum_{i=1}^{i=3} n_i \mathbf{a}_i \quad n = 1, 2, 3, ..., \infty. \tag{2.39}$$

In Eq. 2.39, the vectors $\mathbf{a}_i$ are known as *primitive vectors*. The three vectors cannot lie in the same plane, and two vectors lying in the same plane cannot be parallel. It is important to note that not all the three-dimensional periodic lattices can be defined as Bravais lattices. In fact, in order to identify a periodic lattice as a Bravais lattice, the arrangement as well as the orientation of the lattice must appear the same at every point of the lattice. This is not the case, *e.g.* for the graphene honeycomb lattice.

Given a Bravais lattice, the minimal repeat unit, containing precisely one lattice point, from which the infinite periodic system can be constructed by means of the translations, is called the *primitive unit cell*. Once the primitive unit cell and the underlying Bravais lattice are known, a physical periodic system, *i.e.*, a *crystal*, can be described by considering the arrangement of atoms within the former, *i.e*, its *basis*, and repeating this arrangement in space according to the latter. In addition to translations, which form a group by their self [1], point group symmetry

[1] A group is defined by the condition that a sum of two or more symmetry operations leads to another operation belonging to the same group

operations, such as rotations, reflections and inversions, may exist in the *primitive unit cell*, so that the final, periodic, structure of a crystal can be classified by considering its *space group*, which describes the crystal in terms of the full set of translation and point symmetry operations [169, 170]. Alternatively, it is also possible to define *conventional unit cells* (or, more generally, *unit cells*), which are not primitive, but still describe the full periodic solid when translated through some subset of the vectors of the Bravais lattice. For any of the possible choices of cells, their volume in three dimensional space is given by

$$\Omega = |\mathbf{a}_1 \cdot (\mathbf{a}_2 \times \mathbf{a}_3)|. \tag{2.40}$$

In practice, it is common to express the primitive vectors in three dimensional space using a square matrix:

$$a_{i,j} = \begin{pmatrix} a_{1,1} & a_{1,2} & a_{1,3} \\ a_{2,1} & a_{2,2} & a_{2,3} \\ a_{3,1} & a_{3,2} & a_{3,3} \end{pmatrix}, \tag{2.41}$$

where i and j denote the components of the cartesian vectors and the unit cell parameters, respectively.

One last important concept associated with the Bravais lattice is that of *lattice plane*, which is that plane containing at least three non collinear lattice points. The two-dimensional set of points spanned by the lattice plane also constitutes a Bravais lattice, since it is a subset of the initial three-dimensional one. A *family of lattice planes* will be formed by a set of equally spaced, parallel lattice planes.

2.5 Reciprocal lattice

The periodicity of a crystal does not only implies periodic variations in its geometrical structure, but also in its electronic structure. Two important concepts to describe the latter are those of *reciprocal lattice*, and *Brillouin zone*. The former can be described by considering that, for a given Bravais lattice with periodicity $\mathbf{R}$, it is possible to consider a periodic function, which remains unaltered for any allowed value of $\mathbf{R}$:

$$f(\mathbf{r}) = f(\mathbf{r} + \mathbf{R}). \tag{2.42}$$

Such as a periodic function can be represented in Fourier space by a plane wave, $f(\mathbf{r}) = e^{i\mathbf{kr}}$. Since we are considering a periodic lattice, $f(\mathbf{r})$ must satisfy the *Born - Von Karman periodic*

boundary conditions [171],

$$\begin{aligned} f(\mathbf{r}) &= f(\mathbf{r} + n_1\mathbf{a}_1), \\ f(\mathbf{r}) &= f(\mathbf{r} + n_2\mathbf{a}_2), \\ f(\mathbf{r}) &= f(\mathbf{r} + n_3\mathbf{a}_3), \end{aligned} \tag{2.43}$$

which leads to the condition:

$$e^{i\mathbf{k}(n_1\mathbf{a}_1)} = e^{i\mathbf{k}(n_2\mathbf{a}_2)} = e^{i\mathbf{k}(n_3\mathbf{a}_3)} = 1. \tag{2.44}$$

For an infinite periodic crystal, Eq. 2.44 is verified only for those values of $\mathbf{k}$ satisfying $\mathbf{k} \cdot \mathbf{a}_i = 2\pi N$, where N is any integer number. For this well defined set of values of the wave vector $\mathbf{k}$, $f(\mathbf{r})$ will have the same periodicity of the Bravais lattice, *i.e.*, $f(\mathbf{r}) = f(\mathbf{r} + \mathbf{R})$. The full set of such wave vectors $\mathbf{k}$ satisfying this condition constitutes the reciprocal lattice of the associated Bravais lattice - the latter, in this case, may also be referred to as the *direct lattice*. The lattice parameters $\mathbf{b}_i$ of this new lattice are reciprocal with respect to those of the direct lattice:

$$\mathbf{b}_i \cdot \mathbf{a}_j = 2\pi\delta_{ij}. \tag{2.45}$$

Therefore, the reciprocal lattice constitutes a Bravais lattice by itself. In the 3D space, the reciprocal lattice vectors can be obtained in terms of the direct lattice ones (see Eq. 2.39) by means of the following transformations (see Fig. 2.1):

$$\begin{aligned} \mathbf{b}_1 &= 2\pi \frac{\mathbf{a}_2 \cdot \mathbf{a}_3}{\mathbf{a}_1 \cdot (\mathbf{a}_2 \times \mathbf{a}_3)}, \\ \mathbf{b}_2 &= 2\pi \frac{\mathbf{a}_3 \cdot \mathbf{a}_1}{\mathbf{a}_3 \cdot (\mathbf{a}_1 \times \mathbf{a}_2)}, \\ \mathbf{b}_3 &= 2\pi \frac{\mathbf{a}_1 \cdot \mathbf{a}_2}{\mathbf{a}_2 \cdot (\mathbf{a}_3 \times \mathbf{a}_1)}. \end{aligned} \tag{2.46}$$

The vectors $\mathbf{b}_{1,2,3}$ define the reciprocal lattice vector $\mathbf{k}$:

$$\mathbf{k} = \sum_{i=1}^{i=3} x_i \mathbf{b}_i \quad x = 1, 2, 3, ..., \infty. \tag{2.47}$$

Just as in the case of the direct lattice, a primitive cell can be defined for the reciprocal lattice. In particular, the Wigner-Seitz cell[1] of the reciprocal lattice is know as the first Brillouin Zone (BZ) (see Fig. 2.1). In different terms, the BZ is that region of reciprocal space enclosed by the planes that are the perpendicular bisectors of the vectors from the origin to the reciprocal lattice points [28]. On these planes, the Bragg condition is satisfied for elastic scattering [171].

[1] The Wigner-Seitz cell is defined as that primitive cell around one point which is closer to that point than to any other point of the lattice.

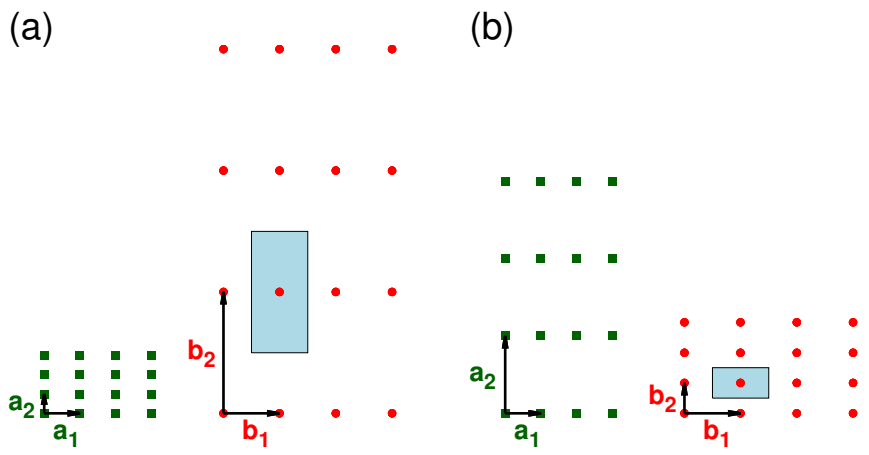

Figure 2.1: Two examples of two-dimensional rectangular Bravais lattices (green dots), and the associated reciprocal lattices (red dots). Notice that, for a two dimensional rectangular lattice, the three terms of Eq.2.46 are reduced to $\mathbf{b}_i = \frac{2\pi}{\mathbf{a}_i}, i = 1, 2, 3$. The black arrows indicate the lattice vectors. In (a) the dimensions of the direct lattice are $\mathbf{a}_1 = 2 \times \mathbf{a}_2$, while in (b) the dimensions are $\mathbf{a}_1 = 0.5 \times \mathbf{a}_2$. $\mathbf{a}_1$ has the same lenght in (a) and (b). The light-blue rectangles indicate the 1^{st}BZ in the two reciprocal lattices.

By geometrical considerations, it can be derived that the volume of the BZ associated with a n- dimensional unit cell having volume Ω is $\Omega_{BZ} = \frac{(2\pi)^n}{\Omega}$. Therefore, small unit cell will be associated with large 1^{st} BZ and vice versa (see Fig. 2.1).

The definition of the wave vector $\mathbf{k}$ in Eq. 2.47 provides a simple way to classify all the possible families of lattice planes that can be defined in a crystal, by means of the following theorem [171]:

> *For any family of lattice planes separated by a distance d, there are reciprocal lattice vectors perpendicular to the planes, the shortest of which have a lenght of $2\pi/d$. Conversely, for any reciprocal lattice vector* $\mathbf{k}$*, there is a family of lattice planes normal to* $\mathbf{k}$ *and separated by a distance d, where $2\pi/d$ is the length of the shortest reciprocal lattice vector.*

Therefore, it is possible to define the orientation of a plane - or a family of lattice planes - in the direct lattice, by considering a set of integer numbers (h, k, l), known as *Miller indices*, which define the shortest reciprocal lattice vector $\mathbf{k} = h\mathbf{b}_1 + k\mathbf{b}_2 + l\mathbf{b}_3$ normal to the direct lattice plane. While the Miller indices are usually given in parentheses, a similar convention can be also used to specify a particular direction in the direct lattice, but, in that case, square brackets must used.

2.6 Bloch's theorem

The *Bloch's theorem* describes the behaviour of electrons in crystalline solids. In a crystal, the negatively charged electrons are subjected to the periodic potential created by the positively charged nuclei. This periodic potential, here denoted by $V(\mathbf{r})$, has the periodicity of its underlying Bravais lattice with position vector $\mathbf{R}$:

$$V(\mathbf{r}) = V(\mathbf{r} + \mathbf{R}). \tag{2.48}$$

Since the scale of the periodicity of $V(\mathbf{r})$ is of the order of Angstrom, which is similar to the size of the typical *de Broglie* wavelength for a free electron, $\lambda = \frac{2\pi}{\mathbf{k}}$, quantum effects are important, and quantum mechanics must be used to describe properly the electronic problem [171]. If a single electron is considered, the electronic TISE for this electrons in the periodic potential $V(\mathbf{r})$ reads:

$$\hat{H}_{el}|\psi(\mathbf{r})\rangle = \left[\frac{\hbar^2}{2m_e}\nabla^2 + V(\mathbf{r})\right]|\psi(\mathbf{r})\rangle = E|\psi(\mathbf{r})\rangle. \tag{2.49}$$

In the case of more than one electron, such equation can be solved by considering the *independent electron model*, therefore replacing $V(\mathbf{r})$ by an effective potential $V(\mathbf{r})_{eff}$, which describes the potential felt by the electron in the field of the nuclei plus the remaining electrons. Such kind of electrons are known as *Bloch electrons*. Conversely, for $V(\mathbf{r}) = 0$, the electrons behave as free electrons.

To obtain a proper expression for the eigenstates $|\psi(\mathbf{r})\rangle$ in Eq. 2.49, we recall Eq. 2.42, and consider a translation operator $\hat{T}_{\mathbf{R}}$ applied to the function $f(\mathbf{r})$, so that:

$$\hat{T}_{\mathbf{R}} f(\mathbf{r}) = f(\mathbf{r} + \mathbf{R}). \tag{2.50}$$

Because the Hamiltonian in Eq. 2.49 is invariant to any choice of successive translations, it follows that $\hat{H}_{el}$ commutes with the translation operator $\hat{T}_{\mathbf{R}}$. Moreover, since the translation operators associated with all the possible translations within the Bravais lattice form a simple group, they obey to the relation:

$$\hat{T}_{\mathbf{R}}\hat{T}_{\mathbf{R}'} = \hat{T}_{\mathbf{R}+\mathbf{R}'}. \tag{2.51}$$

Under these conditions, the eigenstates of $\hat{H}_{el}$ can be chosen to be simultaneous eigenstates of all the $\hat{T}_{\mathbf{R}}$, *i.e.*,

$$\begin{aligned} \hat{H}|\psi(\mathbf{r})\rangle &= E|\psi(\mathbf{r})\rangle, \\ \hat{T}_{\mathbf{R}}|\psi(\mathbf{r})\rangle &= c(\mathbf{R})|\psi(\mathbf{r})\rangle, \end{aligned} \tag{2.52}$$

where c($\mathbf{R}$) is the eigenvalue associated with the translation operator $\hat{T}_{\mathbf{R}}$. Since Eq. 2.51 holds,

it follows that

$$c(\mathbf{R}+\mathbf{R}') = c(\mathbf{R})c(\mathbf{R}'). \tag{2.53}$$

Within the Born - Von Karman periodic boundary conditions, any $c(\mathbf{R})$ can be written as a periodic function of the form

$$c(\mathbf{R}) = e^{2\pi i x_i} \quad x_i = 1, 2, 3, ..., \infty. \tag{2.54}$$

Therefore, recalling the orthonormality relation between the reciprocal and direct lattice vectors Eq. 2.45, we can express Eq. 2.54 in the form

$$c(\mathbf{R}) = e^{i\mathbf{k}\mathbf{R}}, \tag{2.55}$$

where $\mathbf{k}$ and $\mathbf{R}$ are the wave and position vectors in the reciprocal and direct space, respectively. This means that it is possible to choose eigenstates of $|\psi(\mathbf{r})\rangle$ so that, for every Bravais lattice vector $\mathbf{R}$, the following relation holds:

$$\hat{T}_{\mathbf{R}}|\psi(\mathbf{r})\rangle = |\psi(\mathbf{r}+\mathbf{R})\rangle = c(\mathbf{R})|\psi(\mathbf{r})\rangle = e^{i\mathbf{k}\mathbf{R}}|\psi(\mathbf{r})\rangle. \tag{2.56}$$

Eq. 2.56 implies that, for each value of $\mathbf{k}$, the eigenstate $|\psi(\mathbf{r})\rangle$ of the one-electron Hamiltonian in a periodic potential (Eq. 2.48) can be chosen to have the form of a plane wave times a function having the periodicity of the underlying Bravais lattice:

$$\begin{aligned} |\psi(\mathbf{r})\rangle &= e^{i\mathbf{k}\mathbf{r}}u(\mathbf{r}), \\ u(\mathbf{r}) &= u(\mathbf{r}+\mathbf{R}). \end{aligned} \tag{2.57}$$

The most important consequence of the Bloch theorem is that, in a periodic system, $|\psi(\mathbf{r})\rangle$ depends on the wave vector $\mathbf{k}$. Indeed, due to the Born - Von Karman boundary conditions, Eq. 2.56 will have the same solution for two wave vectors $\mathbf{k}'$ and $\mathbf{k}''$, lying inside and outside of the 1^{st} BZ, respectively, and connected by a reciprocal lattice vector $\mathbf{k}$. As a result, for any value of $\mathbf{k}$ within the 1^{st} BZ, there will be a discrete set of solutions, due to the finite volume of the unit cell. The corresponding one-electron Schödinger equation is obtained by inserting the expression for $|\psi(\mathbf{r})\rangle$ in terms of $u(\mathbf{r})$ in Eq. 2.49, which leads to:

$$e^{-i\mathbf{k}\mathbf{r}}\hat{H}_{el}e^{i\mathbf{k}\mathbf{r}}u(\mathbf{r}) = \left[-\frac{\hbar}{2m_e}\left(\nabla + i\mathbf{k}\right)^2 + V(\mathbf{r})\right]u(\mathbf{r}) = Eu(\mathbf{r}). \tag{2.58}$$

Once the solution of Eq. 2.58 is known, the ground state of a system of N electrons can be constructed by occupying each set of the resulting one-electron levels, for those values of $\mathbf{k}$ lying within the 1^{st} BZ, according to the *aufbau* principle.

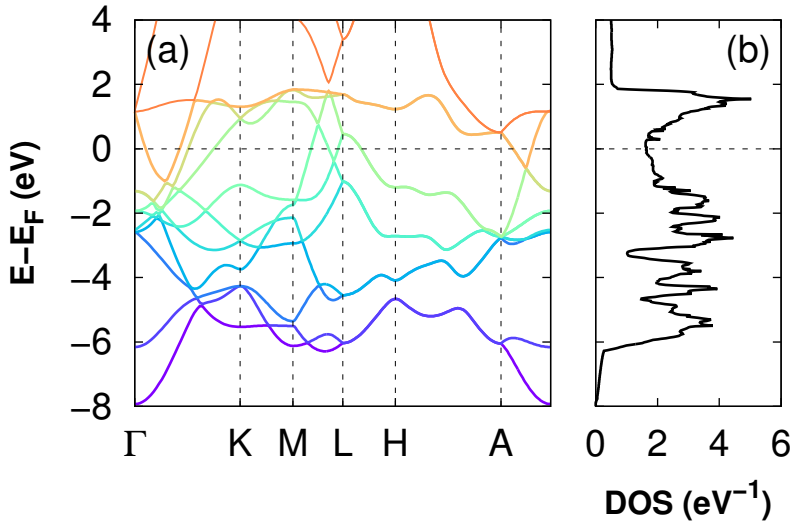

Figure 2.2: (a) Band structure along the high symmetry path $\Gamma \rightarrow K \rightarrow M \rightarrow K \rightarrow H \rightarrow A \rightarrow \Gamma$ (see Ref. [172]) of the 1^{st} BZ, and (b) total density of states of ruthenium, calculated using density functional theory (see Chapter 3). In (a) each different colour correspond to a different band, according to the definition in Eq. 2.59 and Eq. 2.60. The energy on the y-axis has been scaled with respect to the Fermi energy $\mathrm{E_F}$.

2.7 Band structure and density of states

As already mentioned, due to the boundary conditions, the solutions of Eq. 2.58 for a value $\mathbf{k}''$ of the wave vector lying outside the 1^{st} BZ will be identical with those associated with a wave vector $\mathbf{k}'$ lying within its boundaries, and connected to $\mathbf{k}'$ by a reciprocal lattice vector $\mathbf{k}$. Due to this periodic character of the solutions of the Schrödinger equation, it is possible to categorize the eigenstates and eigenvalues in terms of their energy, so that they represent periodic functions of $\mathbf{k}$ in the reciprocal lattice. Every different band will be associated with a set of eigenstates and eigenvalues for which the following relations hold:

$$|\psi(\mathbf{r};\mathbf{k}')\rangle = |\psi(\mathbf{r};\mathbf{k}'')\rangle, \tag{2.59}$$

$$E(\mathbf{k}') = E(\mathbf{k}''). \tag{2.60}$$

The complete set of such functions is referred to as the band structure (see Fig. 2.2). This definition permits to distinguish between two different situations. The first one is that in which the bands will be either completely filled or completely empty. This leads to the appearance of a *band-gap*, defined as the energy difference between the "top" of the last occupied and

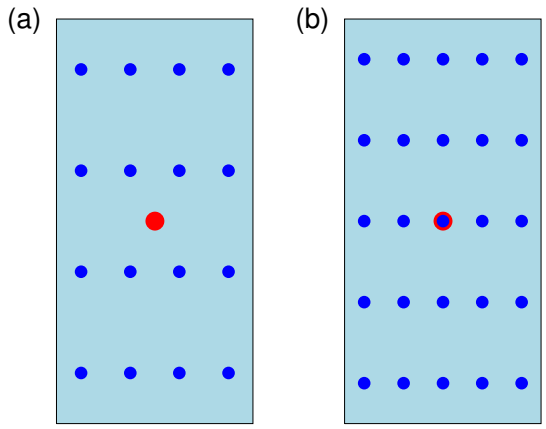

Figure 2.3: Grids of **k**-points (blue points) generated using the Monkhorst-Pack scheme, sampling the 1^{st}BZ (light-blue rectangle) associated with the Bravais lattice shown in Fig. 2.1(a). An even 4×4 grid is shown in (a), while an odd 5×5 grid is shown in (b). The red dot in (a) and (b) indicates the center of the 1^{st} BZ, *i.e.*, the Γ-point.

the "bottom" of the first unoccupied one. This situation is characteristic of materials with semiconducting and insulating properties. In the second situation a certain number of bands will remain only partially filled, leading to the presence of a surface in the reciprocal space, called the *Fermi surface*, separating the occupied electronic levels, the energy of the highest one being referred to as the *Fermi energy*, from the unoccupied ones. The presence of this second situation defines a metallic system.

For a single electronic band, the integration of the energy level across the whole range of allowed values of **k**, permits to define a *density of states* (DOS) associated with that particular band:

$$DOS_{band}(E) = \int \frac{d\mathbf{k}}{4\pi^3} \delta(E_{band}(\mathbf{k}) - E). \tag{2.61}$$

Accordingly, the total DOS of the system will correspond to the sum of the DOS contributed by each band (see Fig. 2.2).

2.8 Brillouin zone integration

The calculation of many quantities, such as the total energy or the electronic density, requires the integration of functions of the band structure over the 1^{st} BZ. For a general quantity **Q**(E) associated with a function **F**(E), the corresponding integrals is

$$\mathbf{Q}(E) = \frac{1}{\Omega_{BZ}} \int_{\Omega_{BZ}} \mathbf{F}(E) \delta(E_{band}(\mathbf{k}) - E) d\mathbf{k}, \tag{2.62}$$

where the integral over the BZ volume spans all bands and all values of the wave vector. In practical calculations, the integration is carried out by considering the sum over a discrete set of **k**-points, and this approximation is justified as long as the integrand varies smoothly with **k**. In insulators, the number of filled bands is unambiguously defined, and the integration can be done using sets of well-chosen **k**-points [173, 174]. Conversely, metals require careful integration, due to the presence of bands crossing the Fermi level. Concerning the choice of the **k**-points, the most general method, applicable to both kinds of systems, is the one proposed by Monkhorst and Pack [175], which provides a uniform set of points, distributed homogeneously across the 1^{st} BZ, with rows or columns of uniformly spaced points running parallel to the reciprocal lattice vectors. For a Bravais lattice such as that defined in Eq. 2.39, the wave vector associated with each of these points in the reciprocal space is:

$$\mathbf{k}_{u_i,u_k,u_k} = u_i\mathbf{b}_1 + u_j\mathbf{b}_2 + u_k\mathbf{b}_3, \tag{2.63}$$

where the coefficients $u_{i,j,k}$ are determined by the expressions:

$$\begin{aligned} u_i &= \frac{2i - q_i - 1}{2q_i}, \quad (i = 1, 2, 3, ..., q_i) \\ u_j &= \frac{2j - q_j - 1}{2q_j}, \quad (j = 1, 2, 3, ..., q_j) \\ u_k &= \frac{2k - q_k - 1}{2q_k}, \quad (k = 1, 2, 3, ..., q_k) \end{aligned} \tag{2.64}$$

with the $q_{i,j,k}$ being integers that determine the number of points in each direction of the reciprocal lattice.

It is worth noticing that the convergence of the 1^{st} BZ sampling with respect to the density of points provided by the Monkhorst-Pack method is not systematic. Therefore, the convergence of the sampling with respect to a desired property must be always verified by appropriate convergence tests. In this respect, one major distinction concerns the cases in which the values that the numbers $q_{i,j,k}$ assume are even or odd. In particular, it can be seen from Fig. 2.3, that the center of the 1^{st} BZ, *i.e.*, the Γ-point, is sampled only when $q_{i,j,k}$ take odd values [1].

2.9 Smearing methods

In the case of insulators and semiconductors, the functions $\mathbf{F}(E)$ to be integrated, in order to obtain a given property $\mathbf{Q}$(E) (see Eq. 2.62), are infinitely many times differentiable, due to the bands gap separation between occupied and empty bands. In this case, the integrals converge exponentially with respect to the values of $q_{i,j,k}$ in Eq. 2.64. On the other hand, in the case of a metal, the bands crossing the Fermi level are only partially occupied, and a discontinuity exists

[1] However, it is also possible to use shifted grids, where the points generated by the MonkhorstPack scheme are displaced by value of $\frac{q_{i+1,j+1,k+1} - q_{i,j,k}}{2}$. This makes the Γ-point, to include in the sampling the Γ-point, as well as the high symmetry points at the BZ boundaries

at the Fermi surface, where the occupancies suddenly jump from unity to zero. This constitutes a serious problem for the numerical integration of the bands structure over the 1^{st} BZ, since the functions defined in this way are not even once differentiable. In this case, a prohibitively large number of **k**-points should be used in order to obtain properly converged results.

Several approaches have been proposed to overcome this problem. The most accurate one is the so-called *tetrahedron method* [176, 177], in which the discrete set of **k**-points used for the 1^{st} BZ integration is used to define a set of tetrahedra that fill the reciprocal space, and the value of the integrand in Eq. 2.62 is approximated at every points of the tetrahedron using an interpolation scheme. The main problem of this method is that the number of **k**-points used must be large enough to define the tetrahedra, which hinders its applicability to very large unit cells, where only very few **k**-points - *e.g.* one to three - are used. In this case, it is possible to resort on different solutions, like the one provided by the *smearing methods*. Within this class of methods, the δ function in Eq. 2.62 is replaced by a smoothly varying function, thus eliminating the discontinuity problem at the Fermi level. Concerning the choice of the function, one of the possibilities is to use a Fermi-Dirac distribution,

$$f\left(\frac{E_{band}(\mathbf{k})-E}{\sigma}\right)=\frac{1}{e^{\frac{E_{band}(\mathbf{k})-E}{\sigma}}+1}, \tag{2.65}$$

or a Gaussian distribution [178, 179, 180],

$$f\left(\frac{E_{band}(\mathbf{k})-E}{\sigma}\right)=\frac{1}{2}\left(1-\mathrm{erf}\left[\frac{E_{band}(\mathbf{k})}{\sigma}\right]\right). \tag{2.66}$$

In Eq. 2.65 and Eq. 2.66, the width of the distribution is controlled by the parameter σ. In the limit $\sigma \to 0$, the correct step function should be recovered for an infinitely large grid of **k**-points. On the other hand, the method proposed by Methfessel and Paxton [181] converges to the exact result in the limit $\sigma \to 0$, independently on the density of **k**-points. In this method, the Dirac step function is expanded in a complete orthonormal set of functions, leading to successive approximations of order N to the step function, in which the Gaussian function is only the first approximation:

$$\begin{aligned} f_N\left(\frac{E_{band}(\mathbf{k})-E}{\sigma}\right)=&\frac{1}{2}\left(1-\mathrm{erf}\left[\frac{E_{band}(\mathbf{k})}{\sigma}\right]\right)\\ &+\sum_{n=1}^{N}A_n H_{2n+1}\left(\frac{E_{band}(\mathbf{k})-E}{\sigma}\right)e^{\left(\frac{E_{band}(\mathbf{k})-E}{\sigma}\right)^2}. \end{aligned} \tag{2.67}$$

In Eq. 2.67, H_n is the Hermite polynomial of degree n, and the coefficients A_n have the form:

$$A_n=\frac{(-1)^n}{n!4^n\sqrt{\pi}}. \tag{2.68}$$

It should be noted that the expansion of the delta function in terms of Hermite polynomials

introduces a numerical artefact, due to the non-monotonous decay of the step function. This results in the presence of unphysical negative occupancies of the electronic states, which can lead to problems in the analysis of some properties, such as the DOS. This anomaly can be avoided by increasing the order N of the expansion.

3 Density functional theory

This Chapter is dedicated to density functional theory, which is the electronic structure method used to describe the molecule/surface systems studied in this work. Section 3.1 defines the meaning of electronic density and recall the Thomas-Fermi model, which has been the first electronic structure method that use the electronic density as the basic variable. Section 3.2 deals with the Hohenberg-Kohn theorems, which have posed the theoretical foundations of modern density functional theory, and the extensions made by Levy and Lieb, that generalize to arbitrary densities the concepts introduced by these theorems. Section 3.3 presents the Kohn-Sham method, which is the most successful and widely used practical implementation of density functional theory, while section 3.4 is dedicated to the exchange correlation functional, the central quantity over which the Kohn-Sham approach is built. Section 3.5 describes how the Kohn-Sham equations are practically solved in modern computer programs, such as those employed in this work. Finally, Section 3.6 deals with the complex problem of modelling dispersion interactions in Kohn-Sham density functional theory, and present the details of one of the recent semi-empirical approaches, that has been proposed to take them into account in a pragmatic and efficient way.

3.1 Electronic density and energy functional

The fundamental idea behind density functional theory (DFT) is that the electronic properties of a system can be viewed as a functional of the ground state *probability density function* $\rho(\mathbf{r})$, which, in this context, is also referred to as the *eletronic density*. In a system formed by n electrons with an electronic ground state determined by the wavefunction $|\psi(\mathbf{r})\rangle$, $\rho(\mathbf{r})$ determines the probability of finding any of the n electrons within an infinitesimal volume element, while the other n-1 electrons have arbitrary positions (for simplicity, here we do not consider the electronic spin variable) [146]:

$$\rho(\mathbf{r}) = n \int ... \int |\psi(\mathbf{r}_1, \mathbf{r}_2, \mathbf{r}_3, ..., \mathbf{r}_n)|^2 d\mathbf{r}_2 ... d\mathbf{r}_n. \tag{3.1}$$

In Eq. 3.1, $\mathbf{r}_{1,2,...,n}$ are the positions of the n electrons, and $d\mathbf{r}_{2,...,n}$ the infinitesimal volumes associated with the n-1 electrons. By definition, $\rho(\mathbf{r})$ is a scalar function, that depends only on the position $\mathbf{r}$, which vanishes in the limit $\mathbf{r} \to \infty$, and integrates to the total number of

electrons:

$$\int \rho(\mathbf{r}) d\mathbf{r}_1 = n. \tag{3.2}$$

The advantages of constructing an electronic structure theory based solely on $\rho(\mathbf{r})$ appear clear if one considers that this quantity depends only on the three cartesian components of the vector $\mathbf{r}$, while the wavefunction $|\psi(\mathbf{r})\rangle$ depends on $3n$ variables, *i.e.*, the positions of the n electrons. In this respect, the first attempt to use the $\rho(\mathbf{r})$ to describe a quantum system is due to Thomas [182] and Fermi [183], who considered the functional dependence of the total energy with respect to the electronic density. Their scheme assumes that the interelectronic repulsion is given by a purely electrostatic Hartree energy, $E_{Hartree}$

$$E_{Hartree}[\rho(\mathbf{r})] = \frac{q_e^2}{2} \int d\mathbf{r} \int d\mathbf{r}' \frac{\rho(\mathbf{r})\rho(\mathbf{r}')}{|\mathbf{r} - \mathbf{r}'|}, \tag{3.3}$$

and the electronic kinetic energy can be described by a local approximation of the uniform gas of noninteracting electrons:

$$T_e[\rho(\mathbf{r})] = \frac{3\hbar^2(3\pi^2)^{\frac{2}{3}}}{10m_e} \int d\mathbf{r}[(\rho(\mathbf{r}))]^{\frac{5}{3}} = C \int d\mathbf{r}[(\rho(\mathbf{r}))]^{\frac{5}{3}}. \tag{3.4}$$

Therefore, the energy functional $E_{\mathrm{TF}}[\rho(\mathbf{r})]$, for n electrons moving in an external potential V_{ext}, can be written as a sum of the terms in Eq. 3.3 and Eq. 3.4, plus a third term describing the interaction of the electronic cloud with the external potential:

$$E_{\mathrm{TF}}[\rho(\mathbf{r})] = T_e[\rho(\mathbf{r})] + E_{Hartree}[\rho(\mathbf{r})] + \int V_{ext}(\mathbf{r})\rho(\mathbf{r}) d\mathbf{r}. \tag{3.5}$$

The ground state density and energy can be obtained my minimizing this functional for all the possible $\rho(\mathbf{r})$, subject to the constrain on the total number of electrons.

Despite being the first model to use the density as a basic variable, the Thomas-Fermi model has found only limited applicability, mainly due to the drastic approximation it involves, which make it incapable of describing some very basic features of matter, such as the atomic shell structure, and the formation of molecules and solids starting form their constituent atoms. [184, 185, 186, 187].

3.2 Hohenberg-Kohn theorems and the Levy-Lieb extension

Hohenberg and Kohn have improved further the ideas of Thomas and Fermi, by demonstrating that the properties of a many-body ground state can be related in a rigorous way to its probability density function [188, 189]. This is particularly important, since it provides the basis for an exact description of the electronic structure in terms of $\rho(\mathbf{r})$. Their formulation applies to the non-degenerate ground state of any system of interacting particles described by the electronic

Hamiltonan $\hat{H}_e$ presented in Eq. 2.22, and to all those densities that are "V-representable", that is, to all those electronic densities that are associated to a ground state wave function of some electronic Hamiltonian with local external potential V_{ext}. These initial restriction have been lifted by the reformulation presented by Lieb and Levy, which is also discussed.

3.2.1 First theorem

The first 1^{st} Hohenberg-Kohn theorem states that for any system of interacting particles, having a non-degenerate ground state determined by the wavefunction $|\psi(\mathbf{r})\rangle$, and moving under the influence of an external potential $\mathrm{V}_{ext}(\mathbf{r})$, the potential $\mathrm{V}_{ext}(\mathbf{r})$ is a unique functional of its ground state density, $\rho(\mathbf{r}) = \langle\psi(\mathbf{r})|\psi(\mathbf{r})\rangle$, apart form trivial additive constants. Consequently, the ground state $|\psi(\mathbf{r})\rangle$ is a unique functional of $\rho(\mathbf{r})$ as well, and the properties of the many-body system, such as its total energy E, can be determined not only as the expectation value of $\hat{H}_{el}$, but also as the functional of the density of the system:

$$E = \langle\psi(\mathbf{r})|\hat{H}_{el}|\psi(\mathbf{r})\rangle = E[\rho(\mathbf{r})]. \tag{3.6}$$

3.2.2 Second theorem

The 2^{nd} Hohenberg-Kohn theorem establish a general variational principle, by introducing the concept of an exact total energy functional of the electronic density, $E[\rho(\mathbf{r})]$, which is valid for any external potential $V_{ext}(\mathbf{r})$. For any possible value of $V_{ext}(\mathbf{r})$, the exact ground state energy is determined by the minimum value of this functional, and the corresponding density that minimizes this functional is that of the exact ground state. Therefore, once V_{ext} is known, the problem of determining the ground state energy, and its density, is trivial, as it requires the minimization of the energy functional $E[\rho(\mathbf{r})]$, starting from an arbitrary trial initial probability density function. $E[\rho(\mathbf{r})]$ can, in turn, be constructed as a sum of a functional term representing the electrostatic interaction of the electrons with the external potential $V_{ext}(\mathbf{r})$ created by the nuclei,

$$E_{eN}[\rho(\mathbf{r})] = \sum_{\alpha=1}^{N} \frac{1}{4\pi\epsilon_0} \int d\mathbf{r}\rho(\mathbf{r}) \frac{Z_\alpha q_e^2}{|r - R_\alpha|}, \tag{3.7}$$

where Z_α and R_α are the nuclear charge and position of nucleus α, and a universal functional $F[\rho(\mathbf{r})]$, accounting for the kinetic and potential energy of the interacting electron system:

$$E[\rho(\mathbf{r})] = F[\rho(\mathbf{r})] + E_{eN}[\rho(\mathbf{r})]. \tag{3.8}$$

It follows that, if the exact analytical form of the functional $F[\rho(\mathbf{r})]$ is known, the exact ground state density and energy can be determined.

3.2.3 Levy-Lieb extension

An alternative derivation, made by Levy and Lieb [190, 191, 192], overcomes some of the limitations of the Hohenberg-Kohn approach to the total energy functional. In particular, it provides a formal definition for a functional which is valid for any "N-representable" density, *i.e.*, for any generic density that can be constructed from a given wavefunction $|\psi(\mathbf{r})\rangle$ - we will call this generic density $n(\mathbf{r})$. Starting from the initial representation of the energy as the expectation value of the electronic Hamiltonian shown in Eq. 2.22, the Levy-Lieb approach constrains the search of the minimum of $E[\rho(\mathbf{r})]$ to that subset of wavefunctions having a certain density. In this case, the minimization of the energy functional for all these wavefunctions, results in a unique lowest energy, thus eliminating the restriction of the original Hohenberg-Kohn theorem to non-degenerate ground states:

$$\begin{aligned} E[n(\mathbf{r})] &= \min_{\psi \to n(\mathbf{r})} [\langle \psi(\mathbf{r}) | \hat{T}_e | \psi(\mathbf{r}) \rangle + \langle \psi(\mathbf{r}) | \hat{V}_{ee} | \psi(\mathbf{r}) \rangle] + E_{eN}[n(\mathbf{r})], \\ &= \min_{\psi \to n(\mathbf{r})} [\langle \psi(\mathbf{r}) | \hat{T}_e + \hat{V}_{ee} | \psi(\mathbf{r}) \rangle] + E_{eN}[n(\mathbf{r})] \\ &= F[n(\mathbf{r})] + E_{eN}[n(\mathbf{r})]. \end{aligned} \tag{3.9}$$

Since Eq. 3.9 is valid for any generic $n(\mathbf{r})$, it is possible to generalize the Hohenberg-Kohn arguments to consider functionals that depend not only on the electronic density $\rho(\mathbf{r})$, but also on the spin density $\mathbf{s}(\mathbf{r})$. However, similarly to the case of the Hohenberg-Khon theorem, no indications are given on how to construct analytically the functional $F[n(\mathbf{r})]$, apart from the original definition in terms of the many body wavefunctions.

3.3 Kohn-Sham approach

The approach developed by Kohn and Sham [193, 189] to construct $F[\rho(\mathbf{r})]$ allows for a practical implementation of density functional theory into an analytically tractable scheme. The entire method relies on an ansatz, which is that of assuming that the ground state density of a many-body quantum system of n interacting electrons can be mapped into that of an auxiliary fictitious system of n non-interacting electrons, described by reference single particle orbitals $|\varphi^{\alpha,\beta}_{1,2,...,n}(\mathbf{r})\rangle$, and interacting with an effective potential, called $V_{KS}(\mathbf{r})$, which describes the interaction of each single electron with the nuclei and with the remaining electrons. The wave-function is assumed to have a closed-shell electronic configuration, *i.e.*, the relationship between the number of α electrons and the number of β electrons is $n_\alpha = n_\beta = \frac{n}{2}$. Since electrons are fermionic particles, the total wavefunction associated with these single particle orbitals is expressed by a single Slater determinant,

$$|\Psi(\mathbf{r})\rangle = \frac{1}{\sqrt{n!}} |\varphi^\alpha_1(\mathbf{r}) \varphi^\beta_1(\mathbf{r}) \varphi^\alpha_2(\mathbf{r}) \varphi^\beta_2(\mathbf{r}) ... \varphi^\alpha_{n/2}(\mathbf{r}) \varphi^\beta_{n/2}(\mathbf{r})|, \tag{3.10}$$

and the correspondent total density is given by:

$$\rho(\mathbf{r}) = \sum_{i=1}^{n} |\varphi_i(\mathbf{r})|^2. \tag{3.11}$$

In the auxiliary system, the electronic kinetic energy functional $T_e[\rho(\mathbf{r})]$ can be expressed in terms of the kinetic energies of the single particle orbitals:

$$T_e[\rho(\mathbf{r})] = -\frac{\hbar^2}{2m_e} \sum_{i=1}^{n} \langle \varphi_i(\mathbf{r}) | \nabla^2 | \varphi_i(\mathbf{r}) \rangle \tag{3.12}$$

Consequently, the Hohenberg-Kohn functional in Eq. 3.7 can be rewritten as a sum of individual functional terms associated with the auxiliary, non-interacting, system:

$$E[\rho(\mathbf{r})] = T_e[\rho(\mathbf{r})] + E_{Hartree}[\rho(\mathbf{r})] + E_{eN}[\rho(\mathbf{r})] + E_{XC}[\rho(\mathbf{r})]. \tag{3.13}$$

In Eq. 3.13, $T_e[\rho(\mathbf{r})]$ has the form of Eq. 3.12, $E_{Hartree}[\rho(\mathbf{r})]$ and $E_{eN}[\rho(\mathbf{r})]$ are analogue of Eq. 3.3 and Eq. 3.7, respectively, and the last term $E_{XC}[\rho(\mathbf{r})]$ is the *exchange-correlation* (XC) energy term, which accounts for the many-body effects due to electronic exchange and electronic correlation, that are missing in the terms $T_e[\rho(\mathbf{r})]$ and $E_{Hartree}[\rho(\mathbf{r})]$. Notice that, in this functional, only the kinetic energy term is an explicit functional of the single-particle orbitals, while the remaining terms are explicit functionals of the density. In principle, such an expression of the energy functional would be capable of providing the exact energy and density of the many-body ground state. However, the exact functional form of the XC energy term is unknown, and approximations have to be used - see Section 3.4 -, limiting somehow the reliability of the whole method on the ability of these approximated functional forms to account for the many-body effects in the system. In any case, compared to the Hohenberg-Kohn functional, Eq. 3.8, this method constitutes a significant advance, since the contribution of this approximated term to the total energy is much smaller than that of the Hohenberg-Kohn universal functional $F[\rho(\mathbf{r})]$.

Once the functional in Eq. 3.13 has been defined, the corresponding Kohn-Sham (KS) equations for the n electrons can be obtained by exploiting the fact that only $T_e[\rho(\mathbf{r})]$ is expressed in terms on the single-particle orbitals, while the other terms are functionals of the electronic density only. Therefore, by minimizing the total energy functional with respect to the single-particle orbitals $|\varphi_i(\mathbf{r})\rangle$, subject to the orthonormality constrain $\langle \varphi_i^{\alpha}(\mathbf{r}) | \varphi_j^{\beta}(\mathbf{r}) \rangle = \delta_{i,j}^{\alpha\beta}$, the following single-particle equations are obtained:

$$\hat{H}_{KS} |\varphi_i(\mathbf{r})\rangle = E_i |\varphi_i(\mathbf{r})\rangle, \tag{3.14}$$

where the KS effective hamiltonian has the form

$$\hat{H}_{KS} = -\frac{\hbar^2}{2m_e}\nabla^2 + V_{KS}(\mathbf{r}), \tag{3.15}$$

$$V_{KS}(\mathbf{r}) = V_{eN}(\mathbf{r}) + V_{Hartree}(\mathbf{r}) + V_{XC}(\mathbf{r}). \tag{3.16}$$

3.4 Exchange-correlation functional

As already mentioned, the approximations made in the functional form of the XC energy term in Eq. 3.13, and the associated potential term $V_{XC}(\mathbf{r})$ in Eq. 3.16, determine the quality of the results obtained by solving Eq. 3.14. In general, the dependence of the XC energy term on the electronic density is expressed by the interaction between the density $\rho(\mathbf{r})$, and the *energy density functional*, $\epsilon_{XC}[\rho(\mathbf{r})]$:

$$E_{XC}[\rho(\mathbf{r})] = \int d\mathbf{r}\ \rho(\mathbf{r})\epsilon_{XC}[\rho(\mathbf{r})]. \tag{3.17}$$

Therefore, the different approximations of $E_{XC}[\rho(\mathbf{r})]$ can also be discriminated in terms of the way in which $\epsilon_{XC}[\rho(\mathbf{r})]$ is described.

3.4.1 Local density approximation

The simplest approximation of $\epsilon_{XC}[\rho(\mathbf{r})]$ is the *local density approximation* (LDA) , in which the exchange and correlation energy at each point in space are assumed to be those of an homogeneous electron gas of density $\rho(\mathbf{r})$:

$$\epsilon_{XC}^{LDA}[\rho(\mathbf{r})] = \epsilon_{X}^{LDA}[\rho(\mathbf{r})] + \epsilon_{C}^{LDA}[\rho(\mathbf{r})]. \tag{3.18}$$

In Eq. 3.18, the exchange term, $\epsilon_{X}^{LDA}[\rho(\mathbf{r})]$, has the analytic form obtained for the homogeneous electron gas [194],

$$\epsilon_{X}^{LDA}[\rho(\mathbf{r})] = -\frac{3}{4}\left(\frac{3}{\pi}\right)^{\frac{1}{3}}\rho(\mathbf{r})^{\frac{1}{3}}, \tag{3.19}$$

whereas, for the correlation term, $\epsilon_{C}^{LDA}[\rho(\mathbf{r})]$, various parametrizations have been proposed [195, 196], on the basis of the data for the correlation energy of the homogeneous electron gas obtained by accurate quantum Monte Carlo simulations [197]. These accurate calculations are mandatory, because the exact analytic expressions for the correlation energy are known only for the high-density and low-density limits [198].

Due to the nature of the underlying approximations, the LDA favours the homogeneous electronic densities, and therefore works better for systems having an electronic structure close to that of the homogeneous electron gas - *e.g.*, noble metals -, than for systems with strongly inhomogeneous densities - *e.g.*, heteroatomic molecules - [199].

3.4.2 Generalized gradient approximation

An important improvement with respect to the LDA, in terms of accuracy in the description of electronically inhomogeneous systems, has been the introduction of XC functionals which depend also on the magnitude of the gradient of the density, $|\nabla\rho(\mathbf{r})|$. Calculations performed with the so-called *generalized gradient approximation* (GGA) [200] functionals, lead to improved structures, energy barriers and energy differences [201], thus broadening the applicability of DFT with respect to problems of interest in chemistry. In a typical GGA functional, the dependency on $|\nabla\rho(\mathbf{r})|$ is included in Eq. 3.18 by means of dimensionless enhancement factors for exchange and correlation, $F_{XC}[\rho(\mathbf{r}), |\nabla\rho(\mathbf{r})|]$:

$$\epsilon_{XC}^{GGA}[\rho(\mathbf{r})] = \epsilon_{XC}^{LDA}[\rho(\mathbf{r})]F_{XC}[\rho(\mathbf{r}), |\nabla\rho(\mathbf{r})|]. \tag{3.20}$$

Numerous forms of $F_{XC}[\rho(\mathbf{r}), |\nabla\rho(\mathbf{r})|]$ have been proposed, which have the common property to differ from the exact first-order Taylor expansion around a constant density - this latter approach, defined as the *gradient expansion approximation* [202], does not lead to any substantial improvement over the LDA [28]. In particular, it is worth remembering the BP86 [203, 204], which has been one of the first GGA functionals to be proposed, and the PW91 [196] and PBE [205], which are among the most widely used in theoretical surface science. Indeed, the PBE functional is probably the simplest GGA functional. In PBE, the enhancement factor over the exchange term is:

$$E_X[\rho(\mathbf{r})] = \int \rho(\mathbf{r})\epsilon_X^{LDA}(\mathbf{r})F_X^{PBE}(s)d\mathbf{r}, \tag{3.21}$$

$$F_X^{PBE}(s) = 1 + k - \frac{k}{\frac{1+\mu s^2}{k}}, \tag{3.22}$$

where $s = \frac{|\nabla\rho(\mathbf{r})|}{2k_F\rho(\mathbf{r})}$ is a dimensionless density gradient, $k = 0.804$ is chosen to satisfy the Lieb-Oxford bound for the exchange energy,

$$E_X[\rho(\mathbf{r})] \geq E_{XC}[\rho(\mathbf{r})] \geq -1.679 \int \rho(\mathbf{r})^{\frac{4}{3}}d\mathbf{r}, \tag{3.23}$$

and $\mu = 0.21951$ is chosen to recover the linear response form of the local approximation. It has also been suggested that choosing a larger value for k leads to improved energetics for molecules on surfaces [206]. The form for the correlation is expressed as the local correlation plus an additive term, chosen to satisfy several conditions [205] - in principle, the term depends also on

the spin polarization, but here we have assumed the spin-unpolarized case for simplicity:

$$E_C[\rho(\mathbf{r})] = \int n(\mathbf{r}) \left[\epsilon_{XC}^{LDA}(r_s) + H_C^{PBE}(r_s, t)\right], \tag{3.24}$$

$$H_C^{PBE}(r_s, t) = \frac{q_e^2}{a_0}\gamma\phi^3 log\left(1 + \frac{\beta}{\gamma}t^2\frac{1 + At^2}{1 + At^2 + A^2t^4}\right), \tag{3.25}$$

$$A = \frac{\beta}{\gamma}\left[exp\left(\frac{-\epsilon_C^{LDA}}{\gamma\phi^3\frac{e^2}{a_0}}\right)\right], \tag{3.26}$$

where r_s is the local value of the density parameter, and $t = \frac{|\nabla\rho(\mathbf{r})|}{2\phi k_{TF}\rho(\mathbf{r})}$ is a dimensionless gradient, k_{TF} is the screening wave vector, q_e is the electronic charge, a_0 the Bohr radius, $\Gamma = \frac{1ln2}{\pi^2}$, $\beta = 0.066725$ comes from the generalized gradient expansion for the correlation [207], and $\phi = \frac{3}{2}$ for the spin-unpolarized case.

3.4.3 Spin-polarized density functional theory

The Kohn-Sham formalism has been also generalized to include the dependency on the spin variable [208]. In the most general implementation of *spin-polarized DFT*, each orbitals is represented in terms of two-components spinors,

$$|\varphi^{\alpha\beta}(\mathbf{r})\rangle = \begin{vmatrix}\varphi^{\alpha}(\mathbf{r})\\ \varphi^{\beta}(\mathbf{r})\end{vmatrix}, \tag{3.27}$$

where $\varphi^{\alpha}(\mathbf{r})$ and $\varphi^{\beta}(\mathbf{r})$ are complex orbitals. Accordingly, the scalar quantity $\rho(\mathbf{r})$ is reformulated in terms of a 2×2 density matrix,

$$n^{\alpha\beta}(\mathbf{r}) = \sum_{i=1}^{n}\langle\varphi_i^{\alpha}(\mathbf{r})|\varphi_i^{\beta}(\mathbf{r})\rangle, \tag{3.28}$$

Therefore, the relationships between the electronic density $\rho(\mathbf{r})$, the vectorial quantity *spin density* $\mathbf{s}(\mathbf{r})$, and $n^{\alpha\beta}(\mathbf{r})$ are

$$\rho(\mathbf{r}) = \sum_{\alpha} n^{\alpha\alpha}(\mathbf{r}), \tag{3.29}$$

$$\begin{aligned}\mathbf{s}(\mathbf{r}) &= s_x(\mathbf{r}) + s_y(\mathbf{r}) + s_z(\mathbf{r})\\ &= \sum_{\alpha\beta}\sigma^{\alpha\beta}n^{\alpha\beta}(\mathbf{r}),\end{aligned} \tag{3.30}$$

and

$$n^{\alpha\beta}(\mathbf{r}) = \frac{1}{2}(\rho(\mathbf{r})\mathbf{I} + \sigma\mathbf{s}(\mathbf{r})) = \frac{1}{2}\begin{pmatrix}\rho(\mathbf{r}) + s_z(\mathbf{r}) & s_x(\mathbf{r}) - is_y(\mathbf{r})\\ s_x(\mathbf{r}) + is_y(\mathbf{r}) & \rho(\mathbf{r}) + s_z(\mathbf{r})\end{pmatrix}, \tag{3.31}$$

where $\mathbf{I}$ is a 2×2 identity matrix and the Pauli spin matrices $\sigma = (\sigma_x, \sigma_y, \sigma_z)$ are

$$\sigma_x = \begin{pmatrix} 0 & 1 \\ 1 & 0 \end{pmatrix}, \quad \sigma_y = \begin{pmatrix} 0 & -i \\ i & 0 \end{pmatrix}, \quad \sigma_z = \begin{pmatrix} -1 & 0 \\ 0 & -1 \end{pmatrix}. \tag{3.32}$$

In the Kohn-Sham equations expressed in this two-component spinor basis, the kinetic energy operator, the electron-nuclear potential and the Hartree potential are diagonal in the two dimensional spin space, but the exchange correlation potential $\mathbf{V}_{XC}(\mathbf{r})$ is a non-diagonal 2×2 matrix that couples the two spinor components $\varphi^{\alpha}(\mathbf{r})$ and $\varphi^{\beta}(\mathbf{r})$ (notice that, in a relativistic Hamiltonian, the spin-orbit operator also couples the two spinor components, so that also the Hartree term is non-diagonal [209]). The scalar part of $\mathbf{V}_{XC}(\mathbf{r})$ depends on the choice of the exchange correlation energy functional, $\epsilon_{XC}[n^{\alpha\beta}(\mathbf{r})]$, and therefore, the coupling between $\varphi^{\alpha}(\mathbf{r})$ and $\varphi^{\beta}(\mathbf{r})$ depends exclusively on $\epsilon_{XC}[n^{\alpha\beta}(\mathbf{r})]$. This formulation of spin-polarized Kohn-Sham DFT can describe any magnetic configuration, but is computationally extremely demanding, due to the representation of the wavefunction in terms of spinors. However, the computational cost can be greatly reduced by simplifying the spin-polarized problem, and considering the direction of the quantization axis to be the same at every point in space - normally, the direction is chosen to be aligned along the z cartesian axis. In this case, $\mathbf{V}_{XC}(\mathbf{r})$ also becomes diagonal, so that the energy and all other physical observables are again functionals of the two scalar quantities $\rho(\mathbf{r})$ and $|\mathbf{s}(\mathbf{r})|$ only. Therefore, two sets of Kohn-Sham equations can be obtained, which have a similar form, and a similar computational cost, to the expressions shown in Eq. 3.14:

$$\hat{H}^{\alpha}_{KS}|\varphi^{\alpha}_i(\mathbf{r})\rangle = E^{\alpha}_i|\varphi^{\alpha}_i(\mathbf{r})\rangle, \tag{3.33}$$

$$\hat{H}^{\beta}_{KS}|\varphi^{\beta}_i(\mathbf{r})\rangle = E^{\beta}_i|\varphi^{\beta}_i(\mathbf{r})\rangle. \tag{3.34}$$

In this simplified form of the spin-polarized equations, $V^{\alpha}_{XC}(\mathbf{r})$ may still differ from $V^{\beta}_{XC}(\mathbf{r})$:

$$V^{\alpha}_{XC}(\mathbf{r}) = \frac{\delta E[n^{\alpha\beta}(\mathbf{r})]}{\delta n^{\alpha}} \neq V^{\beta}_{XC}(\mathbf{r}) = \frac{\delta E[n^{\alpha\beta}(\mathbf{r})]}{\delta n^{\beta}}, \tag{3.35}$$

$$n^{\alpha}(\mathbf{r}) = \sum_{i=1}^{n^{\alpha}} |\varphi^{\alpha}_i(\mathbf{r})|^2, \tag{3.36}$$

$$n^{\beta}(\mathbf{r}) = \sum_{i=1}^{n^{\beta}} |\varphi^{\beta}_i(\mathbf{r})|^2. \tag{3.37}$$

If Eq. 3.35 is verified, the ground state density of the α electrons, $n^{\alpha}(\mathbf{r})$, differs from that of the β electrons, $n^{\beta}(\mathbf{r})$, leading to the emergence of a total magnetic moment, which, in units of Bohr magnetons, reads:

$$M = \int d\mathbf{r} \ \left(n^{\alpha}(\mathbf{r}) - n^{\beta}(\mathbf{r})\right). \tag{3.38}$$

3.5 Solutions of the Kohn-Sham equations

The single-particle Kohn-Sham equations presented in Eq. 3.14 represent a complicated system of coupled integro-differential equations (the kinetic energy operator is differential, while the Hartree term is expressed through an integral operator). Even if, in principle, the numerical solution of these equations is possible, more efficient alternatives have been devised. In particular, recalling the second Hohenberg-Kohn theorem it is possible to extract the condition for an electronic density to minimize the functional of Eq. 3.13:

$$\delta E[\rho(\mathbf{r})] = 0. \tag{3.39}$$

Eq. 3.39 leads to the condition:

$$V_{KS}(\mathbf{r}) = V_{eN}(\mathbf{r}) + V_{Hartree}(\mathbf{r}) + V_{XC}(\mathbf{r}). \tag{3.40}$$

This means that the problem of finding the minimum of $E[\rho(\mathbf{r})]$ can be translated into that of finding the potential $V_{KS}(\mathbf{r})$ which satisfies Eq. 3.40.

Usually, the procedure to find the ground state involves an iterative cycle with the following basic steps:

1. The initial effective potential $V_{KS}^{in}(\mathbf{r})$ is constructed starting from an input density $\rho^{in}(\mathbf{r})$.

2. The Kohn-Sham equations are solved for this effective potential:

$$\hat{H}_{KS}^{in}|\varphi_i(\mathbf{r})\rangle = \left[-\frac{\hbar^2}{2m_e}\nabla^2 + V_{KS}^{in}(\mathbf{r})\right]|\varphi_i(\mathbf{r})\rangle = E_i|\varphi_i(\mathbf{r})\rangle. \tag{3.41}$$

   The general equations which are used to solve Eq. 3.41 might be slightly different depending on the functions which are used to construct the single particle orbitals $E_i|\varphi_i(\mathbf{r})\rangle$. In particular, in Section 3.5.1 we will describe the use of localized gaussian function in real space, with no boundary conditions, and in Section 3.5.2, the use of plane-wave functions with three-dimensional periodic boundary conditions. While these are the approaches that have been used in this work, it must be noted that several other possibilities exists [210, 211, 212, 213, 214].

3. A new output density, $\rho^{out}(\mathbf{r})$, is built from the solutions of Eq. 3.41. If $\rho^{in}(\mathbf{r})$ and $\rho^{out}(\mathbf{r})$ are equal within a given convergence threshold, the procedure is stopped. Conversely, $\rho^{out}(\mathbf{r})$ is used to contruct a new density $\rho^{in}(\mathbf{r})$, and the procedure is repeated again.

Therefore, the procedure of this *self-consistent field* (SCF) cycle can be summarized into the iterative progression:

$$\rho_i^{in}(\mathbf{r}) \rightarrow V_{KS}^{in}(\mathbf{r}) \rightarrow \rho_{i+1}^{in}(\mathbf{r}) \rightarrow V_{KS}^{in}(\mathbf{r}) \rightarrow ... \tag{3.42}$$

Modern DFT codes, instead of solving exactly Eq. 3.41, at every i-th step of Eq. 3.42 - which would be computationally very expensive even for systems composed by few atoms -, obtain a good approximation to its exact solution by means of *iterative algorithms* [215]. The idea of using algorithms not relying on exact matrix diagonalization has been introduces in the 80's by Car and Parrinello [216], who unified molecular dynamics (MD) techniques with the DFT for the electronic structure problem. A different approach has been also considered later in *direct minimization* algorithms [217, 218, 219], which apply conjugate gradient techniques to the electronic structure problem. On the other hand, it has been shown how, based on the ideas of of Wood and Zunger [220], traditional diagonalization algorithms can be exploited to construct robust yet powerful iterative schemes for matrix diagonalization [221, 222, 223]. The latter scheme has the advantage of not begin affected by the adiabaticity problem of the Car-Parrinello method [224, 225] - this is particularly important in the case of metals - and of having a much simpler mathematical formulation than both Car-Parrinello and *direct minimization* algorithms. The basic idea of iterative methods is to iterate an equation of the form

$$(\hat{H} - E_i^n)|\varphi_i^n(\mathbf{r})\rangle = |\mathbf{R}[\varphi_i^n(\mathbf{r})], \rangle \tag{3.43}$$

where n is the iteration step, $|\varphi_i^n(\mathbf{r})\rangle$ and E_i^n are approximate eigenvectors and eigenvalues, and $|\mathbf{R}[\varphi_i^n(\mathbf{r})]\rangle$ is the *residual vector*. This iterative cycle is continued until the residual vector falls below some predefined tolerance. Eq. 3.43 can be rewritten as:

$$|\varphi_i^n(\mathbf{r})\rangle = K(\hat{H} - E_i^n)|\varphi_i^n(\mathbf{r})\rangle + |\varphi_i^n(\mathbf{r}), \rangle \tag{3.44}$$

where K is called *preconditioning matrix*. The complete iteration sequence is:

$$E_i^n = \frac{\langle\varphi_i^n(\mathbf{r})|\hat{H}|\varphi_i^n(\mathbf{r})\rangle}{\langle\varphi_i^n(\mathbf{r})|\varphi_i^n(\mathbf{r})\rangle}, \tag{3.45}$$

$$\delta|\varphi_i^{n+1}(\mathbf{r})\rangle = K(\hat{H} - E_i^n)|\varphi_i^n(\mathbf{r})\rangle) = K|\mathbf{R}[\varphi_i^n(\mathbf{r})]\rangle, \tag{3.46}$$

$$\begin{aligned} |\varphi_i^{n+1}(\mathbf{r})\rangle &= |\varphi_i^n(\mathbf{r})\rangle, + \delta|\varphi_i^{n+1}(\mathbf{r})\rangle \\ &= |\varphi_i^n(\mathbf{r})\rangle + K|\mathbf{R}[\varphi_i^n(\mathbf{r})]\rangle, \end{aligned} \tag{3.47}$$

where the product $K|\mathbf{R}[\varphi_i^n(\mathbf{r})]\rangle$ can be evaluated efficiently by using one of the several different strategies existing in the literature [226, 227, 222, 223, 228].

A second key step in iterative algorithms is that the density is not updated according to $\rho^{in}(\mathbf{r}) = \rho^{out}(\mathbf{r})$. Indeed, to improve the numerical stability during the SCF cycle, a weighted mix of the input and output densities is used. This smoothen the variation between two successive solutions of Eq. 3.41. The most simple type of mixing is indeed a linear one, in which a certain fraction α of the charge density residual vector, $\mathbf{R}[\rho_i^{in}(\mathbf{r})] = \rho_i^{out}(\mathbf{r}) - \rho_i^{in}(\mathbf{r})$, is added to the

current input charge density:

$$\rho_{i+1}^{in}(\mathbf{r}) = \rho_i^{in}(\mathbf{r}) + \alpha \mathbf{R}[\rho_i^{in}(\mathbf{r})]. \tag{3.48}$$

In alternative to simple linear mixing, it is possible to use more elaborate schemes such as that proposed by Pulay [227], in which the input charge density at the i-th step is obtained as a linear combination of the input charge densities of a certain number x of previous steps,

$$\rho_i^{in,opt}(\mathbf{r}) = \sum_{j=1}^{x} c_j \rho_j^{in}(\mathbf{r}), \tag{3.49}$$

where c_j are the linear combination coefficients. The optimal density constructed in this way must minimize the norm of the residual vector, $\langle \mathbf{R}[\rho_i^{in,opt}(\mathbf{r})] | \mathbf{R}[\rho_i^{in,opt}(\mathbf{r})] \rangle$, under the constraint $\sum_{i=1}^{x} c_i = 1$, which makes that the number of electrons is conserved. Apart from the aforementioned two ones, a number of other mixing schemes have been also proposed in the literature [229, 230, 231, 232, 233].

Another important remark must be done concerning the use of smearing methods - see Chapter 2.9, which are fundamental to obtain a fast convergence of the SCF cycle in metallic systems. In this case, due to the effects of the smearing function, the single-particle orbitals occupancies f_i can assume fractional values, *i.e.*, $0 \leq f_i \leq 1$, so that the number of occupied orbitals m is larger than the number of electrons n. For such a situation, the total energy functional of Eq. 3.13 assumes the general form [234]:

$$\tilde{E}[f_i, \varphi_i(\mathbf{r})] = \tilde{T}_e[f_i, \varphi_i(\mathbf{r})] + E_{Hartree}[\rho(\mathbf{r})] + E_{eN}[\rho(\mathbf{r})] + E_{XC}[\rho(\mathbf{r})], \tag{3.50}$$

$$\tilde{T}_e[f_i, \varphi_i(\mathbf{r})] = -\frac{\hbar^2}{2m_e} \sum_{i=1}^{m} f_i \langle \varphi_i | \nabla^2 | \varphi_i \rangle. \tag{3.51}$$

In this case, the functional depends on the single particle orbitals $\varphi_i(\mathbf{r})$, as well as on occupancies f_i. By considering the unconstrained variation of $\tilde{E}[f_i, \varphi_i(\mathbf{r})]$ with respect to a single occupation f_i of the orbital $\varphi_i(\mathbf{r})$, while allowing the orbitals to relax, it can be proved that, independently of the form of $E_{XC}[\rho(\mathbf{r})]$ employed:

$$\frac{\partial \tilde{E}[f_i, \varphi_i(\mathbf{r})]}{\partial f_i} = E_i, \tag{3.52}$$

Eq. (3.52) is usually referred to as the *Janak's theorem* [235].

The actual values of the fractional occupations f_i, can be obtained by convoluting the original density of states with a suitable smearing function, such as those presented in Section 2.9. In this case, similarly to what happens in the extension of the Hohenberg-Kohn functional to finite temperature proposed by Mermin [236], it turns out that the total energy is no more variational with respect to the partial occupancies at the electronic ground state. A proper variational

function can, indeed, be obtained by replacing the total energy by a functional form equivalent to a generalized free energy. Hence, the variational function becomes [237, 238],

$$A[f_i, \varphi_i(\mathbf{r})] = \tilde{E}[f_i, \varphi_i(\mathbf{r})] - \sum_{band} \sum_{\mathbf{k}} \sigma S\left(f_{band,\mathbf{k}}\right), \tag{3.53}$$

where $S\left(f_{band,\mathbf{k}}\right)$ is the equivalent to an entropy term, which functional form depends on the particular choice of the smearing function, and σ is the parameter which determines the width of the smearing - see Eq. 2.65 and Eq. 2.66. It should be noted that, in conjunction with a Fermi-Dirac statistic for the occupancies, the entropy term might be interpreted as the free energy of the electrons at some finite temperature $\sigma = k_B T$, but for all the other methods, its physical significance remains undefined. Once the free energy functional has been minimized, the energy at $T \to 0K$, $E_{\sigma=0}$, can be obtained by an appropriate extrapolation of the free energy at $\sigma \to 0$ [219, 239]. A functional such as that of Eq. 3.53 offers the great advantage of begin a variational one even in the case of fractional occupancies, so that the nuclear forces can be calculated exactly by virtue of the Hellmann-Feynmann theorem (see Chapter 2.2):

$$F_\alpha = -\frac{\partial A}{\partial \mathbf{R}_\alpha} = -\nabla_\alpha A. \tag{3.54}$$

However, in this case, the forces are defined as the derivative of the generalized free energy. As a consequence, when they are used to relax the atoms towards their equilibrium positions, the obtained geometry is likely to be different from that of the equilibrium at $T = 0K$. For the typical values of σ that are used in practical calculations, $\sim$100 meV, the deviations of A from $E_{\sigma=0}$ in the Fermi-Dirac Eq. 2.65 and Gaussian methods Eq. 2.66 tend to be large - they are quadratic with σ -, and careful checks of the convergence of σ are required to ensure the reliability of the results. On the other hand, in the Methfessel-Paxton method (Eq. 2.67), these deviations tend to be much smaller, making it the method of choice when very accurate forces are required [240, 241].

3.5.1 Localized basis sets

For systems with electronic states that are relatively localized (*e.g.*, molecules in the gas-phase), it is convenient, from a computational point of view, to apply the *linear combination of atomic orbitals* (LCAO) ansatz to solve the Kohn-Sham equations [146]. This approach relies on the traditional view that molecular bonds are associated with an increased probability of finding electrons between two nuclei, due to the overlap between atomic orbitals. Therefore, the one particle Kohn-Sham orbitals can be expressed as a linear expansion of a set of L localized basis functions centered at the atomic positions, which describe at best the atomic orbitals of the

individual atomic species:

$$|\varphi_i(\mathbf{r})\rangle = \sum_{\mu=1}^{L} c_{i,\mu}|\eta_\mu(\mathbf{r})\rangle. \tag{3.55}$$

If the basis set was complete, which would require $L = \infty$, each Kohn-Sham orbital would be described exactly using Eq. 3.55. In practical calculations, L is always finite, and it is therefore of primary importance to choose the most appropriate set of basis functions to represent accurately the property of interest. Inserting Eq. 3.55 in the Kohn-Sham equations (Eq. 3.14) leads to:

$$\hat{H}_{KS} \sum_{\mu=1}^{L} c_{i,\mu}|\eta_\mu(\mathbf{r})\rangle = E_i \sum_{\mu=1}^{L} c_{i,\mu}|\eta_\mu(\mathbf{r})\rangle, \tag{3.56}$$

By multiplying Eq. 3.56 by an arbitrary basis function $\langle\eta_\nu(\mathbf{r})|$, we obtain a set of L equations, which in compact notation reads:

$$\mathbf{F}^{KS}\mathbf{C} = \mathbf{SCE}, \tag{3.57}$$

where $\mathbf{F}^{KS}$ is the $L \times L$ dimensional *Kohn-Sham matrix*, with elements:

$$F^{KS}_{\nu,\mu} = \langle\eta_\nu(\mathbf{r})|\hat{H}|\eta_\mu(\mathbf{r})\rangle, \tag{3.58}$$

which is the counterpart of the Fock matrix in the Hartree-Fock method [242]. $\mathbf{S}$ is the $L \times L$ *overlap matrix* with elements:

$$S_{\nu,\mu} = \langle\eta_\nu(\mathbf{r})|\eta_\mu(\mathbf{r})\rangle, \tag{3.59}$$

$\mathbf{C}$ is the $L \times L$ dimensional matrix of the expansion coefficients:

$$\mathbf{C} = \begin{pmatrix} c_{1,1} & c_{1,2} & \cdots & c_{1,L} \\ c_{2,1} & c_{2,2} & \cdots & c_{2,L} \\ \vdots & \vdots & \ddots & \vdots \\ a_{L,1} & a_{L,2} & \cdots & c_{L,L} \end{pmatrix}, \tag{3.60}$$

and $\mathbf{E}$ is an $L \times L$ dimensional diagonal matrix of the orbital energies:

$$\mathbf{E} = \begin{pmatrix} E_1 & 0 & \cdots & 0 \\ 0 & E_2 & \cdots & 0 \\ \vdots & \vdots & \ddots & \vdots \\ 0 & 0 & \cdots & E_L \end{pmatrix}. \tag{3.61}$$

As it can be seen, the complex integro-differential problem of Eq. 3.14 has been translated

in a much simpler linear one, which can be expressed using standard linear algebra.

Among the possible choices for the basis functions $|\eta_\mu(\mathbf{r})\rangle$, *Gaussian Type Orbitals* (GTO) [243] are the most used ones for applications in molecular gas-phase chemistry. In GTOs, the single particle orbitals may be expressed either in terms of Gaussian functions times spherical harmonics $Y_{l,m}(\theta,\phi)$:

$$\eta^{GTO}(\mathbf{r}) = Nr^{(2n-2-l)}e^{-\xi r^2}Y_{l,m}(\theta,\phi), \tag{3.62}$$

or in terms of cartesian functions:

$$\eta^{GTO}(\mathbf{r}) = Nx^l y^m z^n e^{-\xi r^2}, \tag{3.63}$$

where N is a normalization coefficient. The advantages of using GTO is that any orbital expressed in terms of the basis functions, and centred at any atomic site, can be expressed in terms of the basis functions on neighbouring sites. This means that the multi-center integrals, *i.e.*, all the matrix elements in Eq. 3.58, can be evaluated analytically, greatly simplifying and speeding up the calculations. However, gaussian function do not represent correctly important characteristics of actual atomic wavefunction, such as its decay behaviour or the cusp at the nuclear positions. Indeed, these characteristics are reproduced correctly by Slater type orbitals (STOs) [244]:

$$\eta^{STO}(\mathbf{r}) = Nr^{(n-1)}e^{-\xi r^2}Y_{l,m}(\theta,\phi), \tag{3.64}$$

For this reason, it is common practice to use linear combinations of GTOs, in order to try to reproduce as close as possible the behaviour of STOs [245]. Hence, it is possible to construct a whole hierarchy of basis sets with a desired balance between accuracy and computational efficiency. The *minimal* basis set will correspond to 1 GTO per atomic orbital. In *double-zeta* basis sets, the set of GTOs used for each orbital is doubled. If the doubled functions are limited to the atomic valence shell, *split-valence* basis sets are defined. A particular basis set may also be enhanced by adding *polarization functions*, *i.e.*, functions of higher angular momentum than those occupied in the atom, to ensure that the orbitals can distort from their original atomic symmetry, and better adapt to the molecular environment. In the cases where electrons lying very far from the nucleus have to be described, *diffuse functions* can also be defined in GTO as functions in which the exponent ξ is taken to be very small.

3.5.2 Plane-waves basis sets

Plane waves are periodic functions and, as such, are suitable as $u(\mathbf{r})$ - a function with the periodicity of the unit cell - in Bloch's equations (see Eq. 2.56 and Eq. 2.57). Indeed, they represent one of the most straightforward ways to implement the Kohn-Sham equations within periodic boundary conditions. Hence, in a plane-waves basis set, the Kohn-Sham i-th state at

the Brillouin zone point k-th can be expressed as:

$$|\varphi_{i,\mathbf{k}}(\mathbf{r})\rangle = e^{i\mathbf{k}\cdot\mathbf{r}} \sum_{\mathbf{G}} c_{i,\mathbf{k},\mathbf{G}} e^{i\mathbf{G}\cdot\mathbf{r}} = \sum_{\mathbf{G}} c_{i,\mathbf{k},\mathbf{G}} e^{i(\mathbf{k}+\mathbf{G})\cdot\mathbf{r}} = \sum_{\mathbf{G}} c_{i,\mathbf{k},\mathbf{G}} |\mathbf{k}+\mathbf{G}\rangle, \tag{3.65}$$

where the set of $\mathbf{G}$ vectors is limited to those having the same periodicity of the unit cell, *i.e*,

$$\mathbf{G} = i\mathbf{b_1} + j\mathbf{b_2} + k\mathbf{b_3}, \tag{3.66}$$

where $\mathbf{b_1}, \mathbf{b_2}, \mathbf{b_3}$ are the reciprocal lattice vectors. Plane-wave basis sets have the useful property to be orthonormal. Therefore, whenever a plane-wave basis set is used, the overlap matrix $\mathbf{S}$ (Eq. 3.59) is diagonal.

Inserting Eq. 3.65 in the solution of the Schrödinger equation according to Bloch's theorem, Eq. 2.56, multiplying by $\langle \mathbf{k}+\mathbf{G}'|$, with $\mathbf{G} \neq \mathbf{G}'$, and using the Kohn-Sham Hamiltonian, leads to the Kohn-Sham equations in Fourier space:

$$\sum_{\mathbf{G}} \langle \mathbf{k}+\mathbf{G}'|\hat{H}_{KS}|\mathbf{k}+\mathbf{G}\rangle c_{i,\mathbf{k},\mathbf{G}} = E_{i,k} \sum_{\mathbf{G}} \langle \mathbf{k}+\mathbf{G}'|\mathbf{k}+\mathbf{G}\rangle c_{i,\mathbf{k},\mathbf{G}} = E_{i,k} c_{i,\mathbf{k},\mathbf{G}'}. \tag{3.67}$$

In a plane-waves basis, the kinetic energy term of Eq. 3.67 is assume a diagonal form:

$$\langle \mathbf{k}+\mathbf{G}'|\hat{T}_{KS}|\mathbf{k}+\mathbf{G}\rangle = \begin{pmatrix} |\mathbf{k}+\mathbf{G_0}|^2 & 0 & \cdots & 0 \\ 0 & |\mathbf{k}+\mathbf{G_1}|^2 & \cdots & 0 \\ \vdots & \vdots & \ddots & \vdots \\ 0 & 0 & \cdots & |\mathbf{k}+\mathbf{G_{N_G}}|^2 \end{pmatrix}, \tag{3.68}$$

where $\mathbf{N_G}$ is the total number of $\mathbf{G}$ vectors. The latter is usually defined in terms of the so-called kinetic energy cutoff, which defines the longest $\mathbf{G}$ vector in the plane-wave expansion:

$$\frac{1}{2}|\mathbf{k}+\mathbf{G_0}|^2 \leq E_{cut}. \tag{3.69}$$

Applying straightforwardly Eq. 3.67 does not lead to an efficient algorithm for a plane-waves basis. This is due to the fact that the term $\langle \mathbf{k}+\mathbf{G}'|\hat{H}_{KS}|\mathbf{k}+\mathbf{G}\rangle$ still constitutes a dense matrix, due to the fact that the potential part is, in general, non-null for all $\mathbf{G}, \mathbf{G}'$. However, this problem can be circumvented by considering that the potential terms in Eq. 3.67 are diagonal in real space. Thus, both kinetic and potential terms can be evaluated efficiently by making use of Fast Fourier Transform (FFT) , leading to an efficient sparse algorithm for plane-waves.

Compared to localized basis sets, plane-wave basis sets offer the main advantages that (i) the convergence of the basis set can be systematically checked by simply increasing the kinetic energy cutoff and (ii) the basis functions fill the entire simulation box, and therefore describe correctly those features of the electronic structure that are not centred at the nuclear positions. However, pure plane waves basis sets have the strong disadvantage that an extremely large number of

Fourier components is needed to describe the strong oscillation of the wavefunctions close to the nuclei, which ensure orthogonality between the different single-particle states. This makes calculations on real materials practically unfeasible using a pure plane waves basis set.

3.5.3 Projector augmented wave method

Several techniques have been developed to reduce the number of plane-waves needed in the calculations, and to permit the application of this basis set to real materials. They rely on the common observation that, far from the nucleus positions, core wavefunctions are zero, and valence wave functions are smooth. Among the most recent methods is certainly the *projector augmented waves* (PAW) method [246], a generalization of the much older *linearly augmented plane waves* (LAPW) method [247]. In the latter, the space is divided into atom-centered augmentation spheres inside which the wave functions are taken as some atom-like partial waves, and an interstitial region outside the spheres, where some envelope functions are defined. The partial waves and envelope functions are then matched at the boundaries of the spheres.

In the PAW method a *pseudo single-particle wavefunction* $\tilde{\varphi}(\mathbf{r})$ is defined, which is identical to the all-electron single particle wavefunction $\varphi(\mathbf{r})$ beyond a arbitrary cutoff radius - usually chosen between the ionic and covalent radius of each element. The region of space inside the cutoff radius is defined as the *augmentation sphere*. Inside this region, $\tilde{\varphi}(\mathbf{r})$ differs from $\varphi(\mathbf{r})$ in being nodeless, which allows it to be well represented by a much lower number of planewaves, compared to the number of plane-waves used to represent all-electron single-particle wavefunction. This definition of $\tilde{\varphi}$ is analogue to that done in the *pseudopotential* (PP) method [248, 249, 250]. This explains why several of the first implementations of the PAW method have been done on original PP-based codes [251] - in particular, the variant of the PP method defined as ultrasoft PP [252]. However, at difference with the PP method, in the PAW method the all-electron single-particle wavefunction φ can be recovered from $\tilde{\varphi}$ by means of a linear transformation[1]:

$$|\varphi_i(\mathbf{r})\rangle = |\varphi_i(\mathbf{r})\rangle + \sum_{\mu}(|\phi_\mu(\mathbf{r})\rangle - |\tilde{\phi}_\mu(\mathbf{r})\rangle)\langle\tilde{p}_\mu(\mathbf{r})|\tilde{\varphi}_i(\mathbf{r})\rangle, \tag{3.70}$$

where the index μ runs over the ionic sites $\mathbf{R}_\alpha$, the angular momenta $\{l_\mu, m_\mu\}$ of the atomic wavefunction and the multiple reference energies, which can be defined for each angular momentum. Eq. 3.70 states that the all-electron single-particle wavefunction $|\varphi_i(\mathbf{r})\rangle$ associated to each i-th pseudo wave function $|\tilde{\varphi}_\mu(\mathbf{r})\rangle$ can be reconstructed by adding a combination of one-center corrections $|\phi_\mu(\mathbf{r})\rangle - |\tilde{\phi}_\mu(\mathbf{r})\rangle$. The wavefunctions $|\phi_\mu(\mathbf{r})\rangle$ are the all-electron single-particle solutions of the spherical scalar-relativistic Schrödinger equation [253], for a spin-unpolarized atom,

$$\left[-\frac{\hbar^2}{2m_e}\nabla^2 + V_{eff}(\mathbf{r})\right]|\phi_\mu(\mathbf{r})\rangle = E_\mu|\phi_\mu(\mathbf{r})\rangle,$$

where $V_{eff}(\mathbf{r})$ is the spherical component of the all-electron potential. $|\tilde{\phi}_\mu(\mathbf{r})\rangle$ are the correspond-

[1] we have dropped the index for the k-points $\mathbf{k}$ in the definition of $|\varphi_i(\mathbf{r})\rangle$

ing pseudo wavefunctions, which are nodeless, and identical to $|\phi_\mu(\mathbf{r})\rangle$ outside the augmentation sphere. The functions $|\tilde{p}_\mu(\mathbf{r})\rangle$ are *projector functions*, which are constructed in order to have the important property of being dual, *i.e.*, $\langle\tilde{p}_\mu(\mathbf{r})|\tilde{\phi}_\nu(\mathbf{r})\rangle = \delta_{\mu,\nu}$ and $|\tilde{p}_\mu(\mathbf{r})\rangle = 0$ outside the augmentation sphere.

The *projection operator*, which allows to map $|\varphi_i(\mathbf{r})\rangle$ into the corresponding $|\tilde{\varphi}_i(\mathbf{r})\rangle$, is:

$$\tau = 1 + \sum_\mu (|\phi_\mu(\mathbf{r})\rangle - |\tilde{\phi}_\mu(\mathbf{r})\rangle)\langle\tilde{p}_\mu(\mathbf{r})|. \tag{3.71}$$

Considering a generic operator A, using Eq. 3.71 it possible to define a *pseudo operator* $\tilde{A}$ acting on $|\tilde{\varphi}_i(\mathbf{r})\rangle$:

$$\begin{aligned}\tilde{A} &= \tau^\dagger A \tau \\ &= A + \sum_{\mu,\nu} |\tilde{p}_\mu(\mathbf{r})\rangle \Big(\langle\phi_\mu(\mathbf{r})|A|\phi_\nu(\mathbf{r})\rangle - \langle\phi_\mu(\mathbf{r})|A|\phi_\nu(\mathbf{r})\rangle \Big) \langle\tilde{p}_\mu(\mathbf{r})| + \Delta A.\end{aligned} \tag{3.72}$$

ΔA is a term which contains mixed one-center and plane-waves terms. It is expressed in terms of the generic operator B:

$$\Delta A = B - \sum_{\mu,\nu} |\tilde{p}_\mu(\mathbf{r})\rangle\langle\tilde{\phi}_\mu(\mathbf{r})|\hat{B}|\tilde{\phi}_\nu(\mathbf{r})\rangle\langle\tilde{p}_\nu(\mathbf{r})|, \tag{3.73}$$

and is used to remove the unwanted singularity in the Hartree term in the equation for the pseudo wavefunctions, leaving a term which can be dealt with in the radial equations about each nucleus.

The motivation behind the idea of transforming the operators rather than the wavefunction, is that, by proceeding in this way, it is possible to treat the pseudo wavefunction $|\tilde{\varphi}_i(\mathbf{r})\rangle$ and the one-center all-electron orbitals $|\phi_\mu(\mathbf{r})\rangle$ as two separated problems. Accordingly, it can be shown that the pseudo wavefunctions are exact solutions of a Kohn-Sham equation of the form

$$\begin{aligned}\left[-\frac{\hbar^2}{2m_e}\nabla^2 + V_{KS}^{in}(\mathbf{r}) + \sum_{\mu,\nu} |\phi_\mu(\mathbf{r})\rangle D_{\mu,\nu} \langle\tilde{p}_\mu(\mathbf{r})| \right] |\tilde{\varphi}_i(\mathbf{r})\rangle \\ = E_i \Big(1 - \sum_{\mu,\nu} |\phi_\mu(\mathbf{r})\rangle Q_{\mu,\nu} \langle\tilde{p}_\mu(\mathbf{r})| \Big) |\tilde{\varphi}_i(\mathbf{r})\rangle,\end{aligned} \tag{3.74}$$

where $Q_{\mu,\nu}$ are compensation charges having the form:

$$Q_{\mu,\nu} = \langle\phi_\mu(\mathbf{r})|\phi_\nu(\mathbf{r})\rangle - \langle\tilde{\phi}_\mu(\mathbf{r})|\tilde{\phi}_\nu(\mathbf{r})\rangle, \tag{3.75}$$

and $D_{\mu,\nu}$ are one-center correction terms defined as:

$$D_{\mu,\nu} = \langle\phi_\mu(\mathbf{r})| - \frac{\hbar^2}{2m_e}\nabla^2 + V_{eff}(\mathbf{r})|\phi_\nu(\mathbf{r})\rangle, \tag{3.76}$$

$$+ \langle\phi_\mu(\mathbf{r})| - \frac{\hbar^2}{2m_e}\nabla^2 + V'_{eff}(\mathbf{r})|\phi_\nu(\mathbf{r})\rangle, \tag{3.77}$$

where V'_{eff} is the spherical potential obtained from the construction of $|\tilde{\phi}_i(\mathbf{r})\rangle$. Hence, the total electronic density can be evaluated as:

$$\rho(\mathbf{r}) = \tilde{\rho}(\mathbf{r}) - \tilde{\rho}(\mathbf{r})' + \rho(\mathbf{r})', \tag{3.78}$$

where the three terms in Eq. 3.74 are:

$$\tilde{\rho}(\mathbf{r}) = \sum_i \langle\tilde{\varphi}_i(\mathbf{r})|\tilde{\varphi}_i(\mathbf{r})\rangle, \tag{3.79}$$

$$\tilde{\rho}(\mathbf{r})' = \sum_i \sum_{\mu,\nu} \langle\tilde{\varphi}_i(\mathbf{r})|\tilde{\phi}_\mu(\mathbf{r})\rangle\langle\tilde{\phi}_\mu(\mathbf{r})|\tilde{\phi}_\nu(\mathbf{r})\rangle\langle\tilde{\phi}_\nu(\mathbf{r})|\tilde{\varphi}_i(\mathbf{r})\rangle, \tag{3.80}$$

$$\rho(\mathbf{r})' = \sum_i \sum_{\mu,\nu} \langle\tilde{\varphi}_i(\mathbf{r})|\tilde{\phi}_\mu(\mathbf{r})\rangle\langle\phi_\mu(\mathbf{r})|\phi_\nu(\mathbf{r})\rangle\langle\tilde{\phi}_\nu(\mathbf{r})|\tilde{\varphi}_i(\mathbf{r})\rangle. \tag{3.81}$$

The term $\tilde{\rho}(\mathbf{r})$ is constructed from the self-consistent single-particle pseudo wavefunctions $|\tilde{\varphi}_i(\mathbf{r})\rangle$, while the terms $\rho(\mathbf{r})'$ and $\tilde{\rho}(\mathbf{r})'$ are one-center densities constructed from the pseudo and all-electron atomic wavefunctions, respectively. $\tilde{\rho}(\mathbf{r})$ is expanded in plane-waves, while $\rho(\mathbf{r})'$ and $\tilde{\rho}(\mathbf{r})'$ can be stored on radial support grids, localized inside the augmentation sphere.

An analogous decomposition can be done for the rest of the quantum-mechanical operators. In particular, the total energy can be written as

$$E[\rho(\mathbf{r})] = \tilde{E}[\rho(\mathbf{r})] - \tilde{E}'[\rho(\mathbf{r})] + E'[\rho(\mathbf{r})], \tag{3.82}$$

where each term in Eq. 3.82 consists of a kinetic, Hartree and exchange-correlation contribution. Eq. 3.74 is solved for a selected number of outer shell electrons, normally the valence and eventually the semi-core ones, while the wavefunctions of the inner core electrons are not optimized, *i.e.*, their configuration is frozen to that of the isolated atoms. Therefore, the PAW method provides access to the all-electron wavefunction, but only within the *frozen core* approximation. However, this approximation is usually legitimate for most of chemistry-related problems. It should also be noted that, in the PAW method, Pulay contributions to the forces must be evaluated explicitly, since the one-center terms depend on the atomic coordinates.

3.6 Dispersion interactions in density functional theory

It is a well recognized fact, that common XC functionals such as the LDA and GGA give an erroneous description of dispersion interactions. This failure can be easily understood by considering a Møller-Plesset perturbational approach to the second order (MP2), which is the simplest way to add rigorously the electronic correlation energy to an uncorrelated Hartree-Fock wavefunction. In MP2, the correlation energy between two fragments A and B is calculated as [242]:

$$E_C^{MP2} = \sum_{i<j} \sum_{k<l} \frac{[\langle ij|kl\rangle - \langle ij|lk\rangle]^2}{E_i + E_j - E_k - E_l}, \tag{3.83}$$

where the sum is carried over occupied (vacant) single-particle states i and j (k and l), localized on A and B, respectively, $\langle ij|kl\rangle - \langle ij|lk\rangle$ is a bi-electronic integral of the form

$$\langle ij|kl\rangle - \langle ij|lk\rangle = \int\int \frac{\psi_i(\mathbf{r})\psi_j(\mathbf{r}')\psi_k(\mathbf{r})\psi_l(\mathbf{r}')}{|r - r'|} d\mathbf{r}d\mathbf{r}', \tag{3.84}$$

and $\mathrm{E}_{i,j,k,l}$ are the corresponding orbital energies. It can be seen that the exact treatment of correlation energy involves the explicit consideration of vacant single-particle orbitals. The reason for this is that correlation effects arise due to excitations to higher energy electronic states in the two fragments, produced by the electromagnetic fluctuations present in the system. These excitations may also be explained in terms of the formation of fluctuating multipole moments due to instantaneous variations in the charge distribution of the two fragments [254]. An exact XC functional, which in principle should be able to capture these effects, should obey the requirement of having a Coulomb-like decay [146]. This should cancel out the spurious *self-interaction* of each electron with itself which arises in the Hartree term of Eq. 3.13. In a similar way to what happens in Hartree-Fock, that is:

$$E_{Hartree}[\rho(\mathbf{r})] = -E_{XC}[\rho(\mathbf{r})]. \tag{3.85}$$

One of the conditions for Eq. 3.85 to hold is that the decay of XC term must be $\propto R$, *i.e.*, equal to that of the Hartree term. However, in practical realisations of the Kohn-Sham DFT scheme the approximations to the exchange-correlation energy employed are independent of $E_{Hartree}[\rho(\mathbf{r})]$, and this identity does not hold. In particular, the decay of the LDA and GGA functionals is exponential, *i.e.*, much faster than that of the Hartree term [146]. Therefore, when two electrons are far apart, these functionals are not able to describe their interaction, thus failing in describing correctly very weakly bound situations. This is the case of *van der Waals* (vdW) forces, which are the main responsible for the interaction between the neutral fragments which wavefunction have very small overlap. It also shall be noted that, in some cases, the LDA functional has been found to provide good results for selected properties of vdW-bound materials. This is the case, *e.g.*, for the interlayer distance of graphite. However, this is due to

a unphysical tendency of the exchange term in the XC functional to overestimate binding [255], while vdW interactions should be described by the correlation term of the XC functional [256]. For this reason, the LDA functional cannot be considered as universally capable of describing vdW interactions, and the use of this functional to describe vdW-bound materials has to be treated with particular care.

3.6.1 Grimme's DFT+D2 approach

Numerous schemes have been considered to remedy the poor description of vdW forces provided by standard XC functionals. The most pragmatic one is certainly that of adding an empirical potential term to the usual DFT energy:

$$E_{DFT+D} = E_{DFT} + E_D. \tag{3.86}$$

This concept has originally been developed to include correlation in pure Hartree-Fock calculations [257]. However, modern approaches for vdW interactions based on DFT have evolved considerably, so that the potential term E_D included can assume a variety of different forms.

The most simple one considers only pairwise interactions and has the form:

$$E_D = -\sum_{a,b} s_6 \frac{C_6^{a,b}}{R_{a,b}^6} f_{damp}(R_{a,b}) = -\sum_{a,b} s_6 \frac{C_6^{a,b}}{|\mathbf{R}_a - \mathbf{R}_b|^6} f_{damp}(R_{a,b}), \tag{3.87}$$

which corrects the exponential asymptotic behaviour of XC potential, leading to the correct asymptotic behaviour of the energy for two closed-shell atoms:

$$E \propto R^{-6}, \tag{3.88}$$

In Eq. 3.87, s_6 is a scaling factor, which is used to adjust the correction of the repulsive behaviour of the underlying XC functional, $\mathbf{R}_a$ and $\mathbf{R}_b$ are the positions of the atoms a and b, and $C_6^{a,b}$ is a material dependent coefficient which describes the isotropic dipole-dipole interaction between the two atoms, which is linked to the frequency dependent polarizability by the integral relation (in Hartree atomic units) [258]:

$$C_6^{a,b} = \frac{1}{\pi} \int_0^\infty \alpha(i\omega)\beta(i\omega) d\omega, \tag{3.89}$$

where ω is the frequency and α and β are the polarizabilities of atoms a and b, respectively. $f_{damp}(R_{a,b})$ is a *damping function*, which is used to avoid double counting effects of correlation at intermediate internuclear distances, and the singularities in the limit $\lim_{R_{a,b}\to 0} R_{a,b}^{-6} = -\infty$, thereby taking into account that at typical bonding distances the R^{-6} is not longer appropriate. In the case of a periodic system, Eq. 3.87 must be computed for all possible L translations of

the unit cell [259]:

$$E_D = -\sum_{a,b}\sum_{L} s_6 \frac{C_6^{a,b}}{R_{a,b}^6} f_{damp}(R_{a,b,L}),$$
$$= -\sum_{a,b}\sum_{L} s_6 \frac{C_6^{a,b}}{|\mathbf{R}_{a,0} - \mathbf{R}_{b,L}|^6} f_{damp}(R_{a,b,L}). \tag{3.90}$$

In principle, the sum over the L translations should be performed over an infinite number of translations. In practice, L is a finite number, and interactions over distances larger than a certain suitably chosen cutoff radius are ignored.

The formula shown in Eq. 3.87 looks very appealing because of its simplicity. In fact, being a simple sum, it provides access to the vdW energy term basically at a negligible computational cost, compared to that of a common DFT calculation, especially for systems of large dimensions. However, the method has also the serious disadvantage that it is very difficult to define a set of universal parameters to make it generally applicable. Indeed, several variants of the method have been proposed [260, 255], but most of them never gained popularity due to lack of this general character.

The first significant advance in this respect has been made by the method proposed by Grimme [261], and in particular by its second variant, DFT+D2 [147]. In DFT+D2, $f_{damp}(R_{a,b})$ is a Fermi-like functions having the form

$$f_{damp}(R_{a,b}) = \frac{1}{1 + e^{d(R_{a,b}/R_r - 1)}}, \tag{3.91}$$

where R_r is the sum of the scaled atomic van der Waals radii of the two atoms, and $d = 20$ is a dimensionless empirical parameter which determines the steepness of the Fermi function [262]. The scaled atomic van der Waals radii are determined by Hartree-Fock atomic calculations and taking the same electronic density contour for all the atoms (0.01 a_0^3, a_0 being the Bohr radius), while the scheme for the calculation of the atomic C_6 coefficients is derived from London's dispersion formula, and it is based on DFT calculation with hybrid functionals of the atomic ionization potential I_p and the static dipole polarizabilities α:

$$C_6^a = 0.05 N I_p^a \alpha^a, \tag{3.92}$$

where $N = 2, 10, 18, 36, 54$ for the $1^{st,}$, 2^{nd}, 3^{rd}, 4^{th} and 5^{th} row atoms, and the proportionality constant s_6 is adjusted over a range of reference values [147, 262]. For a pair of atoms a and b, the corresponding dispersion coefficient is then derived as the geometrical average of the atomic C_6 coefficent:

$$C_6^{a,b} = \sqrt{C_6^a C_6^b}. \tag{3.93}$$

For transition metals, this approach has little physical meaning, since the difference between the bound and the free atom are extremely large. Therefore, the corresponding values have been taken as the average between the C_6 coefficients of the preceding rare gas and the following group III element.

Despite the significant degree of empiricism involved in the method, the popularity of DFT+D2 has been boosted by the fact that it provides a reasonable description of vdW effects at a minimal computational effort. However, it should be remarked that, since its proposal, several new methods have been developed, that are able to treat very large systems with considerably lower degree of empiricism and much higher accuracy [263, 264]. In particular, many new schemes do not treat the C_6 coefficients as predetermined constant quantities, but consider the environmental dependency of the C_6: two notorious examples are the last version of the Grimme's method, DFT+D3 [265], and the method by Tkatchenko and Scheffler, DFT+vdW [266]. Non-empirical functionals such as the vdW-DF [267], despite being more computationally expensive of the aforementioned ones, can now be applied to systems formed by hundreds of atoms thanks to new and efficient algorithmic improvements [268]. In addition, many-body terms beyond the simple pair-wise interactions are being considered actively [269, 270], resulting in very accurate description of vdW bonding.

3.6.2 DFT+D2 applied to organic molecules on metallic surfaces

Due to its simplicity and computational efficiency, the DFT+D2 method has been applied to large scale numerous problems. In particular, the description of organic molecules on metallic surfaces [271, 272, 273, 88, 274] often involves unit cells formed by a large number of atoms, which are necessary to describe realistically the surface of the metal.

However, the very crude approximations on which DFT+D2 relies seriously call into question the applicability of the method in the case of extended metallic solids. In fact, in metals, the presence of a delocalized Fermi sea makes that the response properties of the system [275] are significantly different with respect to those of an insulating system, such as a molecule or an insulating solid, which are the actual targets of Grimme's method. One of the major consequences of this, is that the asymptotic behaviour of the energy deviates form that of Eq. 3.88 [276, 277]. Therefore, in principle, DFT+D2 is not expected to be neither accurate nor reliable for metallic systems.

In view of this, benchmarks against accurate experimental results have been particularly important to assess the quality and the limits of the applicability of DFT+D2 to describe organic molecular systems on metals. In particular, Mercurio *et al.* [278] have shown how the inclusion of vdW interactions using the DFT+D2 and the DFT+vdW methods can alter significantly the characteristics of the adsorption geometry of organic molecules on metallic surfaces [279], globally leading to a better agreement with the experimental data. Moreover, they have shown that the adsorption energies predicted by these two methods are systematically too high. This overestimation has been attributed to the neglect of screening of the metallic electrons, since

considering only the topmost metallic layer in the PBE+vdW calculations lead to a considerable improvement of the agreement between theory and experiment. Similarly Tonigold and Größ [280] have compared the experimental adsorption geometries and energetics of small aromatic molecules with calculations performed using PBE+D2, and an hybrid method [281], which combines MP2 calculations on metallic clusters with DFT calculations to derive the C_6 coefficients of the metal. Also in this case, similar results to the aforementioned ones have been obtained, with reasonable adsorption geometries but adsorption energies overestimated with respect to the experimental ones. In this case, the "corrected" C_6 coefficients of the metal obtained with the hybrid methods have been found to be smaller by ∼50 % with respect to the DFT+D2 ones. Indeed, the adsorption energies calculated with these new coefficients, have been found to be in good agreement with experiments. The fact that overestimation of the adsorption energies is essentially an artefact, which derives from the neglect of the screening effects, has been also supported by recent calculations [282], in which the effect of screening has been incorporated in the DFT+vdW method by combining it with the Lifshitz Zaremba-Kohn theory for the vdW interaction between an atom and a solid surface [283, 284]. These calculations also lead to C_6 coefficients for noble metals much smaller with respect to the original DFT+vdW ones.

In synthesis, the DFT+D2 must be always treated with care when applied to organic systems adsorbed on metallic surfaces. Normally, forces - and hence geometries - are in reasonable agreement with the experimental data, as also confirmed recently by single-molecule mechanics measurements [285] . However, for a description of the systems that goes beyond the simple qualitative description of vdW interactions, the errors deriving from the aforementioned limitations must be always considered and evaluated.

4 Analysis Tools

This Chapter provides a brief overview of the main methods that have been used for the analysis of the density functional theory calculations presented in this work. First, two important tools for the characterization of the electronic structure details are described, which are the projection of the total density of states on selected atoms, and the definition of the density of states on an arbitrary point in space. Then, the atoms in molecules theory is introduced as a tool to calculate atomic charges, and the details of an efficient algorithm, which allows to perform such analysis on very large systems, are presented.

4.1 Projected density of states

One of the limitations of plane-wave basis sets is that they not depend on the atomic positions $\mathbf{R}_\alpha$, which prevents any analysis based on atomic properties. Therefore, to obtain this type of informations from a plane-wave calculation, it is necessary to project the plane-wave basis set onto an LCAO basis set [286]. As discussed in Section 3.5, the latter is much more useful for this type of analysis, because of its dependence on the atomic positions. Hence, the *projected density of states* (PDOS) at the energy E_i and over a specific atomic orbital η_ν centred at the atomic position $\mathbf{R}_\alpha$, is calculated as [1]:

$$\mathrm{PDOS}(E_i) = \sum_i |\langle \eta_\nu(\mathbf{r}) | \psi_i(\mathbf{r}), \rangle|^2 \delta(E - E_i), \tag{4.1}$$

where, if it is the case, the dirac delta can be substituted for one of the smearing functions described in Section 2.9. Similarly, the analogue of Eq. 4.1 for the spin-polarized case is:

$$\mathrm{PDOS}(E_i^\alpha) = \sum_i |\langle \eta_\nu(\mathbf{r}) | \psi_i^\alpha(\mathbf{r}) \rangle|^2 \delta(E - E_i^\alpha), \tag{4.2}$$

$$\mathrm{PDOS}(E_i^\beta) = \sum_i |\langle \eta_\nu(\mathbf{r}) | \psi_i^\beta(\mathbf{r}) \rangle|^2 \delta(E - E_i^\beta), \tag{4.3}$$

It is clear that the choice of the LCAO basis determines the final quality of the projection [287, 288]. For the PAW plane-wave calculations presented in this work, the LCAO basis set used to calculated the PDOS is formed by orbitals which are solution of atomic all-electron

[1] we have dropped the dependency on the wave vector $\mathbf{k}$ for simplicity

single-particle calculations used to generate the PAW projectors, and the overlap is calculated only within the region of space spanned by the PAW augmentation sphere. Clearly, this basis is by no means complete. This makes the calculated PDOS only qualitatively meaningful, and their interpretation possible only in terms of relative quantities [289].

4.2 Local density of states

In some cases, one might not be interested in analyizing the DOS at some specific atomic positions, but rather in exploring its features at some arbitrary point $\mathbf{r}_0$ in the unit cell. The corresponding quantity is then defined as the *local density of states* (LDOS) . The LDOS at $\mathbf{r}_0$ and E_i is obtained directly from the single-particle Kohn-Sham orbitals as:

$$\mathrm{LDOS}(\mathbf{r}_0, E_i) = \sum_i \langle \psi_i(\mathbf{r}_0) | \psi_i(\mathbf{r}_0) \rangle \delta(E - E_i). \tag{4.4}$$

It should be noted that, since the LDOS is not the projection of the total DOS over some specific atomic orbitals, its features, in principle, cannot be attributed to individual atomic orbital features as in the case of the PDOS.

4.3 Charge Analysis in large systems using the theory of atoms in molecules

One of the possible ways to define atomic charges in molecular systems is to make explicit use of the concept of PDOS defined in Section 4.1 [290, 291, 292]. However, for a plane wave basis set, the non-orthogonality of the LCAO basis used for projection may result in some electronic charge being left out from the integration, making it difficult to determine the actual atomic charge state [293].

One less arbitrary fashion of approaching this problem is the decomposition of the charge density on the basis of its topology, by using the *atoms in molecules* (AIM) theory [294, 295]. In AIM, the electronic density is decomposed into a series of disjoint regions Ω, which are called *basins*. The surfaces that enclose these regions are defined as *zero-flux surfaces*, which share the common property of being normal to the gradient vector field of the electronic density, $\nabla\rho(\mathbf{r})$, *i.e.*,

$$\nabla\rho(\mathbf{r}) \cdot \vec{n}(\mathbf{r}) = 0, \tag{4.5}$$

where $\vec{n}(\mathbf{r})$ is a vector normal to the surface $S(\Omega)$, and $\mathbf{r}$ is a point of space lying on the same surface. This boundary condition leads to a partitioning of a molecular system in which each region Ω contains a maximum that corresponds to an *electron density attractor*, *i.e.*, a nucleus. The charge N within each region Ω is then defined as:

$$N = \int_\Omega \rho(\mathbf{r}) d\mathbf{r}, \tag{4.6}$$

As it can be seen, this analysis is based solely on the charge density, and therefore it is rather insensitive to the basis set used in the electron wavefunction calculation. This makes it easily applicable to plane wave based calculations. However, it comes natural that, since the method is based on the gradient of the density, assigning one particular point of space to one region or the other becomes increasingly difficult when the changes in the electronic density are smooth, such as in metallic systems.

Early algorithms, which have been implemented with relatively small molecules in mind, used to calculate the gradient of the charge density by finding the critical points of the charge density where $\nabla\rho(\mathbf{r}) = 0$, followed by the construction of the zero-flux surfaces which intersect these points, and the integration of the electronic density within each region [296]. For large systems, this type of algorithm is highly impractical, since it requires a high density of trajectories to accurately represent the surface away from the critical points.

For larger systems, more efficient algorithmic approaches, such as that developed by Henkelman et al. [297], are more suitable. In particular, Henkelman's algorithm does not involve an explicit representation of the zero-flux surfaces, and does not aim at locating the stationary points. Indeed, it takes advantage of the fact that $\rho(\mathbf{r})$ is usually represented in terms of a 3D orthogonal grid defined over a volume of space V enclosing the system. Using this grid, the regions Ω are identified using only the steepest ascent trajectories confined to the grid points. This makes that the algorithm scales linearly with the number of grid points used to represent the electronic density, which is particularly important in the case of very large systems. The most recent version of the algorithm [298] makes use of a corrector step, which eliminates the tendency to align the zero-flux surfaces along the grid directions [299]. The algorithm follows these main steps:

1. An initial grid point $\mathbf{r}(r_1, r_2, r_3)$ is chosen. A path of the steepest ascent is followed between neighbouring grid points along the charge density gradient, determined by considering:

$$\frac{\Delta\rho(\mathbf{r})}{|\Delta\mathbf{r}|} = \frac{\rho(r_1 + dr_1, r_2 + dr_2, r_3 + dr_3) - \rho(r_1, r_2, r_3)}{\mathbf{r}(r_1 + dr_1, r_2 + dr_2, r_3 + dr_3) - \mathbf{r}(r_1, r_2, r_3)}, \tag{4.7}$$

   where the vector of integers (dr_1, dr_2, dr_3) describing the step along the grid to the neighbour can take the values $\{1, 0, -1\}$. The hop is then done to the neighbouring grid point that maximizes Eq. 4.7.

2. At the grid point $\mathbf{r}(r_1, r_2, r_3)$, $\nabla\rho(\mathbf{r})$ is calculated from the charge density of the neighbouring points using a central finite difference scheme:

$$\nabla\rho_x(\mathbf{r}) = \frac{\rho(r_1+1,r_2,r_3)-\rho(r_1-1,r_2,r_3)}{|\mathbf{r}(r_1+1,r_2,r_3)-\mathbf{r}(r_1+1,r_2,r_3)}|, \tag{4.8}$$

$$\nabla\rho_y(\mathbf{r}) = \frac{\rho(r_1,r_2+1,r_3)-\rho(r_1,r_2-1,r_3)}{|\mathbf{r}(r_1,r_2+1,r_3)-\mathbf{r}(r_1,r_2-1,r_3)}|, \tag{4.9}$$

$$\nabla\rho_z(\mathbf{r}) = \frac{\rho(r_1,r_2,r_3+1)-\rho(r_1,r_2,r_3-1)}{|\mathbf{r}(r_1,r_2,r_3+1)-\mathbf{r}(r_1,r_2,r_3-1)}|. \tag{4.10}$$

3. The step along the gradient vector $\mathbf{r}_{grad}$ is calculated as:

$$\begin{aligned}\mathbf{r}_{grad} &= C(\nabla\rho_x(\mathbf{r}),\nabla\rho_y(\mathbf{r}),\nabla\rho_z(\mathbf{r})) \\ &= min\left(\frac{dx}{\nabla\rho_x(\mathbf{r})},\frac{dy}{\nabla\rho_y(\mathbf{r})},\frac{dz}{\nabla\rho_z(\mathbf{r})}\right)(\nabla\rho_x(\mathbf{r}),\nabla\rho_y(\mathbf{r}),\nabla\rho_z(\mathbf{r})),\end{aligned} \tag{4.11}$$

   where dx, dy and dz are the grid spacing along the three cartesian directions.

4. The deviation from the trajectory of the gradient is accounted for by calculating a correction vector as $\mathbf{r}_{grad} - \mathbf{r}_{grid}$, where $\mathbf{r}_{grid}$ is the step between neighbouring grid points.

5. For each new point along the ascent trajectory, the vectors $\mathbf{r}_{grad}$ and $\mathbf{r}_{grid}$ are calculated, and the correction vector is accumulated. When the length of any component of $\Delta\mathbf{r}$ is larger than half of the grid spacing, a correction step is taken in that direction. The correction vector is then recalculated by subtracting the correction step.

6. The ascent trajectory is ended if a charge density maximum is reached or, at some point, there is no non-assigned neighbours.

The procedure is repeated for all the grid points. Depending upon the order in which the grid points are analyzed, the grid point adjacent to the zero-flux surface can be assigned to one of the two volumes on either side of the dividing surface. This ambiguity is due to the fact that the trajectory between grid points deviates from the true trajectory by up to half a grid step. Thus, when all the points are assigned, a final refinement of the grid points is required to identify all grid points on the boundary of a volume.

It should be noted that, accordingly with the original theory of atoms in molecules [294], the algorithm presented works on the total electronic density. However, the PAW/plane-waves calculations presented in this work provide only the self-consistently optimized valence electronic density, *i.e.*, the electronic density of those electrons which are explicitly considered in the self-consistent field calculation. Thus, applying the algorithm presented in Ref. [297, 299, 298] to valence electrons only may result, in some cases, in an incorrect assignment of the charges. The reliability of the Bader charges calculated considering only the valence electronic density can be checked by adding the electronic density of the frozen-core electrons to the valence electronic

density. In the present case, this procedure did not lead to any variation in the calculated electronic charges.

5 Simulation of scanning probe techniques

Most of the results presented in this work have been conducted in parallel with experiments, based on scanning probe techniques, such as scanning tunnelling microscopy, described in Sections A.1 and A.2 of Appendix A, and non-contact atomic force microscopy, described in Sections A.4 and A.5 of Appendix A. In order to compare theory and experiments, the latter have been simulated by means of density functional theory calculations. This Chapter describes the basics of the methodologies employed in these simulations. Section 5.1 describes the Tersoff-Hamann approximation, which is useful to reproduce scanning tunnelling microscopy experiments, while section 5.2 presents the quasi-static approximation, in an attempt to describe the relevant physics involved in a non-contact atomic force microscopy experiment.

5.1 Modelling STM with DFT: Tersoff-Hamann approximation

The mechanism behind *scanning tunnelling microscopy* [148, 149, 300] (STM) (see Appendix A.1) involves the quantum tunnelling of electrons between a conductive tip and a conductive sample placed in close proximity, usually between 5 Å and 10 Å, and subjected to a potential difference created by applying a bias voltage between them. The approximation developed by Tersoff and Hamann [301, 302] provides a conceptually simple framework to interpret this process in terms of the sample density, which can be calculated straightforwardly with DFT.

The approximation rests on the Bardeen's description of the tunnelling process [303], which treats the tip and the sample as two separate entities. Therefore, the tunnelling current between the unperturbed states of the tip and those of the sample is calculated by considering the proximity of the tip to the sample as a perturbation, and applying time-dependent perturbation theory. The tunnelling current, to the first order, is then given by:

$$I = \frac{2\pi q_e}{\hbar} \sum_{\nu,\mu} f\left(E_\mu\right) \left[1 - f(E_\nu + q_e V_{bias})\right] |M_{\nu,\mu}|^2 \delta(E_\mu - E_\nu), \tag{5.1}$$

where $f(E)$ is the Fermi function, q_e is the electronic charge, V_{bias} is the bias voltage, and $M_{\nu,\mu}$ is the transition matrix element - *i.e.*, the amplitude of the electron transfer - between the

electronic state ψ_μ of the tip, with energy E_μ, and the state ψ_ν of the sample, with energy E_ν:

$$M_{\nu,\mu} = \frac{\hbar^2}{2m_e} \int_S \left(\psi_\mu^* \nabla\psi_\nu - \psi_\nu \nabla\psi_\mu^*\right) d\mathbf{S}, \tag{5.2}$$

where the integration is performed over any surface S lying entirely between the tip and the sample. For $T \to 0\ K$ and $V_{bias} \to 0\ V$, Eq. 5.1 can be approximated by

$$I \approx \frac{2\pi q_e V_{bias}}{\hbar} \sum_{\nu,\mu} |M_{\nu,\mu}|^2 \delta\left(E_\nu - E_F\right) \delta\left(E_\mu - E_F\right), \tag{5.3}$$

where E_F is the Fermi level.

The evaluation of Eq. 5.3 is a not trivial task, since the matrix element $M_{\nu,\mu}$ depends on the precise details of the tip-sample interaction, such as the tip-sample distance, and the tip shape. The Tersoff-Hamann approximation greatly simplifies this problem, by modelling the tip as a locally spherical potential well:

$$\psi_\mu(\mathbf{r}) = \Omega_\mu^{-\frac{1}{2}} \mathbf{k} R e^{\mathbf{k}R} \frac{1}{k|\mathbf{r} - \mathbf{r}_0|} e^{-\mathbf{k}|\mathbf{r}-\mathbf{r}_0|}, \tag{5.4}$$

where $k = \sqrt{\frac{2m_e\Phi}{\hbar^2}}$ is the decay length into the vacuum, Φ the work function, r_0 and R are the center and the radius of the tip curvature, and Ω_ν the volume of the tip. A simplified description for the current can then be found if one considers the surface wavefunction a free-electron Bloch wave, which decays exponentially into the vacuum:

$$\psi_\nu(\mathbf{r}) = \Omega_\nu^{-\frac{1}{2}} \sum_{\mathbf{G}} a_{\mathbf{G}} e^{\sqrt{k^2 + |\mathbf{k}_{||} + \mathbf{G}|^2} z} e^{i\left[\mathbf{k}_{||} + \mathbf{G}\right]\mathbf{r}}, \tag{5.5}$$

where $\mathbf{G}$ is a reciprocal lattice vector, $\mathbf{k}_{||}$ is the wave vector of the surface Bloch wave, and Ω_ν is the surface volume. By expanding Eq. 5.4 in the same form as Eq. 5.5, and neglecting the possible angular dependence of ψ_μ, it is possible to simplify the expression for the matrix element $M_{\nu,\mu}$ and rewrite Eq. 5.3 as

$$I = \frac{32\pi^3}{\hbar k^4} q_e^2 V_{bias} \Phi R^2 e^{2kR} \frac{1}{\Omega_\nu} \sum_{\mu,\nu} |\psi(\mathbf{r}_0)|^2\ \delta(E_\mu - E_F)\ \delta(E_\nu - E_F). \tag{5.6}$$

By using the definition of the LDOS of the tip given by the spherical potential well approximation,

$$\rho_\mu(E) = \frac{1}{\Omega_\mu} \sum_{\mu} \delta(E_\mu - E), \tag{5.7}$$

and that of the LDOS of the ν-th state of the sample at $\mathbf{r}_0$ (see Section 4.2),

$$\rho_\nu(E, \mathbf{r}_0) = \sum_\nu |\psi_\nu(\mathbf{r}_0)|^2 \delta(E_\nu - E), \tag{5.8}$$

it can be seen that Eq. 5.6 states that, if the current is maintained constant, the STM tip probes isosurfaces of constant LDOS of the sample at the Fermi level and at the position $\mathbf{r}_0$:

$$I \propto V_{bias}\ \rho_\nu(E_F, \mathbf{r}_0)\ \rho_\mu(E_F). \tag{5.9}$$

These observations can be further generalized to small finite biases [304, 305], by considering that the dependence of the current on the tip-sample distance d, on the energy and on the voltage V_{bias} are represented by a *transmission coefficient* $T(d, E, V_{bias})$:

$$I \propto \int_{E_F}^{E_F + q_e V_{bias}} \rho_\nu(E, \mathbf{r}_0)\ \rho_\mu(E)\ T(d, E, V_{bias})\ dE. \tag{5.10}$$

For small finite biases, $\rho_\mu(E)$ and $T(d, E, V_{bias})$ can be considered to be constant. Therefore, under these assumption the tunnelling current will be proportional to the integral of $\rho_\nu(E, \mathbf{r}_0)$ between E_F and $E_F + q_e V$. This quantity can be easily calculated from DFT, as explained in Section 4.2.

A rough estimation for the appropriate isosurface contour, which can be employed to simulate the experimental topographies from the calculated LDOS, can be obtained by considering that the tip and the sample have the same metallic character, and that the transition matrix element $M_{\nu,\mu}$ between the electronic states of the tip and the sample can be approximated by the term $\Delta S^2 k^2 \rho_\nu(E, \mathbf{r}_0)$, where ΔS is the area of the wavefunction overlap. Eq. 5.1 then is simplified to [306]:

$$I \approx C \cdot \Delta S^2 k^2 \rho_\nu(E, \mathbf{r}_0), \tag{5.11}$$

where C is a constant that includes all the constants obtained from the simplification of Eq. 5.1. Both terms can be estimated by comparing STM simulations performed with both the Tersoff-Hamann and Bardeen approximations [135]. By doing this, it is possible to obtain the following estimation for the appropriate value for the density contour:

$$\rho(E, \mathbf{r}_0) \approx 2 \times 10^{-4} \sqrt{I}, \tag{5.12}$$

where the units of I and $\rho(E, \mathbf{r}_0)$ are nA and Å^3, respectively.

Starting from the Tersoff-Hamann theory, it is possible to build a general theory which is valid also for spin-polarized currents [307]. This can be done by redefining the wavefunctions entering in the matrix elements of Eq. 5.6 in terms of spinors, in analogy to what is done in spin-polarized DFT - see Section 3.4.3. In this case, Eq. 5.8 is not valid anymore, since the term

$\sum_\nu |\psi_\nu(\mathbf{r}_0)|^2$ now refers to both the electronic and the spin density (see Section 3.4.3). As a consequence, the expression for the current becomes:

$$I \propto \left[\rho_\mu(E,\mathbf{r}_0)\ \tilde{\rho}_\nu(V,\mathbf{r}_0) + \mathbf{s}_\mu(E,\mathbf{r}_0)\ \tilde{\mathbf{s}}_\nu(V,\mathbf{r}_0)\right], \tag{5.13}$$

where $\tilde{\rho}_\nu(V,\mathbf{r}_0)$ and $\tilde{\mathbf{s}}_\nu(V,\mathbf{r}_0)$ are the energy integrals of the local electronic density $\rho_\nu(E,\mathbf{r}_0)$ and of the local spin density $\tilde{\mathbf{s}}_\nu(E,\mathbf{r}_0)$. Because of this complex dependence, modelling *spin-polarized scanning tunnelling microscopy* (SP-STM) is considerably more complex than modelling non-spin polarized STM, because, apart from "trivial" ferromagnetic and antiferromagnetic states, it generally requires the system to be simulated using a non-collinear spin-polarized DFT formalism [308, 309].

5.2 Modelling NC-AFM using DFT: quasi-static approximation

In *non-contact atomic force microscopy* [310, 311] (NC-AFM) (see Appendix A.4), an oscillating tip vibrates at constant amplitude in the vicinity of the surface of the sample, and the change in the frequency of this vibration - the *frequency shift* ($\Delta f(z)$) -, due to the tip-surface interaction forces, is the observable used as the imaging signal.
Nowadays, DFT calculations can only provide a partial description of the dynamic problem involved in a NC-AFM experiment [306], which is reflected by the fact that it is not possible to calculate the experimental observable $\Delta f(z)$. There are two main reasons for these limitations:

- In order to simulate the interaction between the tip and the sample with a minimum degree of realism, the atomistic structure of the tip must be included explicitly in the calculation. Therefore, approximations based on idealized tips such as the Tersoff-Hamann described in Section 5.1 cannot be considered. Since the forces involved acts over large distances - *e.g.* vdW interactions - large portions of the macroscopic tip are expected to contribute to the overall tip-sample interaction. This calls for the use of very large models to describe realistically the relevant tip sample interactions. Unfortunately, models having the appropriate sizes [312] are too large to be calculated with DFT, due to the present computational capabilities.

- In order to calculate $\Delta f(z)$, one should be able to simulate the full dynamic problem of the NC-AFM experiment. However, even with reduced tip models formed by just few atoms, this would require DFT-based molecular dynamics runs over time scales which go beyond those that can be faced with the present supercomputers. In fact, to describe the dynamics of the NC-AFM tip, one should consider the 1D equation of motion for an oscillator driven by an external force F_{ext} in a force field $F(z)$ [310, 306]:

$$\ddot{z} + \frac{f_0^2}{k}\alpha\ \dot{z} + f_0^2\ z - \frac{f_0^2}{k}\alpha\ F = \frac{f_0^2}{k}\alpha\ F_{ext} \tag{5.14}$$

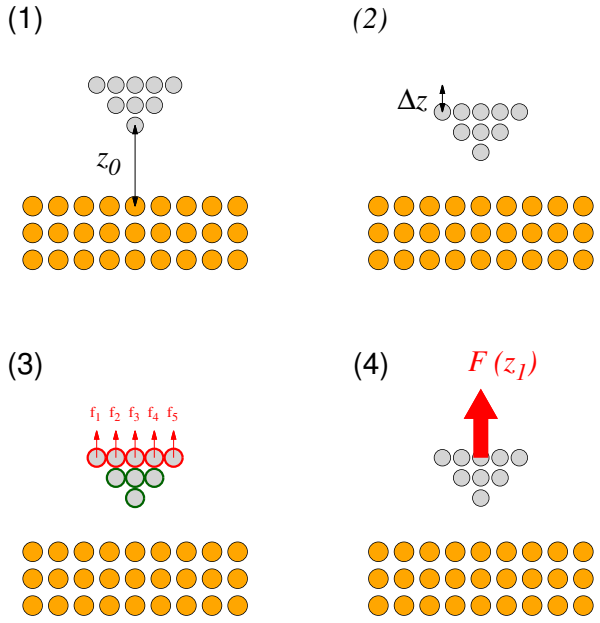

Figure 5.1: Main steps involved in the calculation of an $F(z)$ curve using the quasi-static method: (1) the nanotip (light grey points) is positioned an height z_0 over the surface (orange points); (2) the nanotip is displaced by a quantity Δz; (3) the structure of the nanotip is optimized, keeping fixed the topmost atoms (red circles) and allowing the rest of the atoms to relax (green circles); (4) the force F_α acting on the tip at position z_1 is calculated summing up the vertical components of the individual atomic forces on the fixed atoms of the nanotip ($f_1, \ldots, f_5$ in panel 3)

where f_0 is the oscillation frequency of the oscillating tip in the absence of any interaction with the surface - $\sim 10^5$ Hz -, k is the spring constant of the cantilever, α is the damping coefficient due to the interaction between the tip and surface, and h is the equilibrium height of the cantilever above the surface in the absence of interaction. The time scales involved in this dynamic problem ($\sim 10ms$) are therefore dictated by the tip oscillation frequency f_0. While similar time scales can be approached using classical molecular dynamics [313, 314, 315], they remain computationally too expensive if one wants to employ DFT.

Therefore, to model NC-AFM with DFT, one has to rely on approximate models, which try to account for all the relevant physics involved in the experiment. The tip is usually described by small clusters, formed by tents of atoms, which mimic the very last atoms of the apex of the macroscopic tip - in this sense, such clusters are also referred to as *nanotips*. The structure and the composition of these reduced models are critical to determine their interaction with the

surface. For this reason, several studies in the literature have focussed on understanding which are the tip geometries and chemical composition which can reproduce at best the experimental results obtained for a particular experiment [316, 317]. In the case of Si-based tips, which have been used in the experiments discussed in this work, it has been found that the reactivity of the tip is mainly determined by the presence of dangling bonds at the end of the tip apex [318]. Different models have been discussed in the literature which present this characteristic: small clusters formed by ∼10 atoms, derived from the Si(111) 7×7 reconstruction, have been found to be generally too reactive, while larger models, formed by ∼50 atoms, and based on the dimer reconstruction of Si(100), have been found to be more inert, providing a better comparison with the experiments [317, 319]. In those rare cases - *e.g.* silicon interacting with silicon - in which the Hamaker constant between the materials of the tip and the sample is known, the background due to the vdW interactions between the macroscopic tip and the sample can be included analytically [320, 321]. More recently, the effect of vdW interactions between the nanotips and inert carbon structures, such as graphite and carbon nanotubes, has been studied by means of dispersion corrected approaches to DFT [322] - see Section 3.6. In this case, the inclusion of dispersion interactions has been found to be fundamental to describe the qualitative features of NC-AFM experiments [323], as vdW forces have been found to be the main responsible for the tip-sample interaction. Electrostatic forces are usually neglected in plane-wave based periodic DFT calculations, which treat the three-dimensional simulation cell as neutral. In this respect, recent approaches which try to include electrostatic effects are based on the combination of DFT calculations with continuum mechanics analytic models [324].

In order to bypass the description of the complex dynamic problem describing the motion of the NC-AFM tip, a quasi-static approach is usually employed in DFT calculations to describe the nanotip-sample interaction. These calculations do not allow to simulate directly the $f(z)$ curves, but permit to obtain a theoretical $F(z)$ curve which can be compared with those obtained by numerical inversion of the experimental $f(z)$ curves - see Appendix A.5 for a brief description of how the experimental curves are obtained. The main steps involved in this approach are the following (see Fig. 5.1):

1. The nanotip is suspended at height z_0 from the surface at a given postion (x, y). The value of the height is chosen to be sufficient to render the interaction between the tip and the surface negligible - usually, z_0 takes values between 7 and 10 Å.

2. The nanotip is rigidly displaced towards the surface of a certain quantity Δz, so that the tips-surface heigh is changed to z_1

3. The geometry of the nanotip at position z_1 is optimized, by constraining the positions of a certain number of atoms, usually those belonging to the uppermost layer, while the rest of the atoms is allowed to relax freely. In this way, it is possible to account for the macroscopic tip deformation due to the interaction with the surface, at least qualitatively. Note that, because of this relaxation, z_1 is not necessary equal to $z_0 - \Delta z$

4. The force $F(z_1)$ acting on the nanotip at position z_1 is then calculated by summing up the vertical component of the individual forces acting on those tip atoms which positions have been constrained during the optimization, *i.e.*,

$$F(z_1) = \sum_{\alpha} \mathrm{f}_{\alpha}(z_1), \tag{5.15}$$

where f_{α} is the force acting on the tip atom α which have been kept fixed.

Steps 2-4 are usually iterated using a regular step Δz, with $0.25\text{Å} \leq \Delta z \leq 0.5\text{Å}$. The calculation normally stops when $F(z) > 0$, because this region lies outside the range of $F(z)$ which can be probed experimentally. Notice that, similarly to what happens in the experiment, the meaning of the force in the $F(z)$ curve must be attributed to the whole tip-sample system, and not only to the interaction between the tip and the sample.

Part III

Results

6 Geometry of graphene on Ru(0001): the role of dispersion interactions

The important role played by dispersion interactions in determining the actual morphology of a graphene monolayer grown on Ru(0001) is analysed, and the consequences of including vdW interactions are discussed with respect to the analysis of the experimental STM images.

The results presented have been published in:

- "Role of dispersion forces in the structure of graphene monolayers over Ru surfaces"
  D. Stradi *et al.*, *Physical Review Letters*, **106**, 186102 (2011)
- "Lattice-matched versus lattice-mismatched models to describe epitaxial monolayer graphene on Ru(0001)"
  D. Stradi *et al.*, *Submitted* (2013)

As it has been already mentioned in Section 1.3, a monolayer of graphene, grown epitaxially on lattice mismatched metallic substrates, tends to form superstructures with large periodicities [70], which can be understood in terms of moiré patterns [101]. In graphene grown on the Ru(0001) surface [74], hereafter denoted simply by *gr.*/Ru, the presence of such moiré has been recognized since the early STM studies [137, 139]. An atomically resolved STM image of *gr.*/Ru is presented in Fig. 6.1. The periodic superstructure, which has a C_{3v} symmetry, appears as a regular array of dark and bright areas. In particular, it is possible to distinguish between three different regions: two of them are darker (green dots), while the third one is brighter (cyan dot). Therefore, in STM images, they appear as depressions and protrusions, respectively. For this reason, in the following, we will refer to them as *Low* (L) and *High* (H) regions. Surface X-ray diffraction (SXRD) has shown that the periodic cell of this superstructure is formed by 25×25 unit cells of graphene, matched to 23×23 unit cells of Ru(0001) [138]. In Fig. 6.1, this large moiré unit cell is the one marked in black. In turn, this unit cell can be decomposed in four subunits, each one similar to the one marked in red in Fig. 6.1. The latter has a lateral periodicity of $\sim$30 Å and comprise one H and two L regions.

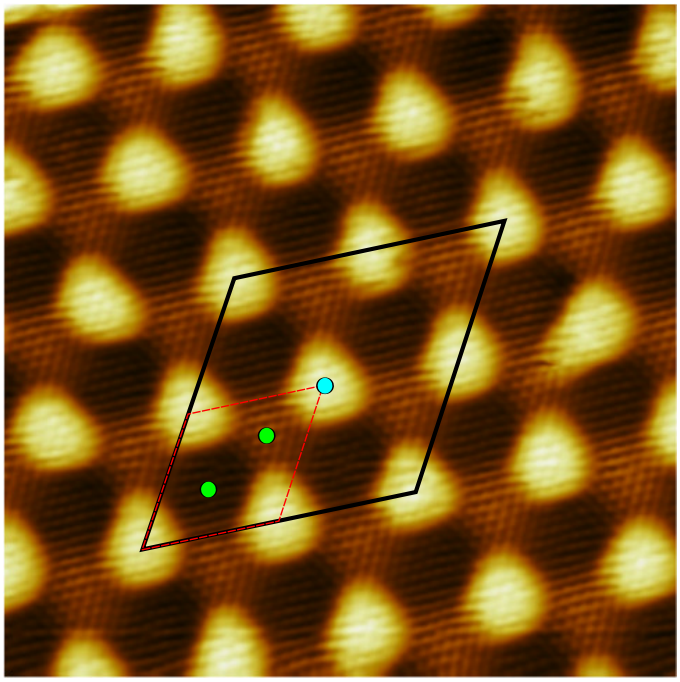

Figure 6.1: Atomically resolved STM image of graphene on Ru(0001) ($100 \times 100 nm^2$, V_{bias}=-1V, I=200pA). Green and cyan dots mark the L and H regions, respectively. The actual 25×25/23×23 periodic unti cell, as determined by SXRD[138], is represented in black (solid lines). One of the four subunits, in which the actual supercell can be divided, is represented in red (dashed lines).

The STM image (Fig. 6.1) shows that the moiré can be described as an alternating series of hill (H regions) and valleys (L regions). However, STM maps the electronic density of the surface, and not its geometry[1]. Therefore, by looking at Fig. 6.1, it is not possible to determine unambiguously whether this periodically corrugated pattern has a geometric or an electronic origin - as it will become evident later, it has both. Several complementary techniques have been used to try to determine the actual geometry of the superstructure. However, in spite of the efforts to determine its structural corrugation, *i.e.*, the difference in height between the H and L regions, this value was still uncertain, at the time when this thesis started: low energy electron diffraction (LEED) experiments have provided a value of 1.5 Å [100], while SXRD measurements has suggested two possible values, 0.82 Å and 1.5 Å [138, 137]. In scanning tunnelling microscopy (STM) measurements, the apparent corrugation of the moiré was found to decrease from 1.1 Å to 0.5 Å when the tunnelling bias voltage was changed from -0.8 V to 0.8 V [139], whereas helium atom scattering (HAS) experiments, that are sensitive to the surface total charge corrugation, gave values between 0.15 Å - 0.4 Å [144].

[1] See Appendix A.1

To clarify these contradictory experimental results, DFT/GGA calculations[1] have been carried out using a unit cell large enough to account for the formation of the moiré pattern [325, 140, 100, 89, 326]. These models have been limited to only one of the four subunits of the actual unit cell, because a model of the $25 \times 25/23 \times 23$ unit cell, would be too large for a DFT/GGA calculation, even on a massively parallel supercomputer. However, using a unit cell which is exactly one fourth of the $25 \times 25/23 \times 23$ is not possible, as it would lead to model with a fractionary number of unit cells. Therefore, approximated models formed by an integer number of periodic unit cells have been used. In these models, one tries to maintain the lattice constant of graphene as much as possible at its equilibrium value ($a_{graphene} = 2.46$ Å), so that, by considering large enough unit cells, the lattice mismatch between the graphene layer and the metal ($a_{Ru(0001)} = 2.7$ Å) permits a realistic description of the consequently formed moiré pattern. Different models have been used, which have the common characteristic of being formed by an array of $(n) \times (n)$ graphene unit cells, which is adsorbed on an array $(n-1) \times (n-1)$ Ru(0001) unit cells. The values of n that have been considered are $n = 11, 12, 13$, which correspond to models in which the graphene layer is artificially stretched, with respect its equilibrium lattice constant, $0.3\%, 1.1\%$, and 1.8%, respectively [326]. Using such models, the details of the chemical interaction between graphene and Ru(0001) have been clarified [89, 325]. In particular, it has been shown that the interaction between the π-cloud of graphene and the d-band of the underlying Ru(0001) surface depends critically on their relative configuration. When one of the two carbon atoms of a single graphene unit cell sits over a *Top* site of Ru(0001), the graphene and the metal form strong covalent bonds [89]. This situation can be found twice in any (n)×(n)/(n-1)×(n-1) *gr.*/Ru unit cell, because the second atom of the graphene unit cell can sit either over a *Hcp* site of Ru(0001), or over an *Fcc* site. Conversely, when both carbon atoms sit over the two hollow sites of Ru(0001), *i.e.*, *Hcp* and *Fcc*, the interaction is much weaker. Both X-ray diffraction and DFT calculations have shown that the strongly bound regions experience a significant in-plane expansion of the graphene honeycomb [100]. Due to this effect, the weakly bound regions are subjected to a compressive strain, which is released by outward relaxation. The outcome of this complex scenario is a geometrically corrugated superstructure, in which there is a continuous change between covalently bound regions, where the graphene lies closer to Ru(0001) - $d_{gr./Ru} \approx 2.2$Å -, and weakly bound regions, where the distance between graphene and Ru(0001) is larger. By comparing the experimental STM topographic images, and the corresponding simulations [89] performed on one of these large models, the former regions have been identified with the L regions, while the latter have been identified with the H regions. Nevertheless, depending on the actual size of the unit cell, different values of corrugation have been reported for the different models: 1.62 Å [325] and 1.75 Å [140] for $n = 11$, 1.50 Å [140], 1.67 Å [325], 1.51 Å [326] and 1.50 Å [100] for $n = 12$, 1.44 Å [140] and 1.59 Å [100] for $n = 13$. Most of these value are higher than the experimental ones, in spite of the large dispersion of the latter. Therefore, while these calculations have succeeded in elucidating the chemical origin

[1] All these calculations have used the PBE functional.

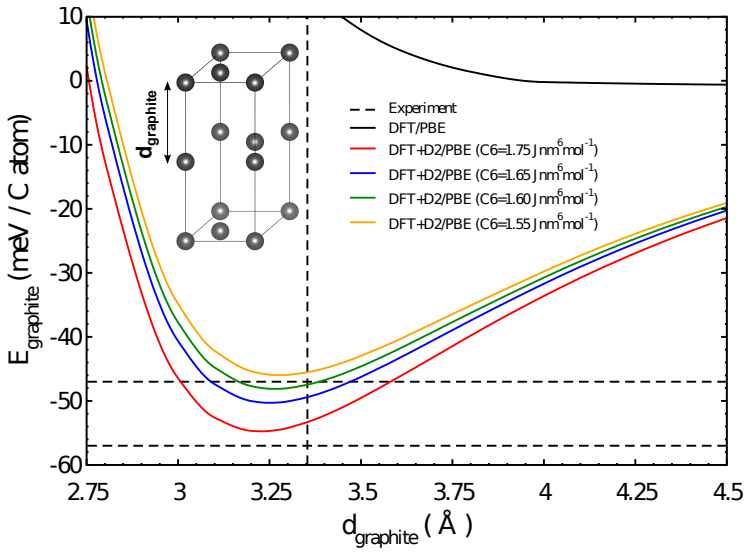

Figure 6.2: Exfoliation energy of graphite ($E_{graphite}$), as a function of the interlayer distance $d_{graphite}$ (see inset) calculated using DFT/PBE and DFT+D2/PBE, with different values of the carbon C_6 coefficient - see the text for the details of the calculations. The inset shows the graphite unit cell (black lines) used for the calculations, with carbon atoms printed in gray. The dashed lines indicate the experimental values of $d_{graphite}$ and of $E_{graphite}$ (in the latter case, two lines have been used to indicate the actual value plus the experimental error bars.)

of the corrugated superstructure, and have shown that *gr.*/Ru is geometrically corrugated, they have not provided a clear answer to which is the actual corrugation of the graphene moiré.

The first step towards the accurate description of the *gr.*/Ru corrugation, is to verify if all the possible physical effects that may contribute to determine the actual geometry of the graphene superstructure have been considered. In particular, in all the calculations mentioned in the previous paragraph, vdW interactions have not been taken into account. As it has been explained in Section 3.6, DFT/GGA calculations tends to underestimate severely the effect of vdW forces. At the DFT level of theory, this deficiency can be corrected by using efficient schemes based on semi-empirical potentials [147, 266].

A first hint that dispersion interactions may play an important role in *gr.*/Ru comes from the fact that taking into account vdW interactions is fundamental to reproduce correctly the properties of many graphene-based materials. The most straightforward example is that of graphite [327]. Figure 6.2 shows the calculated exfoliation energy of graphite, $E_{graphite}(th.)$, as a function of the interlayer spacing, $d_{graphite}(th.)$[1]. It can be seen that the PBE functional predicts graphite to be practically unbound, *i.e.*, DFT/PBE calculations do not result in any

[1]For these calculations, the lattice constant of the carbon layers has been fixed to its experimental value of 2.462 Å [259]. The `VASP` program have been used [222], together with the PAW method [251]. The Brillouin Zone has been sampled using a $16 \times 16 \times 8$ k-points and the tetrahedron method has been used (see Section 2.8). Single-point energies have been calculated for different values of $d_{graphite}$, ranging from 1.5 Å to 10.0 Å.

physically meaningful minimum. On the other hand, DFT+D2/PBE calculations, using the default C_6 coefficient for carbon, $C_6 = 1.75$ Jnm^{6}mol^{-1}, correct this unphysical behaviour, and provide a well defined well with $d_{graphite}(th.) = 3.25$ Å and $E_{graphite}(th.) = -54.68$ meV/C atom, in reasonable agreement with the experimentally determined values, $E_{graphite}(exp.) = -52 \pm 5$ meV/C atom and $d_{graphite} = 3.35$ Å [328, 329]. As mentioned in Section 3.6, the C_6 parameters of the DFT+D2 method have been derived for the isolated atomic species. However, the polarizability of an atom in a molecule changes significantly with respect to the isolated atom, and consequently also the C_6 coefficient [254]. To take this fact into account, we have studied the dependence of $E_{graphite}(th.)$ and $d_{graphite}(th.)$ on the C_6 value. A slightly better agreement is obtained when $C_6 = 1.65$ Jnm^{6}mol^{-1}, $E_{graphite}(th.) = -50.29$ meV/C atom and $d_{graphite} = 3.25$ Å, whereas using smaller values of C_6 results in values of $E_{graphite}$ which are too small, and lie outside the experimental error bars, or at their edge.

In many respects, graphene can be considered as a single layer of graphite, *i.e.*, an aromatic system with an extended π electronic cloud above and below its molecular plane. If this aromatic layer is adsorbed on another polarizable surface, *e.g.*, a metal, and the interaction between the two is weak, *i.e.*, if there are neither covalent nor ionic bonds, vdW interactions will determine the ground state geometry of the system. However, in *gr.*/Ru, the situation is more complex, because the compressive strain field created in the H regions by the in-plane expansion of the surrounding L regions tends to increase the corrugation of the monolayer. Therefore, the final geometry will be determined by the subtle interplay between these two competing effects.

To address this problem, an accurate analysis has been carried out in two parts, which differ mainly on the models used to describe the surface. In Section 6.1, a systematic investigation on the characteristics of the interaction between graphene and Ru(0001) has been performed, using a series of idealized models of the *gr.*/Ru interface. In these models, a planar graphene layer has been stretched to adapt pseudomorphycally to a single Ru(0001) unit cell. In the following, such models will be referred to as 1×1 models, or *lattice-matched* models. Due to their idealized nature, they are expected to provide only qualitative results, but, as it will become evident, they can be extremely useful to obtain a detailed insight into the dependence of the graphene-Ru(0001) interaction on the precise configuration of the graphene atoms over the metal surface. In Section 6.2, the information obtained by using these 1×1 models have been used to characterize the role of dispersion interactions in a much larger model, which is able to account realistically for the formation of the moiré. Subsequently, the latter model has been used to simulate the STM topographies, and to compare our theoretical results with the available STM images, in order to quantify the influence of vdW interaction in the apparent height of the STM images measured experimentally.

6.1 1×1 lattice matched models

This section shows how *lattice-matched* models can be used to explore the characteristics of the graphene-Ru(0001) bonding in the individual regions of the *gr.*/Ru moiré.

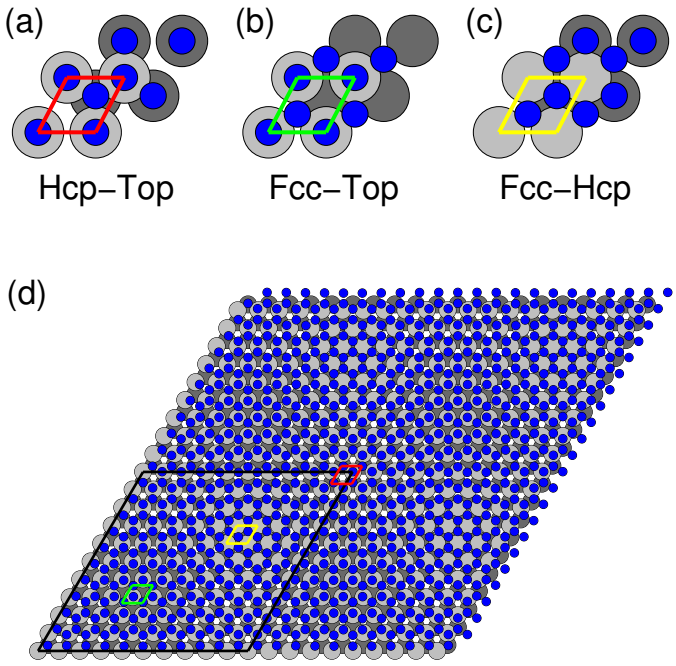

Figure 6.3: Top view of (a-c) the idealized *gr.*/Ru models used in Section 6.1, and (d) of the large 11×11/10×10 lattice-mismatched model used in Section 6.2. For each model, a total of four (2×2) unit cells are shown. Carbon, Ru(0001) topmost layer and Ru(0001) topmost-1 layer atoms are printed in blue, light grey and dark grey, respectively.

Computational details

All the DFT calculations presented have been performed using the `VASP` code [222]. The electronic exchange-correlation energy has been described using the GGA, and, in applying the GGA, the PBE [205] functional has been used. The effect of vdW interactions has been included in the DFT/PBE calculations by means of the DFT+D2 method [147]. The PAW method has been used to describe the ionic cores, treating explicitly the semi-core p electrons of ruthenium. A 400 eV kinetic energy cutoff for the plane-wave expansion has been used. In order to sample the 1^{st} BZ of the 1×1 *gr.*/Ru models, a Monkorst-Pack grid [175] of 11×11×1 has been used, together with a Methfessel-Paxton smearing [181] of 0.2 eV. Three metal layers have been used to describe the Ru(0001) surface, and the vacuum layer in the z direction has been set to ∼15 Å.

The 1D-PES of the *gr.*/Ru models have been obtained by displacing the planar, stretched, graphene layer towards the Ru(0001) surface at regular steps of 0.1 Å. The points obtained have been interpolated with spline functions, and the position ($d_{gr./Ru(0001)}$) and depth (E_{min}) of

the adsorption well has been extracted from the interpolated data. The three models that have been considered are shown in Fig. 6.3 (a-c). They are representative of the two L regions Fig. 6.3 (a-b) and the H region Fig. 6.3 (c) of the *gr.*/Ru moiré. According to configuration of the graphene atoms over the Ru(0001) in each model, they will be referred to as $1\times1-(Hcp-Top)$, $1\times1-(Fcc-Top)$ and $1\times1-(Fcc-Hcp)$, respectively.

Discussion

Fig. 6.4 shows the 1D-PESs calculated at the DFT/PBE and at the DFT+D2/PBE level of theory, for the three 1×1 models shown in Fig. 6.3. It is evident that the behaviour of each 1D-PES critically depends on the adsorption site. For the $1\times1-(Hcp-Top)$ and $1\times1-(Fcc-Top)$ configurations (Fig. 6.4 (a) and Fig. 6.4 (b)), a well-defined minimum is predicted. Using DFT/PBE, $d_{gr./Ru}$ = 2.16 Å and E_{min} = -0.28 eV/C atom for the $1\times1-(Hcp-Top)$ model, and $d_{gr./Ru}$ = 2.17 Å and E_{min} = -0.32 eV/C atom for the $1\times1-(Fcc-Top)$) model. In both cases, the graphene-Ru(0001) distance is very similar to the sum of the covalent radii of C and Ru (∼2.18 Å), and the adsorption energies are also indicative of a rather strong convalent interaction. This qualitative picture does not change using DFT+D2/PBE, which gives $d_{gr./Ru}$ = 2.14 Å and E_{min} = -0.46 eV/C atom for the $1\times1-(Hcp-Top)$, and $d_{gr./Ru}$ = 2.15 Å and E_{min} = -0.49 eV/C atom for the $1\times1-(Fcc-Top)$) model. On the other hand, the situation is radically different for the $1\times1-(Fcc-Hcp)$ model, where the DFT/PBE PES is always repulsive in the entire range of $d_{gr./Ru}$ considered. In this case, the inclusion of vdW interactions using DFT+D2/PBE modifies qualitatively the PES, leading to the appearance of a shallow minimum having $d_{gr./Ru}$ = 2.80 Å and E_{min} = 0.1 eV/C atom. Therefore, in the $1\times1-(Fcc-Hcp)$ model, the attractive behaviour of the PES is due exclusively to vdW forces.

As already stressed in Section 3.6, the DFT+D2 method has been developed and benchmarked exclusively for gas-phase neutral species. While this has been proven to be a valid approach for many studies of aromatic species on metallic surfaces [278, 280, 274, 279, 263], results obtained with DFT+D2 on metals must be carefully checked to ensure their validity. In particular, DFT+D2 has been shown to provide reliable geometries [278, 280]. However, the calculated adsorption energies are considerably overestimated, due to the neglect of electronic screening in the metallic surface [282]. To check for the validity of the present qualitative observations, the method proposed by Tonigold and Groß [280] has been employed, *i.e.*, a rescaling of the C_6 coefficients of the metal to account empirically for the screening of the substrate[1]. The value of the ruthenium C_6 coefficients (C_6^{Ru}) has been varied between 30.51 Jnm^{6}mol^{-1} (value similar to the Ru-Ru C_6 coefficient obtained by the more recent DFT+D3 method [265], C_6^{Ru} = 31.12 Jnm^{6}mol^{-1}) and 15.16 Jnm^{6}mol^{-1}. The latter value has been chosen taking into account that, in Ref. [280], a value of C_6 about half of the original one has resulted in geometries and adsorption energies in good agreement with the experiments. In addition, we have also considered how the variation of the carbon C_6 coefficients affects the PES. In this case, we have varied C_6^C in the

[1] see "DFT+D2 applied to organic molecules on metal surfaces" in Section 3.6 for further details

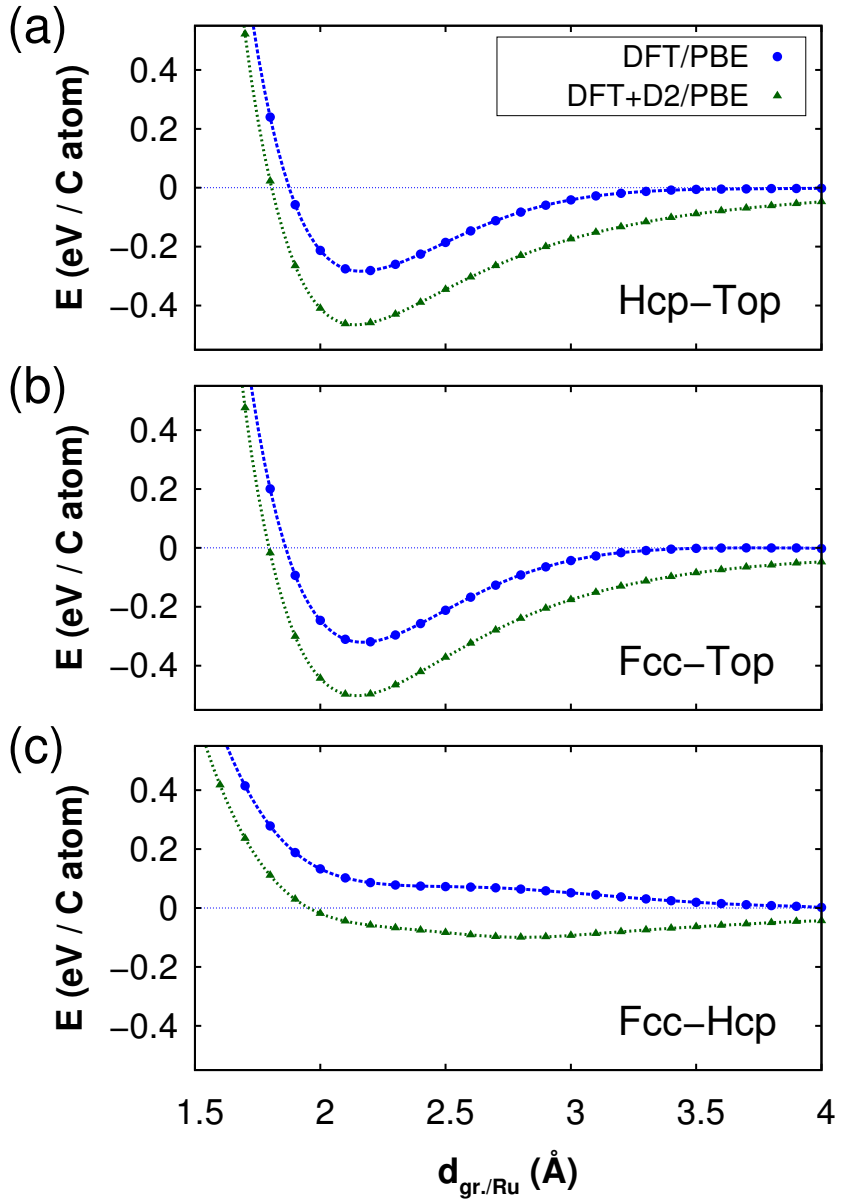

Figure 6.4: PES obtained for the three models shown in Fig. 6.1, as a function of the graphene-Ru(0001) separation $d_{gr./Ru}$. Blue and Green curves correspond to DFT/PBE and DFT+D2/PBE calculations, respectively.

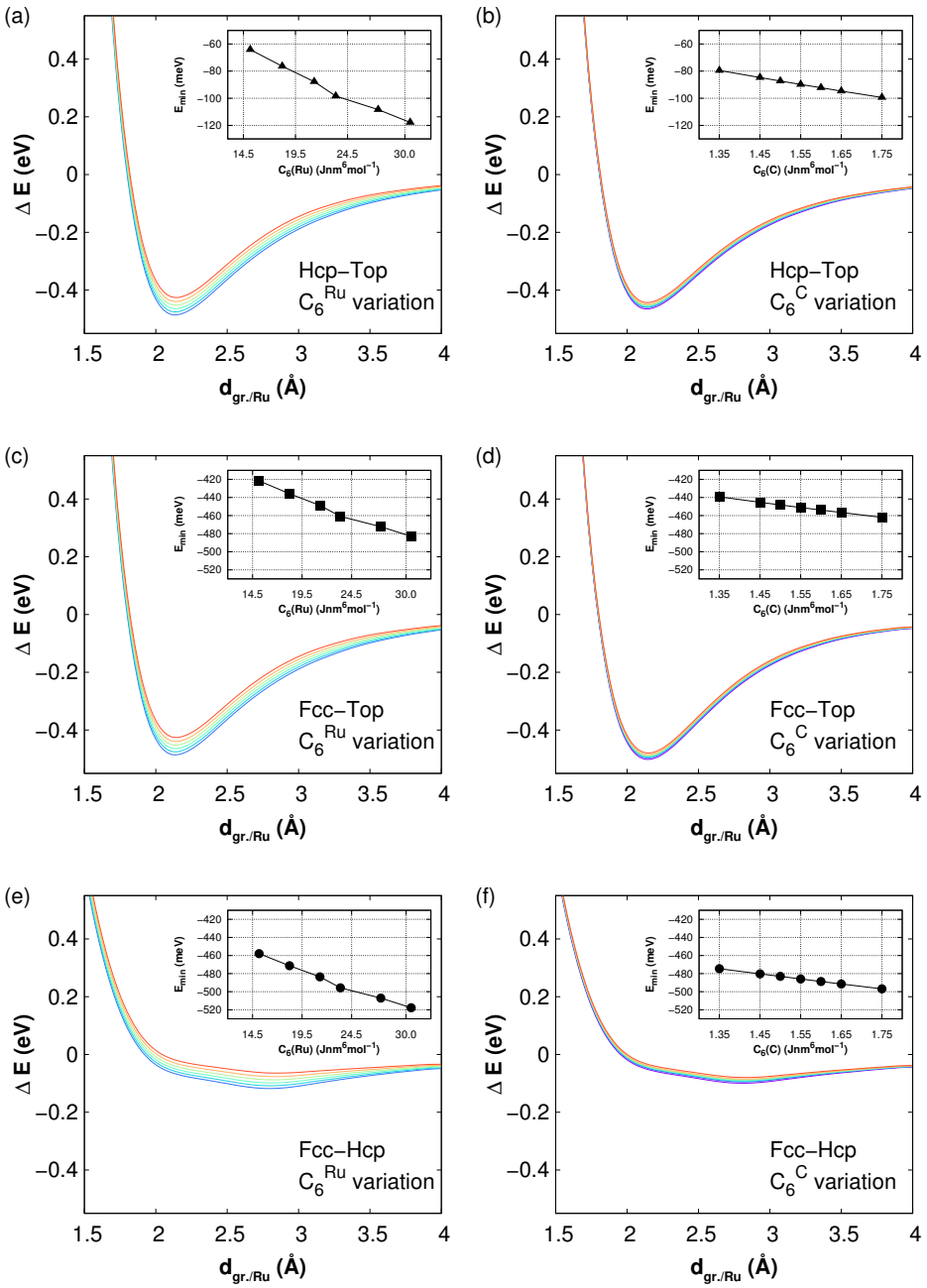

Figure 6.5: PES of the three models shown in Fig. 6.1, calculated at the DFT+D2/PBE level of theory, but varying the C_6 coefficient of ruthenium (a,c,e), and by varying the C_6 coefficient of carbon (b,d,f). Blue (red) refers to PES obtained using larger (smaller) values of the C_6 coefficients. The inset in each panel indicated the value of E_{min}, obtained for each value of C_6, relative to the coefficient varied in that panel.

range from 1.75 Jnm^{6}mol^{-1} to 1.35 Jnm^{6}mol^{-1}. The lowest values of C_6 have been considered only in order to obtain a meaningful trend, because, as shown in Fig. 6.1 a value of $C_6^C = 1.60$ Jnm^{6}mol^{-1} already results in a calculated exfoliation energy which lies at the margin of the experimental error bars. The results of these tests are shown in Fig. 6.5. It can be seen that, independently of the configuration considered, lowering one of the two C_6 coefficients does not change considerably $d_{gr./Ru}$ (changes are within ±0.1Å), but leads to a significant decrease of E_{min}. The decrease, similar for the three configurations, is more pronounced versus C_6^{Ru} (see insets in Fig. 6.5 (a,c,e)), than versus C_6^C (see insets in Fig. 6.5 (b,d,f)). Within the C_6^{Ru} range [14.5 - 31.5] Jnm^{6}mol^{-1}, E_{min} decreases by 61.3 meV, 59.9 meV and 53.7 meV for the $Hcp-Top$, $Fcc-Top$ and $Fcc-Hcp$ configurations, respectively. On the other hand, within the C_6^C range [1.35 - 1.75] Jnm^{6}mol^{-1}, the corresponding variations are 22.7 meV, 22.3 meV, and 19.9 meV for the $Hcp-Top$, $Fcc-Top$ and $Fcc-Hcp$ configurations, respectively.

In summary, the results obtained with the strained 1×1 models demonstrate that the role of the vdW forces depends critically on the configuration. Whereas dispersion forces account for about 30-40 % of the binding between the graphene layer and the metal surface for the configurations corresponding to the L regions of the *gr.*/Ru moiré, where covalent binding plays a major role, in the model representative of the H regions, they are the only ones responsible for the binding. In these weakly bound areas, similarly to what happens in graphite, a description based on DFT/PBE leads to a repulsive interaction, while an attractive interaction can only be recovered by introducing an additional vdW term.

6.2 10×10/11×11 lattice mismatched models

The results presented in Section 6.1 suggest that DFT/PBE calculations of graphene over Ru(0001) lead to an unphysical repulsive interaction, when the configuration of the graphene atoms over Ru(0001) resembles that of the H regions of the *gr.*/Ru moiré. However, in the actual *gr.*/Ru surface, the corrugation is determined by a delicate balance between strain effects and the attractive potential exerted by vdW interactions. The former are completely neglected in the simplified 1×1 models. Therefore, to take both effects into account, we have considered a *lattice-mismatched* model (see Fig. 6.3(d)), in which the different configurations are collectively taken into account within a single unit cell. In the latter model, the two main factors that are responsible for the actual graphene geometry, namely, the strength of the interaction between graphene and Ru(0001) with respect to their relative configuration, and the strain due to lateral modification of the graphene honeycomb, are considered on an equal footing.

Computational methods

For the calculations presented in this section, we have used similar simulation parameters to those employed for the calculations presented in Section 6.1, but we have limited the sampling of the 1^{st} BZ to the Γ-point due to the dimensions of the unit cell. The model that has been considered

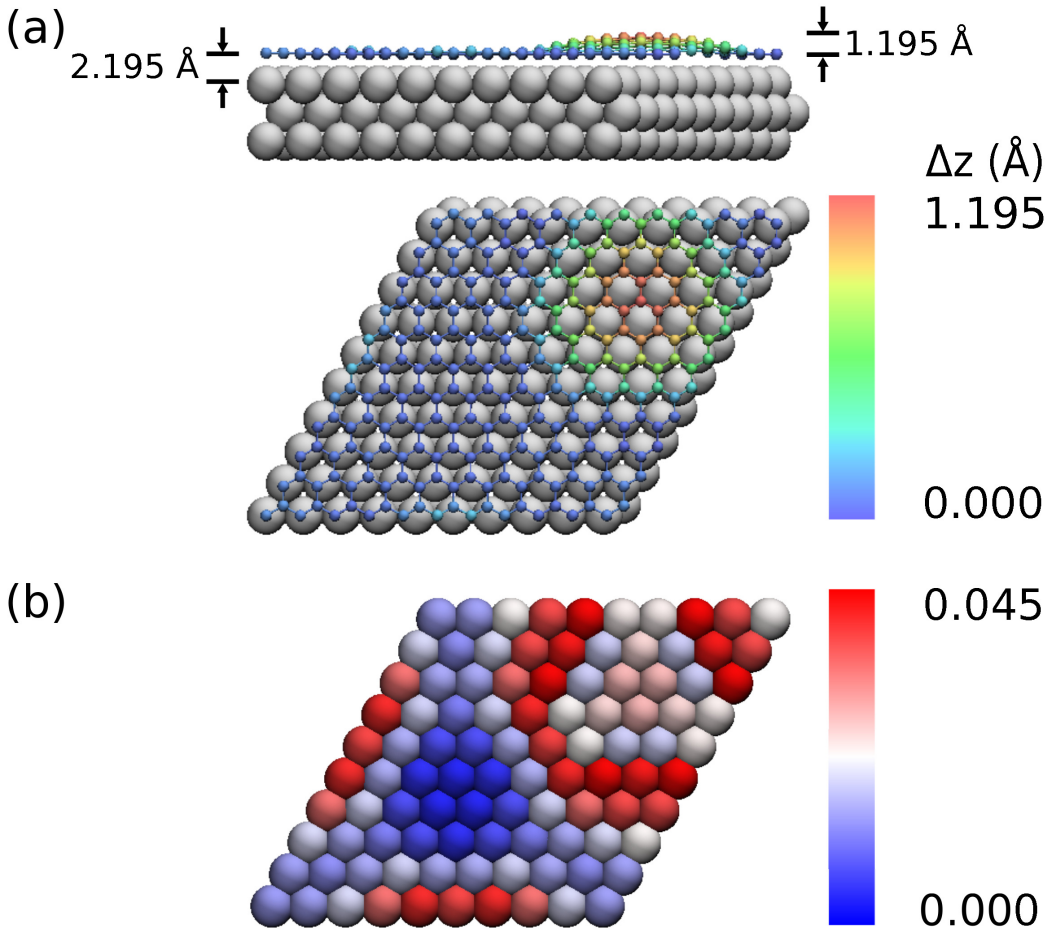

Figure 6.6: Top: calculated ground state geometry of gr./Ru(0001) with 11×11/10×10 periodicity. The carbon atoms of the graphene layer are printed in different colours depending on their relative height (the lowest atom is set to z = 0.000Å), while ruthenium atoms are printed in grey. Bottom, reconstruction of the topmost Ru(0001) layer in the DFT+D2/PBE geometry (the lowest atom is set to z = 0.000 Å).

to describe the *gr.*/Ru surface is formed by an array of 11×11 unit cells of graphene over 10×10 Ru(0001) unit cells. Compared to the other (n)×(n)/(n-1)×(n-1) models the 11×11/10×10 periodicity offers the advantage that the lateral deformation needed to conform the 11×11 graphene layer to the 10×10 Ru(0001) substrate is minimum [326], thereby minimizing any fictitious effect due to an artificial stretching of the graphene layer. Geometry optimizations have been performed by relaxing the graphene and the topmost Ru(0001) layer, using a convergence criterion for the Hellmann-Feynman forces of 0.01 eV/Å[3][1]. Starting from a planar graphene sheet adsorbed on the metallic surface, the geometry has been relaxed first at the DFT+D2/PBE, and, subsequently, at the DFT/PBE level of theory.

[1]additional relaxations of selected geometries with a criterion for the forces set to 0.005 eV/Å^3 lead to variations of the optimized atomic positions below 0.015 Å

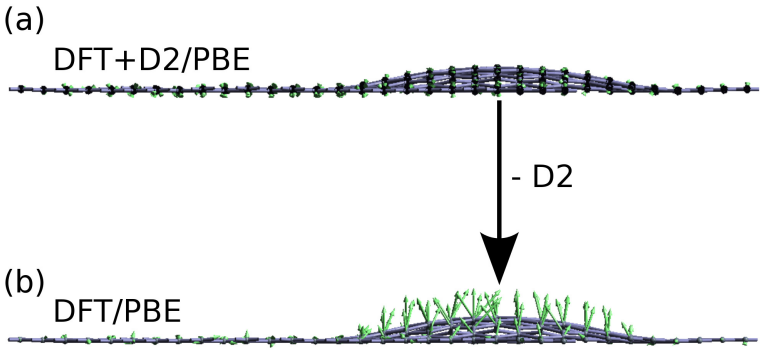

Figure 6.7: Residual forces (green arrows) acting on the carbon atoms of the graphene layer (printed in gray), in the DFT+D2/PBE geometry, when the correction for vdW interactions is included (top) or removed (bottom). The ruthenium layer are not shown for visualization purposes.

Discussion

The details of the DFT+D2/PBE ground state geometry are shown in Fig. 6.6. The ripple height is 1.195 Å (see Fig. 6.6(a)), which is between 0.40 Å and 0.55 Å smaller than that obtained in previous DFT/PBE [325, 326] calculations. This is a very clear signal that the reduction in the corrugation is due to the vdW interaction between the graphene sheet and the ruthenium substrate. This interpretation is further supported by the results shown in Fig. 6.7. If the DFT+D2/PBE geometry is kept frozen, but the Grimme's correction is removed, forces of the order of 0.1 eV/Å^3, *i.e.*, one order of magnitude larger than the convergence threshold used for the forces, act on the carbon atoms of the H regions, in the sense of increasing graphene corrugation. Indeed, a subsequent relaxation of the structure at the DFT/PBE level, lead to a corrugation of 1.60 Å (see Fig. 6.8), which is in line with the values of corrugation reported for previous DFT/PBE calculations using unit cells with the same periodicity [325, 326]. Another interesting result is that, as shown in Fig. 6.6 (b), in agreement with the LEED measurements [100], the buckling of the Ru topmost layer approximately follows that of the graphene layer, *i.e.*, in general, Ru atoms below ripples lie higher than those below valleys. This subtle effect is not well reproduced by DFT/PBE calculations, in which several Ru atoms lying just below the top of the ripple lie in the same plane as those lying below the center of the valleys [100]. Nevertheless, the magnitude of the Ru vertical displacements, in the DFT+D2/PBE geometry, is smaller than that suggested by LEED, probably due to the fact that only the topmost Ru(0001) layer has been allowed to relax.

Following the analysis performed with the strained 1×1 models, the influence of the C_6 coefficients values on the geometry and energetics of this larger model has been tested. In this case, it has not been possible to perform a systematic study, due to the large dimensions of the unit cell involved. Therefore, the structure of the 11×11/10×10 unit cell has been optimized

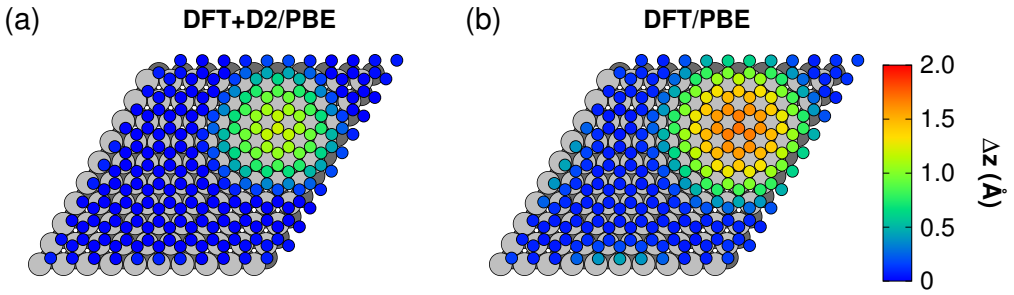

Figure 6.8: Height maps of the carbon atom of the graphene layer in the 11×11/10×10 *gr.*/Ru unit cell, with the geometry optimized at the DFT+D2/PBE (a) and DFT/PBE (b) level of theory. Carbon atoms are printed in different colors depending on their heigth (the lowest carbon atom is set to $\Delta z = 0.0$ Å). Ruthenium atoms of the topmost and topmost-1 layer are printed in gray and dark-gray, respectively.

again, using values of $C_6^C = 1.65$ Jnm^{6}mol^{-1} and $C_6^{Ru} = 15.56$ Jnm^{6}mol^{-1}, in order to estimate an upper bound to the possible errors due to the use of an inaccurate value of the C_6 coefficients. If these new parameters are used, the corrugation rises slightly up to 1.24 Å, and the binding energy decreases from 206 meV/C atom to 167 meV/C atom, showing a trend similar to that predicted by the 1×1 models. The second methodology described in Chapter 3.6 [278], which considers empirically the screening of the substrate by including the uppermost layers of the substrate in the vdW potential[1], has also been considered, leading to very similar qualitative results[2].

Finally, we have compared our results with the geometrical corrugation obtained from the apparent height measured with the STM [75, 139, 144]. Notice that STM, in contrast to diffraction techniques, offers the advantage that fitting is not necessary to extract the information about the surface corrugation from the rough experimental data. Nevertheless, one has always to be aware of the fact that the apparent height is related to the DOS of the sample, and not to its geometry[3]. Fig. 6.9 (a-b) shows a comparison between the experimental and simulated images at $V_{bias} = -1.0$ V. The simulated images have been obtained by applying the Tersoff-Hamann approach, to the DFT+D2/PBE geometry, on an electronic density isocountour of 1.69×10^4 Å^{-3}, estimated as explained in Section 5.1[4]. From Fig. 6.9 (a-b) it can be seen that the periodic pattern in the STM image is well reproduced by theory. A more stringent test is to compare pro-

[1] See "DFT+D2 applied to organic molecules on metallic surfaces" in Section 3.6

[2] In this case, the error of the DFT+D2 approach has been evaluated by performing calculations in which vdW corrections between the graphene layer and the third topmost layer of Ru(0001) are switched off. Screening of the latter layer by the two upper ones should lead to the largest error due to the ABABAB arrangement in Ru(0001). The results of these modified vdW calculations lead to a variation of vertical displacements of the order of 0.001 Å.

[3] See Appendix A.1

[4] similar results have been obtained by using neighboring contours compatible with typical STM currents and tip-surface distances

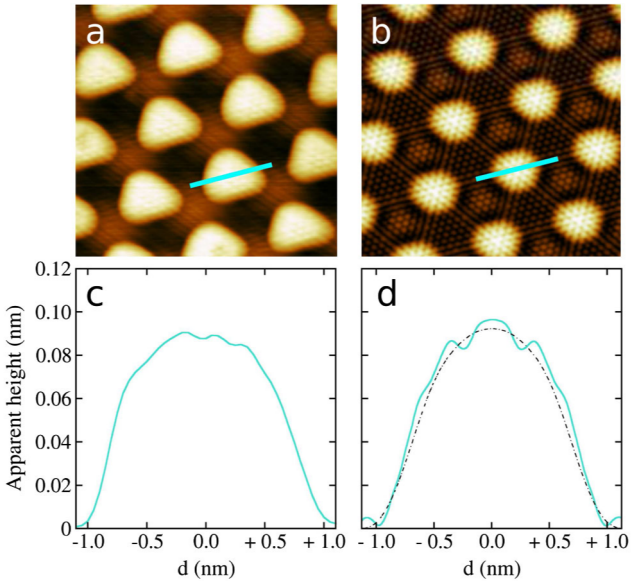

Figure 6.9: (a) Experimental STM image of *gr.*/Ru, taken at V_{bias} = -1.0 V. Simulated STM image at V_{bias} = -1.0 V. (c-d) Apparent height profiles taken along the paths shown in (a) and (b), respectively, as a function of the distance d from the beginning of the path. The dashed line has been obtained by Gaussian smearing of the original simulated image.

files of apparent height along specific directions [306]. Fig. 6.9 (c-d) shows the results along the path shown in panels (a) and (b). The pattern of inverted muffin tins is reasonably reproduced by theory, especially when the latter takes into account the experimental resolution.

Along the same path, Fig. 6.10 shows the variation of the apparent corrugation as a function of V_{bias} of the simulated STM images, calculated using the DFT/PBE and the DFT+D2/PBE geometry. The simulations are compared to the measured values of the apparent height *vs.* V_{bias}, which have been obtained for many different experimental conditions[1] [144]. It is evident that the reduction of the corrugation of the graphene ripple due to vdW interactions has a direct influence on the calculated topographies. The corrugation of the DFT/PBE moiré geometry lies considerably above the measured one in the entire bias range explored (-2.0 V $\leq V_{bias} \leq$ 3.0 V). If the topographical images are calculated using the DFT+D2/PBE geometry, the situation improves substantially. For example, the calculated corrugation at V_{bias} = -1.0 V (+1.0 V) decreases from 1.25 Å (0.99 Å) to 0.98 Å (0.61 Å), in better agreement with the experimental one, 1.0±0.2 Å (0.5±0.2 Å). However, although the inclusion of vdW interactions increases the agreement between the simulated and the measured topographic images, the three-layers models still miss some important features present in the measured data. In particular, they are unable to capture the reduction of corrugation occurring in the close vicinity of the Fermi level between

[1] different tips, different samples, tunnelling currents between 0.1 nA and 10 nA, and sample temperatures between 4.6 K and 300K

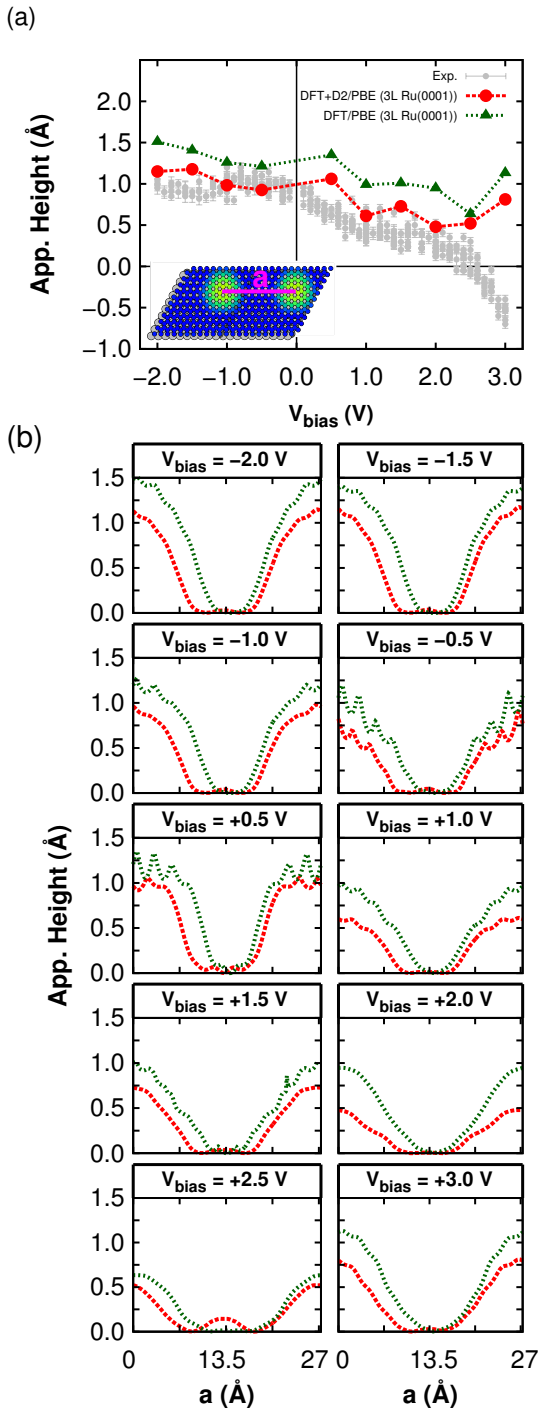

Figure 6.10: Apparent height of the simulated STM images as a function of the V_{bias}, for the corrugated 11×11/10×10 *gr.*/Ru model calculated at the DFT/PBE (green points) and DFT+D2/PBE level of theory. The points are connected by lines to guide the eye. The theoretical data are compared with the experimental ones (gray points). The inset indicate the moiré unit cell vector a over which the corrugation has been measured both in the experimental and in the simulated topographies. (b) Line profiles of the simulated STM topographies along a, at different values of V_{bias}, using the DFT/PBE (green lines) geometry and DFT+D2/PBE geometry (red lines).

V_{bias} = -0.5 V and V_{bias} = 0.5 V, along with the contrast inversion - *i.e.*, a negative value of the apparent height - observed in the experimental topographies above V_{bias} = +2.5 V. As is will be shown in Chapter 7, these deficiencies can be overcome, if the description of the Ru(0001) surface is improved by using a larger number of layers.

7 Localized electronic states in graphene adsorbed on Ru(0001)

The relationship between the corrugated nature of gr./*Ru, and the presence of localized electronic states on its surface, is examined. Two energy ranges, which have been explored experimentally, are considered. The first one is the region spanned by the energy window that goes from ∼1 eV below to ∼1 eV above the Fermi level. The second region lies at higher energies, from ∼1 eV above the Fermi level up to ∼1 eV below vacuum level. In both regions, new localized states are predicted to appear, as a consequence of the spatially modulated interaction between the graphene and the metallic surface.*

The results presented have been published in:

- "Electron localization in epitaxial graphene on Ru(0001) determined by moiré corrugation" D. Stradi *et al.*, *Physical Review B(R)*, **85**, 121404 (2012)
- "Lattice-matched versus lattice-mismatched models to describe epitaxial monolayer graphene on Ru(0001)" D. Stradi *et al.*, *Submitted* (2013)

The periodic variations in the graphene-Ru(0001) interaction across the *gr.*/Ru unit cell (see Chapter 6) have profound consequences on the electronic structure of the surface [75, 139, 103, 330, 331]. The most important one is probably that the electronic bands of graphene are significantly distorted, with respect to those of a flat, free-standing graphene. Indeed, such modifications have been evidenced by several STS measurements, that have reported spectra exhibiting highly structured profiles [104, 142, 103, 332].

As a consequence of these distortions, the interpretation of STS spectra and STM images measured on *gr.*/Ru represents a formidable challenge. A straighforward example is the quantification of the moiré corrugation from the topographical images measured by the STM (see, Fig. 6.10 in Chapter 6). The apparent height measured varies dramatically as a function of the bias voltage [139, 144], and it even turns negative at $V_{bias} > 2.6$ V, *i.e.*, there is an inversion of contrast in the topography (see Fig. 7.1) [144]. This means that the geometrical information provided by the STM images is convoluted with strong electronic effects, that arise as a consequence of the strongly inhomogeneous geometric and electronic characteristics of *gr.*/Ru

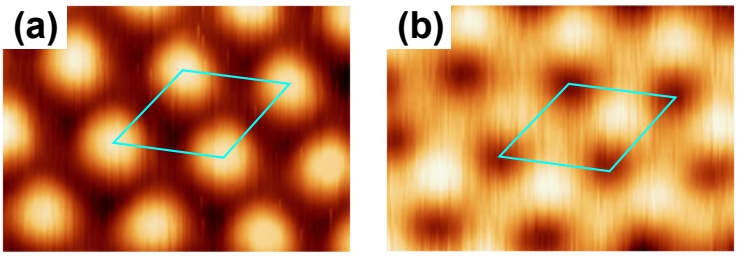

Figure 7.1: Contrast inversion in the STM topographical images measured by the STM. The two panels show two topographical images of the same sample (a) at V_{bias} = -1 V and (b) at V_{bias} = +2.8 V. The *gr.*/Ru moiré unit cell subunit is shown in cyan.

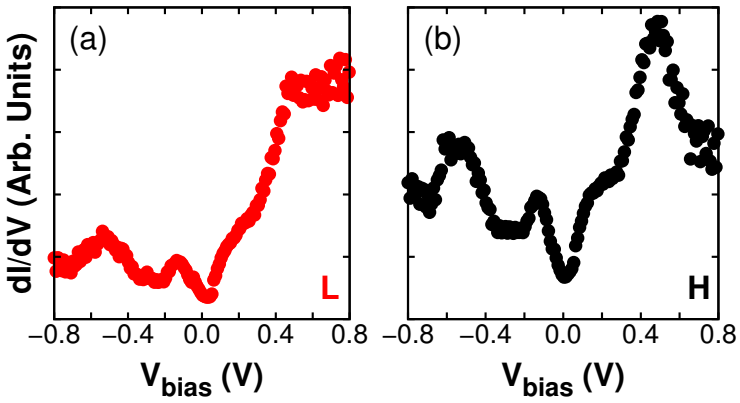

Figure 7.2: Experimental low-temperature (T = 77 K) STS near the Fermi level, measured over the L region (a) and H region (b) of the graphene moiré. Individual I(V) curves were measured at every pixel of the corresponding topographic image with a bias voltage of +1 V and a tunnelling current of 0.4 nA. The dI/dV curves were obtained by numerical differentiation of the I(V) curves.

[75, 103].

In an attempt to measure spatially resolved STS spectra around the Fermi level, an asymmetry of the local density of states (LDOS) in the high and low areas of the moiré pattern has been found [75]. In addition to this asymmetry, pronounced peaks in the STS spectra around the Fermi level have been observed [75, 333, 332, 104], which intensity has been found to vary across the different regions of the *gr.*/Ru moiré [145]. A typical example of spatially resolved STS spectra, measured over the H and L regions of the graphene moiré, is shown in Fig. 7.2. It can be seen that the spectra vary considerably with the position of the tip over the different regions of the corrugated superstructure. Spectra measured over the H regions show a well-defined series of peaks both at negative and positive bias voltages, whereas these structures are much less pronounced for spectra over the L regions. In the latter region, there is also a strong asym-

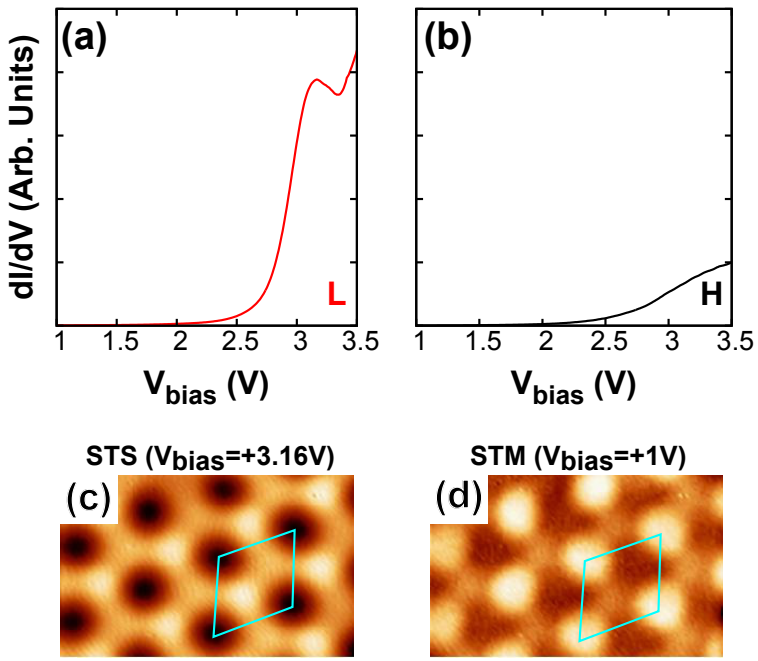

Figure 7.3: (a-b) STS spectra at high positive biases taken over the L (a) and H (b) regions of the *gr.*/Ru moiré. (c) STS 2D maps measured at the energy of the peak shown in (a), $V_{bias} = +3.16$ V. Topographic image measured at $V_{bias} = +1$ V. In (c) and (d), the *gr.*/Ru unit cell subunit is shown in cyan.

metry in the intensity of the spectra at negative and positive bias voltages. The exact origin of these features is unclear. Based on the experimental results and simple theoretical model using a planar graphene sheet, Vázquez de Parga et al. [75] have associated the asymmetry in the STS spectra measured over the different regions of the moiré to the electron doping of the H regions. On the other hand, based only on the experimental results, Lu et al. [332] have related the peaks observed in the STS spectra to a shift of the Dirac cone of graphene, whereas Gyamfi et al. [145] have related them to a Ru bulk state contributing to the tunnelling current.

The unoccupied electronic structure of *gr.*Ru, below the vacuum level, has also been discussed intensely [103, 141, 142, 143, 331]. In particular, there has been a controversy concerning the assignment of a well defined spectral feature, which appears in the STS spectra measured over the L area at $V_{bias} \approx +3.0$ eV [103, 142]. Typical STS spectra showing this characteristic feature are shown in Fig. 7.3 (a-b). From Fig. 7.3 (a), it can be seen that the spectrum measured over the H regions is essentially featureless, while the spectrum measured over the L regions shows a peak centred at $V_{bias} \approx +3.0$ V[1]. Based on DFT calculations, in which the surface has been described by lattice matched 1×1 *gr.*/Ru models, Borca et al. [103] have conjectured that the STS peak is due to the presence of a new interface state, which arises as a result of the strong

[1]Note that in these measurements, the resonance energy is likely to be upshifted, as a consequence of the electric field created between the tip and the sample at large bias voltages.

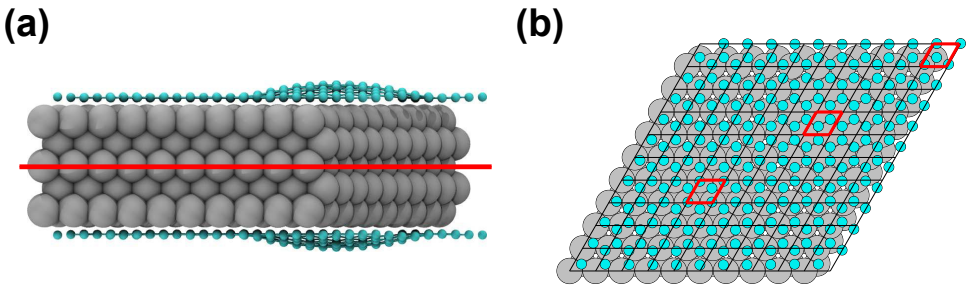

Figure 7.4: (a) Structure of the symmetric five-layers 11×11/10×10 *gr.*/Ru model. The red line identifies the mirror symmetry plane. (b) Subdivision of the *gr.*/Ru into the array of unit cell equivalent to that of Ru(0001), for the evaluation of the region-dependent LDOS. The three regions marked in red, are those over which the LDOS have been calculated.

interaction between graphene and Ru(0001) in the L regions of the moiré. However, Zhang et al. [142] have assigned this peak to the lowest field emission resonance (FER) of the surface. The former authors have also claimed that the interface state is responsible for the inversion of contrast observed in STM topographical images above $V_{bias} \approx +2.6$ eV. This picture has been further supported by independent time-resolved *Two photon photoemission* (2PPE) on *gr.*/Ru [331]. In these measurements, the results obtained for the lifetimes of the empty states probed during the measurement appear to be consistent with the interpretation of Borca et al. [103].

In this Chapter, it will be shown how the lattice-mismatched 11×11/10×10 model can rationalize these experimental observations, and provide insight on the nature of the electronic features observed experimentally[1].

Computational details

With only three layers to the describe the Ru(0001) surface, the 11×11/10×10 lattice-mismatched model is not able to reproduce two important features observed in the trend of the apparent height *vs.* V_{bias} measured experimentally (see Fig. 6.10). These are: (i) the trend in close proximity of the Fermi level (-0.5 V $\leq V_{bias} \leq$ +0.5 V); (ii) the topographic contrast inversion observed at bias voltages larger than $V_{bias} \approx +2.6$ V. This theoretical deficiency is caused by the poor description of the metallic substrate provided by the three-layers slab, which results in a discretization of the ideal continuum of the semi-infinite metallic surface which is too high. To minimize such effect, a larger lattice-mismatched model has been considered. This model has been built by adding to the three-layers 11×11/10×10 *gr.*/Ru unit cell - with the DFT+D2/PBE geometry (see Chapter 6) its mirror replica. The mirror plane has been placed at the bottommost Ru layer (see Fig. 7.4 (a)).

The electronic structure calculations have been performed using a computational set-up sim-

[1] For a complete comparison between the description of the electronic structure provided by the lattice-matched and lattice-mismatched models, see Appendix B.

ilar to that described in the computational details of Chapter 6. However, in the present case, a Gaussian smearing of 0.1 eV has been used, as well as a vacuum gap of 20-Å vacuum gap.

STM simulated topographies and local density of states (LDOS) over selected areas of G/Ru have been computed by using the Tersoff-Hamann [301] approximation (see Section 5.1 in Chapter 5). The LDOS has been evaluated according to Eq. 4.4, and substituting the δ function by a normal distribution, in order to take into account the finite size effects due to the finite number of layers used to describe the surface [334]:

$$\delta(E - E_i) \approx \frac{1}{\sigma\sqrt{2\pi}} e^{-(E-E_i)/(2\sigma^2)}, \tag{7.1}$$

with $\sigma = 0.1$ eV. To calculate the LDOS in the different regions of the *gr.*/Ru unit cell, the *xy*-plane of the five-layers 11×11/10×10 unit cell has been divided in an array of 10×10 smaller cells, each one being equivalent to a single Ru(0001) unit cell (see Fig. 7.4 (b)). Within each of these unit cells, an average LDOS has been evaluated as the average of a grid of 30×30 LDOS.

Discussion

Fig. 7.5 (a) shows a comparison between the apparent height measured by the STM as a function of V_{bias}, and the apparent height calculated from the simulated STM images in the same energy range, using the five-layers lattice-mismatched *gr.*/Ru unit cell. The improvement over the data obtained using the three-layers model (Fig. 6.10 (a)) is evident: the complete trend of the apparent height versus V_{bias} is reproduced correctly[1]. The line profiles taken along the *gr.*/Ru unit cell vector (Fig. 7.5(b)) show that, at biases larger than $V_{bias} = +3.0$ V, the contrast in the topography is mainly due to a large increase in the electronic density over the L regions of the graphene moiré. As mentioned above, such feature is completely absent in the topographies obtained using the three-layers metallic slab model (Fig. 6.10 (b)), which fails to capture the contrast inversion shown in Fig. 7.1.

The fact that the five-layers 11×11/10×10 DFT+D2/PBE geometry is able to reproduce correctly the topographical contrast, observed in the STM experiments, indicates that such model provides a reliable description of the electronic structure of *gr.*/Ru, in the range of energies probed experimentally.

In order to characterize the electronic structure of *gr.*/Ru in the proximity of the Fermi level, the changes in the shape of the LDOSs taken over the different regions of the moiré (see Fig. 7.4), as a function of the tip-surface distance, have been studied. Fig. 7.6 shows the LDOSs calculated over the center of the H region (Fcc-Hcp) and over the center of the two L regions (Hcp-Top and Fcc-Top) of lattice-mismatched *gr.*/Ru unit cell (see Fig. 7.4 (b)). Three different

[1]It should be noted that for the five-layer model, the major contribution to the surface LDOS at $V_{bias} = +3.0$ V comes from unoccupied electronic states that are considerably extended towards the vacuum. Because of this, the correct characteristics of the simulated topographic images cannot be obtained using the same isocontour employed at lower values of V_{bias} (1.69×10^{-4} Å^{-3}), due to the relatively small vacuum gap employed in our calculations (∼20 Å). Indeed, by considering the isosurface value a factor 10 larger, meaningful topographies that can be compared with the experimental ones can be obtained

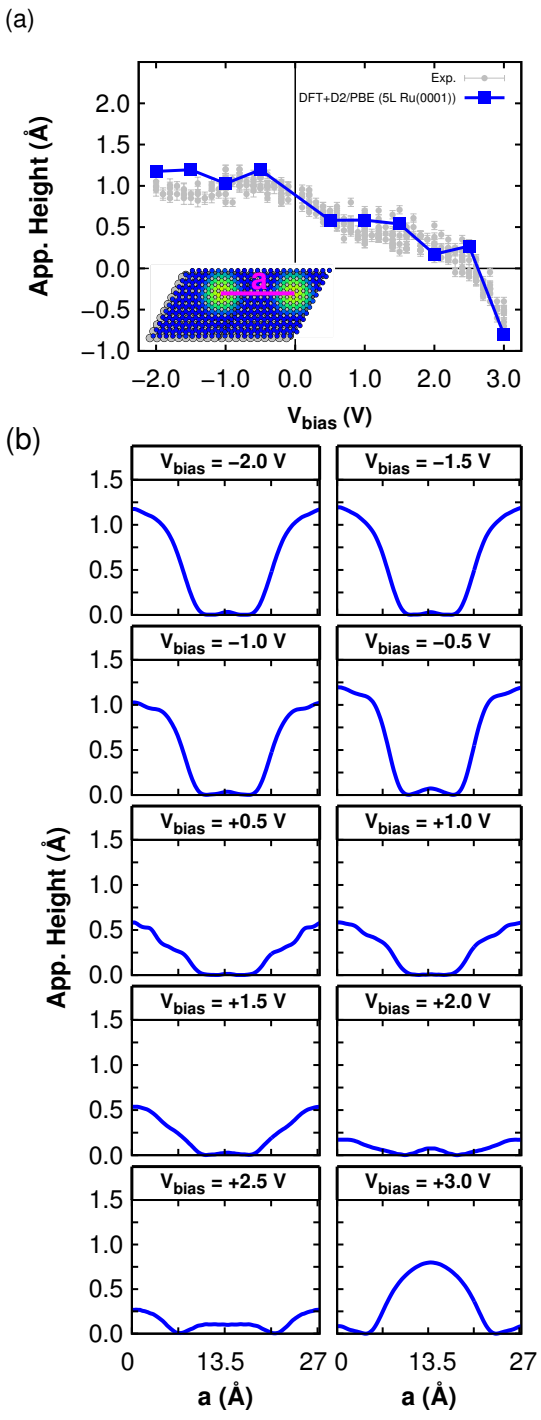

Figure 7.5: Apparent height of the simulated STM images as a function of the V_{bias}, for the corrugated 11×11/10×10 *gr.*/Ru model with the DFT+D2/PBE geometry and 5 ruthenium layers. The points are connected by lines to guide the eye. The theoretical data are compared with the experimental ones (gray points). The inset indicate the moiré unit cell vector a over which the corrugation has been measured both in the experimental and in the simulated topographies. (b) Line profiles of the simulated STM topographies along a, at different values of V_{bias}.

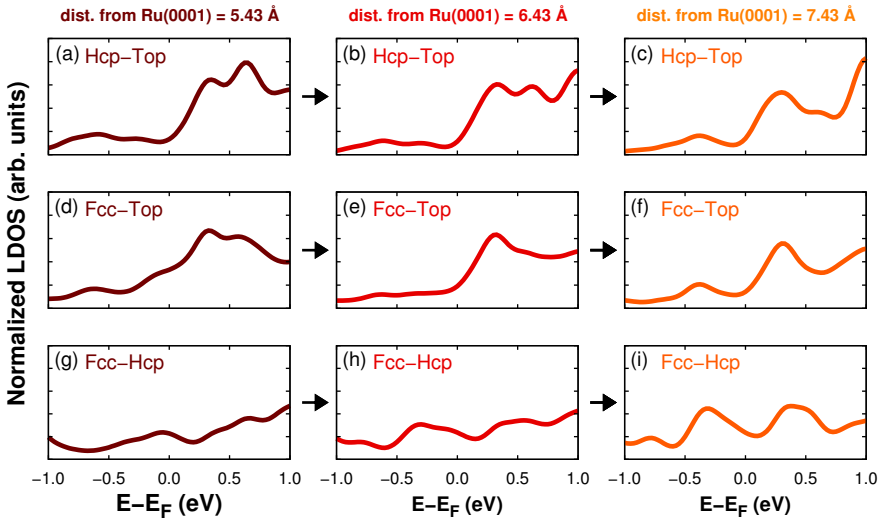

Figure 7.6: LDOS calculated over the Hcp-Top (a-c), Fcc-Top (d-f) and Fcc-Hcp (g-j) regions of the gr./Ru(0001) moiré of the 11×11/10×10 supercell in the energy range -1.0 eV ≤ E-E$_F$ ≤ 1.0 V. The distance from the Ru(0001) topmost layer surface plane is 5.43 Å (a,d,g), 6.43 Å (b,e,h) and 7.43 Å (c,f,i). Arrows indicate the direction of increasing distance from the surface. The LDOSs have been normalized to have the same area under each curve

distances from the surface (the zero is set to the Ru(0001) topmost layer) have been considered, and the LDOSs have been scaled by a normalization factor, so that the area below each curve is the same[1]. For distances from Ru(0001) close to the experimental tip-sample distance (7.43 Å, Fig. 7.6 (c,f,i)), the LDOSs reproduce qualitatively the features observed experimentally[2]. At the L regions of the graphene moiré (Fig. 7.6 (c,f)), the LDOSs exhibits an asymmetry above and below the Fermi level, similar to that observed in the experiments (see Fig. 7.2 (b)), whereas for the LDOS at the H region, where the coupling between the graphene and the metal substrate is weaker, this asymmetry is much less pronounced (Fig. 7.6 (i)). Moreover, in both the LDOSs at the H and at the L regions well defined peaks are present below and above the Fermi level. These peaks appear at E-E$_F$ = -0.4 V and E-E$_F$ = +0.35 V in the L region, and at E-E$_F$ = -0.35 eV and E-E$_F$ = +0.45 eV in the H regions. However, the overall number and the energy position of these peaks do not match with that of the peaks in the measured spectra. This is especially true in the region below the Fermi level, where the STS data show clearly the presence of two peaks. These discrepancies can be associated to the numerous approximations introduced in the model employed. In fact, the 11×11/10×10 geometry remains only an idealized model for *gr.*/Ru moiré. In addition, a very reduced finite number of layer to describe the semi-infinite

[1]This has been done to get rid of the exponential decrease in the LDOS intensity, with increasing distance from the surface, thus simplifying the comparison between the shapes of the different spectra.

[2]It has been checked that calculated LDOSs remain qualitatively the same in the range 7-8Å

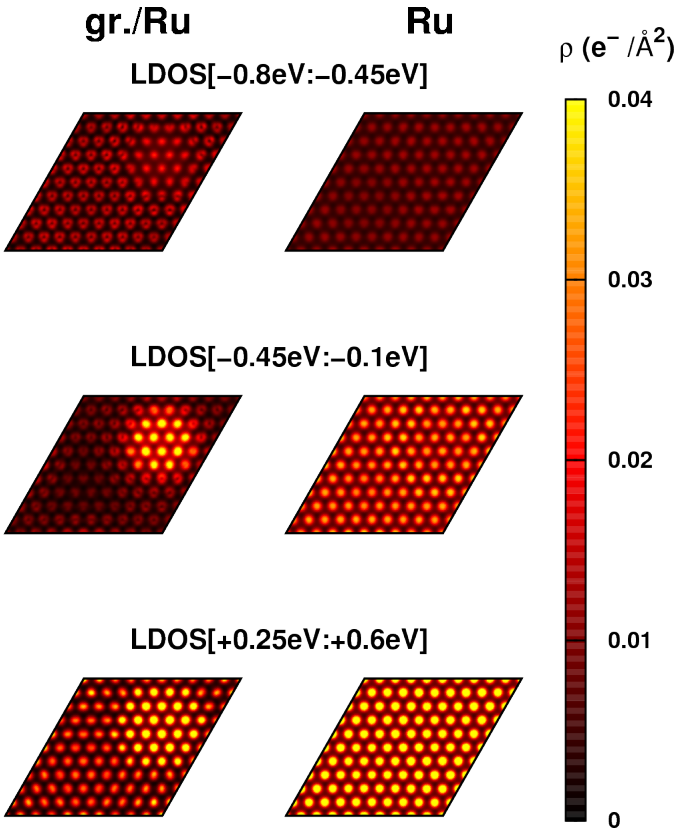

Figure 7.7: 2D cuts taken at ∼1 Å above the Ru(0001) topmost layer for selected integration ranges of the DOS, for G/Ru (left-hand column) and clean reconstructed Ru (right-hand column).

surface, and the reciprocal space is sampled only at the 1^{st} BZ just at the Γ-point only. Due to the intrinsic limitations of the model, the analysis based on the LDOSs is not able to capture all the fine details of the measured spectra. However, it reproduces, at least qualitatively, the main features observed in the experiment, and in particular, it predicts the appearance of peaks below and above the Fermi level.

In order to get some insight on the origin of the peaks observed in the LDOSs, the DOS has been integrated in different energy ranges. The left-hand column of Fig. 7.7 shows two-dimensional (2D) cuts (*xy*-plane) obtained after DOS integration, at 1 Å from the Ru(0001) surface, *i.e.*, in between the graphene layer and the Ru surface. When the DOS integration energy range includes a LDOS spectrum peak, a high electronic density is observed in the region right below the graphene ripple. On the contrary, accumulation of electronic density is barely seen if the integration energy range leaves out these LDOS peaks. To rule out that such an effect is due to the Ru surface reconstruction present on this system (see Fig. 6.6), the DOS of the

clean reconstructed Ru surface has been integrated[1]. The latter system does not exhibit any localization of the electron density. Therefore, the features present in the LDOS above the surface, at distances similar to the tip-surface distance in an STS experiment, can be associated with the accumulation of electronic density below the graphene ripple, which results from the corrugated nature of the graphene monolayer. This accumulation is consequence of the doping of the H regions of graphene by Ru(0001) [75, 335] and of the associated overlap between two interacting electronic densities. The fact that a weak interaction between graphene and Ru(0001) persists is in agreement with the charge transfer rates measured by *core hole clock* (CHC) spectroscopy, which have been found to be only marginally slower than on the L regions [330].

As already remarked, the periodic corrugations of the graphene moiré do not affect only the electronic spectrum close to the Fermi level, but also the unoccupied bound states at higher energies. In particular, DFT calculations [103] using symmetric lattice-matched 1×1 models with 23 Ru(0001) layers, have suggested that the contrast inversion is related to the presence, in the clean Ru(0001) surface, of a surface resonance state located just above the projected gap at the Γ-point. This resonance can combines with the first image state of graphene (1^+) [29], forming a new interface state, which is considerably extended towards the vacuum [103]. However, the formation of this new state depends critically on the overlap between the wavefunctions of the graphene (1^+) state and the Ru(0001) surface resonance. For this reason, the interface state is formed only when the graphene-Ru(0001) distance is similar to that of the L regions of the moiré ($d_{gr/Ru} \approx 2.2$ Å), whereas it is not present when the graphene-Ru(0001) distance is similar to that of the H regions ($d_{gr/Ru} \approx 3.4$ Å). For $d_{gr/Ru} = 2.2$ Å, this new state has an energy E-E_F ≈ 3.0 eV. Despite the fact that this explanation seems to be consistent with the experimental STS data, this interpretation has been questioned, because of the idealized nature of the 1×1 models employed [143, 141].

A three-layers Ru(0001) slab is not sufficient to reproduce the aforementioned surface resonance[2], which only appears when the number of layers is equal to, or larger than, five[3]. Because of this, the five-layers 11×11/10×10 lattice-mismatched model (Fig. 7.1) represents the minimum model which is able to account simultaneously: (i) the presence of the surface resonance; (ii) the presence of the moiré pattern. Therefore, with this model it is possible to characterize the new surface state, without the limitations imposed by the idealized 1×1 geometries. Fig. 7.8 shows the LDOS above the different regions of the *gr.*/Ru moiré, in the energy range +0.0 eV ≤ E-E_F ≤ +3.5 eV. In this case, the LDOSs have not been normalized, so that it is possible to examine their decay at increasing the distance from the surface. A prominent peak can be identified in the Hcp-Top and Fcc-Top regions - the two L regions of the moiré - at E-E_F ≈ +2.8 V, in good agreement with the position of the interface state measured by 2PPE (E-E_F =

[1] Clean reconstructed Ru surface means the structure obtained by removing the graphene layer while keeping all Ru atoms in the positions they had in the presence of graphene.

[2] Calculations performed using `VASP` code, the PBE functional and the PAW method. Kinetic energy cutoff for the plane-waves expansion set to 400 eV. Vacuum gap set to ∼30 Å. The Brillouin zone has been sampled using a regular grid of 15×15×1 K-points and a Gaussian smearing of 0.1 eV.

[3] This has been checked by performing calculations on Ru(0001) slabs of 3, 5 and 15 layers.

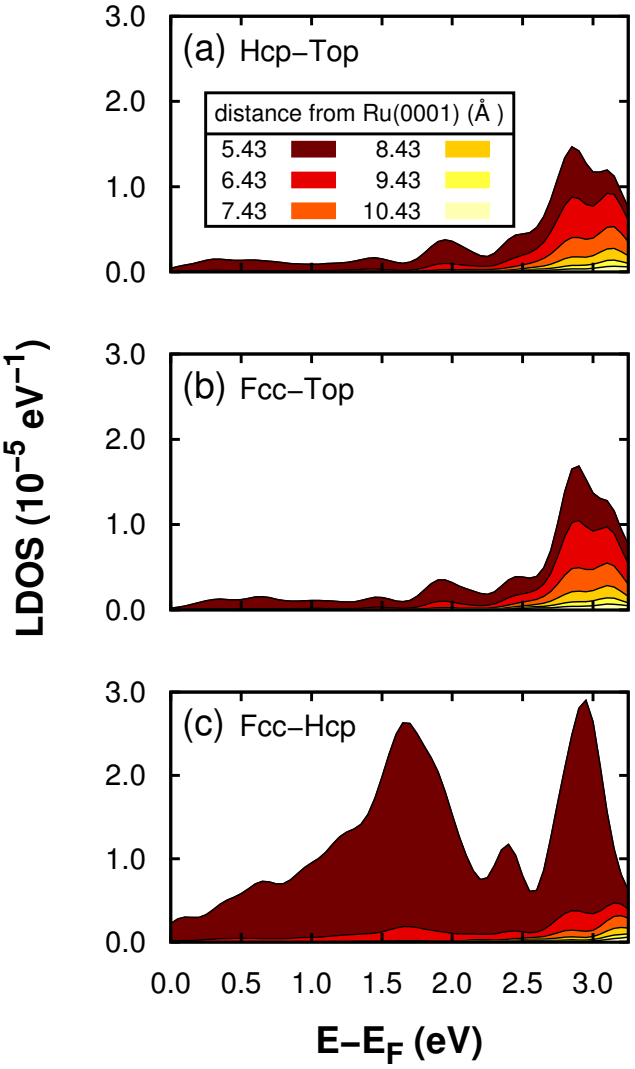

Figure 7.8: Local density of states (LDOS) computed in the energy range 0.0 eV $\leq$ E-E$_F$ $\leq$ 3.5 eV above the Hcp-Top (a), Fcc-Top (b) and Fcc-Hcp (c) regions of the 11×11/10×10 gr./Ru(0001) supercell. The zero is set at the topmost layer of the Ru(0001) surface plane. The LDOS are printed with increasingly brighter colors depending on their distance from this plane.

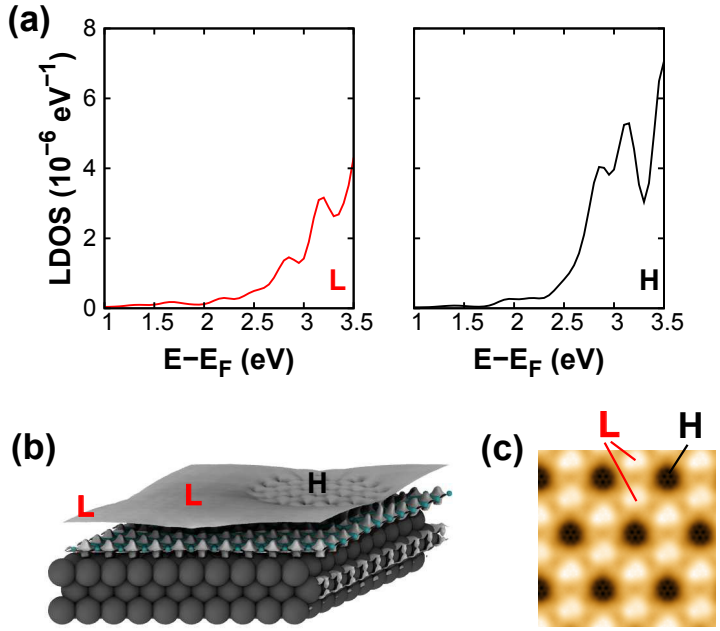

Figure 7.9: (a) LDOS calculated at 7.43 Å above the Ru(0001) plane over the L (red, left panel) and H (black, right panel) areas of the *gr.*/Ru moiré. The LDOS relative to the Hcp-Top region is shown. The behaviour of the LDOS relative to the Fcc-Top region is very similar. (b) Electronic density distribution obtained from the integration of the density of states (DOS) in the range between +2.75 and +3.2 eV. Carbon and ruthenium atoms are printed in dark-gray and cyan, the electronic density isosurface is printed in gray. (c) Simulated STM topography at V_{bias} = +3.5 V on an electronic density contour of 1.69 × 10^{-3} Å^{-3}.

+2.58±0.04 eV) [331]. The peak decays very slowly into the vacuum, as it should be expected for an interface state which is considerably extended outside the surface. On the other hand, in the Fcc-Hcp region, the decay of the LDOS towards the vacuum is much faster that in the two L regions of the moiré. This indicates that, in the H regions, those electronic states which derive from the graphene (1^+) state lie at energies E-E$_F$ > 3.25 eV. According to 2PPE measurements [331], the position in energy of the 1^{st} image state in *gr.*/Ru is E-E$_F$ = +3.44±0.05 eV.

A more direct comparison between the calculated LDOSs and the the measured STS data (see Fig. 7.3) can be done by examining the behaviour of the LDOSs in the H and L regions at the same distance from the Ru(0001) surface. Fig. 7.9 (a) shows the LDOSs calculated at 7.43 Å from Ru(0001), in the energy interval +1.0 eV ≤ E-E$_F$ ≤ +3.0 eV, *i.e.*, at a distance form the surface and in an energy range, which are comparable to the experimental ones. Around E-E$_F$ ≈ +2.8 eV, the LDOS is considerably sharper in the L regions than in the H regions. The analysis of the electronic density, obtained by integration of the DOS in the interval +2.75 eV ≤ E-E$_F$ ≤ +3.2 eV (Fig. 7.9 (b)), shows that the origin of such a maximum in the LDOS is the protrusion of the electronic charge density outside the graphene layer in the L areas of the moiré.

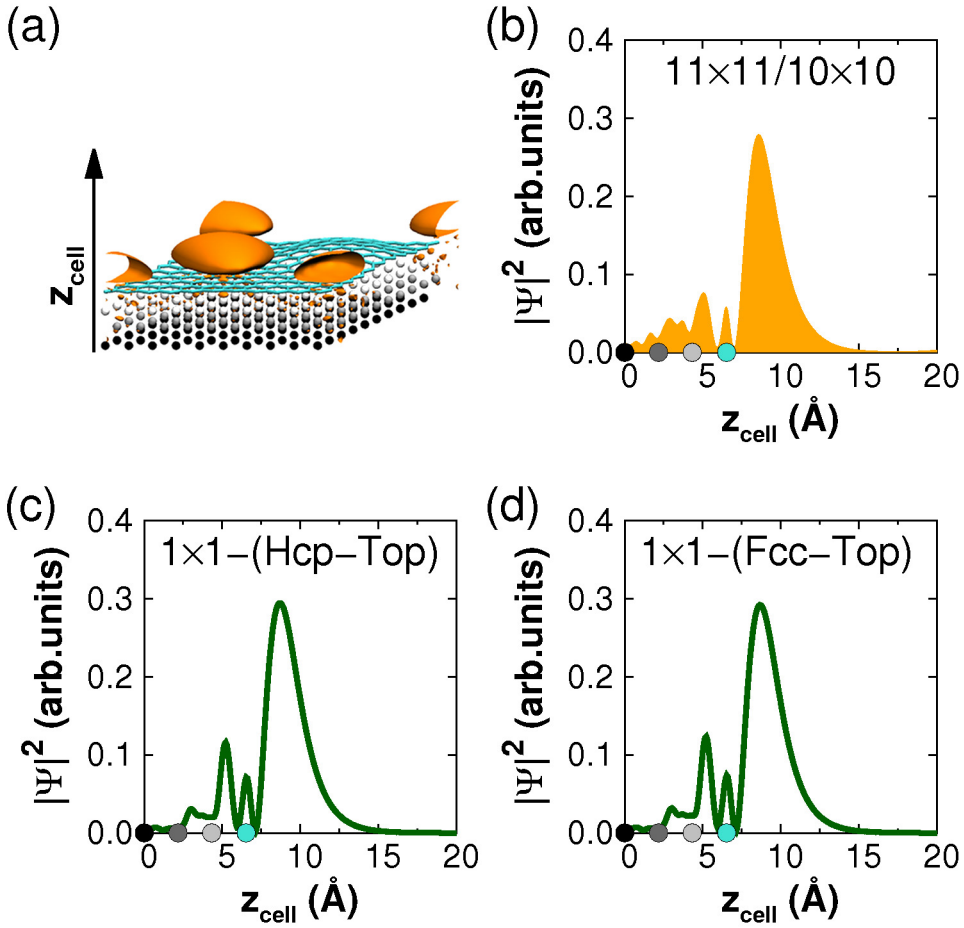

Figure 7.10: (a) Isosurface (isocontour value = $1{\times}10^{-4}$ eV/Å^3) of the lowest eigenstate associated with the *gr.*/Ru interface state of the 11×11/10×10 model. Only three Ru layers are shown for simplicity. (b) Probability density $|\Psi|^2$ averaged over the *xy*-plane of the eigenstate shown in (a). The graphene layer atoms are shown in cyan. The topmost, topmost-1 and topmost-2 ruthenium layers are shown in light gray, dark gray and black.(c,d) Probability densities $|\Psi|^2$ averaged in the *xy*-plane of the lowest eigenvalues associated with the gr./Ru(0001) interface state in the $1 \times 1 - (Hcp - Top)$ and $1 \times 1 - (Fcc - Top)$ models. In (b,c,d), the position of the three uppermost ruthenium layers and of the graphene layers is indicated by the dots on the x-axis (same colours as in (a)).

By simulating the Tersoff-Hamann images at large positive voltages, *i.e.*, $V_{bias} = +3.5$ V, on an electronic density contour of 1.69×10^{-3} Å^{-3}, which reflects the shape of the electronic density shown in Fig. (7.9(b)), a topographical image such as that in Fig. 7.9 (c) is obtained, which is very similar to that obtained experimentally at a similar value of V_{bias} (compare with Fig. 7.1 (b)).

Finally, the individual eigenstates in the energy region where new interface state appears ($+2.7$ eV $\leq$ E-E$_F$ $\leq +3.3$ eV) have been analyzed. The first one corresponding to the bottom of the interface state, is located at E-E$_F$ $= +2.85$ eV. Its probability density ($|\Psi|^2$) is shown in Fig. 7.10 (a). In agreement with the previous analysis, $|\Psi|^2$ is almost exclusively localized outside the surface over the L regions of the moiré structure (Fig. 7.10 (b)). By integrating $|\Psi|^2$ in the *xy*-plane, the individual eigenstate can be compared directly with the corresponding ones at the Γ-point of the 1^{st} Brillouin zone of two five-layers $1 \times 1 - (Hcp - Top)$ and $1 \times 1 - (Hcp - Fcc)$ models (Fig. 7.10 (c-d)), describing the L regions of the graphene moiré[1]. The probability distributions obtained from the 1×1 models overlap almost perfectly with that calculated using the 11×11/10×10 supercell. Therefore, the calculations performed with the five-layers 11×11/10×10 model allow to conclude that the inversion of contrast observed in the STM topographies is effectively related to the presence of an interface state, with energy E-E$_F$ $\approx +2.8$ eV, which is strongly localized in the L regions of the *gr.*/Ru corrugated moiré.

[1]Calculations performed using VASP code, the PBE functional and the PAW method. Kinetic energy cutoff for the plane-waves expansion set to 400 eV. Symmetric 1×1 unit cells with graphene at both sides of a five-layers Ru(0001) slab have been used. The vacuum gap has been set to ∼20 Å. Brillouin zone sampling of 15×15×1 K-points with a Gaussian smearing of 0.1 eV. $d_{gr./Ru}$ set to 2.2 Å.

8 Elastic response of graphene on Ru(0001)

The mechanical properties of the H regions of the corrugated moiré superstructure of gr./Ru *are investigated by combining non-contact atomic force microscopy experiments and density functional theory calculations. The experiments suggest that the elevations of the graphene superstructure can be deformed by pressure, and that this deformation is perfectly reversible. Theory verifies this behaviour, and provide a quantitative analysis of the mechanical properties of the H regions of the moiré.*

The results presented have been published in:

- "Elastic response of graphene nanodomes"
  S. Koch, D. Stradi *et al.*, *ACS Nano*, **7**, 2927 (2013)

Gr./Ru, because of its peculiar geometry, in which the weakly coupled H regions are kept fixed by the surrounding L regions, where the graphene is strongly bound to the Ru(0001) substrate, represent an ideal system to study the mechanical properties of graphene samples at the nanoscale. In fact, one of the most important features of graphene is its exceptional mechanical strength, with a remarkably high Young's modulus of the order of 1 TPa [17], as reported for free-standing membranes with linear sizes of tens to hundreds of micrometers. Despite the potential for graphene to be used in nanoelectromechanical devices [39, 40], such mechanical properties have never been verified for samples of only few atoms. The reason for this is that the controlled production of atomically defined graphene nanostructures of such reduced dimensions remains a significant challenge, which is further complicated by the lack of experimental techniques to properly characterize their mechanical behaviour. In this respect, the first step towards the quantification of the mechanical properties of graphene, at the nanoscale, is the experimental verification of the elasticity of supported graphene membranes of such dimension. The H region of the *gr.*/Ru moiré is a perfect candidate for this role, because of its very well defined dimensions (diameter $\approx$ 1-2 nm), and its relatively weak coupling to the underlying substrate.

Figure 8.1 (a) shows four topographical images of the *gr.*/Ru superstructure, obtained by NC-AFM [1]. The advantages related to the use of NC-AFM technique to probe the mechanical behaviour of *gr.*/Ru are related to its non-destructive character, *i.e.*, the sample is not indented,

[1] For a description of this technique, see Appendix A.4

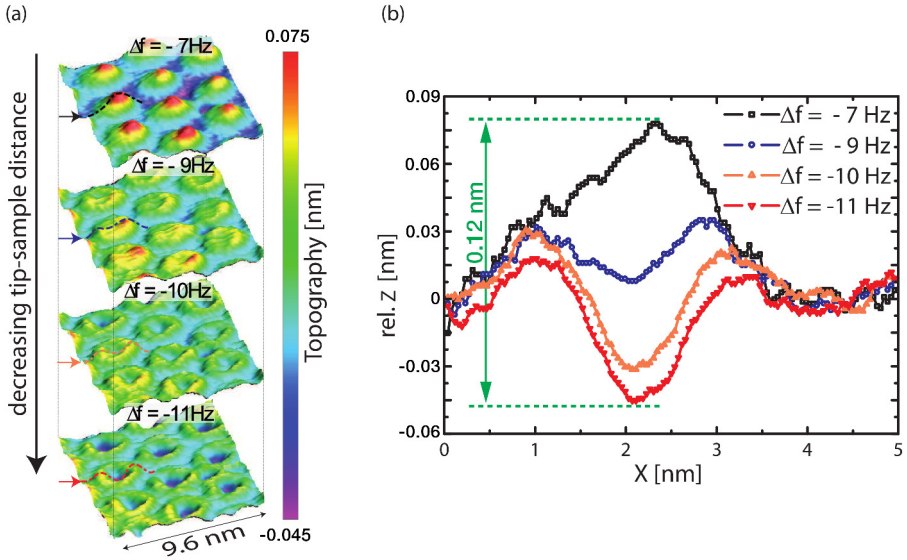

Figure 8.1: Four AFM topographies (9.6×9.6 nm^2) recorded at different frequency shifts Δf=-7,-9,-10 and -11Hz. The electrostatic force was continuously compensated while scanning, using kelvin force probe microscopy (see Appendix A.4). Parameters: amplitude = 8 nm, U_{bias} = -512 mV. The cross sections in (b), taken along the fast scan direction, show the elastic deformation of the hill sites marked by the corresponding colored lines in (a). The valley site of every curve is adjusted to rel. z = 0 nm.

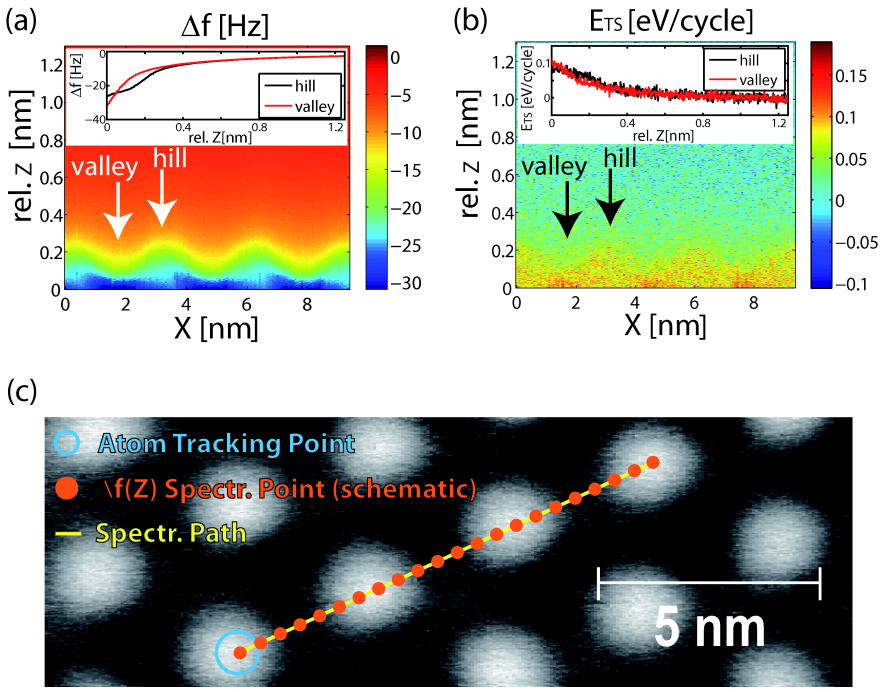

Figure 8.2: 2D spectroscopy plots of (a) frequency shift $\Delta f(z)$ and (b) energy dissipation E_{ts}. The insets of (a) and (b) are spectroscopic curves measured over the H regions (hills) and the L regions (valleys), extracted out of the 2D data, averaged over three curves. Parameters: amplitude = 7 nm, U_{bias} = - 819 mV. (c) Topographic NC-AFM image of the area used for 2D spectroscopy on the graphene/Ru(0001) subtrate. The yellow line represents the original spectroscopy path. The red dots indicate the 128 Δf spectroscopy points with a resolution of 512 points each. Parameters: Δf = - 7 Hz, amplitude = 8 nm, U_{bias} = - 556 mV.

and to its very high lateral resolution, which allows to address the mechanics of the individual elevations of the periodic moiré. The four images in Fig. 8.1 differ in the value of the frequency shift, Δf, that has been used during the scan. As explained in Appendix A.4, by varying Δf it is possible to control the relative tip-sample distace. Approaching the tip to the surface, by using an increasingly larger value of Δf - from Δf = -7 Hz to Δf = -11 Hz -, changes considerably the measured topography. The L region does not show any visible change, but the H regions appear to be gradually compressed. Further insight can be obtained by looking at the cross-sections of the topographical images along one of the *gr.*/Ru H regions (see Fig. 8.1(b)). At Δf = -7 Hz, which corresponds to the maximum tip-surface distance, the undistorted H regions show an apparent height of 0.075 nm. By decreasing the tip-surface distance, the H region is continuously deformed. At Δf = -11 Hz, which corresponds to the minimum tip-surface distance that can be achieved without crashing the tip, the relative vertical deformation of the H region, with respect to their initial apparent height, is 0.12 nm. On the other hand, the relative height of the profile over the L regions remains unchanged. After each scan, the H regions recover their initial shape,

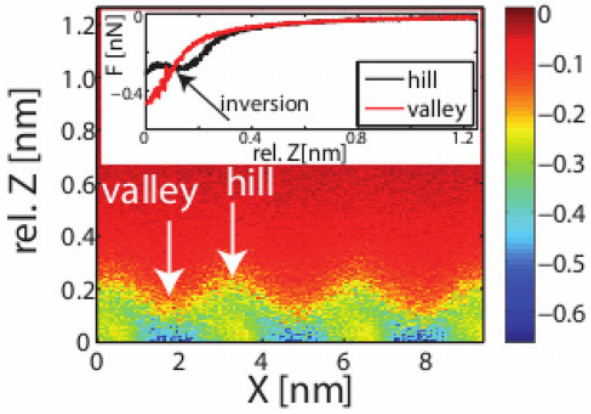

Figure 8.3: 2D $F(z)$ maps as obtained from the numerical inversion of the the $\Delta f(z)$ maps shown in Fig. 8.2 (a). The inset shows the correspondent 1D $F(z)$ curves over the H and L regions.

which suggests that the observed deformation is reversible.

The reversibility of the deformation induced on the H regions by the probing tip is further confirmed by 2D force spectroscopy (for a description of this technique, see Appendix A.5). Fig. 8.2 (a) shows a map of the frequency shift as a function of the tip-surface distance z, $\Delta f(z)$, measured over the H (hill) and L (valley) regions of the *gr.*/Ru moiré, along the points shown in Fig. 8.2 (c). The analysis of two site-specific $\Delta f(z)$ curves measured over the H and L regions (inset in Fig. 8.2 (a)), permits to understand the origin of the deformed profiles observed in Fig. (8.1). At a relative height z lower than 0.15 nm, the frequency shift is larger on the L regions than on the H regions, whereas this trend is the opposite at values larger than 0.15 nm. Thus, the point at $z = 0.15$ nm represent the onset of the topographical contrast change observed in Fig. 8.1.

Fig. 8.2 (b) shows the energy dissipated per each oscillation cycle of the cantilever, E_{TS}, as a function of z, along the same points shown in Fig. 8.2 (c). In the range of relative z considered, the dissipated energy is approximatively the same over the H and over the L regions. E_{TS} increases continuously with z (see the inset in Fig. 8.2 (b)), which suggests that the dissipation is presumably due to Joule heating [336, 337]. In fact, in the 2D force spectroscopy measurements, the compensation of the electrostatic forces has been done at one single point over the surface, which could result in uncompensated electrostatic charges, due to the inhomogeneous electronic structure of the *gr.*/Ru surface.

Fig. 8.3 shows the map of the total force F acting on the tip, versus z, extracted from the data in Fig. 8.2 (a) by means of the Sader-Jarvis method (see Appendix A.4). Similarly, the inset shows the $F(z)$ curves obtained from the $f(z)$ curves shown in the inset of Fig. 8.2 (a). In the L regions, F continuously increases in modulus up to $F(z) =$ - 0.5 nN at $z = 0$ nm. On

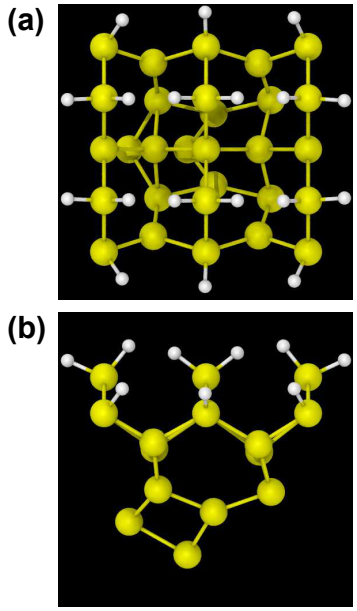

Figure 8.4: Top view (a) and side view (b) of the nanotip employed in this work, based on the 2×1 dimer recontruction of Si(100). Silicon atoms are shown in yellow, and hydrogen atoms are shown in white.

the other hand, the $F(z)$ curve over the H region shows a completely different behaviour. After first increasing in modulus, up to to 0.3 nN at $z \approx 0.2$ nm, $F(z)$ decreases and becomes slightly less attractive. At $z \approx 0.15$ nm, *i.e.*, at the value of z associated with the beginning of the deformation in the H region, the $F(z)$ curves measured at the H and at the L sites cross. After this point, similarly to the trend observed in the $f(z)$ curves in the inset in Fig. 8.2 (a), the absolute value of $F(z)$ is larger over the L regions than over the H regions.

These NC-AFM results show that the response of the H region of the *gr.*/Ru superstructure to an external perturbation (by means of the probing tip) is qualitatively different from that of the L regions, and suggest that the H region undergo a fully reversible deformation. To verify this hypothesis, extensive DFT calculations have been performed to probe the mechanical response of the H regions of the *gr.*/Ru moiré under heavy deformation.

Computational details

As explained in Section 5.2 of Chapter 5, the computational cost associated with DFT calculations is too high to describe the complex dynamic problem involved in a NC-AFM experiment. Nowadays, the simulation of the quasi-static interaction of an idealized tip with the surface (see Section 5.2) represents the state-of-the-art. For the present calculations, the three-layers 11×11/10×10 lattice mismatched unit cell, optimized at the DFT+D2/PBE geometry (see Chapter 6), has been used. The computational parameters have been taken similar to those described

in the "computational methods" section of Chapter 6. However, in the present calculations, the vacuum gap has been increased up to ∼30 Å, in order to include a suspended nanotip over the surface. Following the experiments, silicon tips have been employed. The nanotip employed in the calculations is shown in Fig. 8.4. Essentially, it is an asymmetric cluster of 47 atoms, that has been cut from a model of the 2×1 dimer reconstruction of the Si(100) surface [317]. The uppermost silicon atoms of the nanotip have been saturated with hydrogen atoms, whereas the bottom apex of the cluster is formed by one of the terminating dimers of the Si(100) 2×1 dimer reconstruction. The most important characteristic of this nanotip model, which makes it suitable for the present calculations, is its chemical inertness towards carbon nanostructures [322]. In fact, more symmetric tip models, based, *e.g.*, on the 7×7 reconstruction of Si(111) have been found to be too reactive [322], and inadequate to describe NC-AFM experiments performed on carbon-based materials such as graphite [338] and carbon nanotubes [339]. On the other hand, the inert nanotip shown in Fig. (8.4) has been found to provide theoretical $F(z)$ curves in semi-quantitative agreement with the same experimental data [322]. Thus, this low reactivity ensures that, in the H regions, where the graphene monolayer is weakly perturbed by the substrate, the behaviour of the $F(z)$ will not be affected by the formation of chemical bonds between the sample and the tip.

In order to calculate the $F(z)$ curves, the tip has been initially positioned at the center of the H (L) regions, with its lowest atom lying above the carbon atom at the Ru(0001) hollow site[1]. In the H regions, the hollow site corresponds to the highest graphene atom, which lies exactly in the center of the H region. In the L regions (only the Hcp-Top regions have been considered in the present calculations), both the hollow site and the top site have been considered, because it has been shown that these two sites exhibit very different reactivities [340]. In both cases (H and L regions), the tip has been initially positioned with its lowest atom lying 0.8 nm above the highest one of graphene. Therefore, on the H (L) regions, the initial tip-sample distance is 0.8 nm (0.92 nm). This theoretical shift is chosen to mimic the difference between the $F(z)$ curves measured in the H and L regions, whose value is obtained by matching the tails of the experimental $F(z)$ curves (0.093 nm). The $F(z)$ curves has been calculated using the quasi-static approximation described in Section 5.2. At each quasi-static step the tip has been displaced by 0.05 nm, and the lowest 15 atoms of the tip have been relaxed, together with graphene and the topmost Ru layer.

Discussion

Fig. 8.5 shows the calculated $F(z)$ curves at the H and L regions of the graphene moiré. It can be seen that the important features observed in the experimental $F(z)$ are consistent with the

[1] In the calculations presented in this Chapter, the orientation of the nanotip has been chosen so that the Si-Si bond of the apex dimer of the nanotip lies anti-parallel to one of the C-C bonds connecting the highest C atom in the H region. In the L region, the nanotip has a similar orientation. The study of the effect of the tip orientation on the calculated $F(z)$ curves is presented in Appendix C. No qualitative differences have been observed between the $F(z)$ calculated with different orientations of the nanotip.

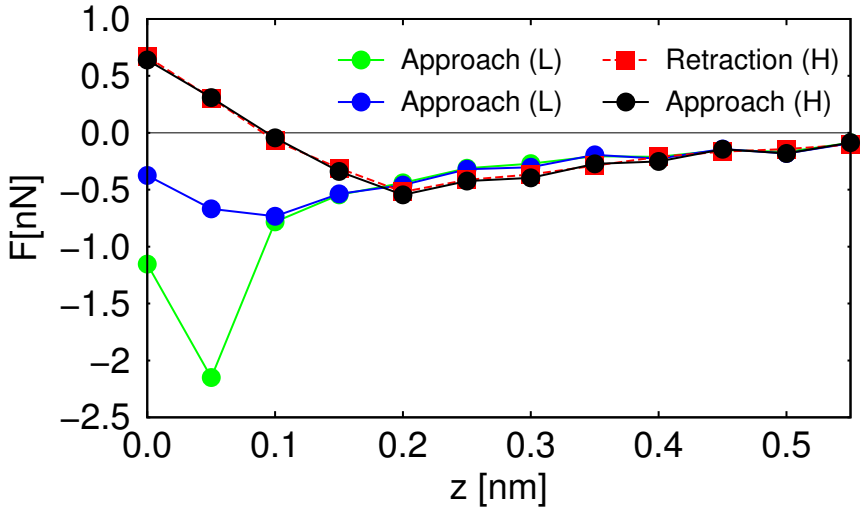

Figure 8.5: $F(z)$ curves at the H region (approach and retraction) and at the Hcp-Top L region (only approach). Of the two curves relative to the L regions, the green (blue) one refers to the geometry in which the tip has been positioned with its apex over the Hcp (Top) site.

theory. When the nanotip is far away from the surface ($z > 0.2$ nm), the interaction is purely attractive, due to the background provided by vdW forces. At the H regions, the attraction increases up to the curve minimum ($z = 0.2$ nm), where the force reaches a maximum modulus value of 0.5 nN. A further approach of the tip to the surface ($z < 0.2$ nm) leads to the onset of the repulsive forces, as evidenced by the abrupt change of sign of the $F(z)$ curve slope. On the other hand, the overall force on the valleys remains attractive (*i.e.*, $F(z) < 0$ nN) over the whole range of tip-surface distances explored. Due to the superstructure corrugation, in this region, the onset of the repulsive forces occurs at a value of z lower than in the hills ($z < 0.1$ nm). The interaction between the tip and the surface is considerably stronger if the tip is positioned over the Hcp site than over the Top site, as evidenced by the sudden increase in the absolute value of $F(z)$ at $z = 0.05$ nm, which indicates the formation of a contact. This is in agreement with previous work, which has identified the Hcp site as the most reactive one in the L regions of the moiré [340]. Nevertheless, this regions is not explored in the experiment. In fact, at the same values of z, the $F(z)$ curve at the H region assumes positive values. This situation is never observed in the experiment. Therefore, at the onset of the repulsive forces over the H region (0.1 nm $< z < 0.2$ nm), the attractive forces in the L region are still increasing. These results qualitatively reproduce the behaviour observed in the experimental $F(z)$ curves.

The relationship between the calculated $F(z)$ curves and the deformation of the H regions can be better understood by considering the ground-state geometries at the different points of the

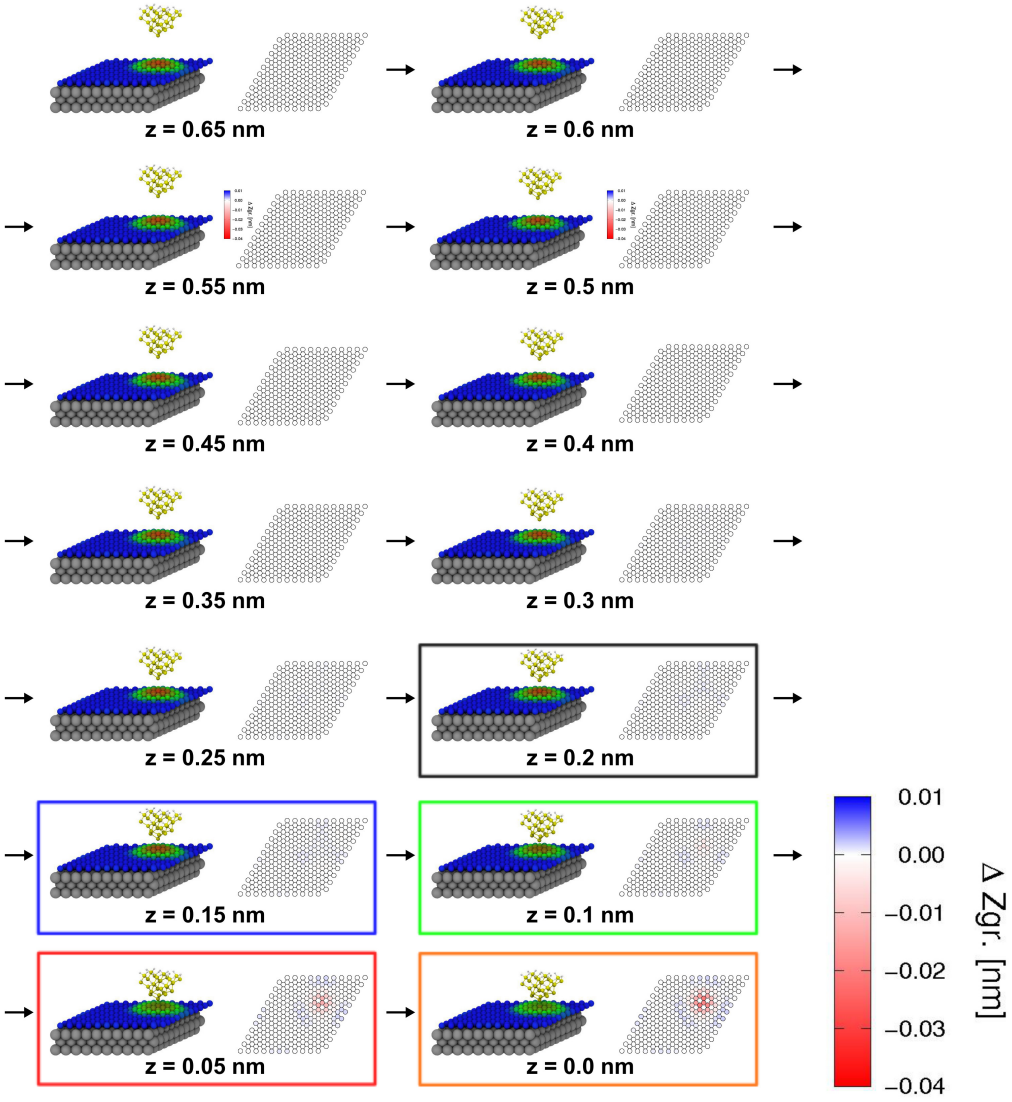

Figure 8.6: Ground state geometries of the points of the $F(z)$ curve calculated for the nanotip approaching the H region of *gr.*/Ru. (black in Fig. 8.5). For each point, the left panel shows the 3D model of the ground state geometry, whereas the right panel shows the vertical deformation $\Delta z_{gr.}$ of the carbon atoms of the graphene monolayer, relative to the "unperturbed" geometry at $z = 0.65$ nm. Ruthenium, silicon, and hydrogen atoms are represented in silver, yellow, and white, respectively. C atoms of the graphene monolayer are shown in different colors depending on their height (blue: lower; red: higher). The coloured panels highlight the geometries which are considered in Fig. 8.7

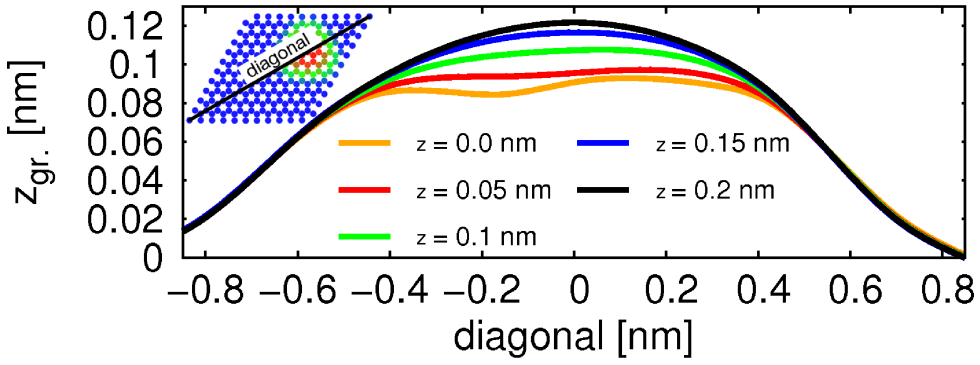

Figure 8.7: Profiles of the graphene hill for the geometries shown in Fig. (8.6) (Z $\leq$ 0.2 nm) along the moiré unit cell diagonal. The zero on the x-axis is set at the central atom of the graphene dome. Each color is relative to a different point of the $F(z)$ curve (compare with the colors in Fig. (8.6)).

$F(z)$ curve (see Fig. 8.6). Up to the curve minimum (z = 0.2 nm), the shape of the H region is hardly affected by the presence of the nanotip. However, after the onset of the repulsive forces, the contribution of the repulsive forces becomes more and more important, and the H region starts to deform under the nanotip compression, reaching a maximum vertical deformation of 35 pm at z = 0 nm. Figure 8.7 shows the profiles of the H region of the ground state geometries at $z \leq$ 0.2 nm. It can be seen that when the deformation is modest, 0.1 nm $\leq z \leq$ 0.2nm, the H region maintains its symmetric character, but, when the deformation becomes larger, it becomes strongly asymmetric, as a consequence of the asymmetry geometry of the nanotip. Finally, when the nanotip is retracted back to its initial position, the H region recovers its initial shape, moving backward along the steps followed during the approach. This latter observation, reflected in the absence of a hysteresis loop in the overall process (the approach and retraction $F(z)$ curves at the H region overlap one with each other), confirms the reversibility of the indentation process.

From a linear fit of the $z <$ 0.2 nm part of the $F(z)$ curve calculated for the tip approaching the H regions, a force gradient k = 7.6$\pm$1 N/m is estimated for the tip-graphene system. This values refers to the entire tip-sample system, *i.e.*, it results from the deformation of the sample, the deformation of the tip, and their mutual interaction. Therefore, it cannot be used to estimate the elastic constant of the H regions of *gr.*/Ru. In order to obtain a proper estimation of the latter quantity, a second set of DFT calculations have been performed. In these calculations, the tip has been removed, and the graphene has been deformed artificially, by constraining the position of the central and highest atom of the graphene H region (having an initial position z_0) and displacing it stepwise of a quantity z - z_0 toward the ruthenium surface. At each step, the graphene and the Ru(0001) topmost layer have been relaxed. This procedure is equivalent to applying point-like load at the center of the graphene hill. The range of displacements considered (0 nm $\leq z$ - $z_0 \leq$ 0.033 nm) is similar to that obtained with the simulations that include the

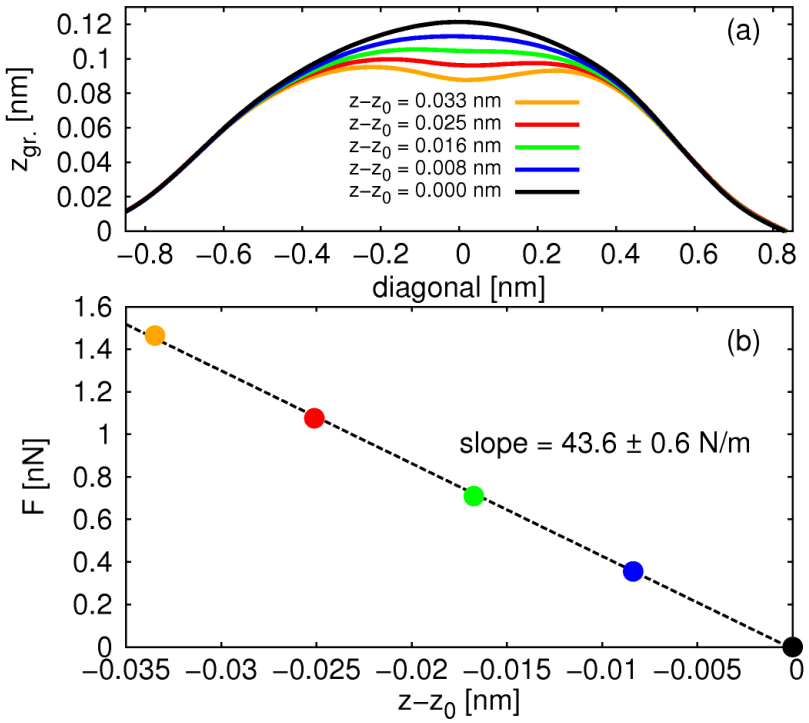

Figure 8.8: (a) Profiles of the artificially deformed graphene hill along the simulation cell diagonal. The zero on the x-axis is set at the central atom of the graphene ripple. (b) Force on the artificially displaced atom of the H region of *gr.*/Ru as a function of z - z_0. The different colors are relative to different values of z - z_0 (same colors in panels a and b). The dashed line is a linear fit to the data to extract the value of the slope.

tip (see Fig. 8.8 (a)). Figure 8.8 (b) shows a plot of the force normal to the surface acting on the atom that has been displaced artificially, as a function of its displacement z - z_0. The force increases linearly with the atom displacement z - z_0. From a fit of these data, a value of k = 43.6 ± 0.5 N/m has been extracted.

Therefore, the simulation of the indentation of the H regions of the *gr.*/Ru moiré by a probing nanotip confirms that the inversion of topographical contrast at different frequency shifts Δf, observed in the NC-AFM measurements performed on *gr.*/Ru, can be associated with the mechanical deformation of such graphene elevations. In addition, theory reproduces qualitatively the absence of an hysteresis loop observed in the experimental $F(z)$ curves, thus verifying the reversibility of the induced mechanical deformation. Consequently, through the combined use of NC-AFM measurements and DFT calculation, the elastic behaviour of the H regions of *gr.*/Ru, which are similar to self-suspended graphene membranes formed by ∼100 atoms, has been demontrated.

9 Magnetic properties of organic electron acceptors deposited on graphene on Ru(0001)

The adsorption of the molecular electron accpetor 7,7′,8,8′-tetracyanoquinodimethane (TCNQ) on the surface of epitaxial graphene on ruthenium is investigated, using a combination of density functional theory calculations and scanning tunnelling microscopy experiments. In Section 9.1 the adsorption of a single molecule on the low regions of the graphene moiré, is considered, and it is shown how each molecule develop a sizeable magnetic moment upon adsorption. The dimer is studied in Section 9.2 as the simplest example of molecular oligomer, and it is evidence is provided that the two coupled molecules adsorbed on the gr./Ru *surface exhibit an open-shell ground state. In Section 9.3, the properties of the full molecular monolayer on* gr./Ru *are investigated. Density functional theory calculations suggest that the full monolayer may exhibit a magnetically ordered open-shell ground state, which is visualized in real-space using spin-polarized scanning tunnelling microscopy.*

The results presented have been published in:

- "Long-range magnetic order in a purely organic 2D layer adsorbed on epitaxial graphene" M. Garnica, D. Stradi *et al.*, *Nature Physics*, 9, 368 (2013)

9.1 TCNQ monomers adsorbed on graphene on Ru(0001) as isolated magnetic impurities

Because of its high electron affinity (1^{st} EA) estimated to be about 3 eV [153, 154], the 7,7′,8,8′ - tetracyanoquinodimethane (TCNQ) molecule [136] is commonly regarded as a prototypical molecular electron acceptor. Its acceptor functionality is due to the presence, in its molecular structure, of four peripheral electron-withdrawing cyano groups, which surround a central hexagonal carbon ring. The Lewis structures of the neutral, singly charged (radical anion) and doubly charged (anion) TCNQ are shown in Fig. 9.1. In the neutral molecule, the hexagonal ring is not aromatic and the molecular conformation is planar and rigid, due to the alternation of multiple and single bonds (*para*-quinoid character). Upon electron addition, the central ring becomes aromatic, whereas the negative charges localize mainly on the electronegative cyano groups. Consequently, the alternation of double and single bonds present in the neutral molecule

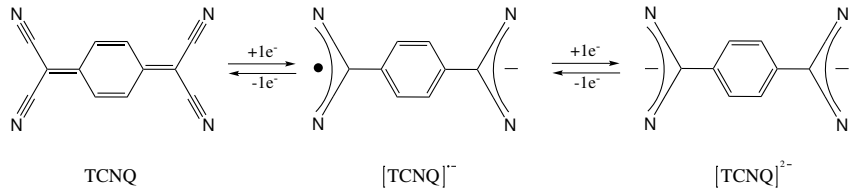

Figure 9.1: Lewis structures of neutral TCNQ (left panel), singly charged TCNQ radical anion (central panel) and doubly charged TCNQ anion (right panel).

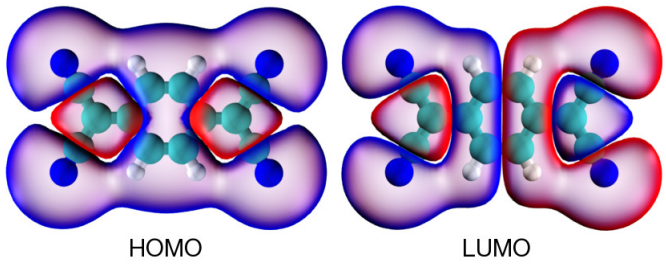

Figure 9.2: Highest Occupied Molecular Orbital (HOMO, left panel) and Lowest Unoccupied Molecular Orbital (LUMO, right panel) of neutral TCNQ. The positive and negative sign of the wavefunction is indicated in blue and red, respectively. Nitrogen, carbon and hydrogen atoms are printed in blue, cyan and white, respectively.

is lost, and the conformational flexibility is strongly enhanced.

TCNQ has received particular attention in the context of molecular electronics because it is one of the two components of the prototype of all organic charge-transfer salts, which is formed by regular 1D stacks of the Tetrathiofulvalene (TTF) and TCNQ molecules [155, 341, 342, 343]. In the molecular solid, each TTF molecule donates, on average, 0.6 electrons to each TCNQ. The electron transfer occurs from the *highest occupied molecular orbital* (HOMO) of TTF to the *lowest unoccupied molecular orbital* (LUMO) of TCNQ, which splits in a *singly occupied molecular orbital* (SOMO) and a *singly unoccupied molecular orbital* (SUMO). Therefore, in the TTF/TCNQ salt, TCNQ is a radical anion [344]. The electrons transferred to the SUMO can hop easily from along the TCNQ molecules in the stacking direction (c axis of the TTF/TCNQ unit cell), while hopping in the direction normal to the stacking direction is hindered by the small overlap between the electronic densities of TCNQ and TTF. For these reasons, the TTF/TCNQ salt exhibit, at room temperature, high conductivities in the c axis direction, and therefore is commonly referred to as an "organic metal". Similarly to the HOMO, the LUMO of TCNQ (see Fig. 9.2) is formed by the linear combination of the $2p_z$ orbitals of the carbon and nitrogen atoms. This explains why the addition of electrons to the neutral molecule lead to a change in the character of its π electronic structure and increases the conformational flexibility [152].

The interface between TCNQ molecules and metallic surfaces has also been widely investigated. The strength of the molecule-surface interaction and the extent of the charge transfer between the molecule and the surface have been found to be strongly dependent on the characteristics of the underlying substrate. For example, on Au(111), TCNQ has been found to be essentially physisorbed and neutral [113][1]. On this surface, charged TCNQ species have been achieved only in the case of mixed TTF/TCNQ monolayers with 1:1 stoichiometry [345]. In this case, the only role of the surface is to confine the molecules on a 2D plane, whereas the physisorbed TCNQ molecules acquire a charge of $\sim$1 e^- only as a consequence of the charge transfer from the TTF molecule. Conversely, on more reactive surfaces such as Cu(100) [112], a large amount of electronic charge ($\sim$1.4 e^-, as calculated from DFT) is transferred from the surface to the molecule. This strongly enhances the molecular flexibility out-of-plane, and permits to the cyano groups to bind directly to the copper atoms of the surface. Consequently, the ground state geometry of TCNQ on reactive surfaces is strongly bent [112]. In this case, the molecular electronic states are strongly mixed with the electronic bands of the metal, as evidenced from the fact that it is impossible to achieve intramolecular resolution in the STM images [112].

In this section, the adsorption of TCNQ molecules on *gr.*/Ru will be discussed. As it will be shown, the properties of the resulting system are very different from the case of TCNQ adsorbed on metal surfaces. This is so because graphene adds important functionalities to Ru(0001). The graphene monolayer passivates the highly reactive Ru(0001) surface, thus avoiding the formation of covalent molecule-surface bonds, and decoupling efficiently the molecular states from those of the metal [128]. At the same time, the transfer of one entire electron from the surface to the molecule is made possible by the fact that the π-system of graphene is heavily n-doped by the underlying Ru(0001) substrate [89, 326]. Due to the weak coupling of the molecular states with the metallic substrate, the electron transferred remains considerably localized on the molecule. Consequently, isolated TCNQ radicals can be created by deposition of neutral TCNQ molecules on *gr.*/Ru.

Computational details

To characterize the adsorption of isolated TCNQ molecules on graphene/Ru(0001), two different models have been employed to describe the *gr.*/Ru surface. The first model is a three-layers 11×11/10×10 lattice-mismatched unit cell, optimized at the DFT+D2/PBE level of theory, which has been already described in Chapter 6. Using this model, the geometries have been optimized at the DFT+D2/PBE level of theory until forces were lower than 0.05 eV/Å. During geometry optimization of the TCNQ molecules on *gr.*/Ru, only the molecular degrees of freedom have been allowed to relax. The second models are formed by a 6×6 lattice-matched *gr.*/Ru unit cells, which have been constructed by multiplying the corresponding three-layer lattice-matched 1×1 unit cell in the *xy*-plane, which have been also described in Chapter 6. To model the two L

[1] A charge transfer of only 0.3 e^- has been estimated based on STS spectroscopy measurements of the shift of the Au(111) surface state [113].

regions of the *gr.*/Ru moiré, both $6 \times 6 - (Fcc - Top)$ and $6 \times 6 - (Hcp - Top)$ lattice-matched unit cells have been considered. The graphene-Ru(0001) distance has been set to 2.2, which is similar to the graphene-Ru(0001) distance calculated at the L regions of the 11×11/10×10 unit cell using DFT+D2/PBE. The 6×6 periodicity has been chosen because it is the minimal periodicity that can be used to simulate the adsorption of an isolated TCNQ molecule, and to ensure at the same time that the K-point in the 1×1 graphene unit cell is folded exactly at the Γ-point. In these models, the molecule has been positioned at 3 Å above the surface, and its geometry has been kept fixed to that of the neutral molecule in the gas-phase[1].

For the calculations of TCNQ adsorbed on both models, computational settings similar to those used in Section 6 have been employed. However, in the present case, a Gaussian smearing of 0.1 eV has been used. By performing additional optimizations using the Methfessel-Paxton method, it has been checked that this choice does not affects the calculated ground state geometries. STM images have been simulated using the Tersoff-Hamann approximation[2]. For the calculations performed using the 6×6 lattice matched unit cells, the 1^{st} BZ has been sampled with a 3×3×1 Monkhorst-Pack grid of k-points. Charge transfer has been evaluated using Bader topological analysis of the electronic charge density. Overall, spin-unpolarized DFT has been used (structures, total energies, charge transfer and STM simulations), spin-polarized DFT has been used only for the electronic structure analysis (PDOS, spin densities, and band structures). The electronic density redistribution ($\Delta\rho$) induced by the adsorption of the molecule on *gr.*/Ru has been calculated as the difference between the ground state electronic density of the full molecule-substrate system, and the reference densities of the isolated molecule and substrate, in the same geometry:

$$\Delta\rho = \rho(\mathbf{r})_{TCNQ-gr./Ru} - \left(\rho(\mathbf{r})_{TCNQ} + \rho(\mathbf{r})_{gr./Ru}\right) \tag{9.1}$$

Gas-phase calculations for the neutral, singly charged and doubly charged TCNQ molecule have been performed using `Gaussian09` [346]. A 6-311G(d,p)++ basis set has been used on carbon, nitrogen and hydrogen atoms. The PBE [205] functional has been used to describe the electronic exchange correlation energy. Adiabatic EAs have been calculated using the ΔSCF method [199]:

$$EA(n \rightarrow n+1) = E(n+1) - E(n) \tag{9.2}$$

where n is the number of the electrons and $E(n)$ is the ground state energy of the molecule with n electrons.

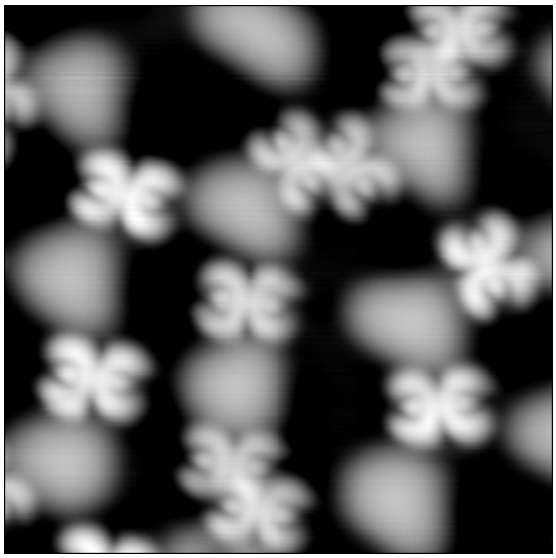

Figure 9.3: 8 nm^2 × 8 nm^2 STM topographical image of TCNQ adsorbed on *gr.*/Ru at low coverage, measured at 4.6 K. Parameters: V_{bias} = - 0.8 V, I_{tunnel} = 50 pA.

Discussion

Fig. 9.3 shows a tipical STM image, measured at cryogenic temperature, of TCNQ molecules on *gr.*/Ru at low coverage[1]. It can be seen that the molecules adsorb exclusively on the L regions of the *gr.*/Ru moiré, where the surface potential is ∼0.25 eV lower [95]. Moreover, they are relatively disordered on the surface, which indicates that there is not an evident preference for any particular adsorption configuration in the L regions of the *gr.*/Ru moiré. A significant part of the molecules tends to remain isolated, whereas other molecules tend to cluster. This latter behaviour will be discussed in the next section, while here the focus will be on the isolated species. A first hint that the molecules are physisorbed on the surface comes from the fact that they can easily be displaced with the STM, if too intense currents - of the order of pA - are used to acquire the images. As the experiments do not give any clear indication for the preferred adsorption site of TCNQ on the L regions of the *gr.*/Ru moiré, several adsorption configurations have been calculated. A single TCNQ molecule has been placed at the center of the two L regions (Fcc-Top and Hcp-Top configurations) and in between the two L regions (Bridge configuration). Two different molecular orientations have been considered, in which the angle between the long axis of the molecule and the long diagonal of the *gr.*/Ru unit cell is either 0° or 30°. Fig. 9.4 shows the optimized geometries of the different molecular configurations considered, and their corresponding adsorption energies. TCNQ is found to adsorb with a large adsorption energy -

[1]This molecule-surface distance and molecular configuration is similar to that obtained by optimizing the molecular geometry on the 11×11/10×10 *gr.*/Ru unit cell.

[2]See Section 5.1

[1]The molecules have been deposited at room temperature and then imaged with the STM at 4.6 K.

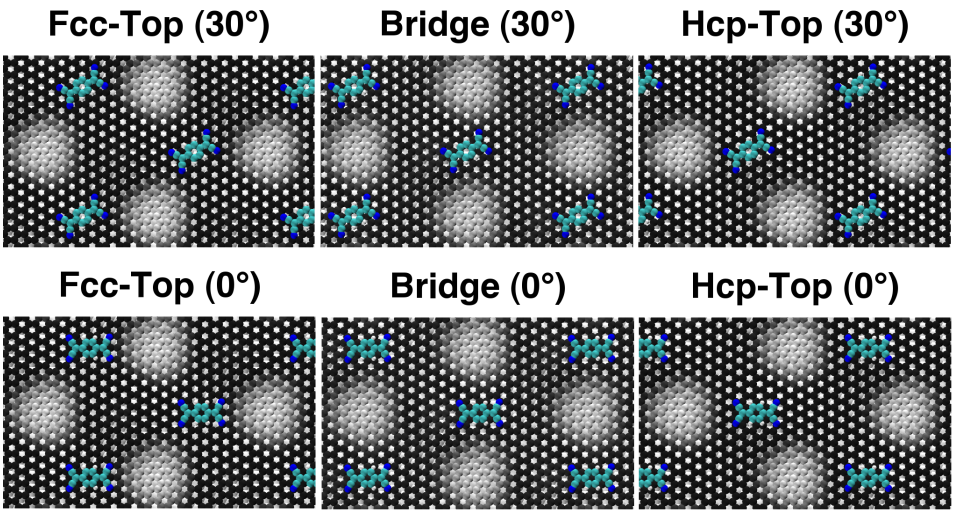

	Fcc-Top	**Bridge**	**Hcp-Top**
30°	-2.38	-2.45	2.48
0°	-2.37	-2.47	-2.53

Figure 9.4: Top view of the adsorption geometries considered for the study of an isolated TCNQ molecule adsorbed on *gr.*/Ru. The table shows the corresponding adsorption energies in electronvolts (eV). Nitrogen, carbon and hydrogen atom of the TCNQ molecule are printed in blue, cyan and white, respectively. The carbon atoms of the graphene monolayer are printed in different colors depending on their height (dark: low; grey: high). Ru atoms are printed in white.

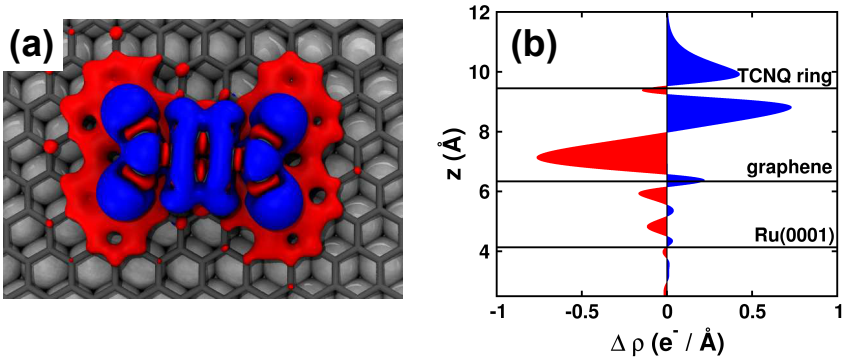

Figure 9.5: (a) Isocountour surfaces (isocountour value = 0.001 electrons /Å^3) of the electronic density redistribution upon adsorption of TCNQ on *gr.*/Ru. Blue and red areas indicate electron density accumulation and depletion. (b) Electronic density redistribution integrated in the *xy*-plane.

between 2.37 eV and 2.53 eV, depending on the particular adsorption site and configuration. However, the energy difference between different configurations in each low area of the moiré is less than 50 meV, in agreement with the experimental observation that there is no preferential adsorption configuration for isolated molecules within the lower areas of the moiré.

Despite the high adsorption energy, there are two important indications that the molecules are not bound covalently to the substrate. The first one is the molecule-surface distance, which is ∼3 Å, in line with that reported for other aromatic molecules physisorbed on noble metal surfaces [278, 282]. The second one is the fact that the molecular geometry lies planar over the surface. This latter observations is in striking difference with the strongly distorted geometry found when TCNQ is strongly bound to a reactive surface, such as Cu(100) [112]. Nevertheless, the molecular resonance observed at negative bias voltages (Fig. 9.3) shows clearly the presence of a node which crosses the molecular long axis. This feature is absent in the HOMO of the neutral molecule, but it is present in the LUMO (see Fig. 9.2). This suggests that the LUMO of the individual TCNQ molecules adsorbed on *gr.*/Ru has been occupied by electrons.

In agreement with this experimental observation, the calculations predict that the molecule acquire a substantial charge form the surface[1]. According to Bader analysis of the electronic density, the charge transfer is 0.99 electrons. The analysis of the electronic density redistribution upon adsorption (see Fig. 9.5) supports the idea that the electron is transferred to the LUMO of the neutral TCNQ molecule. In fact, $\Delta\rho$ is positive just above and below the molecular plane (Fig. 9.5 (b)) and the positive fraction of $\Delta\rho$ on the molecule has a shape which resembles that of the LUMO (Fig. 9.5 (a)) of the neutral TCNQ.

[1]From now on, unless otherwise stated, the only geometry that will be discussed for TCNQ adsorbed on 11×11/10×10 *gr.*/Ru is the Bridge(30°) configuration. The qualitative results are independent on the particular adsorption configuration. The Bridge(30°) has been taken as a representative configuration because in the experiment, the largest fraction of the molecule are found to adsorb over the Bridge site of the graphene moiré.

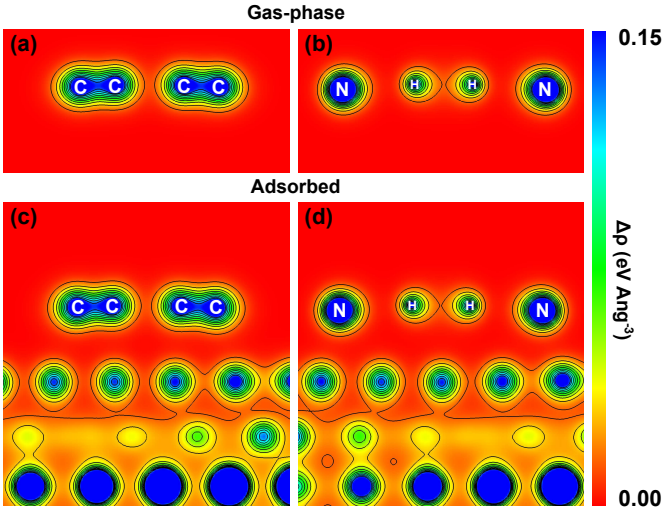

Figure 9.6: (a-b) Charge distribution for a free-standing, charged TCNQ molecule, at the same positions. (c-d) 2D cuts of the electronic charge density $\rho(\mathbf{r})$ in the direction perpendicular to the xy-plane, at two different positions parallel to the molecule long axis.

Nevertheless, this strong charge transfer to the molecule is not accompanied by the formation of covalent bonds with graphene. An analysis of the total electronic density shows that there is no accumulation of electronic density between the molecule and the surface (Fig. 9.6 (c-d)), and that the electronic density of the adsorbed molecule is essentially identical to that of the singly charged gas-phase molecule with the same geometry (Fig. 9.6 (a-b)). These two facts clearly indicate the absence of any strong molecule-surface covalent bond.

Using simple arguments it is possible to obtain a qualitative understanding of why the molecule is not doubly charged upon adsorption. In the case of the gas-phase, the addition of one electron to the TCNQ molecule is a favourable process, because the calculated 1^{st} EA of neutral TCNQ is as high as -3.67 eV[1]. On the contrary, the formation of the doubly charged anion in gas-phase is a disfavoured process, the calculated 1^{st} EA of the radical anion being +0.35 eV. Both values lie above the work function of *gr.*/Ru, $\Phi_{gr./\mathrm{Ru}}$ = -3.9 eV [95]. However, the adsorption of the molecule on a conductive substrate, such as that of *gr.*/Ru, shifts the values of the two EAs, due to polarization effects. In the limit of a weak interaction between the molecule and the surface (i.e., when no strong covalent bonding occurs), the leading correction term to such change can be estimated using a classical image charge model, *i.e.*, by considering the interaction of a point-like charge with a flat conducting surface:

$$E_{image} = -\frac{1}{4(z - z_0)}. \tag{9.3}$$

[1]This value agrees reasonably whit the value of -3.22 eV reported in the literature using multiconfigurational quantum chemistry methods [151]

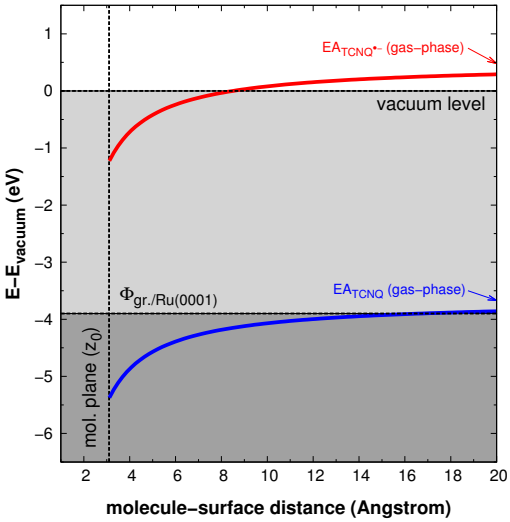

Figure 9.7: Change in the electron affinities of the neutral TCNQ (blue line) and TCNQ radical anion (red line) upon adsorption on *gr.*/Ru. The image plane has been set at z_{image} = 1.0 Å. Dark gray, light gray and white indicated the *gr.*/Ru occupied electronic structure, the *gr.*/Ru empty electronic structure, and the vacuum, respectively. The values of the electron affinities of the TCNQ and TCNQ radical anion are indicated by the blue and red arrows on the right side of the image.

In Eq. 9.3, z and z_0 are the position of the molecular center of mass, and the position of the image plane, respectively. The values of the two EAs, corrected to account for the interaction with the conducting surface, are shown in Fig. 9.7, where it can be seen that the proximity of the surface moves the 1^{st} EA of the neutral molecule below the Fermi energy of *gr.*/Ru. As a consequence, one electron is transferred from the surface to the molecule. On the contrary, the shift induced by image-charge effects is not sufficient to bring the EA of the radical anion below the Fermi energy of *gr.*/Ru, thus preventing the spontaneous formation of the doubly charged anion.

The fact that the LUMO of TCNQ is only partially occupied is corroborated by the comparison between the experimental and the simulated STS data (see Fig. 9.8). At high negative bias voltages (V_{bias} = - 2.0 V in the experiment) a molecular resonance appears, which does not present any central node. By comparing the shape of this resonance with the gas-phase orbitals shown in Fig. 9.2, it is possible to assign it to the HOMO of the neutral TCNQ molecule. On the other hand, a second molecular resonance which has the same shape of the gas-phase LUMO of the neutral TCNQ molecule can be identified both at negative (V_{bias} = - 0.8 V in the experiment) and positive bias voltages (V_{bias} = + 1.0 V in the experiment).

From the previous analysis, it can be concluded that the main role of graphene is that of allowing the charging of the molecule by one electron, and to maintain the molecule decoupled from the substrate. This is the ideal condition for the transferred electron to remain localized

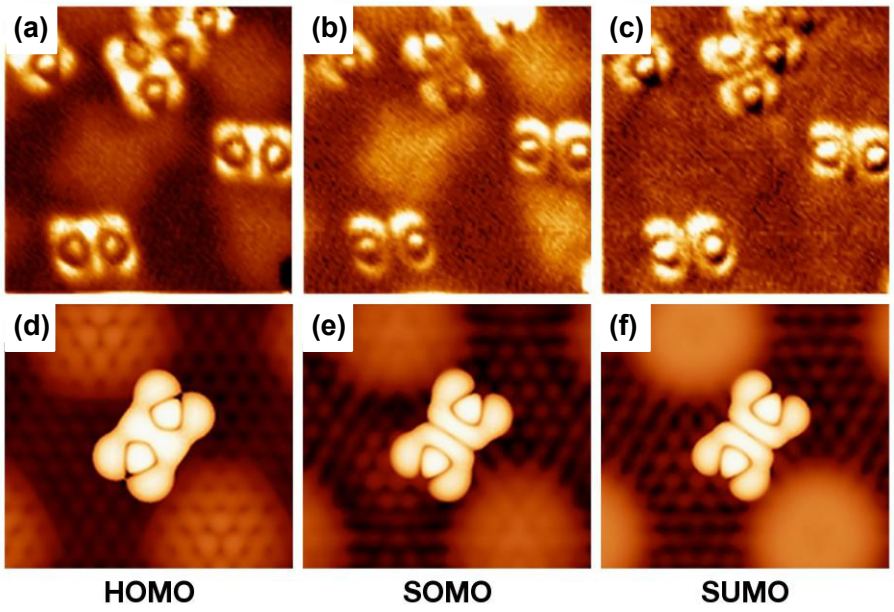

Figure 9.8: Spatial distribution of the molecular frontier orbitals for TCNQ adsorbed on graphene/Ru(0001). (a-c) Spatially resolved dI/dV maps of individual TCNQ molecules adsorbed on *gr.*/Ru recorded at V_{bias} = - 2 V (a), V_{bias} = - 0.8 V (b) and V_{bias} = + 1.0 V (c). (d-f) The corresponding simulated dI/dV maps are shown in panels. To simulate the dI/dV maps, the DOS has been integrated in the energy range [- 1.2 eV : - 0.8 eV] (d), [- 0.3 eV : 0.0 eV] (e) and [0.0 eV : +0.3 eV] (f).

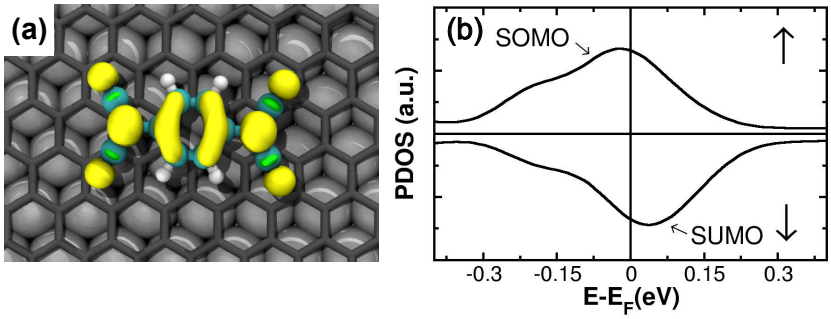

Figure 9.9: (a) Spin-density distribution (isocontour value = 7.5×10^{-4} electrons /Å^3) for a single TCNQ molecule adsorbed on *gr.*/Ru. Yellow and green indicate positive and negative spin densities, respectively. (b) Spin-polarized PDOS over s and p orbitals for the same molecule.

on the molecule, thus transforming neutral TCNQ into the radical anion. This hypothesis is confirmed by spin-polarized DFT calculations, which reveals a net magnetic moment M = 0.4 μ_B. The spin-density associated with this magnetic moment (see Fig. 9.9 (a)) is completely localized on the molecule, and has a central node which resemble that of the LUMO of the neutral TCNQ. Accordingly, the spin-up and spin-down components of the projected DOS on the TCNQ *s* and *p* orbitals (see Fig. 9.9 (b)) do not have the same ratio of filling, and are splitted in two peaks that can be associated with the SOMO and the SUMO of the TCNQ radical anion. This confirms that the electron transferred to the TCNQ molecule remains essentially unpaired. Experimentally, this theoretical prediction is verified by STS. At $V_{bias} = 0.0$ V, a sharp resonance appears in the STS spectra, which can be associated to the formation of a Kondo resonance[1] between the unpaired electron localized on the molecule, and the conduction electrons of the underlying metal (see Fig. 9.10).

A subsequent analysis reveals that the interaction between TCNQ and *gr.*/Ru is not identical across the L regions of the *gr.*/Ru moiré. Indeed, the different contrast observed in the experimental and simulated STM topographical images at the two L regions (see Fig. 6.9 in Chapter 6) indicates that they exhibit a different electronic structure, as a consequence of the different configuration of the graphene atoms over the Ru(0001) surface. This idea is further supported by the fact that different trends of the conductance, as a function of the tip height over the surface, have been measured with the STM at the two L regions of the graphene moiré [340]. In addition, the observation of the Kondo effect indicates that the molecule interacts, although very weakly, with the underlying metal. This may be also inferred from the fact that the peaks in the projected DOS on the atomic orbitals of the molecule exhibit a small, but non-negligible broadened structure. Experimentally, this should be reflected in a variation of the spectral feature at V_{bias} associated with the Kondo scenario, for molecules adsorbed on different regions of

[1] see Appendix A.3

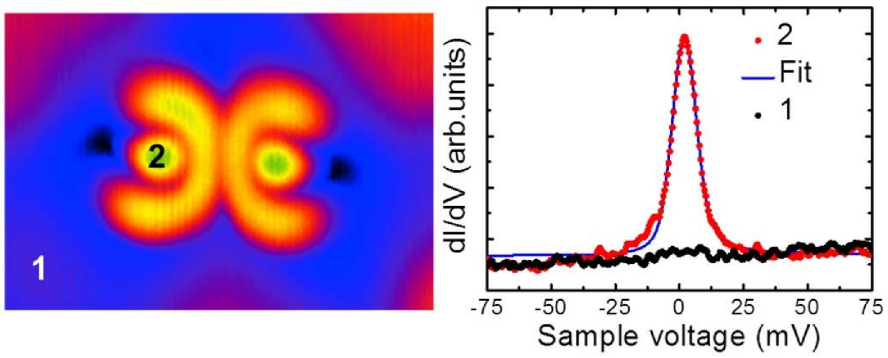

Figure 9.10: Kondo resonance measured by STS over TCNQ on *gr.*/Ru. (1,black) dI/dV spectra above the molecular SOMO resonance and (2,red) dI/dV spectra above *gr.*/Ru. The image on the left is a topography that identifies the sites over which the dI/dV spectra have been measured. The spectra over the molecule has been fitted with a Fano profile, with parameters $q = 40$ and $\Gamma = 10$ meV, which gives an estimation for the Kondo temperature of ∼60 K.

the *gr.*/Ru moiré.

In agreement with these considerations, the magnetic moment is found to vary across the L regions of the moiré, with values M = 1.0 μ_B, M = 0.4 μ_B, and M = 0.2 μ_B, for adsorption sites Fcc-Top or Hcp-Top and Bridge (region in between Fcc-Top and Hcp-Top sites), respectively[1]. The increased coupling with the surface leads to a decrease of the magnetic moment, as evidenced by the fact that lower values of the magnetic moment are associated with broader projected DOS (see Fig. 9.11). This indicates that the coupling of the molecular states with the surface varies across the different L regions, and that this coupling affects the magnetic properties of the individual TCNQ molecule.

To understand the effect of the molecule-substrate coupling on the electronic structure of TCNQ, the interaction between the molecule and two 6×6 lattice-matched models, representative of the two L regions of the *gr.*/Ru moiré, has been studied (see Fig. 9.12). In a first step, the electronic structure of the surfaces in the absence of the molecule has been analyzed. The different configuration of the graphene atoms over Ru(0001) has important consequences on the electronic structure close to the Fermi level. In fact, the bands of the $6 \times 6 - (Fcc - Top)$ model (Fig. 9.12 (e)) are considerably different from those of the $6 \times 6 - (Hcp - Top)$ model (Fig. 9.12 (g)). In particular, the states which has the most relevant weight on the graphene atoms at the Γ-point lie at different energies depending on the configuration of graphene, *i.e.*, at E-E_F = -0.3 eV in the $6 \times 6 - (Fcc - Top)$, and at E-E_F = 0.02 eV in the $6 \times 6 - (Hcp - Top)$ model. The observed complex structure of the electronic bands with relevant weight on the graphene is the results of the folding of the bands associated with this states, which lie at the K-point

[1]For the 0° orientation, a similar trend is observed, with a variation between M = 0.9 μ_B (Fcc-Top) and M = 0.1 μ_B (Hcp-Top)

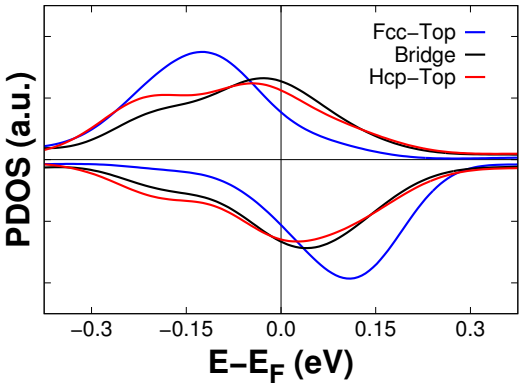

Figure 9.11: Spin-polarized PDOS over s and p orbitals for the TCNQ molecule adsorbed on the 11×11/10×10 *gr.*/Ru unit cell with Fcc-Top(30°), Bridge(30°), and Hcp-Top(30°) configurations (see Fig. (9.4)).

in the corresponding 1×1 models. Thus, the character of the relevant bands in each model should be similar to that of the state at the Γ-point. However, the two states are considerably different. The state of the $6\times6-(Fcc-Top)$ model with energy E-E_F = -0.3 eV at the Γ-point penetrates considerably into the Ru(0001) surface (see Fig. 9.12 (i)). Conversely, the state of the $6\times6-(Hcp-Top)$ with energy E-E_F = 0.02 eV at Γ is strongly confined at the surface (see Fig. 9.12 (k)). Its probability density at the graphene layer is considerably larger than that of the state of the $6\times6-(Fcc-Top)$ model, and after the topmost Ru(0001) it decays very rapidly. This clarifies why the contrast of the two L regions of the *gr.*/Ru is different in the STM images. The probability density at the surface is larger in the Hcp-Top region than in the Fcc-Top region. Therefore, the former region appears brighter, whereas the latter region appears darker.

The different character of these electronic states at the surface influences considerably the properties of the adsorbed molecule. For both models, the calculated electron transfer to the molecule is ∼1 electron, *i.e.*, similar to that calculated using the lattice-mismatched model. However, the presence of a finite magnetic moment depends on the model employed. In the Fcc-Top model, the magnetic moment on the molecule is preserved (M = 0.51 μ_B). On the other hand, in the Hcp-Top model, the magnetic moment is completely quenched (M = 0.02 μ_B). This behaviour can be rationalized in terms of the strength of the interaction between the molecular states and the *gr.*/Ru states at the surface. In the $6\times6-(Fcc-Top)$ model, the coupling of TCNQ with the *gr.*/Ru state that extend above the surface is weaker, due to the small probability density of the relevant *gr.*/Ru states. On the other hand, the behaviour is the opposite for TCNQ adsorbed on the $6\times6-(Hcp-Top)$ model, due to the localized character of the relevant *gr.*/Ru state. These results reproduce qualitatively the trend observed in Fig. 9.11.

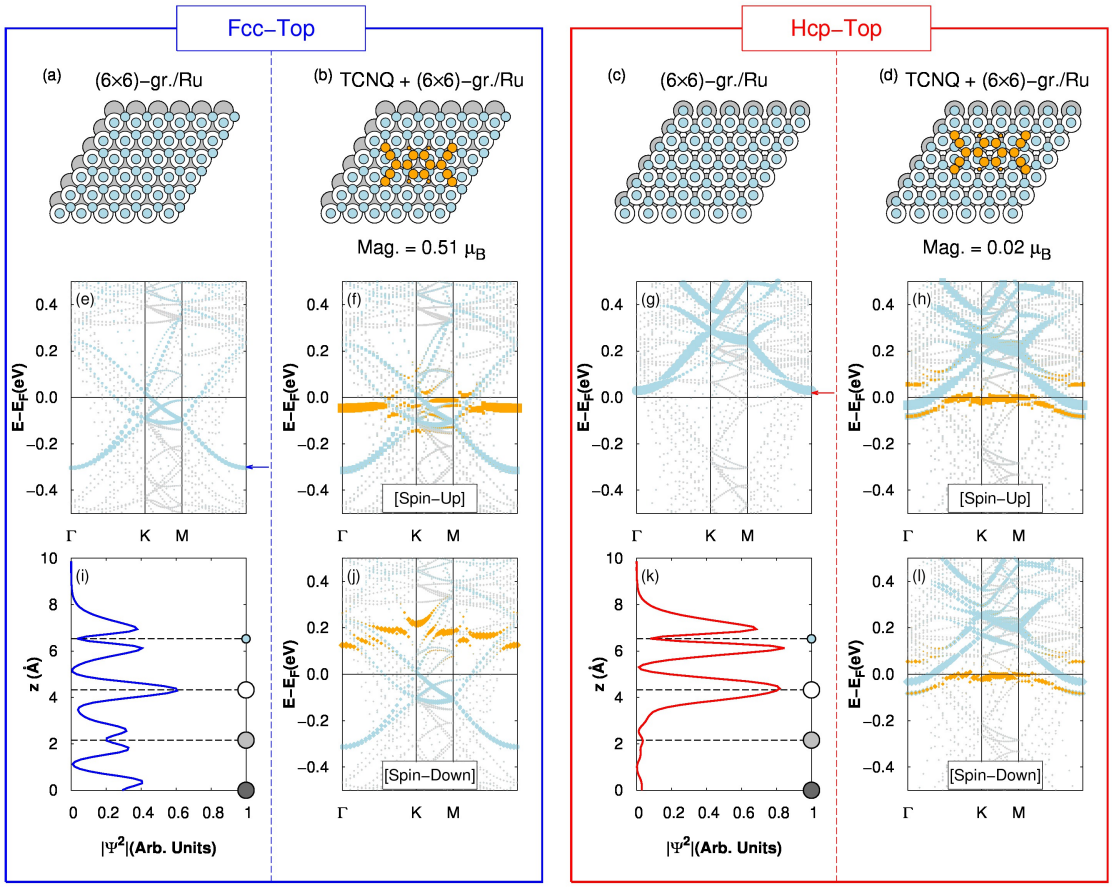

Figure 9.12: (a) Top view geometry of the $6 \times 6 - (Fcc - Top)$ lattice-matched *gr.*/Ru model. (b) Top view of the adsorption geometry of TCNQ on the model shown in (a). (c,d) Same as (a,b), but for the $6 \times 6 - (Hcp - Top)$ model. TCNQ, graphene, topmost Ru(0001) and topmost-1 Ru(0001) atoms are shown in orange, light-blue, white and gray, respectively. (e) Band structure of the $6 \times 6 - (Fcc - Top)$ model along the $\Gamma \rightarrow K \rightarrow M$ path of the 1^{st} Brillouin zone. (g) Same as (e) but for the $6 \times 6 - (Hcp - Top)$ model. (f,j) Spin resolved band structure along the $\Gamma \rightarrow K \rightarrow M$ path for TCNQ adsorbed on the $6 \times 6 - (Fcc - Top)$ model. (h,l) Same as (f,j), but for the $6 \times 6 - (Hcp - Top)$ model. Projections on graphene and TCNQ atoms are shown in light-blue and orange, respectively. (i) Probability density of the state indicated by the blue arrow in (e). (k) Probability density indicated by the red arrow in (g).

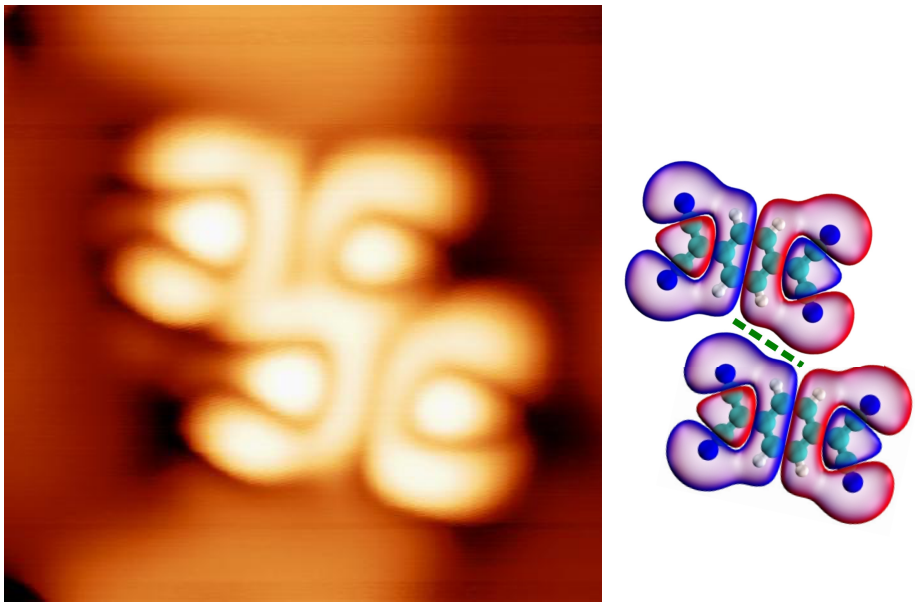

Figure 9.13: Topographic STM image (3×3 nm^2) of a TCNQ dimer on *gr.*/Ru, measured at 4.6 K with the tunneling gap stabilized at I_{tunnel} = 20 pA and V_{bias} = - 0.8 V. The right panel is a scheme of the geometry of a dimer formed by two ideally non-interacting molecules, with the dashed green line indicating where one should expect to find a node for two non-interacting molecules.

However, the interaction of the molecule with the surface in the 6×6 is overestimated, because of the artificial stretch of the graphene layer. For this reason, the magnetic moments for the molecule adsorbed on the two 6×6 lattice matched models are considerably lower than the ones obtained for the molecule adsorbed on the corresponding L regions of the *gr.*/Ru 11×11/10×10 unit cell.

9.2 Interaction between two organic magnetic impurities: TCNQ dimers on graphene on Ru(0001)

As already observed in Fig. 9.3, the deposition of TCNQ on *gr.*/Ru does not lead only to isolated molecules, but also to cluster of molecules. In particular, oligomers of an increasing number of units (up to five units) can be observed on the surface. In the absence of any additional interaction, the adsorbed TCNQ radical anions should repel each other as a consequence of the electrostatic interaction. However, the observation of clustered molecules indicates that there are other intermolecular forces that counterbalance the electrostatic repulsion and tend to stabilize the molecular oligomers on the surface. Indeed, TCNQ radicals are known to be able to form π-stacked dimers [347]. However, theoretical calculations have shown that such dimers are stable only in the presence of counter-ions [348, 349].

Fig. 9.13 shows a close-up of an STM topography taken over a TCNQ dimer. Similarly to the image presented in Fig. 9.3, this image is taken at negative bias voltages, using a value of V_{bias} = - 0.8 V, which corresponds to that used to image the SOMO resonance of the isolated TCNQ molecule. The features of the molecular electronic states observed in the dimer are very similar to those of the isolated molecule. In fact, the shape of the molecular resonance resemble that of the LUMO of the neutral TCNQ. This indicates that, also in this case, the molecules have been charged by deposition on *gr.*/Ru. A more detailed analysis also suggests that the two fragments are indeed interacting. In fact, for two non interacting TCNQ molecules, there should be a nodal plane in between the two molecules, due to the different sign of the SOMO wavefunction. However, no nodes are observed in between the two TCNQ molecules. This fact is unlikely to be related to the finite resolution of the tip, because all the other relevant nodes corresponding to the LUMO of the neutral TCNQ can be perfectly distinguished.

In the following, it will be shown that the analysis of the STM images of isolated TCNQ dimers formed on *gr.*/Ru reveals that such dimers have an open-shell ground state. This is a direct consequence of the degeneracy of the SUMO of the two radical fragments, and of the small, but non-negligible, overlap between their wavefunctions.

Computational details

Calculations for the dimer adsorbed on the three-layers 11×11/10×10 *gr.*/Ru unit cell have been performed using computational settings similar to that employed for the adsorbed monomer. The dimer has been constructed by adding a second molecule to the Bridge (30°) configuration of the isolated molecule. The geometry of the two molecules has been optimized using DFT+D2/PBE. A threshold criterion for the convergence of the forces of 0.05 eV/Å has been used, and the atoms of the surface have been kept frozen during the geometry optimization. Single-points spin-polarized DFT calculations have been performed on the optimized geometry. Here, the charge density redistribution upon adsorption has been calculated by considering the reference densities of the two separate molecules:

$$\Delta\rho = \rho(\mathbf{r})_{TCNQ1-TCNQ2-gr./Ru} - (\rho(\mathbf{r})_{TCNQ1} + \rho(\mathbf{r})_{TCNQ2} + \rho(\mathbf{r})_{substrate}) \tag{9.4}$$

Gas-phase calculations for the doubly charged TCNQ dimer have been performed at the DFT+D2/ PBE level of theory, using a computational set-up similar to that used for the charged monomer. Two electronic configurations have been considered, namely the open-shell triplet and the close-shell singlet. Both configurations can be described by a single Slater determinant. Therefore, spin-contamination is low[1] and the calculated energy differences, even if very small, can be considered reliable. Total energies of the dimer have been calculated on the optimized geometry for each electronic configuration considered.

[1] $< S^2 > = 0.0000$ for the singlet and $< S^2 > = 2.0059$ for the triplet

Discussion

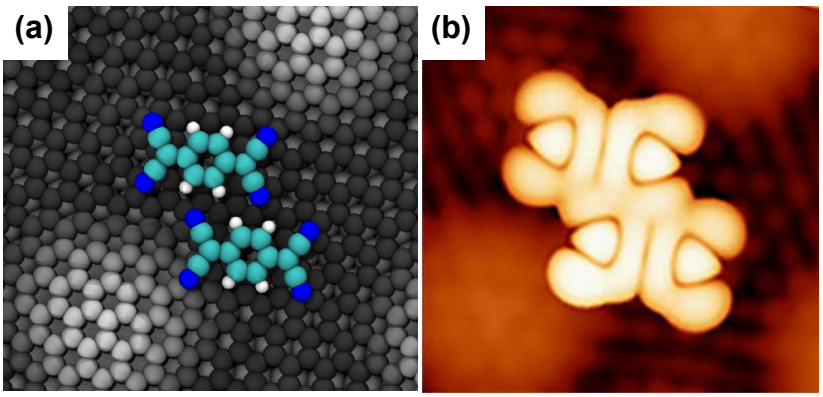

Figure 9.14: (a) Top view of the geometry of TCNQ dimer on *gr.*/Ru. Nitrogen, carbon and hydrogen atoms of the TCNQ molecule are printed in blue, cyan and white, respectively. The carbon atoms of the graphene monolayer are printed in different colors depending on their height (dark: low; grey: high). Ru atoms are printed in white. (b) Simulated STM image at negative bias voltages. To simulate the STM image, the DOS has been integrated in the energy range [- 0.3 eV : - 0.0 eV].

Fig. 9.14 (a) shows the geometry of the optimized TCNQ dimer on *gr.*/Ru. The adsorption energy is calculated to be -2.44 eV / TCNQ molecule, *i.e.*, the dimer is stable when adsorbed on *gr.*/Ru. One of the reasons for this stability is that the cyano groups of one of the TCNQ molecules face the hydrogen atoms belonging to the other one, in a configuration which maximizes the number of possible hydrogen bonds. The adsorption energy is very similar to that calculated for the TCNQ monomer, which is fully consistent with the experimental observation that the TCNQ dimers and monomers coexists on the surface of *gr.*/Ru. The simulated STM image at negative bias voltages (Fig. 9.14 (b)) agrees with the experimental one, and, in particular, the absence of nodal planes between the two molecules is reproduced. This confirms that the calculated geometry is representative of the one observed experimentally, and rules out completely that the features observed in the measured STM images are due to the limited resolution of the STM.

The charge transfer to the dimer is calculated to be 0.99 electrons / TCNQ molecule. Therefore, each molecule gains one electron from the surface. However, the analysis of $\Delta\rho$ (Fig. 9.15), calculated according to Eq. 9.4, indicates that the charge redistribution is not equal to that of the bare sum of the charge redistribution of two isolated molecules. In fact, in the region in between the two molecules, the increase of $\Delta\rho$ is continuous. This further supports the idea that the interaction between the two molecules is not merely electrostatic, and that the transferred electron delocalize across the whole dimer.

Spin-polarized DFT gives a net magnetic moment of M = 1.0 μ_B for the TCNQ dimer adsorbed on *gr.*/Ru. This value doubles that obtained for an isolated TCNQ molecule on *gr.*/Ru.

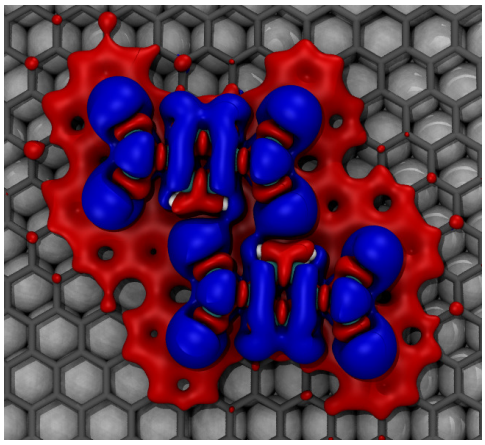

Figure 9.15: Isocountour surfaces (isocountour value = 0.001 electrons /Å^3) of the electronic density redistribution upon adsorption of the TCNQ dimer on *gr.*/Ru. The electronic density redistribution has been calculated according to Eq. 9.4. Blue and red areas indicate electron density accumulation and depletion, respectively.

Also in this case, it can be seen that the substrate has an influence on the magnetization of the molecule, because the spin-density is not distributed equally between the two TCNQ molecules (Fig. 9.16 (a))[1]. Consistently with the presence of a net spin on the TCNQ dimer, the PDOS on the s and p orbitals of the TCNQ dimer indicates that the peak associated with the LUMO in the neutral dimer splits in a spin-up and spin-down components (Fig. 9.16 (b)), in analogy with what occurs for the isolated TCNQ molecule adsorbed on *gr.*/Ru.

Thus, one faces with the problem of how it is possible to have two additional electrons transferred to the TCNQ dimer and, simultaneously, a net spin localized on both molecules. In order to clarify this problem, gas-phase calculations for a doubly charged TCNQ dimer have been performed. Fig. 9.17 shows the orbital energy diagram for the close-shell singlet (M = 0 μ_B) configuration and the open-shell triplet (M = 2 μ_B) configurations of the doubly charged TCNQ dimer. In the close-shell singlet, the HOMO is formed by the anti-symmetric combination of the SOMOs of the two TCNQ radical fragments, while the LUMO is formed by their symmetric combinations. Due to the small overlap between the wavefunctions of the two radical TCNQ fragments, the HOMO and the LUMO of the dimer are extremely close in energy ($\Delta E = 0.01932$ eV). On the other hand, in the open-shell dimer, the α spin-orbital which correspond to the anti-symmetric (SOMO-1) and symmetric (SOMO) combination of the SOMOs of the TCNQ radical fragments are occupied. These two spin-orbitals are also very close in energy ($\Delta E = 0.01769$ eV). Indeed, the open shell triplet is 160 eV more stable than the close shell singlet. Thus, the exchange interaction between the two electrons placed in the SOMO-1 and SOMO orbitals favours the open shell configuration with respect to the close shell configuration, in which the two electrons are placed in the same orbital. This effect, which is very similar to Hund's rule

[1]The second molecule, where the spin density is lower, is pointing towards the Hcp-Top region of the moiré

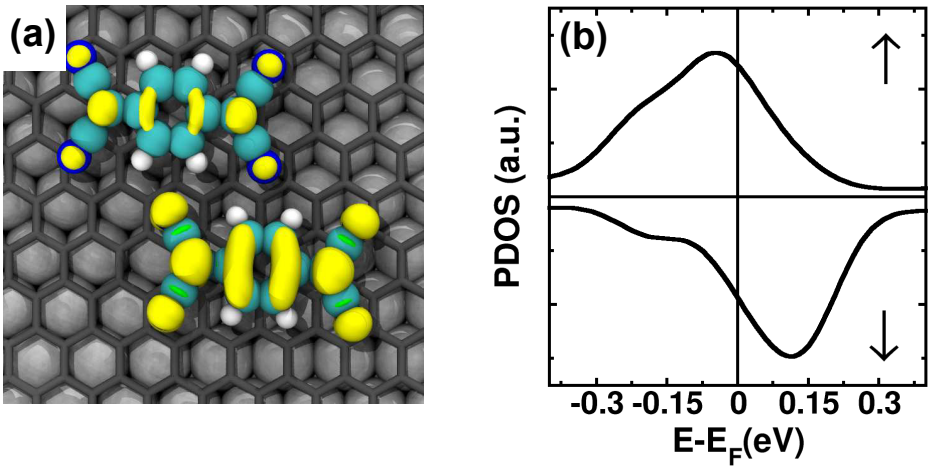

Figure 9.16: (a) Spin-density distribution (isocountour value = 7.5×10^{-4} electrons /Å^3) for a TCNQ dimer adsorbed on *gr.*/Ru. Yellow and green indicate positive and negative spin densities, respectively. (b) Spin-polarized PDOS over s and p orbitals for the same dimer.

in atomic and molecular systems, is the main reason for the lift of the orbital degeneracy. The presence of two orbitals, which correspond to the symmetric and anti-symmetric combination of the SOMOs of two radical anions, is also consistent with the simulated STM images shown in Fig. 9.14 (b). The shape of the electronic density with no nodal planes between the two TCNQ molecules, similar to that calculated for the doubly charged dimer on *gr.*/Ru, can only be obtained by combining the electronic densities SOMO and SOMO-1 of the open-shell gas-phase dimer.

In summary, the analysis of the TCNQ dimer adsorbed on *gr.*/Ru suggests that the electrons transferred from the substrate to the TCNQ dimer occupy orbitals which are spatially delocalized over the TCNQ dimer, and that the electronic configuration of the charged dimer has an open-shell character.

9.3 Magnetically ordered phases of TCNQ monolayers deposited on graphene on Ru(0001)

Similarly to the TTF-TCNQ charge transfer salt, the first organic magnets that have been synthesized are charge transfer compounds, in which the unpaired electrons on the acceptor molecule couple with the unpaired electrons on the donor, which is usually a metal, or a metalorganic compound [350, 156, 351, 352, 353]. On the other hand, stable magnetism in purely organic compounds is considerably more difficult to achieve [354, 355, 356, 357], as the constituent units are usually radical species, which are reactive and difficult to assemble in molecular crystals [358].

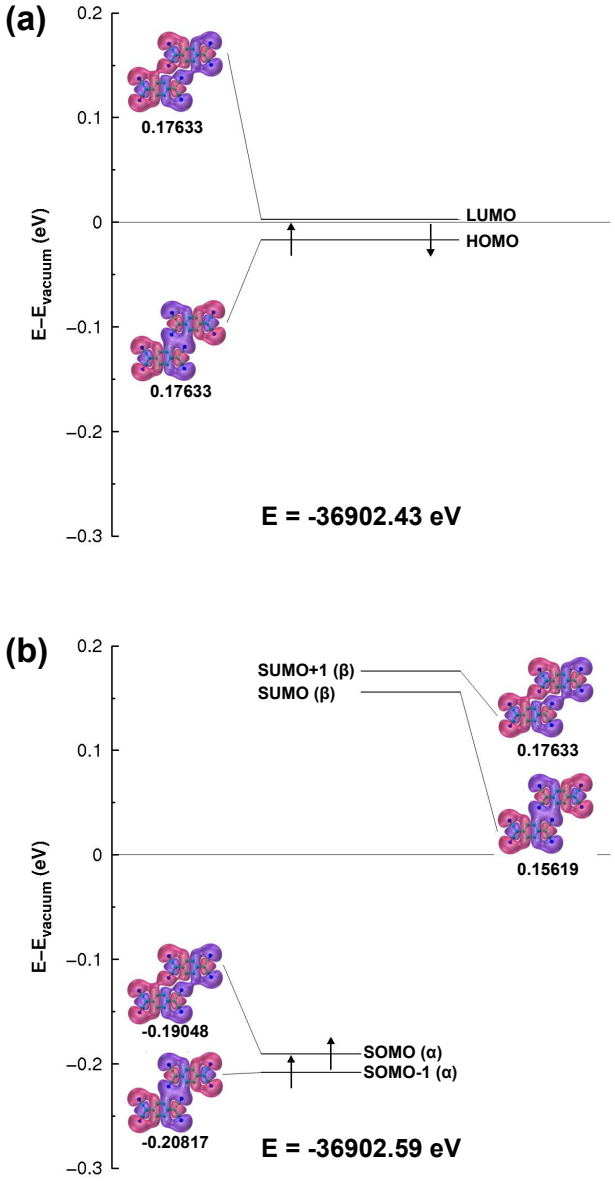

Figure 9.17: Molecular orbital diagram for the frontier orbitals of the closed-shell singlet and the open-shell triplet electronic configurations of the doubly charged TCNQ dimer in the gas-phase.

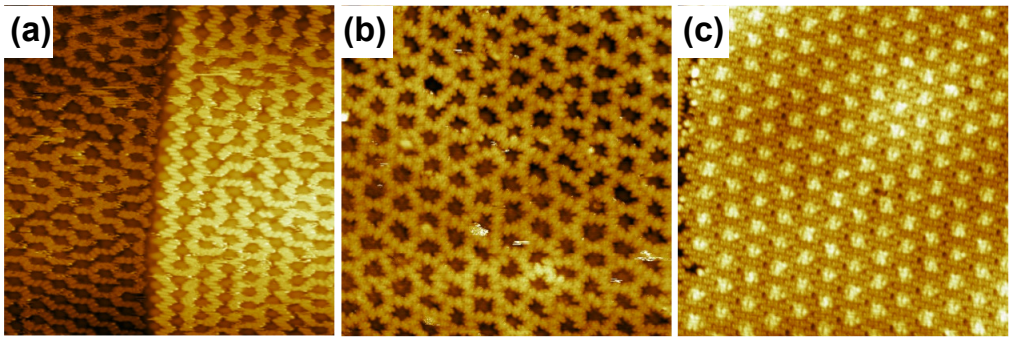

Figure 9.18: Experimental images of the evolution of TCNQ self-assembly patterns on *gr.*/Ru as a function of coverage. (a) 1/3 monolayer, (b) 1/2 monolayer, (c) 1 monolayer.

In Section 9.2, the characteristics of TCNQ dimers adsorbed on *gr.*/Ru, have been studied as a representative example of the charged TCNQ oligomers that are encountered at the low coverage. Increasing the molecular coverage up to one-third and then to half monolayer leads first to the formation of molecular stripes (Fig. 9.18 (a)) and consequently to the complete decoration of the L regions of the *gr.*/Ru moiré (Fig. 9.18 (b)). Further increasing the coverage leads to a radical change in the self-assembly pattern. In fact, once the molecules are forced to occupy the H regions of the moiré, a well ordered self-assembled monolayer is formed (Fig. 9.18 (c)), which extends regularly over the entire moiré. Thus, at one monolayer coverage, the intermolecular interactions prevail over the molecule substrate interaction, that dictates the molecular ordering at lower coverages.

Along this section, evidence will be provided that such TCNQ monolayers maintain the open-shell character present in the TCNQ monomers and dimers adsorbed on *gr.*/Ru. The mechanism which stabilizes the open-shell solution is a direct molecular coupling of the frontier orbitals of neighbouring TCNQ molecules. This coupling leads to the formation of spin-split molecular bands, which are the extension to the infinite 2D periodic monolayer of the delocalized intermolecular bonds described for the dimer in the previous Section 9.2. Calculations performed on an ideal, free-standing TCNQ monolayer confirm that such bands have an almost flat character, which has been demonstrated to be a condition favouring ferromagnetic ordering [359, 360]. Thus, the theoretical calculations suggest that a TCNQ monolayer adsorbed on *gr*/Ru may exhibit magnetic ordering. This theoretical prediction is confirmed by spin-polarized STM experiments.

Computational details

All the calculations for the full TCNQ monolayer (TCNQ-ML) adsorbed on *gr.*/Ru have been performed at the DFT+D2/PBE level of theory using computational settings and procedure similar to that employed in Section 9.2. Two different models have been used, in order to account for all the configurations of the TCNQ molecules over *gr.*/Ru observed in the experiments (see

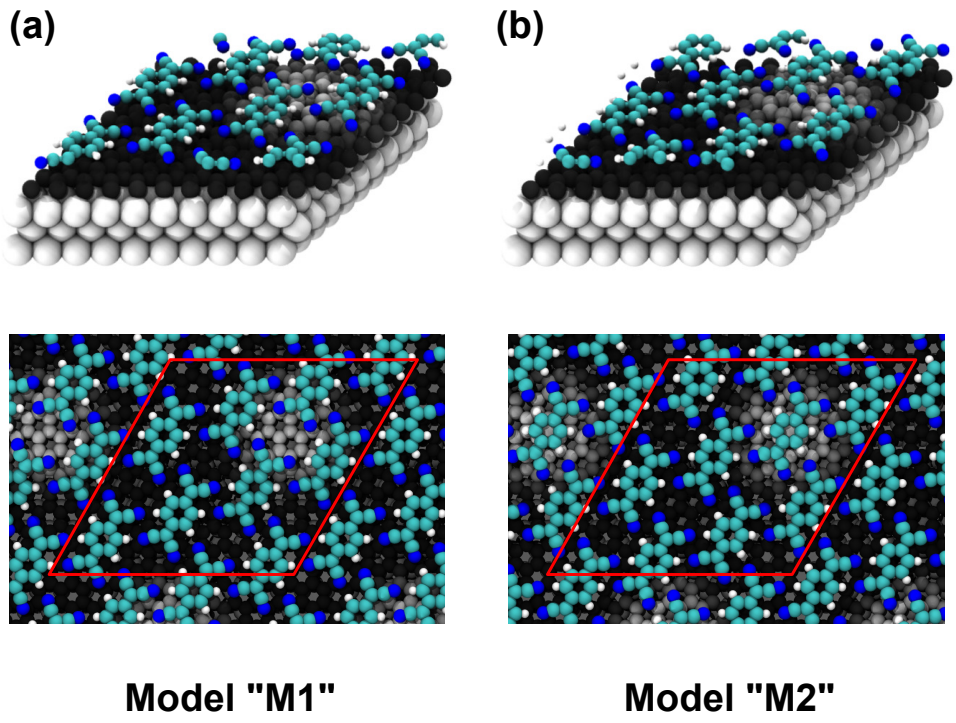

Figure 9.19: The two models employed to simulate a TCNQ monolayer on *gr.*/Ru.. (a) Model "M1" without molecule on the top of the H region of the moiré. (b) Model "M2" with molecule on the top of the H region of the moiré. Top panels show a lateral view of the unit cell employed. Bottom panel show top view of the unit cell (red line). For the TCNQ molecules, nitrogen, carbon and hydrogen atoms are printed in blue, cyan and white, respectively. The carbon atoms of the graphene monolayer are printed in different colors depending on their height (dark: low; grey: high). Ru atoms are printed in white.

Fig. 9.19). A first model (M1) has been constructed by adding seven additional TCNQ molecules to the geometry of the Bridge (30°) configuration (see Fig. 6.3). This model, does not reproduce all the possible adsorption configurations of the TCNQ-ML over *gr.*/Ru. In particular, it does not consider the case in which a molecule is placed exactly on top of the H region of the *gr.*/Ru moiré. To describe this feature, a second model (M2) has been built, in which the TCNQ-ML has been shifted in the *xy*-plane, so that one molecule lies exactly at the center of the H region of the moiré. It should be noticed that, due to the periodic boundary conditions imposed by the 11×11/10×10 *gr.*/Ru unit cell, the intramolecular distance in these models is slightly lower than that obtained for the adsorbed TCNQ dimer, *i.e.*, the monolayer is slightly compressed in the *xy*-plane.

In order to characterize the properties of the TCNQ-ML in the absence of the substrate, two different models have been employed: (i) a rectangular unit cell formed by two planar TCNQ molecules, which reproduces a planar TCNQ-ML; (ii) the isolated TCNQ-ML with the same geometry as that obtained after adsorption on *gr.*/Ru (model M1 has been used). In (i) an

11×11×1 mesh has been used, while in (ii) a 3×3×1 and a 5×5×1 k-point meshes have been used to sample the 2D Brillouin Zone. In (i) and (ii) it has been checked that the results remain unchanged if a non-collinear DFT formalism that include the spin-orbit coupling is used. In these calculations, the magnetization density obtained from the collinear spin-polarized DFT calculations [361] has been used as an initial guess for the atomic magnetic moments [362]. To check for the stability of the open-shell solution with respect to the close-shell solution, as a function of the charging ratio (CR)[1] of the monolayer, a third model has been employed. This latter model has been constructed by multiplying by four times in the *xy*-plane the unit cell of the planar TCNQ-ML (2 molecules / unit cell) , in order to consider a much larger number of molecules within a single unit cell (16 molecules / unit cell).

To study the nature of the bonding between the TCNQ molecules, calculations for the gas-phase neutral and singly charged TCNQ molecule, TCNQ dimer and a TCNQ tetramer have been performed. In the tetramer, four TCNQ molecules form a cross. For this geometry, in the neutral state, the LUMO is formed by the anti-symmetric combination of the LUMOs of the four constituting TCNQ molecules. All calculations have been performed with `TURBOMOLE` [363]. The molecular orbital analysis has been done on the DFT+D2/PBE optimized geometries using the def2-TVZPP basis set [364].

Discussion

The optimized geometries of both models, M1 and M2, show that the TCNQ monolayer follows the corrugation of the underlying graphene moiré. The adsorption energy is calculated to be -1.88 eV / TCNQ molecule and - 1.84 eV / TCNQ molecule for models M1 and M2, respectively. This confirms that the monolayer is stable and adsorbed on the surface with a large energy gain. The average TCNQ-graphene distance of the monolayer is very similar to that obtained for the TCNQ monomer and the dimer, ∼3 Å.

Similarly to what observed for the monomer, the experimental STM topographical images reveal that the molecular electronic density exhibit striking variations as a function of V_{bias} (Fig. 9.20(a-c)). At V_{bias} = -2.0 V, *i.e.*, where the resonance of the HOMO of the isolated monomer is observed, no nodes are observed in the central region of the molecules. However, at V_{bias} = -0.8 V and V_{bias} = 1.0 V, well-resolved, tube-like structures separated by clear nodes appear, which resemble that observed for the TCNQ SOMO and SUMO resonances (see Fig. 9.9). These features are fully reproduced by the simulated STM images, for both model M1 (Fig. 9.20 (d-f)) and model M2 (Fig. 9.20 (g-i)). In addition, subtler features are also reproduced, such as the lower resolution observed for the TCNQ molecules lying above the H regions of the moiré at V_{bias} = -0.8 V. This confirms that the models employed describe reliably the geometry of the TCNQ monolayer on *gr.*/Ru observed experimentally.

The presence of molecular bands having similar characteristics both at negative and positive

[1] For charging ratio it is intended the number of additional electrons added to the unit cell with respect the neutral configuration.

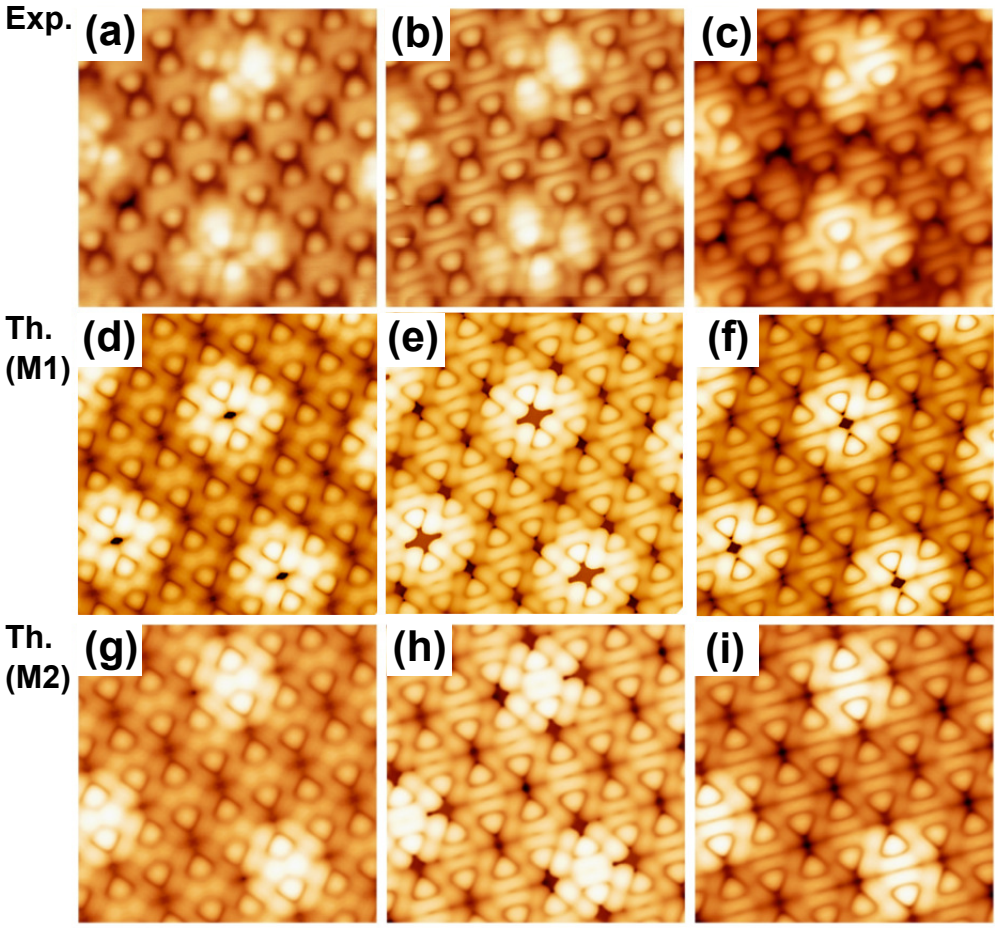

Figure 9.20: (a-c) STM topographical images obtained for a TCNQ monolayer adsorbed on gr./Ru, recorded at Vbias = - 2 V (a), Vbias = - 0.8 V (b) and Vbias = + 1.0 V (c). The corresponding simulated STM topographical images are shown in panels (d-f) for the M1 model, and in panels (g-i) for the M2 model. To simulate the STM topographical images, the DOS has been integrated in the energy range [- 1.2 eV : - 0.8 eV] (d,g), [- 0.3 eV : 0.0 eV] (e,h) and [0.0 eV : +0.3 eV] (f,i).

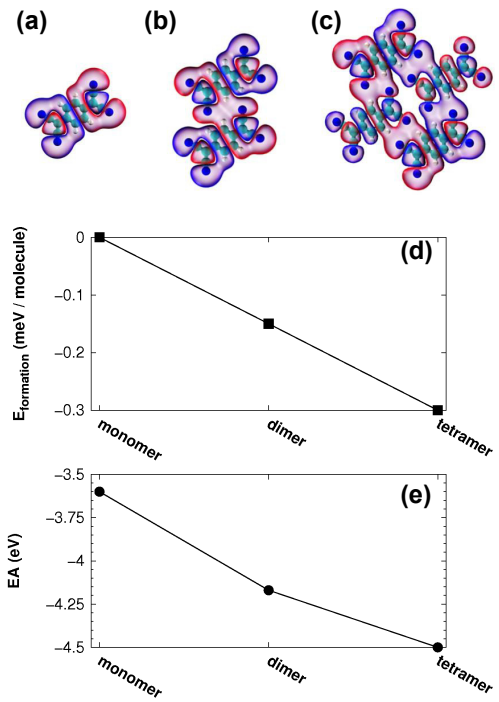

Figure 9.21: (a-c) LUMOs of the neutral monomer, dimer and cross-shaped tetramer. (d) formation energy ($E_{formation}$) per molecule of neutral TCNQ monomer, dimer and tetramer in the gas phase. (e) Electron Affinity (EA) of neutral TCNQ monomer, dimer and tetramer.

values of V_{bias} is also consistent with the calculated charge transfer to the molecule, which is 0.4-0.6 electrons / TCNQ molecule [1]. Therefore, on average, one electron every two molecules is transferred from *gr.*/Ru to the TCNQ monolayer. By ideally extending to the infinite monolayer the results obtained for the doubly charged TCNQ dimer in the gas-phase, where the frontier orbitals are formed by symmetric/antisymmetric combination of the SOMO/SUMO of the TCNQ radical anions, the tube-like features observed in the experimental and simulated images can be described as delocalized electronic bands, which result from the symmetric/antisymmetric combination of the frontier orbitals of the individual TCNQ molecules. Through a mechanism very similar to that described for the TCNQ monomer and dimer on *gr.*/Ru, electrons are transferred to these molecular bands and are delocalized across the entire molecular monolayer.

The formation of extended intermolecular states, for the dimer and the tetramer, is reflected in the formation energy per molecule ($E_{formation}$) of the neutral species. Fig. 9.21 shows that this quantity increases monotonously (*i.e.*, it becomes more negative) with the number of

[1] The precise value of the charge transfer per molecule depends on the position of the molecule over the corrugated graphene moiré

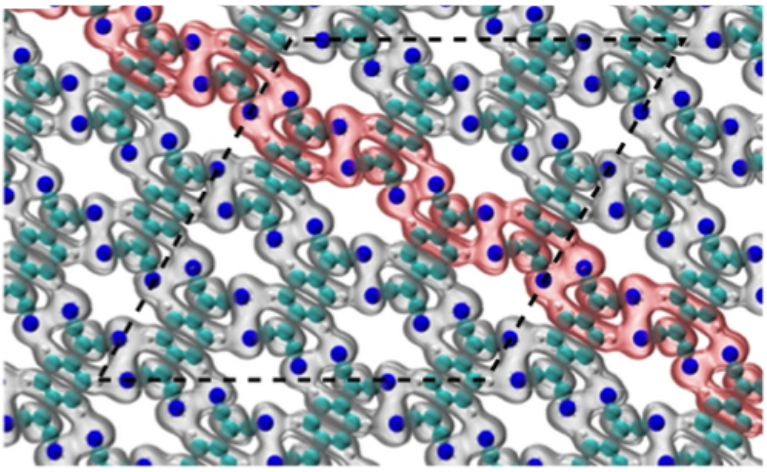

Figure 9.22: Electronic density distribution at the Γ-point of the first empty band for model (ii) of the free-standing TCNQ monolayer. Carbon, nitrogen and hydrogen atoms are shown on cyan, blue and white respectively.

molecules reaching $E_{formation}$ = - 0.30 eV for the tetramer, because of the increasing number of intermolecular interactions and the consequent development of the extended intermolecular orbitals. Fig. 9.21 (e) shows that the 1^{st} EA of the system increases monotonously (in absolute value) from -3.67 eV (monomer) to -4.53 eV (tetramer). This reflects the fact that a singly charged state will be stabilized more and more efficiently with increasing number of molecules because of the delocalization of any additional electron in the extended intermolecular bands.

In addition to the charging, spin-polarized DFT calculations confirm that there is magnetic net moment localized on the TCNQ monolayer. For model M1 and model M2, the net magnetic moment are M = 1.3 μ_B and M = 1.0 μ_B, respectively. This suggests that the ground state of the TCNQ-ML on *gr.*/Ru may exhibit an open-shell character.

The molecular origin of the electronic bands observed in Fig. 9.20 is further confirmed by the calculations performed on model (ii) of the free-standing TCNQ monolayer (Fig. 9.22). For the neutral monolayer, the Kohn-Sham state at the Γ-point relative to the 1^{st} unoccupied band has exactly the same tube-like feature observed for the supported TCNQ monolayer, and is clearly formed by the antisymmetric combination of the LUMOs of the TCNQ molecules. To simulate the effect of doping, the free-standing monolayer has been charged with 0.5 electrons / TCNQ molecule[1]. For this charging ratio (CR), the open-shell solution, in which the spin degrees of freedom have been allowed to relax during the self-consistent cycle, is 53.9 meV more stable than the close-shell configuration. For the former, the net magnetic moment is M = 1.95 μ_B. If the difference between the spin-up and the spin-down electrons is maintained fixed to four electrons, this difference increases to 105.1 meV and the net magnetic moment becomes M = 4.0

[1]For this model this means that the unit cell has been charged with 4 additional electrons.

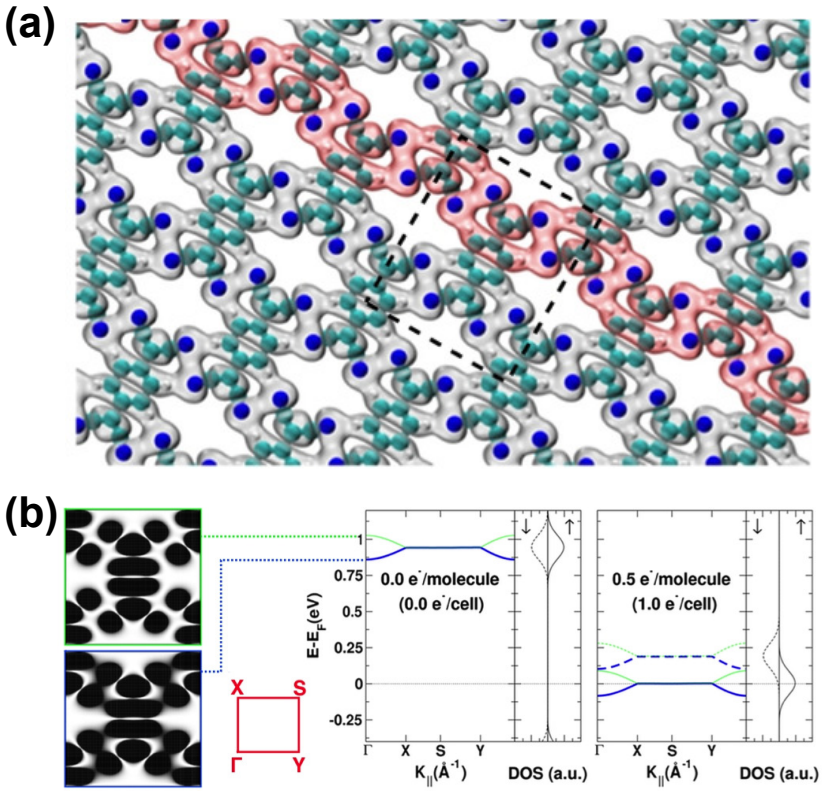

Figure 9.23: (a) Electronic density distribution at the Γ-point for the first unoccupied band of model (i) for the free-standing, flat TCNQ monolayer. The unit cell is shown by the back dashed lines. (b) Band structure and density of states of planar TCNQ ML, for increasing amounts of extra charge (from left to right). Leftmost panels show the electronic density distribution at the Γ-point (averaged in the z-direction) of the bands formed by the anti-symmetric (blue) and symmetric (green) combinations of TCNQs LUMO. Solid and dashed lines refer to spin-up and spin-down components. The red inset shows the unit cell of the 1^{st} Brillouin zone

μ_B. In both cases, this confirms that, when electrons are transferred to the TCNQ monolayer, the open-shell solution is favoured.

To obtain further insight into the nature of the intramolecular bands formed in the TCNQ-ML, model (i) for the free-standing TCNQ-ML has been considered (Fig. 9.23). The Kohn-Sham state at the Γ-point relative to the first unoccupied band of the planar neutral monolayer (Fig. 9.23 (a)) is identical to that shown in Fig. 9.21 for model (ii) for the free-standing TCNQ-ML. This confirms that the formation of the molecular band is a robust result, which does not depends on the particular periodicity or geometry employed. Indeed, the bands of this simple model are almost flat (Fig. 9.23 (b)). Upon charging the unit cell with 0.5 electrons / TCNQ molecule, they maintain their flat character, but the spin-up and spin-down components split in energy, and the spin-up component of the first unoccupied band moves below the Fermi level.

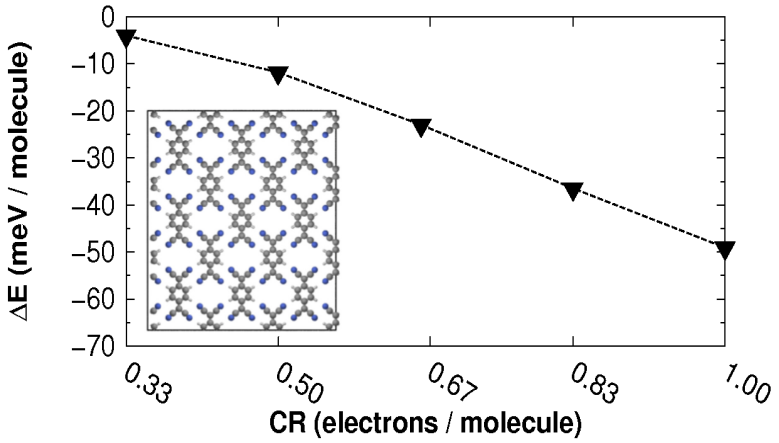

Figure 9.24: Energy difference (ΔE) per molecule between the open-shell (with a fixed difference between spin-up and spin-down electrons) and the close-shell configurations for the free-standing, planar TCNQ monolayer for charging ratios (CR) between 0.33 and 1.0 electrons / TCNQ molecule. The inset shows the unit cell used for the calculations. Nitrogen, carbon and hydrogen atoms are printed in blue, grey and white, respectively.

Consequently, the unit cell acquires a net magnetic moment M = 0.98 μ_B, which corresponds to ∼0.5 μ_B / TCNQ molecule. This behaviour reproduces qualitatively the results obtained for model (ii) of the free-standing TCNQ-ML.

For systems having flat, or almost flat, bands, theoretical predictions based on the Hubbard model [365, 366] have shown that, when such band becomes half-filled or when it is close to half-filling, the system should exhibit a ferromagnetic ground-state [367, 360, 359], which is favoured by electronic exchange. Indeed, for purely organic polimers, the possibility of flat-band ferromagnetism has been demonstrated by spin-polarized DFT calculations [368]. In the present case, however, the planar free-standing model provides a description of the system which is too oversimplified, and therefore cannot be used to predict the ground state magnetic order of the TCNQ monolayer on *gr.*/Ru. Nevertheless, it can still provide insight on the existence of an open-shell ground state in TCNQ-ML on *gr.*/Ru. The presence of an open-shell ground state is the main prerequisite for magnetic ordering, which may arise as a consequence of the flat character of the electronic bands. To this aim, the stability of the open-shell ground state with respect to the close-shell ground state in the flat TCNQ-ML has been investigated[1]. The unit cell which has been employed for these calculations corresponds to the unit cell shown in the inset of Fig. 9.21. This larger unit cell permits to consider a larger number of CRs, ranging from CR = 0.33 electrons / TCNQ molecule to CR = 1.16 electrons / TCNQ molecule. Indeed, the stability of the open-shell solution increase monotonously all the CRs considered up to CR = 1.0 electrons

[1]In this case, to calculate the open-shell ground state, the difference between the number of spin-up and spin-down electrons has been always maintained equal to the number of electrons added in the supercell, in order to consider the open-shell ground state solution having the maximum multiplicity.

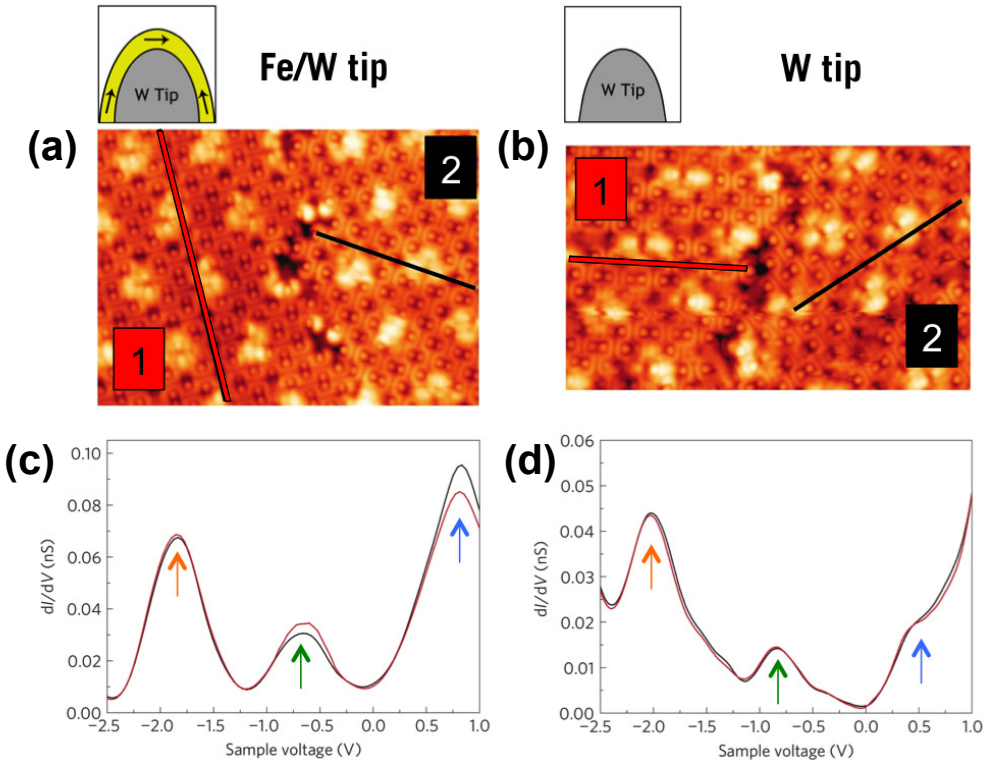

Figure 9.25: (a,b) STM topographic images (left: 16.7 nm × 12.1 nm^2 and right: 14 × 8.5 nm^2) of a TCNQ monolayer on *gr.*/Ru recorded at V_{bias} = +1.5 V and I_{tunnel} = 100 pA (left) and I_{tunnel} = 50 pA (right). (c) dI/dV curves obtained by spin-polarized STS using Fe-coated W tips, averaged over three unit cells of the moir superstructure for the left (red) and right (black) domains of (a). (d) dI/dV curves obtained using non-magnetic W tips, averaged over three unit cells of the moiré superstructure for the left (red) and right (black) domains of (b). The black lines in (a,b) indicate the long axis of the TCNQ molecules in the molecular domains.

/ TCNQ molecule, which correspond to the complete filling of the spin-up components of the electronic bands formed by the symmetric and anti-symmetric combinations of the SUMO of the TCNQ radical anion. At CR = 1.16 electrons, the situation changes, and the open-shell ground state becomes energetically disfavoured by + 316 meV. Thus, it is verified, in the entire range of CR relevant for the calculations of the TCNQ-ML adsorbed on *gr.*/Ru.; that the predicted stability of the open-shell ground state does not depends sensibly on the exact CR considered. This analysis further supports the idea that the a TCNQ-ML on graphene may exhibit an open-shell ground state, and that this ground state may exhibit some kind of magnetic ordering, at least at T = 0 K, which is the temperature considered in the calculations.

In order to verify this theoretical suggestion, spin-polarized STM experiments have been performed. As described briefly in Appendix A.2, the tunnelling current measured in a spin-polarized STM experiment shows a dependence on the angle formed between the magnetization

vector of the tip and the magnetization vector of the sample. Thus, for domains oriented in different directions, since the magnetization vector of the tip is fixed, the tunnelling current for one spin component should change when moving from one domain to the other, whereas, for the second spin component, the tunnelling current should change in the opposite direction. Fig. 9.25 shows a spin-polarized STM experiment performed using a magnetic Fe-coated W tip and the corresponding STM experiments performed using a non-magnetic W tip. It can be seen that, in the spin-polarized experiment, the peaks realtive to the resonance corresponding to the occupied and unoccupied parts of the intramolecular bands, formed by the symmetric/anti-symmetric combinations of the LUMO of the neutral molecule (blue and green arrows), exhibit a magnetic contrast when one moves from one domain to the other. This contrast is not present in a similar STM experiment performed using the non-magnetic W tip. In both experiments, the peak at V_{bias} = -2.0 V (orange arrow) does not exhibit any kind of contrast, because it is associated with an electronic band which is already completely filled. This provides an experimental evidence of the existence of magnetic order in the TCNQ monolayer adsorbed on *gr.*/Ru.

Part IV

Conclusiones

En esta tesis, se han utilizado cálculos DFT para investigar la estructura, y las propiedades electrónicas de una monocapa epitaxial de grafeno crecida sobre Ru(0001) (*gr.*/Ru), y la adsorción de la molécula aceptora de electrones 7,7′,8,8′-tetracianoquinodimetano (TCNQ) en esta superficie. Todo el trabajo ha sido llevado a cabo en una colaboración estrecha con grupos experimentales expertos en microscopía de efecto túnel (STM) y microscopía de fuerza atómica (AFM). En esta colaboración, los resultados que se han presentado han contribuido a aclarar las detalles estructurales y electrónicos de *gr.*/Ru, y también las propiedades electrónicas y magnéticas de las monocapas moleculares depositadas en esta superficie.

La simulación de *gr.*/Ru no es trivial, debido a la presencia de una superestructura de moiré corrugada, que aparece como consecuencia de la falta de correspondencia entre la constate reticular del grafeno y la de Ru(0001). Por esta razón, se ha hecho un esfuerzo considerable para obtener un modelo realista de esta superficie. Al principio, se ha investigado el papel de las interacciónes de van der Waals en la estructura de la monocapa de grafeno. Se ha observado que la contribución de las fuerzas de vdW en la interacción grafeno-Ru(0001) varía considerablemente a lo largo del moiré, y es mucho mas fuerte en las regiones que no están enlazadas de manera covalente con la superficie de Ru(0001). Utilizando modélos de gran escala que describen la formación del moiré de manera realista, se ha demonstrado que las interacciónes de vdW son responsables para una redución de la corrugación de moiré de grafeno del 25%. Tal modificación geometrica mejora considerablemente el acuerdo entre las imágenes STM simuladas y aquellas medidas experimentalmente, en comparación con geometrías donde las interacciónes de vdW no se han tenido en cuenta. Po esta razón, esta parte del trabajo a dado la primer evidencia que las interacciónes de vdW deben tenerse en cuenta, al momento de simular monocapas de grafeno en superficies metálicas con una diferencia de constante reticular.

En una segunda fase, se ha estudiado la estructura electrónica de *gr.*/Ru. La geometría corrugada del moiré de grafeno se ha relacionado con modulaciones periódicas en la estructura electrónica de la superficie, que aparecen en distintas regiones del espectro electrónico. Cerca del nivel de Fermi, las características afiladas que se han observado en los espectros de espectroscopía de efecto túnel en las regiones altas del moiré de grafeno, se han asignado a estados electrónicos que están fuertemente confinados por debajo de las protuberancias de grafeno. Además, se ha mostrado inequívocamente que el contraste topografico observado con el STM a voltajes positivos muy altos está relacionado con un nuevo estado de intercara, que está fuertemente localizado en las regiones bajas de la superestructura corrugada de grafeno. Esta inversión de contraste puede ser reproducida por la teoría, solo si los modelos utilizados describen al mismo tiempo la formación del moiré, los estados electrónicos vacíos de Ru(0001). Este último resultado ha puesto fin de manera definitiva a una controversia relacionada con la correcta identificación de los estados vacíos en *gr.*/Ru.

En una tercera fase, se han explorado las propiedades mecánicas de *gr.*/Ru. Las simulaciónes teóricas de la indentación del grafeno corrugado por una punta han mostrado que la respuesta de las partes altas del morié bajo una deformación grande es completamente reversible. Estas

simulaciónes han permitido racionalizar experimentos de AFM complementarios, que han evidenciado como la repuesta mecánica de las partes altas del moiré es distinta de aquella de la las partes bajas, sugiriendo que las primeras puedan deformarse mecanicamente por medio de una punta de AFM. Por esta razón, estos resultados han dado la primera evidencia experimental que las propiedades mecánicas del grafeno se mantienen hasta en muestras formadas por pocas decenas de átomos de carbono.

Finalmente, utilizando los modelos desarrollados en el trabajo previo, se ha investigado la adsroción de la molécula aceptora de electrones TCNQ en *gr.*/Ru. Los cálculos han mostrado que, al adsorberse en *gr.*/Ru, los monomeros de TCNQ reciben un electrón desde el grafeno. Al mismo tiempo, el grafeno desacopla de manera eficaz la molécula de la superficie, de tal manera que el electrón transferido al TCNQ se mantiene desapareado. Esta predicción teórica ha sido verificada por experimentos STS que han observado la existencia de un pico Kondo cuando la punta del STM está posicionada por encima de la molécula. Los cálculos han mostrado tabmién que el caracter de capa abierta de las especies moleculares adsorbidas se mantiene al formarse el dímero y la monocapa completa. Un analysis teórico detallado de un dimero de TCNQ y de la monocapa autosuspendida, ha mostrado que la estabilidad de la solucción a capa abierta es debida a la formación de bandas intermoleculares, que son el resultado de la combinación de los orbitales vacíos mas bajos de las moléculas de TCNQ. La existencia de estas bandas ha sido verificada por las imágenes topográficas de STM medidas en la monocapa completa de TCNQ adsorbida en *gr.*/Ru, y por las simulaciónes correspondientes. Los cálculos para un modelo simplificado de la monocapa de TCNQ autosuspendida han mostrado que las bandas intermoleculares son casi planas, y podrían dar lugar a estructuras ordenadas magneticamente. Por cierto, la presencia de orden magnetico en la monocapa de TCNQ adsorbida en *gr.*/Ru se ha visualizado por medio de medidas STM polarizadas en espin.

Part V

Conclusions

In this thesis, DFT simulations have been used to investigate the structure and the electronic properties of an epitaxial monolayer of graphene grown on Ru(0001) (*gr.*/Ru), and the adsorption of the molecular electron acceptor 7,7′,8,8′-tetracyanoquinodimethane (TCNQ) on this surface. The entire work has been carried out in close collaboration with experimental groups expert in scanning tunnelling microscopy (STM) and atomic force microscopy (AFM). Within this collaboration, the present results have substantially contributed to shed light on the electronic and structural characteristics of *gr.*/Ru, as well as on the electronic and magnetic properties of the molecular monolayers deposited on this surface.

The simulation of *gr.*/Ru is by no means an easy task, because of the presence of a corrugated moiré superstructure, which arises as a consequence of the mismatch between the lattice constant of graphene and that of Ru(0001). Therefore, a significant effort has been made, in order to obtain a reliable model for this surface. Initially, the role of van der Waals (vdW) forces in the structure of the graphene monolayer has been investigated. The contribution of vdW forces to the graphene-Ru(0001) interaction has been found to vary substantially across the moiré, being much more pronounced in those region where graphene is not covalently bound to Ru(0001). By employing large scale models that account realistically for the formation of the moiré, vdW interactions have been found to be responsible for the reduction the corrugation of the graphene moiré by 25%. This geometric modification have considerably improved the agreement between the simulated STM images and the experimentally measured ones, compared to geometries in which vdW interactions have been neglected. Thus, this part of the work have provided the first-ever evidence that vdW interaction should always be considered when simulating graphene monolayers on lattice-mismatched metallic surfaces.

In a second step, the electronic structure of *gr.*/Ru has been addressed. The corrugated geometry of the graphene moiré has been correlated to periodic modulations in the surface electronic structure, which appear in different regions of the electronic spectrum. Close to the Fermi level, the sharp features reported in the scanning tunnelling spectroscopy spectra measured over the high regions of the graphene moiré have been assigned to electronic states which are strongly confined below the graphene protrusions. Moreover, it has been unequivocally shown that the topographical contrast inversion observed with STM at high positive bias voltages is related to the presence of a new interface state, which is strongly localized in the low regions of the corrugated graphene superstructure. Such contrast inversion can be reproduced by theory, provided that the models employed to simulate *gr.*/Ru simultaneously account for the moiré formation and describe correctly the unoccupied electronic structure of Ru(0001). This last result has definitely settled down a long standing controversy related to the correct identification of the unoccupied electronic states in *gr.*/Ru.

In a third step, the mechanical properties of the *gr.*/Ru have been explored. Theoretical simulations of the indentation of the corrugated moiré by a probing tip have shown that the response of the high regions under heavy deformation is perfectly reversible. These simulations have rationalized complementary AFM measurements, which provided evidence that the mechan-

ical response of the high regions of the moiré is different from that of the low regions, suggesting that the former undergo a reversible mechanical deformation when probed by the AFM tip. Thus, these results have provided the first evidence that the exceptional mechanical properties of graphene are preserved even in samples formed by just few tens of carbon atoms.

Finally, using the models benchmarked with the previous work, the adsorption of the molecular acceptor TCNQ on *gr.*/Ru has been investigated. Calculations performed for the adsorbed TCNQ monomers have shown that, upon adsorption on *gr.*/Ru, each molecule receives one electron from graphene. At the same time, graphene decouples efficiently the molecule from the surface, so that the electron transferred to the TCNQ molecule remains unpaired. This theoretical prediction has been verified by STS experiments, which have observed the existence of a Kondo peak when the STM tip is positioned over the molecule. The calculations have also shown that the open-shell character of the adsorbed molecular species is preserved upon the formation of the dimers and of the full monolayer. A detailed theoretical analysis performed on the free-standing dimer and monolayer, have shown that the stability of the open-shell solution is due to the formation of intermolecular bands, which result from the combination of the lowest unoccupied molecular orbitals of the individual TCNQ molecules. The existence of such bands has been verified by STM topographic images measured over the full TCNQ monolayer adsorbed on *gr.*/Ru, and by the corresponding simulations. Calculations employing a simplified model of a free-standing TCNQ monolayer have shown that the intermolecular bands are almost flat, and therefore may results in magnetically ordered structures. Indeed, the presence of a magnetical order for the TCNQ monolayer adsorbed on *gr.*/Ru has been verified by spin-polarized STM measurements.

Part VI

Appendix

A Scanning probe techniques

In this Appendix, a brief overview of the experimental scanning probe techniques that have been employed to measure the experimental data discussed in this work is provided. In Sections A.1 and A.2, scanning tunnelling microscopy and scanning tunnelling spectroscopy are presented as a mean to obtain informations about the electronic structure of a surface. In Sections A.4 and A.5, non-contact atomic force microscopy and 2D force spectroscopy, which permit a more direct analysis of the structural properties of a surface, are discussed.

A.1 Scanning tunnelling microscopy

Scanning tunnelling microscopy (STM) [148, 149, 149] is a surface-sensitive technique that allows to obtain real-space images of the electronic structure of a sample with sub-nanometer resolution.

The functional principle of STM involves, as its basic components, a sharp conductive probe tip made, *e.g.*, of tungsten, and a conductive substrate. The tip and the sample are approached up to 5-10 Å, so that their wavefunctions can overlap, and a small voltage of the order of 1 V is applied between the two. Under these conditions, electrons have a small, but non-vanishing probability of travelling across the classically forbidden vacuum gap, a phenomenon known as *quantum tunnelling* [369]. By solving the time-dependent Schrödinger equation (Eq. 2.1) for a simple 1D model of a free electron with wavenumber k, tunnelling through a rectangular potential barrier having a width d, it is possible to show that the relationship between the current I and the barrier width d is $I \propto e^{-2kd}$, *i.e.*, that the tunnelling probability decreases exponentially by increasing the barrier width. As the tip can be made extremely sharp, this exponential dependence gives to this technique a very high vertical resolution. As a consequence, only few electrons travel across the gap - naively, one could think that the only electrons travelling are those of the last atom of the tip apex -, and tunnelling currents measured in STM are typically in the pA to nA range, thus requiring sophisticated electronics to be detected. Such current is the observable which is then used as the imaging signal.

Due to the extreme sensitivity of the measurement, very clean and controlled experimental conditions must be achieved to obtain meaningful results. External contaminants are usually eliminated by performing the experiments in airtight chambers, maintained under *ultra-high vacuum* (UHV) - $P \sim 10^{-10}$ Bar. At these conditions, atomic resolution can be achieved,

provided that the thermal vibrations of the sample are sufficiently quenched, by maintaining the sample at liquid helium temperature - T = 4.6 K. These strict experimental conditions are indeed very helpful to compare measured and simulated results, because they mimic at best the environmental conditions used in static DFT calculations - 0 Bar and 0 K.

Two-dimensional topographic maps can be recorded by scanning the tip line-by-line over the sample surface. Sub-nanometer precision in the tip positioning can be achieved by means of piezoelectric tube scanners[1] [370], provided that sufficient damping from the external vibrations is ensured. Different imaging modes can be employed. In the experimental data discussed in this thesis, the constant-current mode has been used, in which the tunnelling current is kept at a constant value during scanning. This condition is maintained by controlling the vertical position of the tip by means of a feedback circuit. Therefore, STM operated in constant current mode provides 2D maps of constant current over the sample. Assuming the Tersoff-Hamann approximation described in Section 5.1, these maps can be associated with iso-countour surfaces of the surface LDOS at the position of the tip.

As already mentioned in Section 5.1 STM has the additional capability of detecting magnetic ordering in the sample, if magnetic tips are used [371, 372, 373]. The most straightforward way to build these tip is to cover non-magnetic tips (*e.g.* W) with a sufficiently large number of layers of a magnetic material (*e.g.*, Fe). The choice of the magnetic material is fundamental, because its magnetic ordering over the non-magnetic material will determine the final tip magnetization. Moreover, also the actual tip shape is important. In the case of Fe-coated W tips, which have been used for the SP-STM measurements discussed in this thesis, it is known that Fe grows on W with in-plane anisotropy. Therefore, a spin-polarized experiment performed with a Fe-coated W tip will probe the in-plane magnetization of the sample [374]. In order to maximize the magnetic contrast, blunt tip with almost only in-plane magnetization are desirable. In fact, sharp Fe-covered W tips, which would provide better atomic resolution, are less suitable for spin-polarized measurements, becasuse the in-plane component of the tip magnetization is too small.

A.2 Scanning tunnelling spectroscopy

The STM can be used in spectroscopic mode to obtain spatially resolved informations on the local density of state of the sample, $\rho_\nu(E, \mathbf{r}_0)$, with energy resolution, in accordance with Eq. (5.10). In tunnelling regime, *scanning tunnelling spectroscopy* (STS) is recorded by positioning the tip at the position of interest over the sample, and switching off the feedback control that maintain the current constant. Then, the voltage is ramped and the variation of tunnelling current dI is recorded as a function of the variation of voltage dV. Assuming the Tersoff-Hamann approximation as in Eq. (5.10), at small finite biases, the signal will be proportional to

[1] In piezoelectric materials, an applied voltage causes a change in the crystal structure, that leads to a contraction of the piezo element in some directions and an expansion in the others.

the LDOS of the sample:

$$\frac{dI}{dV} \propto \rho_\nu(E, \mathbf{r}_0)\rho_\mu(E), \tag{A.1}$$

However, the interpretation of the $\frac{dI}{dV}$ data is complicated by the fact that the electronic structure of the tip is unknown. Thus, to ensure the reliability of the obtained results, the measurements are taken using different tips at identical surface locations. Although the electronic structure of the tip is unknown, it is at least constant, for stable STS conditions. Thus, in the tunnelling spectra obtained at different locations, the tip electronic structure will only contribute as a constant background to the measurement. Consequently, the spatially dependent variations in the electronic structure will not be influenced by the tip states.

Spin-polarized scanning tunnelling measurements can be performed on magnetic samples [372, 373]. If the Tersoff-Hamann theory is extended to the spin-polarized case, it can be seen that the proportionality relation shown in Eq. (A.1) becomes:

$$\frac{dI}{dV} \propto \rho_\nu(E, \mathbf{r}_0)\ \rho_\mu(E) + \mathbf{s}_\nu(E, \mathbf{r}_0)\ \mathbf{s}_\mu(E), \tag{A.2}$$

i.e., the tunnelling current will depend critically on the angle θ formed between the magnetization vector of the tip, and the magnetization vector of the sample at $\mathbf{r}_0$. Notice that, in a case of a non-magnetic tip interacting with a magnetic sample, the second term in the right side of Eq. (A.2) will go to zero, and the standard Tersoff-Hamann relationship shown in Eq. (A.1) will be recovered.

A.3 Kondo effect in scanning tunnelling spectroscopy

The Kondo effect describes the screening by conduction electrons of a magnetic impurity embedded in a conductive host [375, 376]. Originally, this effect has been introduced to explain the unusual behaviour of the resistivity as a function of the temperature observed in dilute magnetic alloys [377]. In metals, the electric resistivity is due to electron-phonon interactions and intrinsic defects. Thus, it decreases monotonously as a function of the temperature ($\propto T^5$), due to thermal quenching of the lattice vibrations, and saturates at a value which is ultimately related to the intrinsic defects concentration. However, in some magnetic alloys, it has been observed that the resistivity saturates at a certain temperature, and then increases logarithmically when the temperature is decreased further [378]. This behaviour has been explained by introducing a new scattering mechanism, in which the electrons of the metallic conduction band are scattered by spin-flip excitations of the unpaired electrons localized at the magnetic impurities. In Kondo's model, the interaction between the magnetic impurity and the conduction electrons is treated

perturbatively by means of the following Hamiltonian:

$$H_{Kondo} = H_0 + W, \tag{A.3}$$

$$W = J_K \mathbf{s} \cdot \mathbf{S}, \tag{A.4}$$

where H_0 is the Hamiltonian that describes the non interacting conduction electrons, and W describes the interaction between the total spin of the conduction electrons $\mathbf{s}$ and the spin $\mathbf{S}$ of the inpurity as an antiferromagnetic coupling ($J_K > 0$). Using the hamiltonian presented in Eq. A.3, the final result for the contribution of the impurity to the resistivity is:

$$R = \frac{3\pi m_e J_K^2 \mathbf{S}(\mathbf{S}+1)}{2q_e^2 \hbar \epsilon_F} \left[1 - 4J_K \rho(\epsilon_F) ln\left(\frac{k_B T}{D}\right)\right], \tag{A.5}$$

where k_B is the Boltzmann constant, m_e and q_e are the electronic mass and electronic charge, respectively, D is the half-bandwidth of the metallic conduction band and $\rho(\epsilon_F)$ the DOS at the Fermi level ϵ_F. The second term in the square parenthesis in Eq. A.5 predicts an increase of R as the temperature is lowered, assuming an antiferromagnetic coupling of the local moment with the conduction electrons. Thus, describing the resistivity by taking into account the higher order terms described in Eq. A.5, the non-monotonic behaviour of R at low T is described correctly. However, the model based on Eq. A.5 makes the unphysical prediction that the resistivity should diverge as $T \to 0$ K. Similarly, a perturbational approach leads to the following expression for the impurity susceptibility [375],

$$\chi(T) = \frac{(g\mu_B)^2 \mathbf{S}(\mathbf{S}+1)}{3k_B T} \left[1 - \frac{2J_K}{1 + 2J_K \rho(\epsilon_F) \ln(\frac{k_B T}{D})} + c_2(2J_K \rho(\epsilon_F))\right], \tag{A.6}$$

where g is the g-factor (assumed to be the same for the the impurity and the conduction electrons), μ_B is the Bohr magneton and c_2 is a coefficient that depends on the form used for the conduction density of states. It can be seen this expression for $\chi(T)$ diverges for a critical temperature $T = T_K$, which is called the *Kondo temperature* [375]:

$$k_B T_K = D e^{-\frac{1}{2\rho J_K}}. \tag{A.7}$$

Because of the exponential dependence on J_K, T_K varies dramatically depending on the nature of the magnetic impurity and the conductive host, ranging from 1 mK to 100 K.

A less phenomenological description of the Kondo effect implies that, due to the positive value of J_K, at $T < T_K$ a bound singlet state is formed [379], in which the unpaired electron on the magnetic impurity is completely screened by the surrounding conduction electrons. In a simple

two-orbitals/two-electrons model, in which the two orbitals represent the conduction band and the semi-occupied orbital of the impurity, this bound state can be visualized as an open-shell singlet with a multi-determinant wavefunction $\Psi = \frac{1}{\sqrt{2}}\left[|\varphi_1^\alpha \varphi_2^\beta\rangle - |\varphi_1^\beta \varphi_2^\alpha\rangle\right]$. On the other hand, by considering, more realistically, the metallic character of the host, the singlet state can be viewed as the unpaired electron of the magnetic impurity surrounded by a cloud of conduction electrons polarized with opposite sign. The open-shell nature of Ψ requires that both orbitals φ_1 and φ_2 must be semi-occupied. For the metallic band, this occurs only at the Fermi level. Therefore, the formation of the Kondo singlet results in a new resonant state, localized in energy at the Fermi level of the conductive host.

For magnetic adsorbates on conductive surfaces, the existence of this resonant state at the Fermi level can be verified by STS [380, 381]. Therefore, dI/dV spectroscopy in a range very close to the Fermi level (-100 meV $\leq$ V$_{bias}$ $\leq$ 100 meV) provides a method to confirm indirectly the magnetic nature of an impurity, such as an atom or a molecule, adsorbed on a conductive substrate.

When a magnetic impurity is deposited on a conductive surface, the Kondo singlet will develop at $T < T_K$. Thus, a resonant state will arise at the Fermi level. Notice that the resonance is not isolated, but it is embedded in the continuum of the electrons of the metallic conductor. Consequently, when the STS is positioned above the magnetic impurity, for values of $V_{bias} \approx 0V$, two transmission channels are active simultaneously. The first one involves the *direct* tunnelling to the impurity, whereas the second one involves the *indirect* tunnelling to the impurity, assisted by the conduction electrons of the metal. Therefore, this process is conveniently interpreted in terms of a Fano resonance [382, 383]. Starting from Eq. 5.3, the expression for the tunnelling current in the presence of a Fano resonance can be written as [384, 385]:

$$I = \frac{2\pi q_e V_{bias}}{\hbar}\left[\sum_{\nu',\mu}|M_{\nu',\mu}|^2\delta\left(E_{\nu'}-E_F\right)\delta\left(E_\mu - E_F\right)\right]\frac{(\epsilon'+q)^2}{(1+\epsilon')} + C, \tag{A.8}$$

where $\epsilon = \frac{2(E-E_F)}{\Gamma}$ is a reduced energy, Γ the line width of the resonant state at energy E_F, ν' is an index for those states of the metallic continuum that are coupled to the impurity, μ is an index for the states of the tip, and C is a generic constant that includes the contribution to I of all those states of the continuum that are not coupled to the impurity. The shape of the resonance profile, described by the formula $\frac{\epsilon'+q}{1+\epsilon'}$, is then determined by the asymmetry parameter q, which indicates the ratio between the direct and indirect tunnelling processes. For $q \to \infty$ a perfect Lorentzian shape will be obtained, whereas for $q \to 0$, a dip will be obtained, and $q = 1$ will result in a perfectly asymmetric shape. Indeed, it must be noted that the exact value of q is strongly system-dependent. For examples, even different molecules adsorbed on the same surface have shown clearly different Fano profiles [386, 387, 388].

A.4 Non-contact atomic force microscopy

In *atomic force microscopy* (AFM) [150], a cantilever, having an integrated tip at its end, is approached to the surface of the sample. When the tip is in proximity of the sample, the presence of the surface causes the cantilever beam to deflect. The deflection is monitored by measuring the displacement of a laser beam reflected off the back side of the cantilever via a photosensitive detector [389], and used as imaging signal for generating 2D maps of the surface topography.

Under UHV conditions, it is possible to operate the AFM in a non-destructive manner - *i.e.* without making the tip and the sample touching each other - by using the so-called *dynamic* AFM in *frequency modulated* mode [390]. Most of the the AFM experiments analyzed in this thesis have been performed with this technique, which is also referred to as *non-contact atomic force microscopy* (NC-AFM) [311, 339]. In NC-AFM, the cantilever is mechanically excited at the resonance frequency f_0 of its first flexural mode, and kept vibrating with a constant amplitude A_0. When the tip is approached to the surface, the oscillation frequency f of the cantilever is modified with respect to f_0, due to the interaction of the tip with the surface, while the amplitude is maintained constant by an electronic detection system. The difference between f_0 and f, which varies depending on the tip-sample distance z, is called the *frequency shift*, Δf:

$$\Delta f(z) = f_0(z \to \infty) - f(z), \tag{A.9}$$

Δf, which is the observable used as imaging signal, is maintained at a constant value, while the tip is scanned line-by-line over the surface, by varying the tip-sample distance. Thus, by imposing a predetermined value of Δf, one can explore maps of constant frequency shift over the surface. Alternatively, one may think about the frequency shift as a mean to probe the relative distance of the tip from the surface: larger values of Δf will correspond to the tip beign closer to the surface, and vice versa. Therefore, the frequency shift can be also used as a mean to control the tip-sample distance, and check the effect of this distance on the surface topography.

Unlike STM, where the tunnelling current is the only source of signal, in NC-AFM there are a number of possible interactions between the tip and the sample which contribute to the signal. These interactions have a much slower decay than the tunnelling current, so that larger regions of the macroscopic tip contribute to the overall tip-sample interaction. In UHV, they are divided into two categories, depending on the range of the particular interaction [310]. *Long range* forces can be distinguished in *electrostatic forces* and *vdW forces*, while *short range* forces arise due to the chemical interaction between the tip and the sample. Ideally, during a NC-AFM measurement one would like to eliminate any long range contribution. Nevertheless, this is by no means easy. In particular, electrostatic forces arise because the tip and the sample generally have different work functions. Therefore, when they are brought into contact, electrons flow from the material with smaller work function to the one with higher work function, giving rise to a

potential difference, V_{cpd}. The electrostatic force is then given by [391]:

$$F_{el.}(z) = \frac{1}{2}\frac{\partial C}{\partial Z}\left(V_{bias} - V_{cpd}\right)^2, \tag{A.10}$$

where C is the capacitance between the tip and the sample, and V_{bias} is an external bias voltage applied between the tip and the sample. By looking at Eq. (A.10), it is evident that one can try to minimize $F_{el.}$ by applying a voltage $V_{bias} = -V_{cpd}$. V_{cpd}, in turn, is determined by mapping $f(Z)$ at one point over the surface at large values of Z, where the contribution of chemical forces is negligible. Additionally, the local electrostatic effect due to an electronically inhomogeneous environment may still result in a locally varying electrostatic force. This contribution can be suppressed by measuring continuously the local potential difference, V_{lcpd}, using *kelvin force probe microscopy* (KFPM) [392, 393], and then applying a compensating counter-potential. However, KFPM suffers form the so-called *averaging effect* [394, 395, 396], *i.e.*, the influence on the local contact potential difference of lateral electrostatic interactions, which tend to smoothen the differences in V_{lcpd}.

VdW forces cannot be removed in the same way as electrostatic forces. However, it has been found empirically that appropriate combinations of A_0 and k - usually $A_0 \approx 10$ nm and 25 N/m $\leq k \leq$ 50 N/m - lead to a natural suppression of the vdW background, as shown by the possibility to achieve atomically resolved images [323].

Apart from the frequency, also the amplitude excitation A_0' required to maintain the amplitude of the cantilever at the constant value A_0 can be recorded. In particular, in the limit $\Delta f << f$, the energy dissipated per cycle can be estimated by:

$$E \approx \frac{\pi\ k\ A^2}{Q}\left(\frac{A_0'}{A_0}\right), \tag{A.11}$$

where A is the amplitude of oscillation of the free cantilever and $Q = \frac{f_0}{\delta f}$ is its quality factor, with δf being the bandwidth of the resonance. This provides informations about the dissipative processes occurring between the tip and the sample. These may include the formation of contact between the tip and the surface, deformations of the surface or the probe, or uncompensated electrostatic forces which induce image charges in the tip or the sample, as well as a Joule-dissipation.

A.5 2D force spectroscopy

NC-AFM can also operate in spectroscopic mode, called *2D force spectroscopy* [397]. The advantage of this operational mode over the one mentioned in Section A.4 is that it is possible to recover the information on the forces F involved during the interaction between the tip and the sample [398]. In 2D force spectroscopy the variation of Δf as a function of the displacement

of the cantilever, z, is recorded. Considering a rigid surface and a rigid tip, one can assume that the interaction of the tip with the surface can be described by the equation of motion for a damped harmonic oscillator, with z being the only degree of freedom. Using this model, analytic expressions to determine $\Delta f(z)$ from $F(z)$ have been derived, which, however, are valid only for the of $F(z)$ over one entire oscillation cycle of the cantilever. The exact formula for their analytic inversion is not known, but efficient approximate procedures have been derived [338]. Nowadays, the most widely used one is that by Sader and Jarvis [399], which leads to accurate results over the entire range of amplitudes.

Once an $F(z)$ curve has been obtained, one can attempt to separate the different force component by subtracting the background due to the long range forces [400]. As explained in Section A.4, electrostatic forces can be eliminated by applying an external potential V_{bias} to suppress V_{cpd}. Similarly, the background due to vdW forces can be estimated by fitting the $F(z)$ curve, at large values of z, with an Hamaker-like model for a spherical tip of radius R:

$$F_{vdW}(z) = \frac{HR}{6\ z^2}, \tag{A.12}$$

where H is a material-dependent Hamaker constant.

One must be extremely careful about the current interpretation of $F(z)$. In fact, $F(z)$ represent the tip-sample force only under the assumption of a rigid tip and a rigid sample. In all the other cases, *e.g.*, in the presence of a deformation either of the tip or the sample, or both, $F(z)$ can only be associated to the overall response of the system.

B Electronic structure of the 1×1 *gr.*/Ru lattice-matched models

Despite the fact that they do not describe the formation of the *gr.*/Ru moiré, the lattice-matched 1×1 models provide a simple and intuitive way to obtain a qualitative insight into the electronic properties of *gr.*/Ru. In this Appendix, an analysis of the electronic structure of the three 1×1 models employed in this work is presented, and the results are compared with those obtained for the 11×11/10×10 lattice-mismatched unit cell (see Chapter 7), by comparing the LDOSs above the surface. For the present calculations, Ru(0001) slabs of 5 layers have been used. The distance between the graphene and the Ru(0001) topmost layer has been fixed to $d_{gr./Ru} = 2.2$ Å for the $1\times1-(Hcp-Top)$ and $1\times1-(Fcc-Top)$ models, and $d_{gr./Ru} = 3.4$ Å for the $1\times1-(Fcc-Hcp)$ model. These values are similar to the graphene-Ru(0001) distance in the low (2.195 Å) and high (3.385 Å) regions of the 11×11/10×10 DFT+D2/PBE *gr.*/Ru geometry. A computational set-up similar to that used in Chapter 6 and Chapter 7 has been used. However, in the present case, the Brillouin zone has been accurately sampled by using a Γ-centered 36×36×1 grid of k-points.

Fig. B.1 shows the band structure of the three 1×1 models along the high symmetry directions of the two-dimensional 1^{st} Brillouin zone, as well as the separate contribution of the $2p$ orbitals of the two graphene carbon atoms to each band - it should be noted that, in the energy range considered in Fig. B.1, the only relevant contribution comes from the carbon $2p_z$ orbitals. As shown in previous work [89], the strong interaction between graphene and Ru(0001) in the $1\times1-(Hcp-Top)$ and $1\times1-(Fcc-Top)$ models leads to the disruption of the Dirac cone characteristic of free-standing graphene (Fig. B.1 (a-d)). Due to the different interaction of the two carbon atoms with the metallic surface, the respective electronic bands are also modified differently. On the one hand, the bands with significant contribution on the Top carbon atoms are almost indistinguishable in the two models. On the other hand, differences can be observed for the bands associated with the carbons atom positioned at the hollow sites. In the $1\times1-(Hcp-Top)$ model, a well defined band appears at the K-point in the vicinity of the Fermi level, with a significant contribution of the carbon atom at the Hcp site. This band is absent in the $1\times1-(Fcc-Top)$ model, where the bands with a contribution from the carbon

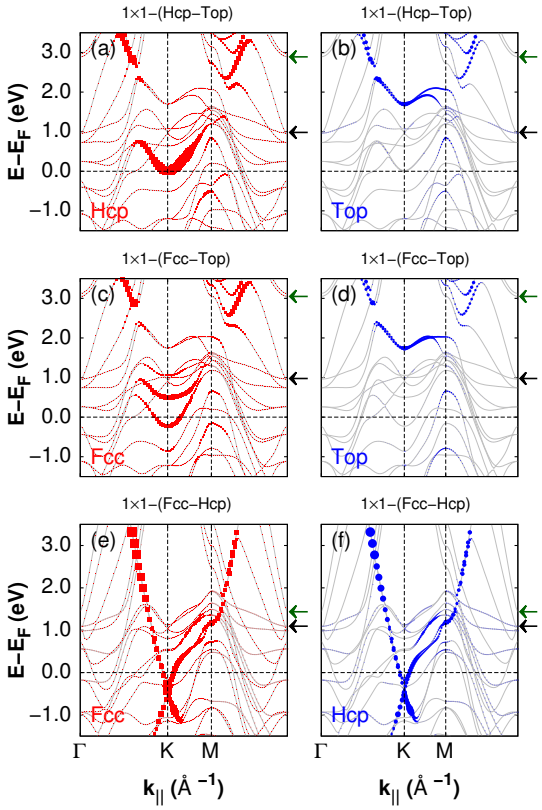

Figure B.1: Band structure of the strained 1×1 models (see Fig.1) along the $\Gamma \rightarrow K \rightarrow M \rightarrow \Gamma$ direction: (a,b) $1 \times 1 - (Hcp - Top)$ model, (c,d) $1 \times 1 - (Fcc - Top)$ model, (e,f) $1 \times 1 - (Fcc - Hcp)$ model. Red squares (a,c,b) and blue points (b,d,g) indicate the weight of the graphene *p*-states of each of the two carbon atoms of graphene (the label at the bottom left of each image indicate the adsorption site). The green and black arrows at the right side of each image indicates the position in energy at the Γ-point of the band associated with the *gr.*/Ru interface state, and with the Ru(0001) projected band gap at the Γ-point, respectively

atom at the *Fcc* site are much less defined. At difference with the models representative of the L regions of the *gr.*/Ru moiré, in the $1 \times 1 - (Fcc - Hcp)$ model the electronic bands of the graphene remain almost intact, becoming weakly n-doped, as evidenced by the downshift below the Fermi level of the Dirac cone (Fig. B.1 (e-f)).

Similarly, also the unoccupied electronic states above E_F exhibit a strong dependence on $d_{gr./Ru}$. Albeit the Ru(0001) gap at the Γ-point is reproduced only approximatively with just five ruthenium layers, its lower boundary at the Γ-point can still be identified at $E\text{-}E_F \sim 1$ eV (black arrows in Fig. B.1 (a-f)). Above this energy, the first band encountered at $E\text{-}E_F = 2.89$ eV ($E\text{-}E_F = 3.05$ eV) in the $1\times1-(Hcp-Top)$ ($1\times1-(Fcc-Top)$) model is associated with the interface state (green arrows in Fig. B.1 (a-d)). Notice that the *xy*-averaged probability density distributions of this state is very similar to the *xy*-averaged probability density distribution

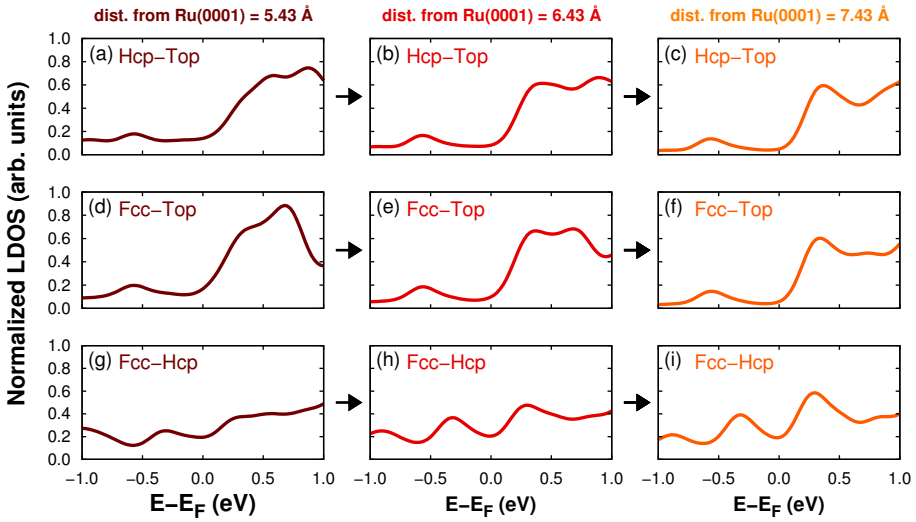

Figure B.2: LDOS computed for the $1 \times 1 - (Hcp - Top)$ (a-c), $1 \times 1 - (Fcc - Top)$ (d-f) and $1 \times 1 - (Fcc - Hcp)$ (g-i) models in the same energy range. The zero is set at the topmost layer of the Ru(0001) surface plane. The distance from the Ru(0001) topmost layer surface plane is 5.43 Å (a,d,g), 6.43 Å (b,e,h) and 7.43 Å (c,f,i). Arrows indicate the direction of increasing distance from the surface. The LDOSs have been normalized to have the same area under each curve.

obtained for the lowest eigenvalue of the new interface state in the 11×11/10×10 model (see Fig. 7.10). The situation is different in the $1 \times 1 - (Fcc - Hcp)$ model, where the larger separation between the graphene and the metal prevents the formation of the new interface state, but the Ru(0001) surface resonance state, which is promoted to a surface state due to the confinement induced by the presence of graphene, can be identified at E-E$_F$ = 1.43 eV (green arrows in Fig. B.1 (e-f)).

The analysis of the LDOSs is useful to obtain a more representative comparison between the electronic structure of the lattice-matched and the lattice-mismatched models. Fig. B.2 shows the LDOS obtained for the three models in the vicinity of the Fermi level. It can be seen that the features of the LDOSs calculated over the two L regions of the 11×11/10×10 model (see Fig. 7.6) are qualitatively reproduced by the LDOSs obtained for the corresponding 1×1 models. In particular, the pronounced asymmetry above and below E-E$_F$ = 0.0 eV is reproduced. In agreement with the results obtained for the lattice-mismatched unit cell, this asymmetry is not present in the $1 \times 1 - (Fcc - Hcp)$ model. In the latter, sharp peaks appear at E-E$_F$ = -0.35 eV and E-E$_F$ = 0.45 eV, at large distances form the surface. This behaviour is similar to that observed for the LDOS calculated using the lattice-mismatched model. In view of this, the close similarity between the shape of the LDOSs of the two models at 7.43 Å further confirms that the characteristics of the measured STS spectra in *gr.*/Ru are strongly connected with the electronic

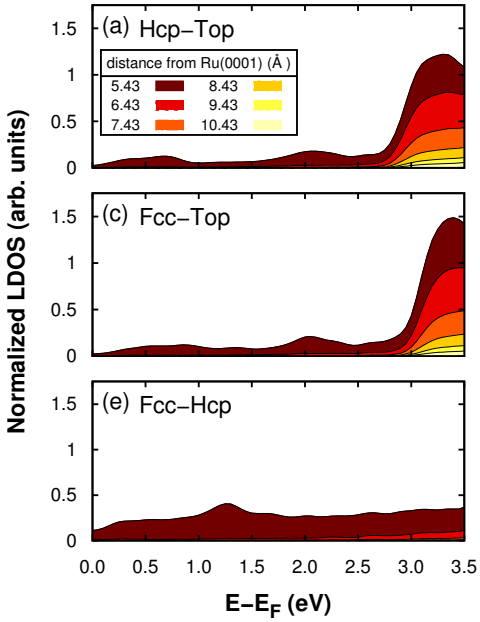

Figure B.3: Local density of states (LDOS) computed in the energy range 0.0 eV $\leq$ E-E$_F$ $\leq$ 3.5 eV above the $1\times1-(Hcp-Top)$ (a), $1\times1-(Fcc-Top)$ (c) and $1\times1-(Hcp-Fcc)$ (d) models. (b,e,f) The zero is set at the topmost layer of the Ru(0001) surface plane. In each panel, the LDOSs are normalized with respect to the area of the LDOS at 5.43 Å. The LDOS are printed with increasingly brighter colors depending on their distance from this plane.

structure of the metallic substrate underneath the graphene layer, which is described almost identically in the two models.

The 1×1 models also reproduce qualitatively the behaviour of the LDOS at larger distances from the surface observed for the lattice-mismatched model (see Fig. 7.8). Fig. B.3 shows the LDOSs obtained for the three models in the energy range 0.0 eV $\leq$ E-E$_F$ $\leq$ 3.5 eV. In the two models representative of the L regions of the moiré (Fig. B.3 (a) and Fig. B.3 (b)), the most remarkable feature is an intense peak located at E-E$_F$ $\sim$ 3.25 eV in the $1\times1-(Hcp-Top)$ model (Fig. B.3 (a)) and at E-E$_F$ $\sim$ 3.4 eV in the $1\times1-(Fcc-Top)$ model (Fig. B.3 (b)). Such peak decays very slowly into the vacuum, which indicates that the associated electronic states extend considerably outside the surface. On the other hand, the LDOS of the $1\times1-(Hcp-Fcc)$ model (Fig. B.3 (c)) exhibits a completely different behaviour, being essentially featureless, and decaying very rapidly when moving away from the surface. Therefore, this analysis shows that the unoccupied electronic structure above E-E$_F$ $\sim$ 3 eV is considerably more extended towards the

vacuum in those models representative of the lower regions of the graphene moiré, in agreement with the behaviour that should be expected for the new interface state.

C Influence of the tip orientation on the calculated force *versus* distance curves

It has been reported that, in some cases, the precise alignment of the nanotip can strongly influence its interaction with the surface [401, 402]. In the present case, this possiblity has been ruled out by calculating the $F(z)$ curves for two additional alignments of the nanotip with respect to graphene. In the calculations for the nanotip interacting with the H region of the graphene moiré (see Chapter 8), the nanotip is positioned over the graphene hill so that the lowest atom of the nanotip and the highest one of graphene are one on top of the other. For the theoretical $F(z)$ curves presented in Chapter 8, the tip apex dimer is oriented antiparallel to one of the three C-C bonds connecting the highest graphene atom. Starting from this geometry, a rotation of the tip around the surface normal of 180° and 30° results in the apex dimer being oriented parallel to the graphene C-C bond and tilted by 150° with respect to the graphene C-C bond, respectively (see schemes $\Phi = 180°$ and $\Phi = 30°$ in Fig. C.1). The $F(z)$ curves calculated for the $\Phi = 180°$ and $\Phi = 30°$ orientations of the tip (see Fig. C.1) show a very similar behaviour to those presented in Chapter 8 and no hysteresis loop. Additionally, it can be noticed that for Z $<$ 0.2 nm (i.e., in the repulsive regime), the calculated force shows a monotonous increase going from the antiparallel to the parallel orientation. This can be associated with the increasing repulsion between the electron clouds of the dimer apex and the graphene, because in this region the interaction is dominated by the short-range repulsive forces. A representative example of this trend is the force calculated at $z = 0.0$ nm, which changes from 0.64 nN for the antiparallel orientation to 1.10 nN for the parallel orientation. However, these small differences do not change the main result that the indentation maintains its reversible character independently of the precise nanotip orientation.

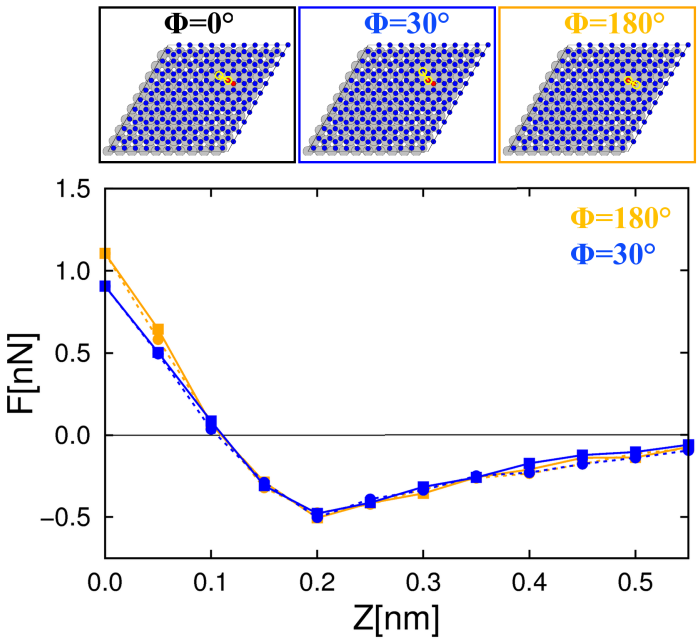

Figure C.1: Top panels: schematic views of the three different orientations of the tip considered with respect to the surface normal. The tip is oriented anti-parallel ($\Phi = 0°$, black), tilted by 150 ($\Phi = 30°$, blue) or parallel ($\Phi = 180°$, orange) to one of the C-C bonds connecting the highest atom of the graphene hill. Graphene and ruthenium atoms are printed in blue and grey, respectively. The yellow empty dots indicate the two silicon atoms of the nanotip apex dimer, the two red dots indicate the graphene C-C bond taken as reference. Bottom panel: Force (F) versus distance (Z) curves calculated for the $\Phi = 30°$ (blue curve) and $\Phi = 180°$ (orange curve) orientations of the silicon nanotip with respect to graphene honeycomb lattice (approach: solid; retraction: dashed).

D Bibliography

[1] K. S. Novoselov and et al. *Nature*, vol. 490, p. 192, 2012.

[2] I. P. O. Patent Informatics Team, "An analysis of worldwide patent filings relating to graphene." http://www.ipo.gov.uk/informatic-graphene.pdf.

[3] Q. Tannok *Nat. Mater.*, vol. 11, p. 2, 2012.

[4] "Graphene in the heart of europe, editorial," *Nat. Nanotech.*, vol. 8, p. 221, 2012.

[5] A. K. Geim *Rev. Mod. Phys.*, vol. 83, p. 851, 2011.

[6] K. S. Novoselov *Rev. Mod. Phys.*, vol. 83, p. 837, 2011.

[7] G. Brumfiel, "Andre geim: in praise of graphene." http://www.nature.com/news/2010/101007/full/news.2010.525.html.

[8] K. S. Novoselov, A. K. Geim, S. V. Morozov, D. Jiang, Y. Zhang, S. V. Dubonos, I. V. Grigorieva, and A. A. Firsov *Science*, vol. 306, p. 666, 2004.

[9] A. K. Geim and K. S. Novoselov *Nat. Mater.*, vol. 6, p. 183, 2007.

[10] A. K. Geim *Science*, vol. 324, p. 1530, 2009.

[11] N. D. Mermin *Phys. Rev.*, vol. 176, p. 250, 1968.

[12] L. D. Landau *Phys. Z. Sowjetunion*, vol. 11, p. 26, 1937.

[13] A. H. C. Neto, F. Guinea, and N. M. R. Peres *Phys. World*, vol. 19, p. 33, 2006.

[14] W. Andreoni, *The Physics of Fullerene-Based and Fullerene-Related Materials*. Berlin: Springer, 2000.

[15] J.-C. Charlier, X. Blase, and S. Roche *Rev. Mod. Phys.*, vol. 79, p. 677, 2007.

[16] A. H. C. Neto, F. Guinea, N. M. R. Peres, K. Novoselov, and A. Geim *Rev. Mod. Phys.*, vol. 81, p. 109, 2009.

[17] C. Lee, X. Wei, J. W. Kysar, and J. Hone *Science*, vol. 321, p. 385, 2008.

[18] P. R. Wallace *Phys. Rev.*, vol. 71, p. 622, 1947.

[19] K. Novoselov, A. Geim, S. Morozov, D. Jiang, M. Katsnelson, I. Grigorieva, S. Dubonos, and A. Firsov *Nature*, vol. 438, p. 197, 2005.

[20] A. Bostwick and et al. *Prog. Surf. Sci.*, vol. 84, p. 380, 2009.

[21] S. D. Sarma and et al. *Rev. Mod. Phys.*, vol. 83, p. 407, 2011.

[22] M. I. Katsnelson *Mater. Today*, vol. 10, p. 20, 2006.

[23] S. V. Morozov, K. S. Novoselov, M. I. Katsnelson, F. Schedin, D. C. Elias, J. A. Jaszczak, and A. K. Geim *Phys. Rev. Lett.*, vol. 100, p. 016602, 2008.

[24] A. S. Mayorov and et al. *Nano Lett.*, vol. 11, p. 2396, 2011.

[25] K. Kim and et al. *Nature*, vol. 457, p. 706, 2009.

[26] S. Bae and et al. *Nat. Nanotech.*, vol. 5, p. 574, 2010.

[27] A. A. Baladin and et al. *Nano Lett.*, vol. 8, p. 902, 2008.

[28] R. M. Martin, *Electronic Structure, Basic Theory and Practical Methods.* Cambridge: Cambridge University Press, 2004.

[29] V. M. Silkin, J. Zhao, F. Guinea, E. V. Chulkov, P. M. Echenique, and H. Petek *Phys. Rev. B*, vol. 80, p. 121408, 2009.

[30] P. M. Echenique and J. B. Pendry *J. Phys.: Condens. Matter*, vol. 11, p. 2065, 1978.

[31] E. V. Chulkov, A. G. Borisov, J. P. Gauyacq, D. Sánchez-Portal, V. M. Silkin, V. P. Zhukov, and P. M. Echenique *Chem. Rev.*, vol. 106, p. 4160, 2006.

[32] X. Wang, L. Zhi, and K. Muellen *Nano Lett.*, vol. 8, p. 323, 2008.

[33] C. Berger and et al. *J. Phys. Chem. B*, vol. 108, p. 19912, 2004.

[34] Y. Zhu and et al. *Adv. Mater.*, vol. 22, p. 3906, 2010.

[35] F. Bonaccorso and et al. *Nat. Photonics*, vol. 4, p. 611, 2010.

[36] V. S. et al. *Progress in Material Science*, vol. 56, p. 1178, 2011.

[37] Y. M. Lin and et al. *Science*, vol. 327, p. 662, 2010.

[38] Y. Wu and et al. *Nature*, vol. 472, p. 74, 2011.

[39] J. S. Bunch, A. M. van der Zande, S. S. Verbridge, I. W. Frank, D. M. Tanenbaum, J. M. Parpia, H. G. Craighead, and P. L. McEuen *Science*, vol. 315, p. 490, 2007.

[40] C. Chen, S. Rosenblatt, K. I. Bolotin, W. Kalb, P. Kim, I. Kymissis, H. L. Stormer, T. F. Heinz, and J. Hone *Nat. Nanotech.*, vol. 4, p. 861, 2009.

[41] F. Schwierz *Nat. Nanotech*, vol. 5, p. 487, 2010.

[42] H. Y. M. et al. *Prog. Surf. Sci.*, vol. 88, p. 132, 2013.

[43] S. N. et al. *J. Phys. Chem. Lett.*, vol. 2, p. 2487, 2011.

[44] V. G. et al. *Chem. Rev.*, vol. 112, p. 6156, 2012.

[45] R. Balog and et al. *Nat. Mater.*, vol. 9, p. 315, 2010.

[46] J. Zhou and et al. *Nano Lett.*, vol. 9, p. 3867, 2009.

[47] D. J. et al. *J. Phys. Chem B*, vol. 110, p. 23628, 2006.

[48] M. Q. et al. *ACS Nano*, vol. 4, p. 3527, 2010.

[49] E. Bekyarova *J. Am. Chem. Soc.*, vol. 131, p. 1336, 2009.

[50] P. Huang, L. Jing, H. Zhu, and X. Gao *Acc. Chem. Res.*, vol. 46, p. 43, 2012.

[51] K. P. Loh and et al. *J. Mater. Chem.*, vol. 20, p. 2277, 2010.

[52] H. Liu, Y. Liu, and D. Zhu *J. Mater. Chem.*, vol. 21, p. 3335, 2011.

[53] F. S. et al. *Nat. Mater.*, vol. 6, p. 562, 2007.

[54] T. O. Wehling and et al. *Nano Lett.*, vol. 8, p. 173, 2008.

[55] S. K. M. et al. *Nat. Nanotech.*, vol. 6, p. 162, 2011.

[56] T. Nelson and et al. *Nano Lett.*, vol. 10, p. 3237, 2010.

[57] Z. Zhang and et al. *J. Phys. Chem. Lett.*, vol. 2, p. 2897, 2011.

[58] W. Chen and et al. *Prog. Surf. Sci.*, vol. 84, p. 279, 2009.

[59] X. Tian and et al. *J. Phys. Chem. C*, vol. 114, p. 20917, 2010.

[60] S. Kozlov, F. Viñes, and A. Görling *Adv. Mater.*, vol. 23, p. 2638, 2011.

[61] X. Tian and et al. *J. Phys. Chem. B*, vol. 113, p. 11377, 2010.

[62] J. T. Sun and et al. *Phys. Rev. B*, vol. 81, p. 155403, 2010.

[63] Y. H. Lu and et al. *J. Phys. Chem. B*, vol. 113, p. 2, 2009.

[64] W. Chen and et al. *J. Am. Chem. Soc.*, vol. 129, p. 10418, 2007.

[65] C. Coletti and et al. *Phys. Rev. B*, vol. 81, p. 235401, 2010.

[66] M. Kim and et al. *Nano Lett.*, vol. 12, p. 182, 2011.

[67] J.-M. Lehn *Angew. Chem. Int. Ed.*, vol. 27, p. 89, 1989.

[68] J.-M. Lehn, *Supramolecular Chemistry, Concepts and Perspectives*. Weinheim: VCH, 1995.

[69] C. Oshima and A. Nagashima *J. Phys. Condens. Matter*, vol. 9, p. 1, 1997.

[70] J. Wintterlin and M. L. Bocquet *Surf. Sci.*, vol. 603, p. 1841, 2009.

[71] H. Zi-Pu, D. Ogletree, M. V. Hove, and G. Somorjai *Surf. Sci.*, vol. 180, p. 433, 1987.

[72] B. Lang *Surf. Sci.*, vol. 53, p. 317, 1975.

[73] J. T. Grant and T. W. Haas *Surf. Sci.*, vol. 21, p. 76, 1970.

[74] P. W. Sutter, J.-I. Flenge, and E. A. Sutter *Nat. Mater.*, vol. 7, p. 406, 2008.

[75] A. L. V. de Parga, F. Calleja, B. Borca, M. C. G. P. Jr., J. J. Hinarejos, F. Guinea, and R. Miranda *Phys. Rev. Lett.*, vol. 100, p. 056807, 2008.

[76] K. S. Novoselov and et al. *Proc. Nat. Acad. Sci.*, vol. 102, p. 10451, 2005.

[77] M. Batzill *Surf. Sci. Rep.*, vol. 67, p. 83, 2012.

[78] X. Li and et al. *Science*, vol. 324, 2009.

[79] G. Giovannetti, P. A. Khomyakov, G. Brocks, V. M. Karpan, J. van den Brink, and P. J. Kelly *Phys. Rev. Lett.*, vol. 101, p. 026803, 2008.

[80] V. M. Karpan, G. Giovannetti, P. A. Khomyakov, M. Talanana, A. A. Starikov, M. Zwierzycki, J. van den Brink, G. Brocks, and P. J. Kelly *Phys. Rev. Lett.*, vol. 99, p. 176602, 2007.

[81] B. Hammer and J. K. Norskov *Adv. Synth. Catal.*, vol. 45, p. 71, 2000.

[82] L. Gao, J. R. Guest, and N. P. Guisinger *Nano Lett.*, vol. 10, p. 3512, 2010.

[83] P. Merino, M. Svec, A. L. Pinnardi, G. Otero, and J. A. Martin-Gago *ACS Nano*, vol. 5, p. 5627, 2011.

[84] P. Sutter, J. T. Sadowski, and E. Sutter *Phys. Rev. B*, vol. 80, p. 245411, 2009.

[85] J. Coraux and et al. *Nano Lett.*, vol. 8, p. 565, 2008.

[86] E. Longinova and et al. *Phys. Rev. B*, vol. 80, p. 085430, 2009.

[87] I. Pletikosić, M. Kralj, P. Pervan, R. Brako, J. Coraux, A. T. N'Diaye, C. Busse, and T. Michely *Phys. Rev. Lett.*, vol. 102, p. 056808, 2009.

[88] C. Busse, P. Lazić, R. Djemour, J. Coraux, T. Gerber, N. Atodiresei, V. Caciuc, R. B. A. T. N'Diaye, S. Blügel, J. Zegenhagen, and T. Michely1 *Phys. Rev. Lett.*, vol. 107, p. 036101, 2011.

[89] B. Wang, M. L. Bocquet, S. Marchini, S. Günther, and J. Wintterlin *Phys. Chem. Chem. Phys.*, vol. 10, p. 3530, 2008.

[90] E. Miniussi, M. Pozzo, A. Baraldi, E. Vesselli, R. R. Zhan, G. Comelli, T. O. Menteş, M. A. Niño, A. Locatelli, S. Lizzit, and D. Alfè *Phys. Rev. Lett.*, vol. 106, p. 216101, 2011.

[91] D. Eom and et al. *Nano Lett.*, vol. 9, p. 2844, 2009.

[92] B. Wang, M. Caffio, C. Bromley, H. Früchtl, and R. Schaub *ACS Nano*, vol. 10, p. 5773, 2010.

[93] S. M. Kozlov, F. Viñes, and A. Görling *J. Phys. Chem. C*, vol. 116, p. 7360, 2012.

[94] Y. Gamo, A. Nagashima, M.Wakabayashi, M. Terai, and C. Oshima *Surf. Sci.*, vol. 374, p. 61, 1997.

[95] T. Brugger, S. Günther, B. Wang, J. H. Dil, M.-L. Bocquet, J. Osterwalder, J. Wintterlin, and T. Greber *Phys. Rev. B*, vol. 79, p. 045407, 2009.

[96] P. Sutter, M. S. Hybertsen, J. T. Sadowski, and E. Sutter *Nano Lett.*, vol. 9, p. 2654, 2009.

[97] A. VArykhalov and et al. *Phys. Rev. Lett.*, vol. 101, p. 157601, 2008.

[98] S. Marchini, S. Günther, and J. Wintterlin *Phys. Rev. B*, vol. 76, p. 075429, 2007.

[99] M. Iannuzzi and J. Hutter *Surf. Sci.*, vol. 605, p. 1360, 2011.

[100] W. Moritz, B. Wang, M. L. Bocquet, T. Brugger, T. Greber, and J. Wintterlin *Phys. Rev. Lett.*, vol. 104, p. 136102, 2010.

[101] K. Hermann *J. Phys.: Condens. Matter*, vol. 24, p. 314210, 2012.

[102] A. B. Preobrajenski, M. L. N. A. S. Vinogradov, and N. Mårtensson *Phys. Rev. B*, vol. 78, p. 073401, 2008.

[103] B. Borca, S. Barja, M. Garnica, D. Sanchez-Portal, V. Silkin, E. V. Chulkov, C. F. Hermanns, J. J. Hinarejos, A. L. V. de Parga, A. Arnau, P. M. Echenique, and R. Miranda, "Potential energy landscape for hot electrons in periodically nanostructured graphene," *Phys. Rev. Lett.*, vol. 105, p. 036804, 2010.

[104] E. Sutter, D. P. Acharya, J. T. Sadowski, and P. Sutter *Appl. Phys. Lett.*, vol. 94, p. 133101, 2009.

[105] R. Otero, J. M. Gallego, A. L. V. de Parga, N. Martín, and R. Miranda *Adv. Mater.*, vol. 23, p. 5148, 2011.

[106] L. Bartels *Nature Chem.*, vol. 2, p. 87, 2010.

[107] J. V. Barth, G. Constantini, and K. Kern *Nature*, vol. 437, p. 671, 2005.

[108] J. V. Barth *Ann. Rev. Phys. Chem.*, vol. 58, p. 375, 2007.

[109] F. Rosei and et al. *Prog. Surf. Sci.*, vol. 71, p. 95, 2003.

[110] K. Sakakibara, J. P. Hill, and K. Ariga *Small*, vol. 7, p. 1288, 2011.

[111] P. Peumans, S. Uchida, and S. R. Forrest *Nature*, vol. 425, p. 158, 2003.

[112] T. C. Tseng, C. Urban, Y. Wang, R. Otero, S. L. Tait, M. Alcamí, D. Écija, M. Trelka, J. M. Gallego, N. Lin, M. Konuma, U. Starke, A. Nefedov, A. Langner, C. Wöll, M. A. Herranz, F. Martín, N. Martín, K. Kern, and R. Miranda *Nat. Chem.*, vol. 2, p. 374, 2010.

[113] I. Fernández-Torrente, K. J. Franke, and J. I. Pascual *Int. J. Mass Spectrom.*, vol. 277, p. 269, 2008.

[114] H. Ishii, K. Sugiyama, E. Ito, and K. Seki *Adv. Mater.*, vol. 11, p. 605, 1999.

[115] S. D. Feyter and F. C. D. Schryver *Chem. Soc. Rev.*, vol. 32, p. 139, 2003.

[116] R. Otero, M. Schöck, L. M. Molina, E. Laegsgaard, I. Stensgaard, B. Hammer, and F. Besenbacher *Angew. Chem. Int. Ed.*, vol. 44, p. 2270, 2005.

[117] J. V. Barth, J. Weckesser, C. Cai, P. Günter, L. Bürgi, O. Jeandupeux, and K. Kern *Angew. Chem. Int. Ed.*, vol. 39, p. 1230, 2000.

[118] J. A. Theobald, N. S. Oxtoby, M. A. Phillips, N. R. Champness, and P. H. Beton *Nature*, vol. 424, p. 1029, 2003.

[119] P. Hana and P. S. Weiss *Surf. Sci. Rep.*, vol. 67, p. 19, 2012.

[120] G. M. Rangger, O. T. Hofmann, L. Romaner, G. Heimel, B. Bröker, R.-P. Blum, R. L. Johnson, N. Koch, and E. Zojer *Phys. Rev. B*, vol. 79, p. 165306, 2009.

[121] L. Romaner, G. Heimel, J.-L. Brédas, A. Gerlach, F. Schreiber, R. L. Johnson, J. Zegenhagen, S. Duhm, N. Koch, and E. Zojer *Phys. Rev. Lett.*, vol. 99, p. 256801, 2007.

[122] S. Bedwani, D. Wegner, M. F. Crommie, and A. Rochefort *Phys. Rev. Lett.*, vol. 101, p. 216105, 2008.

[123] J. Mao, H. Zhang, Y. Jiang, Y. Pan, M. Gao, W. Xiao, and H.-J. Gao *J. Am. Chem. Soc.*, vol. 131, p. 14136, 2009.

[124] A. J. Pollard, E. W. Perkins, N. A. Smith, A. Saywell, G. Goretzki, A. G. Phillips, S. P. Argent, H. Sachdev, F. Müller, S. Hüfner, S. Gsell, M. Fischer, M. Schreck, J. Osterwalder, T. Greber, S. Berner, N. R. Champness, and P. H. Beton *Angew. Chem. Int. Ed.*, vol. 49, p. 1, 2010.

[125] Q. H. Wang and M. C. Hersam *Nat. Chem.*, vol. 1, p. 206, 2009.

[126] P. Liljeroth, J. Repp, and G. Meyer *Science*, vol. 217, p. 1203, 2007.

[127] J. Repp, G. Meyer, S. M. Stojkovic, A. Gourdon, and C. Joachim *Phys. Rev. Lett.*, vol. 94, p. 026803, 2005.

[128] H. T. Zhou, J. H. Mao, G. Li, Y. L. Wang, X. L. Feng, S. X. Du, K. Müllen, and H.-J. Gao *Appl. Phys. Lett.*, vol. 99, p. 153101, 2011.

[129] H. G. Zhang and et al. *Phys. Rev. B*, vol. 84, p. 245436, 2011.

[130] M. Roos and et al. *J. Am. Chem. Soc.*, vol. 9208, p. 133, 2011.

[131] H. Zhang and et al. *J. Phys. Chem. C*, vol. 11091, p. 116, 2012.

[132] J. Lu and et al. *ACS Nano*, vol. 6, p. 944, 2012.

[133] K. Yang and et al. *J. Phys. Chem. C*, vol. 116, p. 14052, 2012.

[134] S. Barja and et al. *Chem. Commun.*, vol. 46, p. 8198, 2010.

[135] W. Hofer and J. Redinger *Surf. Sci.*, vol. 447, p. 51, 2000.

[136] D. S. Acker and W. R. Hertler *J. Am. Chem. Soc.*, vol. 84, p. 3370, 1962.

[137] D. Martoccia, P. R. Willmott, T. Brugger, M. Björck, S. Günther, C. M. Schlepütz, A. Cervellino, S. A. Pauli, B. D. Patterson, S. Marchini, J. Wintterlin, W. Moritz, and T. Greber *Phys. Rev. Lett.*, vol. 101, p. 126102, 2008.

[138] D. Martoccia, M. Björck, C. M. Schlepütz, T. Brugger, S. A. Pauli, B. D. Patterson, T. Greber, and P. R. Willmott *New J. Phys.*, vol. 12, p. 043028, 2010.

[139] A. L. V. de Parga, F. Calleja, B. Borca, M. C. G. P. Jr., J. J. Hinarejos, F. Guinea, and R. Miranda *Phys. Rev. Lett.*, vol. 101, p. 099704, 2008.

[140] B. Wang, M. L. Bocquet, S. Günther, and J. Wintterlin *Phys. Rev. Lett.*, vol. 101, p. 099703, 2008.

[141] B. Borca, S. Barja, M. Garnica, D. Sánchez-Portal, V. M. Silkin, E. V. Chulkov, C. F. Hermanns, J. J. Hinarejos, A. L. Vázquez de Parga, A. Arnau, P. M. Echenique, and R. Miranda *Phys. Rev. Lett.*, vol. 105, p. 219702, 2010.

[142] H. G. Zhang, H. Hu, Y. Pan, J. H. Mao, M. Gao, H. M. Guo, S. X. Du, T. Greber, and H.-J. Gao *J. Phys.: Condens. Matter*, vol. 22, p. 302001, 2010.

[143] H. G. Zhang and T. Greber *Phys. Rev. Lett.*, vol. 105, p. 219701, 2010.

[144] B. Borca, S. Barja, M. Garnica, M. Minniti, A. Politano, J. M. Rodriguez-García, J. J. Hinarejos, D. Farías, A. L. V. de Parga, and R. Miranda *New. J. Phys.*, vol. 12, p. 093018, 2010.

[145] M. Gyamfi, T. Eelbo, M. Waśniowska, and R. Wiesendanger *Phys. Rev. B*, vol. 83, p. 153418, 2011.

[146] W. Koch and M. C. Holthausen, *A Chemist's Guide to Density Functional Theory*. Weinheim: Wiley-VCH Verlag, 2001.

[147] S. Grimme *J. Comp. Chem.*, vol. 27, p. 1787, 2006.

[148] G. Binnig, H. Rohrer, C. Gerber, and E. Weibel *Appl. Phys. Lett.*, vol. 40, p. 178, 1982.

[149] G. Binnig, H. Rohrer, C. Gerber, and E. Weibel *Phys. Rev. Lett.*, vol. 49, p. 57, 1982.

[150] G. Binnig, C. F. Quate, and C. Gerber *Phys. Rev. Lett.*, vol. 56, p. 930, 1986.

[151] B. Milián, R. Pou-Amérigo, R. Viruela, and E. Ortí *Chem. Phys. Lett.*, vol. 391, p. 148, 2004.

[152] B. Milián, R. Pou-Amérigo, R. Viruela, and E. Ortí *J. Mol. Struct*, vol. 709, p. 97, 2004.

[153] C. Klots, R. Compton, and V. Raaen *J. Chem . Phys.*, vol. 60, p. 1177, 1974.

[154] R. Compton and C. Cooper *J. Chem. Phys.*, vol. 66, p. 4325, 1977.

[155] L. B. Coleman *Solid State Commun.*, vol. 12, p. 1125, 1973.

[156] R. Jain and et al. *Nature*, vol. 445, p. 192, 2007.

[157] E. Shröedinger *Phys. Rev.*, vol. 28, p. 1049, 1926.

[158] H. Hellmann, *Einfuhrung in die Quantenchemie*. Liepzig: Franz Deuticke, 1937.

[159] R. Feynman *Phys. Rev.*, vol. 56, p. 340, 1939.

[160] B. M. Deb *Rev. Mod. Phys.*, vol. 45, p. 22, 1973.

[161] P. Pulay *Mol. Phys.*, vol. 17, p. 197, 1969.

[162] M. Born and R. Oppenheimer *Annalen der Physik*, vol. 84, p. 457, 1927.

[163] J. T. Bruer *Synthese*, vol. 50, p. 167, 1970.

[164] A. Messiah, *Quantum Mechanics*. New York: Dover, 1991.

[165] W. Kołos *Adv. Quant. Chem.*, vol. 5, p. 99, 1970.

[166] J. C. Tully, in *Moder Methods for multidimensional dynamics computations in Chemistry*. London: World Scientific, 1998.

[167] H. Goldstein, C. Poole, and J. Safko, *Classical Mechanics*. San Francisco: Addison Wesley, 2002.

[168] A. Bravais, "Mémoire sur les systèmes formés par les points distribués rgulièrement sur un plan ou dans l'espace," *J. Ecole Polytech.*, vol. 1, p. 128, 1850.

[169] V. Heine, *Group Theory*. New York: Pergamon Press, 1960.

[170] J. C. Slater, *Symmetry and Energy Bands in Crystals*. New York: Dover, 1972.

[171] N. W. Ashcroft and N. D. Mermin, *Solid State Physics*. Philadelphia: W. B. Sanders Company, 1976.

[172] W. Setyawan and S. Curtarolo *Comput. Mat. Sci.*, vol. 39, p. 299, 2010.

[173] A. Baldereschi *Phys. Rev. B*, vol. 7, p. 5212, 1973.

[174] D. J. Chadi and M. L. Cohen *Phys. Rev. B*, vol. 8, p. 5747, 1973.

[175] H. J. Monkhorst and J. D. Pack *Phys. Rev. B*, vol. 13, p. 5188, 1976.

[176] O. Jepsen and O. K. Andresen *Solid State Commun.*, vol. 9, p. 1763, 1971.

[177] P.E.Blöchl, O. Jepsen, and O. K. Andersen *Phys. Rev. B*, vol. 49, p. 16223, 1994.

[178] C.-L. Fu and K.-M. Ho *Phys. Rev. B*, vol. 28, p. 5480, 1983.

[179] K.-M. Ho, C.-L. Fu, B. N. Harmon, W. Weber, and D. R. Hamann *Phys. Rev. Lett.*, vol. 49, p. 673, 1982.

[180] R. J. Needs, R. M. Martin, and O. H. Nielsen *Phys. Rev. B*, vol. 33, p. 3778, 1986.

[181] M. Methfessel and A. T. Paxton *Phys. Rev. B*, vol. 40, p. 3616, 1989.

[182] L. A. Thomas *Phil. Roy. Soc.*, vol. 23, p. 542, 1927.

[183] E. Fermi *Rend. Accad. Naz. Lincei*, vol. 6, p. 602, 1927.

[184] E. Teller *Rev. Mod. Phys.*, vol. 34, p. 627, 1962.

[185] J. W. Sheldon *Phys. Rev.*, vol. 99, p. 1291, 1955.

[186] N. Balzas *Phys. Rev.*, vol. 156, p. 42, 1967.

[187] E. H. Lieb and B. Simon *Phys. Rev. Lett.*, vol. 31, p. 681, 1973.

[188] P. Hohenberg and W. Kohn *Phys. Rev.*, vol. 136, p. B864, 1964.

[189] W. Kohn *Rev. Mod. Phys.*, vol. 71, p. 1253, 1999.

[190] M. Levy *Proc. Nat. Acad. Sci.*, vol. 76, p. 6062, 1979.

[191] M. Levy *Phys. Rev. A*, vol. 26, p. 1200, 1982.

[192] E. Lieb *Int. J. Quant. Chem.*, vol. 24, p. 243, 1983.

[193] W. Kohn and L. J. Sham *Phys. Rev.*, vol. 140, p. A1133, 1965.

[194] J. C. Slater *Phys. Rev.*, vol. 81, p. 395, 1951.

[195] J. P. Perdew and A. Zunger *Phys. Rev. B*, vol. 23, p. 5048, 1981.

[196] J. P. Perdew and Y. Wang *Phys. Rev. B*, vol. 45, p. 13224, 1992.

[197] D. M. Ceperley and B. J. Alder *Phys. Rev. Lett.*, vol. 45, p. 566, 1980.

[198] R. G. Parr and W. Yang, *Density-Functional Theory of Atoms and Molecules*. Oxford: Oxford University Press, 1994.

[199] R. O. Jones and O. Gunnarson *Rev. Mod. Phys.*, vol. 61, p. 689, 1989.

[200] D. C. Langreth and M. J. Mehl *Phys. Rev. B*, vol. 28, p. 1809, 1983.

[201] M. Scheffler and C. Stampfl, *Theory of adsorption on metal substrates, in: Handbook of Sur- face Science, Handbook of Surface Science, Vol. 2, ed. by K. Horn and M. Scheffler.* Amsterdam: Elsevier, 2000.

[202] F. Hermann, J. P. V. Dyke, and I. P. Ortenburger *Phys. Rev. Lett.*, vol. 22, p. 807, 1969.

[203] J. P. Perdew *Phys. Rev. B*, vol. 33, p. 8822, 1986.

[204] A. D. Becke *Phys. Rev. A*, vol. 38, p. 3098, 1988.

[205] J. P. Perdew, K. Burke, and M. Ernzerhof *Phys. Rev. Lett.*, vol. 77, p. 3865, 1996.

[206] B. Hammer, L. B. Hansen, and J. K. Nørskov *Phys. Rev. B*, vol. 59, p. 7413, 1999.

[207] J. P. Perdew, J. A. Chevary, S. H. Vosko, K. A. Jackson, M. R. Pederson, D. J. Singh, and C. Fiolhais *Phys. Rev. B*, vol. 46, p. 6671, 1992.

[208] U. von Barth and L. Hedin *Journal of Physics C: Solid State Physics*, vol. 5, p. 1629, 1972.

[209] J. Kübler, K.-H. Hock, J. Sticht, and A. R. Williams *J. Phys. F: Met. Phys.*, vol. 18, p. 469, 1988.

[210] G. te Velde, F. Bickelhaupt, S. van Gisbergen, C. F. Guerra, E. Baerends, J. Snijders, and T. Ziegler *J. Comput. Chem.*, vol. 22, p. 931, 2001.

[211] J. M. Soler, E. Artacho, J. D. Gale, A. Garca, J. Junquera, P. Ordejón, and D. Sánchez-Portal *J. Phys.: Condens. Matt.*, vol. 14, p. 2745, 2002.

[212] J. VandeVondele, M. Krack, F. Mohamed, M. Parrinello, T. Chassaing, and J. Hutter *Comput. Phys. Commun.*, vol. 167, p. 103, 2005.

[213] V. Blum, R. Gehrke, F. Hanke, P. Havu, V. Havu, X. Ren, K. Reuter, and M. Scheffler *Comput. Phys. Commun.*, vol. 180, p. 2175, 2009.

[214] L. Genovese, A. Neelov, S. Goedecker, T. Deutsch, S. A. Ghasemi, A. Willand, D. Caliste, O. Zilberberg, M. Rayson, A. Bergman, and R. Schneider *J. Chem. Phys.*, vol. 129, p. 014109, 2008.

[215] M. C. Payne, M. P. Teter, D. C. Allan, T. A. Arias, and J. D. Joannopulos *Rev. Mod. Phys.*, vol. 64, p. 1045, 1992.

[216] R. Car and M. Parrinello *Phys. Rev. Lett.*, vol. 55, p. 2471, 1985.

[217] M. P. Teter, M. C. Payne, and D. C. Allan *Phys. Rev. B*, vol. 40, p. 12255, 1989.

[218] I. Stich, R. Car, M. Parrinello, and S. Baroni *Phys. Rev. B*, vol. 40, p. 12255, 1989.

[219] M. J. Gillian *J. Phys.: Condens. Matter*, vol. 1, p. 689, 1989.

[220] D. M. Wood and A. Zunger *J. Phys. A: Math. Gen.*, vol. 18, p. 1343, 1984.

[221] J. L. Martins and M. L. Cohen *Phys. Rev. B*, vol. 37, p. 6134, 1988.

[222] G. Kresse and J. Futhmüller *Computational Material Science*, vol. 6, p. 15, 1996.

[223] G. Kresse and J. Futhmüller *Phys. Rev. B*, vol. 28, p. 5480, 1996.

[224] P. E. Blochl and M. Parrinello *Phys. Rev. B*, vol. 45, p. 9413, 1992.

[225] G. Pastore, E. Smargiassi, and F. Buda *Phys. Rev. A*, vol. 44, p. 6334, 1991.

[226] E. R. Davison *J. Comp. Phys.*, vol. 17, p. 87, 1975.

[227] P. Pulay *Chem. Phys.Lett.*, vol. 73, p. 393, 1980.

[228] D. M. Bylander and L. K. nad S. Lee *Phys. Rev. B*, vol. 42, p. 1934, 1990.

[229] G. P. Kerker *Phys. Rev. B*, vol. 23, p. 3082, 1981.

[230] C. G. Broyden *Mathematics of Computation*, vol. 19, p. 577, 1965.

[231] G. P. Srivastava *J. Phys. A: Math. Gen.*, vol. 17, p. L317, 1984.

[232] D. Vanderbilt and S. G. Louie *Phys. Rev. B*, vol. 23, p. 6118, 1984.

[233] D. D. Johnson *Phys. Rev. B*, vol. 38, p. 12807, 1988.

[234] N. Marzari, *Ab-initio Molecular Dynamics for Metallic Systems*. University of Cambridge: Pembroke College, 1996.

[235] J. F. Janak *Phys. Rev. B*, vol. 18, p. 7165, 1978.

[236] N. D. Mermin *Phys. Rev. A*, vol. 137, p. 1441, 1965.

[237] M. Weinert and J. W. Davenport *Phys. Rev. B*, vol. 45, p. 13709, 1992.

[238] R. M. Wentzcovitch, J. L. Martins, and P. B. Allen *Phys. Rev. B*, vol. 45, p. 11372, 1992.

[239] A. de Vita and M. J. Gillian *J Phys.: Cond. Matter*, vol. 3, p. 6225, 1991.

[240] S. de Gironcoli *Phys. Rev. B*, vol. 51, p. 6773, 1995.

[241] F. Wagner, T. Laloyaux, and M. Scheffler *Phys. Rev. B*, vol. 57, p. 2102, 1998.

[242] A. Szlabo and N. L. Ostlund, *Modern Quantum Chemistry: Introduction to Advanced Electronic Structure Theory*. New York: Dover, 1996.

[243] S. F. Boys *Proc. Roy. Soc. London, series A*, vol. 200, p. 542, 1950.

[244] J. C. Slater *Phys. Rev.*, vol. 36, p. 57, 1930.

[245] W. J. Hehre, L. Radom, P. Schleyer, and J. A. Pople, *Ab Initio Molecular Orbital Theory*. New York: Wiley, 1986.

[246] P. Blöchl *Phys. Rev. B*, vol. 50, p. 17953, 1994.

[247] D. J. Singh, *Plane Waves, Pseudopotentials and the LAPW Method*. Norwell, MA: Kluwer Academic, 1994.

[248] N. Troullier and J. L. Martins *Phys. Rev. B*, vol. 43, p. 1993, 1993.

[249] D. R. Hamann, M. Shülter, and C. Chiang *Phye. Rev. Lett.*, vol. 43, p. 1494, 1979.

[250] L. Kleinman and D. M. Bylander *Phys. Rev. Lett.*, vol. 48, p. 1425, 1982.

[251] G. Kresse and D. Joubert *Phys. Rev. B*, vol. 59, p. 1758, 1999.

[252] D. Vanderbilt *Phys. Rev. B*, vol. 43, p. 7892, 1990.

[253] D. D. Koelling and B. N. Harmon *J. Phys. C: Solid State Phys.*, vol. 10, p. 3107, 1977.

[254] S. Grimme *WIREs Computational Molecular Science*, vol. 1, p. 211, 2011.

[255] X. Wu, M. C. Vargas, S. Nayak, V. Lotrich, and G. Scoles *J. Chem. Phys.*, vol. 115, p. 8748, 2001.

[256] D. C. Langreth, B. I. Lundqvist, S. D. Chakarova-Käck, V. R. Cooper, M. Dion, P. Hyldgaard, A. Kelkkanen, J. Kleis, L. Kong, S. Li, P. G. Moses, E. Murray, A. Puzder, H. Rydberg, E. Schröder, and T. Thonhauser *J. Phys.: Condens. Matt.*, vol. 21, p. 084203, 2009.

[257] R. Ahlrichs, R. Penco, and G. Scoles *Chem. Phys.*, vol. 19, p. 119, 1977.

[258] S. J. A. van Gisbergen, J. G. Snijders, and E. J. Baerends *J. Chem. Phys.*, vol. 103, p. 9347, 1995.

[259] T. Bučko, J. Hafner, S. Lebègue, and G. Ángyán *J. Phys. Chem. A*, vol. 114, p. 114, 2010.

[260] M. Elstner, P. Hobza, T. Frauenheim, S. Suhai, and E. Kaxiras *J. Chem. Phys.*, vol. 114, p. 5419, 2001.

[261] S. Grimme *J. Comp. Chem.*, vol. 25, p. 1463, 2004.

[262] Q. Wu and W. Yang *J. Chem. Phys.*, vol. 116, p. 515, 2002.

[263] A. Tkatchenko, L. Romaner, O. T. Hofmann, E. Zojer, C. Ambrosch-Draxl, and M. Scheffler *MRS Bullettin*, vol. 35, p. 435, 2010.

[264] J. Klimes and Michaelides *J. Chem. Phys.*, vol. 137, p. 120901, 2012.

[265] S. Grimme, J. Antony, S. Ehrlich, and H. Krieg *J. Chem. Phys.*, vol. 132, p. 154104, 2010.

[266] A. Tkatchenko and M. Scheffler *Phys. Rev. Lett.*, vol. 102, p. 073005, 2009.

[267] M. Dion, H. Rydberg, E. S. D. C. Langreth, and B. I. Lundqvist *Phys. Rev. Lett.*, vol. 92, p. 246401, 2004.

[268] G. Román-Prez and J. M. Soler *Phys. Rev. Lett.*, vol. 103, p. 096102, 2009.

[269] O. A. von Lilienfeld and A. Tkatchenko *J. Chem. Phys.*, vol. 132, p. 234109, 2010.

[270] A. Tkatchenko, R. A. DiStasio, R. Car, and M. Scheffler *Phys. Rev. Lett.*, vol. 108, p. 236402, 2012.

[271] P. Sony, P. Puschnig, D. Nabok, and C. Ambrosch-Draxl *Phys. Rev. Lett.*, vol. 99, p. 176401, 2007.

[272] J. Brede, N. Atodiresei, S. Kuck, P. Lazić, V. Caciuc, Y. Morikawa, G. Hoffmann, S. Blügel, and R. Wiesendanger *Phys. Rev. Lett.*, vol. 105, p. 047204, 2010.

[273] N. Atodiresei, V. Caciuc, P. Lazić, and S. Blügel *Phys. Rev. Lett.*, vol. 102, p. 136809, 2009.

[274] M. T. Nguyen, C. A. Pignedoli, T. M. Treier, R. Fasel, and D. Passerone *Phys. Chem. Chem. Phys.*, vol. 12, p. 992, 2010.

[275] A. Liebsch *Phys. Scr.*, vol. 35, p. 354, 1987.

[276] J. F. Dobson, K. McLennan, A. Rubio, J. W., T. Gould, H. M. Le, and B. P. Dinte *Aust. J. Chem.*, vol. 54, p. 513, 2001.

[277] J. F. Dobson, J. Wang, B. P. Dinte, K. McLennan, and H. M. Le *Int. J. Quant. Chem*, vol. 101, p. 579, 2005.

[278] G. Mercurio, E. R. McNellis, I. Martin, S. Hagen, F.Leyssner, S. Soubatch, J. Meyer, M. Wolf, P. Tegeder, F. S. Tautz, and K. Reuter *Phys. Rev. Lett.*, vol. 104, p. 036102, 2010.

[279] E. R. M. J. Meyer and K. Reuter *Phys. Rev. B*, vol. 80, p. 205414, 2009.

[280] K. Tonigold and A. Größ *J. Chem. Phys.*, vol. 132, p. 224701, 2010.

[281] Q.-M. Hu, K. Reuter, and M. Scheffler *Phys. Rev. Lett.*, vol. 98, p. 176103, 2007.

[282] V. G. Ruiz, W. Liu, E. Zojer, M. Scheffler, and A. Tkatchenko *Phys. Rev. Lett.*, vol. 108, p. 146103, 2012.

[283] E. M. Lifshitz *Sov. Phys. JETP*, vol. 2, p. 73, 1956.

[284] E. Zaremba and W. Kohn *Phys. Rev. B*, vol. 13, p. 2270, 1976.

[285] S. V. Aradhya, M. Frei, M. S. Hybertsen, and L. Venkataraman *Nat. Mater.*, vol. 11, p. 872, 2012.

[286] R. Hoffmann *Rev. Mod. Phys.*, vol. 60, p. 601, 1989.

[287] D. Sánchez-Portal, E. Artacho, and J. M. Soler *J. Phys.: Cond. Matter*, vol. 8, p. 3859, 1996.

[288] D. Sánchez-Portal, J. M. Soler, and E. Artacho *Solid State Commun.*, vol. 95, p. 685, 1995.

[289] M. D. Segall, R. S. C. J. Pickard, and M. C. Payne *Mol. Phys.*, vol. 89, p. 571, 1996.

[290] R. S. Mulliken *J. Chem. Phys.*, vol. 23, p. 1833, 1955.

[291] R. S. Mulliken *J. Chem. Phys.*, vol. 36, p. 3428, 1962.

[292] P.-O. Lwdin *Avd. Quant. Chem.*, vol. 5, p. 185, 1970.

[293] M. D. Segall, R. S. C. J. Pickard, and M. C. Payne *Phys. Rev. B*, vol. 54, p. 16317, 1996.

[294] R. F. W. Bader, *Atoms in molecules: A quantum theory.* Oxford: Oxford University Press, 1990.

[295] R. F. W. Bader *Chem. Rev.*, vol. 91, p. 893, 1991.

[296] B. B. Stefanov and J. Cioslowski *J. Comput. Chem*, vol. 16, p. 1394, 1995.

[297] G. Henkelman, A. Arnaldsson, and H. Jónsson *Comput. Mat. Sci.*, vol. 36, p. 354, 2006.

[298] W. Tang, E. Sanville, and G. Henkelman *J. Phys.: Condens. Matt.*, vol. 21, p. 1, 2009.

[299] E. Sanville, S. D. Kenny, and R. S. G. Henkelman *J. Comput. Chem.*, vol. 28, p. 899, 2006.

[300] G. Binnig and H. Rohrer *IBM Journal of Research and Development*, vol. 30, p. 4, 1986.

[301] J. Tersoff and D. R. Hamann *Phys. Rev. Lett.*, vol. 50, p. 1998, 1983.

[302] J. Tersoff and D. R. Hamann *Phys. Rev. B*, vol. 31, p. 805, 1985.

[303] J. Bardeen *Phys. Rev. Lett.*, vol. 6, p. 57, 1961.

[304] N. D. Lang *Phys. Rev. B*, vol. 34, p. 5497, 1986.

[305] A. Selloni, P. Carnevali, E. Tosatti, and C. D. Chen *Phys. Rev. B*, vol. 31, p. 2602, 1985.

[306] W. A. Hofer, A. S. Foster, and A. L. Shluger *Rev. Mod. Phys.*, vol. 75, p. 1287, 2003.

[307] D. Wortmann, S. Heinze, P. Kurz, G. Bihlmayer, and S. Blügel *Phys. Rev. Lett.*, vol. 86, p. 4132, 2001.

[308] S. Heinze, K. von Bergmann, M. Menzel, J. Brede, A. Kubetzka, R. Wiesendanger, G. Bihlmayer, and S. Blgel *Nat. Phys.*, vol. 7, p. 713, 2011.

[309] M. Bode, M. Heide, K. von Bergmann, P. Ferriani, S. Heinze, G. Bihlmayer, A. Kubetzka, O. Pietzsch, S. Blügel, and R. Wiesendanger *Nature*, vol. 447, p. 190, 2007.

[310] R. García and R. Pérez *Surf. Sci. Rep.*, vol. 47, pp. 197–301, 2002.

[311] F. J. Giessibl *Rev. Mod. Phys.*, vol. 75, p. 949, 2003.

[312] U. Landman, W. D. Luedtke, N. A. Burnham, and R. J. Colton *Science*, vol. 248, p. 454, 1990.

[313] F. F. Canova and A. S. Foster *Nanotechnology*, vol. 22, p. 045702, 2011.

[314] T. Trevethan, L. Kantorovich, J. Polesel-Maris, and S. Gauthier *Nanotechnology*, vol. 18, p. 084017, 2007.

[315] T. Trevethan, M. Watkins, L. Kantorovich, and A. L. Shluger *Phys. Rev. Lett.*, vol. 98, p. 028101, 2007.

[316] R. A. Bennewitz, A. S. Foster, L. N. Kantorovich, M. Bammerlin, C. Loppacher, S. Schär, M. Guggisberg, E. Meyer, and A. L.Shluger *Phys. Rev. B*, vol. 62, p. 2074, 2000.

[317] P. Pou, S. A. Ghasemi, P. Jelinek, T. Lenosky, S. Goedecker, and R. Perez *Nanotechnology*, vol. 20, p. 264015, 2009.

[318] R. Pérez, M. C. Payne, I. Stich, and K. Terakura *Phys. Rev. Lett.*, vol. 78, p. 678, 1997.

[319] A. Sweetman, S. Jarvis, R. Danza, J. Bamidele, S. Gangopadhyay, G. A. Shaw, L. Kantorovich, and P. Moriarty *Phys. Rev. Lett.*, vol. 106, p. 136101, 2011.

[320] L. Kantorovich and C. Hobbs *Phys. Rev. B*, vol. 73, p. 245420, 2006.

[321] C. Argento and R. H. French *J. Appl. Phys.*, vol. 80, p. 6081, 1996.

[322] M. Ondráček, P. Pou, V. Rozsíval, C. González, P. Jelínek, and R. Pérez *Phys. Rev. Lett.*, vol. 106, p. 176101, 2011.

[323] M. Ashino, A. Schwarz, T. Behnke, and R. Wiesendanger *Phys. Rev. Lett.*, vol. 93, p. 136101, 2004.

[324] A. Sadeghi, A. Baratoff, S. A. Ghasemi, S. Goedecker, T. Glatzel, S. Kawai, and E. Meyer *Phys. Rev. B*, vol. 86, p. 075407, 2012.

[325] D. Jiang, M.-H. Du, and S. Dai *J. Chem. Phys.*, vol. 130, p. 074705, 2009.

[326] B. Wang, S. Günther, J. Wintterlin, and M. L. Bocquet *New J. Phys.*, vol. 12, p. 043041, 2010.

[327] M. Hasegawa and K. Nishidate *Phys. Rev. B*, vol. 70, p. 205431, 2004.

[328] R. Zacharia, H. Ulbricht, and T. Hertel *Phys. Rev. B*, vol. 69, p. 155406, 2004.

[329] Y. X. Zhao and I. L. Spain *Phys. Rev. B*, vol. 40, p. 993, 1989.

[330] S. Lizzit, R. Larciprete, P. Lacovig, K. L. Kostov, and D. Menzel *ACS Nano, article ASAP*, 2013.

[331] N. Armbrust, J. Güdde, P. Jakob, and U. Höfer, ")," *Phys. Rev. Lett.*, vol. 108, p. 056801, 2012.

[332] J. Lu, P. E. Yeo, C. K. Gan, P. Wu, and K. P. Loh *Nature Nanotech.*, vol. 6, p. 247, 2011.

[333] Y. Pan, H. Zhang, D. Shi, J. Sun, S. Du, F. Liu, and H.-J. Gao *Adv. Mater.*, vol. 20, p. 1, 2008.

[334] C. Corriol, J. Hager, R. Matzdorf, and A. Arnau *Surf. Sci.*, vol. 600, p. 4310, 2006.

[335] C. Enderlein, Y. S. Kim, E. Rotenberg, and K. Horn *New J. Phys.*, vol. 12, p. 033014, 2010.

[336] O. Pfeiffer, L. Nony, R. Bennewitz, A. Baratoff, and E. Meyer *Nanotechnology*, vol. 15, p. S101, 2004.

[337] W. Denk and D. W. Pohl *Appl. Phys. Lett.*, vol. 59, p. 2171, 1991.

[338] F. J. Giessibl *Appl. Phys. Lett.*, vol. 78, p. 123, 2001.

[339] W. R. Morita S. and M. E., *Noncontact atomic force microscopy.* New York: Springer, 2002.

[340] S. J. Altenburg, J. Kröger, B. Wang, M.-L. Bocquet, N. Lorente, and R. Berndt *Phys. Rev. Lett.*, vol. 105, p. 236101, 2010.

[341] T. Kistenmacher, T. Phillips, and D. Cowan *Acta Crystallogr., Sect. B: Struct. Crystallogr. Cryst. Chem*, vol. 30, p. 763, 1974.

[342] G. A. T. et al. *Phys. Rev. B*, vol. 13, p. 5205, 1976.

[343] M. Sing, U. Schwingenschlögl, R. Claessen, P. Blaha, J. M. P. Carmelo, L. M. Martelo, P. D. Sacramento, M. Dressel, and C. S. Jacobsen *Phys. Rev. B*, vol. 68, p. 125111, 2003.

[344] W. D. Grobman, R. A. Pollak, D. E. Eastman, E. T. Maas, and B. A. Scott *Phys. Rev. Lett.*, vol. 32, p. 534, 1974.

[345] N. Gonzalez-Lakunza, I. Fernández-Torrente, K. J. Franke, N. Lorente, A. Arnau, and J. I. Pascual *Phys. Rev. Lett.*, vol. 100, p. 156805, 2008.

[346] M. J. Frisch, G. W. Trucks, H. B. Schlegel, G. E. Scuseria, M. A. Robb, J. R. Cheeseman, G. Scalmani, V. Barone, B. Mennucci, G. A. Petersson, H. Nakatsuji, M. Caricato, X. Li, H. P. Hratchian, A. F. Izmaylov, J. Bloino, G. Zheng, J. L. Sonnenberg, M. Hada, M. Ehara, K. Toyota, R. Fukuda, J. Hasegawa, M. Ishida, T. Nakajima, Y. Honda, O. Kitao, H. Nakai, T. Vreven, J. A. Montgomery, Jr., J. E. Peralta, F. Ogliaro, M. Bearpark, J. J. Heyd, E. Brothers, K. N. Kudin, V. N. Staroverov, R. Kobayashi, J. Normand, K. Raghavachari, A. Rendell, J. C. Burant, S. S. Iyengar, J. Tomasi, M. Cossi, N. Rega, J. M. Millam, M. Klene, J. E. Knox, J. B. Cross, V. Bakken, C. Adamo, J. Jaramillo, R. Gomperts, R. E. Stratmann, O. Yazyev, A. J. Austin, R. Cammi, C. Pomelli, J. W. Ochterski, R. L. Martin, K. Morokuma, V. G. Zakrzewski, G. A. Voth, P. Salvador, J. J. Dannenberg, S. Dapprich, A. D. Daniels, . Farkas, J. B. Foresman, J. V. Ortiz, J. Cioslowski, and D. J. Fox, "Gaussian 09 Revision A.1." Gaussian Inc. Wallingford CT 2009.

[347] R. H. Boyd and W. D. Philips *J. Chem. Phys.*, vol. 43, p. 2927, 1965.

[348] I. Garcia-Yoldi, J. S. Miller, and J. J. Novoa *J. Phys. Chem. A*, vol. 113, p. 7142, 2009.

[349] J. Huang and S. K. M. Kertesz *Phys. Chem. Chem. Phys.*, vol. 10, p. 2625, 2009.

[350] J. S. Miller, A. J. Epstein, and W. M. Reif *Science*, vol. 240, p. 40, 1988.

[351] J. M. Manriquez and et al. *Science*, vol. 252, p. 1415, 1991.

[352] W. E. Broederick, J. A. Thompson, E. P. Day, and B. M. Hoffmann *Science*, vol. 249, p. 401, 1990.

[353] H. Zhao and et al. *Chem. Mater.*, vol. 11, p. 736, 1999.

[354] R. Chiarelli, M. A. Novak, A. Rassat, and J. L. Tholence *Nature*, vol. 363, p. 147, 1993.

[355] M. Tamura and et al. *Chem. Phys. Lett.*, vol. 4, p. 401, 1991.

[356] Y. Nakazawa and et al. *Phys. Rev. B*, vol. 46, p. 8906, 1992.

[357] F. Palacio *Phys. Rev. Lett.*, vol. 79, p. 2336, 1997.

[358] S. J. Blundell and F. L. Prat *J. Phys.:Condens. Matter*, vol. 16, p. R771, 2004.

[359] Y. Nagaoka *Phys. Rev.*, vol. 147, p. 392, 1966.

[360] A. Mielke *Phys. Rev. Lett.*, vol. 69, p. 1608, 1992.

[361] D. Hobbs and G. Kresse *Phys. Rev. B*, vol. 62, p. 11556, 2000.

[362] J. H. P. Blønski *J. Phys.: Condens. Matter*, vol. 21, p. 426001, 2009.

[363] "Turbomole 6.3 2011." , a development of University of Karlsruhe and Forschungszentrum Karlsuhe GmbH, 1989-2007, TURBOMOLE GmbH, since 2007; available from http://www.turbomole.com.

[364] A. Shafer, C. Huber, and R. Alrichs *J. Chem. Phys.*, vol. 100, p. 5829, 1994.

[365] J. Hubbard *Proc. Roy. Soc.*, vol. 276, p. 238, 1963.

[366] A. A. Altland and B. Simons, *Condensed Matter Field Theory.* Cambridge: Cambridge University Press, 2006.

[367] H. Tasaki *Phys. Rev. Lett.*, vol. 69, p. 1608, 1992.

[368] R. Arita and et al. *Phys. Rev. Lett.*, vol. 88, p. 127202, 2002.

[369] I. Giaever *Phys. Rev. Lett.*, vol. 5, p. 147, 1960.

[370] G. Binnig and D. P. E. Smith *Rev. Sci. Instr.*, vol. 57, p. 1688, 1986.

[371] R. Wiesendanger, I. V. Shvets, D. Bürgler, G. Tarrach, H. J. Gujntherodt, J. M. D. Coey, and S. Graser *Science*, vol. 255, p. 583, 1992.

[372] R. Wiesendanger, H.-J. Güntherodt, G. Güntherodt, R. J. Gambino, and R. Ruf *Phys. Rev. Lett.*, vol. 65, p. 247, 1990.

[373] R. Wiesendanger *Rev. Mod. Phys.*, vol. 81, p. 1495, 2009.

[374] S. Heinze, M. Bode, A. Kubetzka, O. Pietzsch, X. Nie, S. Blügel, and R. Wiesendanger *Science*, vol. 288, p. 1805, 2000.

[375] A. C. Hewson, *The Kondo problem to heavy fermions*. Cambridge: Cambridge University Press, 1993.

[376] G. D. Scott and D. Natelson *ACS Nano*, vol. 7, p. 3560, 2010.

[377] J. Kondo *Prog. Theor. Phys.*, vol. 37, p. 32, 1964.

[378] J. P. Frank, F. D. Manchester, and D. L. Martin *Proceedings of the Royal Society of London. Series A. Mathematical and Physical Sciences*, vol. 263, p. 494, 1961.

[379] K. Yosida *Phys. Rev.*, vol. 223, p. 147, 1966.

[380] V. Madhavan, W. Chen, T. Jamneala, M. F. Crommie, and N. S. Wingreen *Science*, vol. 280, p. 567, 1998.

[381] J. Li, W.-D. Schneider, R. Berndt, and B. Delley, "Kondo scattering observed at a single magnetic impurity," *Phys. Rev. Lett.*, vol. 80, p. 2893, 1998.

[382] U. Fano *Phys. Rev.*, vol. 6, p. 1866, 1961.

[383] A. E. Miroshnichenko, S. Flach, and Y. S. Kivshar *Rev. Mod. Phys.*, vol. 82, p. 2257, 2010.

[384] V. Madhavan, W. Chen, T. Jamneala, and M. F. Crommie *Phys. Rev. B*, vol. 64, p. 165412, 2001.

[385] O. Újsághy, J. Kroha, L. Szunyogh, and A. Zawadowski, "Theory of the fano resonance in the stm tunneling density of states due to a single kondo impurity," *Phys. Rev. Lett.*, vol. 85, p. 2557, 2000.

[386] P. Wahl, L. Diekhöner, G. Wittich, L. Vitali, M. A. Schneider, and K. Kern, "Kondo effect of molecular complexes at surfaces: Ligand control of the local spin coupling," *Phys. Rev. Lett.*, vol. 95, p. 166601, 2005.

[387] V. Iancu, A. Deshpande, and S.-W. Hla *Phys. Rev. Lett.*, vol. 97, p. 266603, 2006.

[388] T. e. a. Choi *Nano Lett.*, vol. 10, p. 4175, 2010.

[389] G. Meyer and N. M. Amer *Appl. Phys. Lett.*, vol. 53, p. 2400, 1988.

[390] T. R. Albrecht, P. Grütter, D. Horne, and D. Rugar *J. Appl. Phys.*, vol. 69, p. 668, 1991.

[391] D. J. Griffiths, *Introduction to Electrodynamics*. New Jersey: Prentice-Hall, 1999.

[392] M. Nonnenmacher, M. Oboyle, and H. K. Wickramasinghe *Appl. Phys. Lett.*, vol. 58, p. 2921, 1991.

[393] T. Glatzel, S. Sadewasser, and M. C. Lux-Steiner *Appl. Surf. Sci.*, vol. 210, p. 84, 2003.

[394] S. Sadewasser and M. Lux-Steiner *Phys. Rev. Lett.*, vol. 91, p. 266101, 2003.

[395] S. Sadewasser, T. Glatzel, R. Shikler, Y. Rosenwaks, and M. C. Lux-Steiner *Appl. Surf. Sci.*, vol. 210, p. 32, 2003.

[396] S. Sadewasser, P. Carl, T. Glatzel, and M. Lux-Steiner *Appl. Surf. Sci.*, vol. 210, p. 84, 2004.

[397] B. Cappella and G. Dietler *Surf. Sci. Rep.*, vol. 1, p. 34, 1999.

[398] H. Hölscher, S. M. Langkat, A. Schwarz, and R. Wiesendanger *Appl. Phys. Lett.*, vol. 81, p. 4428, 2002.

[399] J. E. Sader and S. P. Jarvis *Appl. Phys. Lett.*, vol. 84, pp. 1801–1803, 2004.

[400] M. Guggisberg, M. Bammerlin, C. Loppacher, O. Pfeiffer, A. Abdurixit, V. Barwich, R. Bennewitz, A. Baratoff, E. Meyer, and H.-J. Güntherodt *Phys. Rev. B*, vol. 61, p. 11151, 2000.

[401] S. Jarvis, A. Sweetman, J. Bamidele, L. Kantorovich, and P. Moriarty *Phys. Rev. B*, vol. 85, p. 235305, 2012.

[402] A. Sweetman, S. Jarvis, R. Danza, J. Bamidele, S. Gangopadhyay, G. A. Shaw, L. Kantorovich, and P. Moriarty *Phys. Rev. Lett.*, vol. 106, p. 136101, 2011.

Publications

List of publications related to this thesis:

1. Role of Dispersion Forces in the Structure of Graphene Monolayers on Ru Surfaces.
   Stradi D, Barja S, Díaz C, Garnica M, Borca B, Hinarejos J J, Sánchez-Portal D, Alcamí, Arnau A, Vázquez de Parga A L, Miranda R, Martín F
   Physical Review Letters 106, 186102 (2011).
2. Electron localization in epitaxial graphene on Ru(0001) determined by moiré corrugation.
   Stradi D, Barja S, Díaz C, Garnica M, Borca B, Hinarejos J J, Sánchez-Portal D, Alcamí, Arnau A, Vázquez de Parga A L, Miranda R, Martín F
   Physical Review B, 85, 121404(R) (2012).
3. Elastic response of graphene nano domes.
   Koch S, Stradi D, Gnecco E, Barja S, Kawai S, Díaz C, Alcamí M, Martín F, Vázquez de Parga A L, Miranda R, Glatzel T, Meyer E
   ACS Nano, 7, 2927 (2013)
4. Long-range magnetic order in a purely organic 2D layer adsorbed on epitaxial graphene.
   Garnica M, Stradi D, Barja S, Calleja F, Díaz C, Alcamí M, Martín N, Vázquez de Parga A L, Martín F, Miranda R
   Nature Physics, 9, 368 (2013)
5. Lattice-matched versus lattice-mismatched models to describe epitaxial monolayer graphene on Ru(0001)
   Stradi D, Barja S, Díaz C, Garnica M, Borca B, Hinarejos J J, Sánchez-Portal D, Alcamí, Arnau A, Vázquez de Parga A L, Miranda R, Martín F
   Submitted

List of publications not related to this thesis:

1. Grazing incidence scattering of vibrationally excited H_2 molecules from metal surfaces.
   Stradi D*, Díaz C, Martín F
   Surface Science 604, 2031 (2010)
2. A density functional theory study of manganese-phthalocyanine.
   Stradi D*, Díaz C, Martín F, Alcamí M
   Theoretical Chemistry Account 128, 497-493 (2011)
3. Ordered arrays of metal-organic magnets at surfaces.
   Barja S, Stradi D, Borca B, Garnica M, Díaz C, Rodríguez-Garcia M J, Alcamí M, Vázquez de Parga A L, Martín F, Miranda R
   J. Phys.: Condens. Matter, Accepted (2013)
4. TCNQ self-assembly on Cu(111).
   Stradi D*, Borca B, Barja S, Garnica M, Díaz C, Rodríguez-Garcia M J, Alcamí M, Vázquez de Parga A L, Martín F, Miranda R
   Submitted